Direct Detection of Brown Dwarf Companions of Nearby Stars

Thesis by

Ben R. Oppenheimer

In partial fulfillment of the requirements

for the degree of

Doctor of Philosophy

California Institute of Technology

Pasadena, California

1999

(Submitted April 30, 1999)

Acknowledgements

I thank first and foremost my advisor Shri Kulkarni. Though we've had rough times now and then, Shri has been incredibly supportive of me and gone far beyond the call of duty. He had the foresight to know when to give me independence and when to be intimately involved in my work. He also had the ability and power to protect my interests and to provide for my research needs. Most importantly, though, he motivated me to improve myself, showed me, by example, what makes a first-rate researcher and taught me the essence of cutting-edge science.

In the same vein I thank Richard Dekany, who, with the whole Palomar Adaptive Optics Team, including Anand Sivaramakrishnan, Dean Palmer, Gary Brack, Kent Wallace, Mitchell Troy, Eric Bloemhof, and our Cornell collaborators Tom Hayward and Bernhard Brandl, taught me the type of thinking required to produce a functioning, extremely complex device. Go AO!!

To my other collaborators in science, particularly Tadashi Nakajima, Keith Matthews, David Golimowski, Gibor Basri and John Stauffer, I owe a tremendous debt of gratitude for being patient and willing to teach me and for joining me in that most pleasurable part of the scientific process when ideas are being formed and later taken to an evolved, mature state. Adam Burrows and Didier Saumon have been true allies and an absolute pleasure to work with.

The crew at Palomar Observatory deserve nothing less than a million dollar raise each. In my 150 or so nights at Palomar, I came to know Skip, Rick, Karl, Kevin and Jean. Without them I never would have gotten one bit of data, nor enjoyed those

cloudy or snowy nights in the expletive-stricken data room. In the day time, Bob Thicksten keeps a tight ship, with the able hands of Merle, Steve, Dave, John, Greg and a bunch of others, who helped me to no end. Without them there would be no observatory. At the same time, Dr. Brucato and Anna-Marie and later Carlton kept things operating smoothly and were ever flexible. Thank you all. Thanks, also, to Martyn Burke who kept me and Keith company on so many observing runs and who took us to see himself in action too.

Certain friends of mine have given me far more than I have deserved. I could not be happier to have met Penelope Kneebone, who has shown me a level of respect between two people I have never before known. To her I owe my deepest feelings. Her selflessness, love and happy energy made the past year not only possible but one of the happiest of my life. I also thank her family down-under who have been shockingly supportive and loving.

Martin Kirby has been a true friend to me. Thank you for talking to me in that bar. Who would have known we would hit it off so well?

Gautam Vasisht, Erik Leitch and I formed the D Office (thanks to Nick Scoville). It has now evolved into Super D with Kurt Adelberger and Josh Bloom. Kurt provided the sanity of frequent breaks with excellent conversations. (We must have about 30 short stories to write up.) Thanks to Josh and Erik for taking my abuse lightly and perhaps someday you will meet Burton Sturton in Fundunst. I can never repay Gautam for being the rare kind of intimate friend whom you can be apart from for ages and see again only to resume the friendship without skipping a beat. Martin Shepherd deserves heartfelt thanks for coming to the office in the wee hours of the night to help me and to give me sane company. Marc Kuchner and Olga Itkin were both extremely tolerant neighbors and good friends. To Brad Behr and Brian Kern I send a hearty Futdism.

I must thank my other friends outside of Caltech as well: Kathryn Zally I thank

for providing the refuge of her wonderful and intimate companionship for more than half of my time at Caltech. I learned so much from her at Columbia and in California. Vast thanks to my college friends Chad Finely, David Fisher, Stevus Levitt, Oradee Imvised, Jay Demas and Krammit Jureidini. The Leicester crowd, in particular Simon Hodgkin and Richard Jameson, command deep respect in me. Simon and I have a bit of an adventure in store for us. May it be as good as it has been, but a must is more carousing in other cities of the world. Peter, Renata and Shawn Landres were there for me so many times and made me feel welcome and at-home in this bizarre part of the country. I thank them for being patient with me, especially in the last few months of this work. It is also a pleasure to have met Maurice Gregory and the wonderful Theo and Sallie ten Brummelaar. I thank Betsy Davis for having the nerve to contact me and for being an excellent friend who thinks alike.

David Helfand was an invaluable source of advice and friendship, and, after all, the man who really convinced me that this astronomy nonsense is for me. I will never be able to repay him. Professor Padmanabhan, thank you for the bad movies, good driving, excellent derivations and friendship.

Finally, it is to my mother, father and sister, Linda Rässa, Paul Oppenheimer and Julie Oppenheimer, that I owe everything. They unfailingly supported me and encouraged me to be true to my own passions, even if sometimes those passions were inscrutable. The friendship we have is, I believe, truly rare among family members. The same goes for Peter Kamali, my cousin, Gertrude Samuels, my Gram, and Mama and Volli Smit, my grandparents. Thank you for believing in me and loving me. My only regret is that Fred Oppenheimer, my Opa, could not live to see me finish this project. Futdi, Poto, Bayris, Zinke and Zephir provided comfort and affection and influenced me in ways I am still realizing. I thank Futdi by the fact that her name appears at least 18 times in this thesis.

Abstract

This thesis presents the first direct detection of a substellar companion of a star other than the Sun. This object, a brown dwarf called Gliese 229B, presented a unique opportunity to characterize low-temperature brown dwarfs for the first time. The discovery and initial spectrum of Gliese 229B show that the object must be substellar based on its intrinsic luminosity of $6.4 \times 10^{-6}\ L_{\odot}$ and its cool surface temperature, 900 K. Detailed study of Gliese 229B includes extensive photometric measurements from 0.5 to 12 μm, high signal-to-noise ratio spectroscopy from 0.84 to 5.0 μm and the detection of $0\farcs1\ \mathrm{yr}^{-1}$ of orbital motion. These results are presented in Chapters 2 and 3.

A detailed review of brown dwarf science leads to a complete and scientifically meaningful definition of the classes "planet" and "brown dwarf" in Chapter 1.

After the discovery of Gliese 229B, which was found in a survey for companions of young stars, we began an extensive search for brown dwarf companions in orbit about all known stars within 8 pc of the Sun and with $\delta > -35°$. The search includes optical coronagraphic and infrared direct imaging of these stars, conducted on the Palomar 60" and 200" telescopes respectively. The search was designed to find companions of each star without color bias. While the search revealed no other brown dwarf companions of these stars, it did uncover 6 new stellar companions. The sensitivity limits of the survey permit the detection of brown dwarfs up to four magnitudes fainter than Gliese 229B around 90% of the stars. The sensitivity is, however, not uniform spatially or from star to star. This limits our ability to make

strong statements about the prevalence of brown dwarf companions of nearby stars. The survey does have sensitivity to all stellar companions between 3 and 30″ from the survey stars, however.

Chapter 5 describes related work on very low-mass stars in the Pleiades star cluster. This optical spectroscopy involved trying to find a brown dwarf member of the Pleiades by identifying lithium absorption features. We revealed no brown dwarf members of the Pleiades but did discover two members with ages much younger than the age of the Pleiades (120 Myr). We provide an adequate explanation for the presence of these stars.

The three appendices summarize work conducted in association with the Palomar Adaptive Optics System. The work includes (1) the detailed study and characterization of the deformable mirror, (2) invention of a fast calibration scheme for the deformable mirror and (3) the design and implementation of the fast steering mirror.

Contents

List of Tables

List of Figures

Chapter 1

Brown Dwarfs[†]

B. R. Oppenheimer, S. R. Kulkarni

Palomar Observatory 105-24, California Institute of Technology, Pasadena, CA 91125, USA

and

J. R. Stauffer

Harvard–Smithsonian Center for Astrophysics, Cambridge, MA 00165, USA

Abstract

After a discussion of the physical processes in brown dwarfs, we present a complete, precise definition of brown dwarfs and of planets inspired by the internal physics of objects between 0.1 and 0.001 $M_\odot$. We discuss observational techniques for characterizing low-luminosity objects as brown dwarfs, including the use of the lithium test and cooling curves. A brief history of the search for brown dwarfs leads to a detailed review of known isolated brown dwarfs with emphasis on those in the Pleiades star cluster. We also discuss brown dwarf companions to nearby stars, paying particular attention to Gliese 229B, the only known cool brown dwarf.

[†]Previously published in *Protostars and Planets IV*, V. Manning, A. Boss, S. Russell eds. (Tucson: University of Arizona Press) 1999.

1.1 What is a Brown Dwarf?

A main sequence star is to a candle as a brown dwarf is to a hot poker recently removed from the fire. Stars and brown dwarfs, although they form in the same manner, out of the fragmentation and gravitational collapse of an interstellar gas cloud, are fundamentally different because a star has a long-lived internal source of energy: the fusion of hydrogen into helium. Thus, like a candle, a star will burn constantly until its fuel source is exhausted. A brown dwarf's core temperature is insufficient to sustain the fusion reactions common to all main sequence stars. Thus brown dwarfs cool as they age. Cooling is perhaps the single most important salient feature of brown dwarfs, but an understanding of their definition and their observational properties requires a review of basic stellar physics.

1.1.1 Internal Physics

In stellar cores, nuclear fusion acts as a strict thermostat maintaining temperatures very close to the nuclear fusion temperature, $T_{\rm nucl} = 3 \times 10^6$ K, the temperature above which hydrogen fusion becomes possible. In the stellar core, the velocities of the protons obey a Maxwell-Boltzmann distribution. However, the average energy of one of these protons is only $kT_{\rm nucl} = 8.6 \times 10^{-8} T$ keV ~ 0.1 keV, where k is the Boltzmann constant. In contrast, the Coulomb repulsion between these protons is on the order of MeV. Despite this enormous difference in energies, fusion is possible because of quantum mechanical tunneling. The nuclear reaction rate is governed by the proton pair energy, E, at the high energy tail of the Maxwell-Boltzmann distribution, which scales as $\exp(-E/kT)$, and the nuclear cross section due to quantum mechanical tunneling through the Coulomb repulsion, which scales as $\exp(-E^{-1/2})$. The product of these two factors defines a sharp peak, the Gamov peak, at a critical energy $E_{\rm crit}$. $E_{\rm crit}$ is approximately 10 keV for the reactions in the pp chain, the most basic form of

hydrogen fusion. Because $E_{\rm crit} >> kT$, the nuclear reactions involve the tiny minority of protons in the high velocity tail of the Maxwell-Boltzmann distribution. In terms of temperature, this reaction rate is proportional to $(T/T_{\rm nucl})^n$ where $n \approx 10$ for temperatures near $T_{\rm nucl}$ and reactions in the pp chain. The large value of n ensures that the core temperature is close to $T_{\rm nucl}$.

For the low-mass main sequence stars in which the above discussion holds, the mass is roughly proportional to the radius. This can be shown with a simplified argument by appealing to the virial theorem. In equilibrium, the thermal energy and the gravitational potential energy are in balance: $GM^2/R \sim (M/m_p)kT_{\rm nucl}$, where m_p is the mass of the proton, M is the mass of the star, R is its radius, and G is the gravitational constant. Therefore, $R \propto M$.

If radius is proportional to mass, then the density, ρ, increases with decreasing mass: $\rho \propto MR^{-3} \propto M^{-2}$. At a high enough density a new source of pressure becomes important. Electrons, because they have half integral spins, must obey the Pauli exclusion principle and are accordingly forbidden from occupying identical quantum energy states. This requires that electrons successively fill up the lowest available energy states. The electrons in the higher energy levels contribute to degeneracy pressure, because they cannot be forced into the filled, lower energy states. The degeneracy pressure, which scales as $\rho^{5/3}$, becomes important when it approximately equals the ideal gas pressure: $\rho T \propto \rho^{5/3}$. Explicit calculation of this relation shows that degeneracy pressure dominates when $\rho > 200$ g cm^{-3} and $T < T_{nucl}$. For the Sun, $\rho \approx 1$ gm cm^{-3}. Using the scaling relations above, one finds that degeneracy pressure becomes important for stars with $M < 0.1 M_\odot$. Objects supported primarily by some sort of degeneracy pressure are called "compact."

An examination of Fig. 1.1 (Burrows and Liebert 1993) demonstrates the key elements described above. This plot of mass versus radius shows the main sequence (labeled "M Dwarfs"), where $R \propto M$, and a line which white dwarfs must obey

because they are completely supported by electron degeneracy pressure. Thus, the energy density of the degenerate electrons ($\propto \rho^{5/3}$) must match the gravitational potential energy density ($GM^2/R/R^3$). In that case, $R \propto M^{-1/3}$. Note that the white dwarf sequence meets the main sequence at about 0.1 $M_\odot$. At this point, the main sequence curve turns and remains at a roughly constant radius for all the masses down to the mass of Jupiter. This mass range, from about 0.1 $M_\odot$ to 0.001 $M_\odot$, has an essentially constant radius because the degeneracy pressure leads to the slow function $R \propto M^{-1/3}$ at the high mass end. Then, at the low mass end the Coulomb pressure, which is characterized by constant density ($\rho \propto M/R^3$ which implies $R \propto M^{+1/3}$), begins to dominate over degeneracy, the net result being approximately $R \propto M^0$ (Burrows and Liebert 1993).

Kumar (1963) calculated the mass at which "star-like" objects could be stable against gravitational collapse through electron degeneracy pressure, instead of ideal gas pressure maintained by energy input from fusion reactions. This mass—the lowest mass at which a star can fuse hydrogen—is now called the "hydrogen burning mass limit" (hereafter abbreviated as HBML). Modern calculations of the HBML place it, for objects of solar metallicity, between 0.080 and 0.070 $M_\odot$ (84 to 73 M_J, where M_J is the mass of Jupiter; Burrows and Liebert 1993, Baraffe et al. 1995).

1.1.2 Definition of "Brown Dwarf" and of "Planet"

The canonical definition of a brown dwarf is a compact object, which has a core temperature insufficient to support sustained nuclear fusion reactions. As shown above, this temperature requirement translates directly into a mass requirement: a brown dwarf's mass must be below the HBML.

This definition does not distinguish planets from brown dwarfs, however. Consensus in the literature on this issue suggests that planets and brown dwarfs be distinguished by their formation processes. Planets form in circumstellar disks while

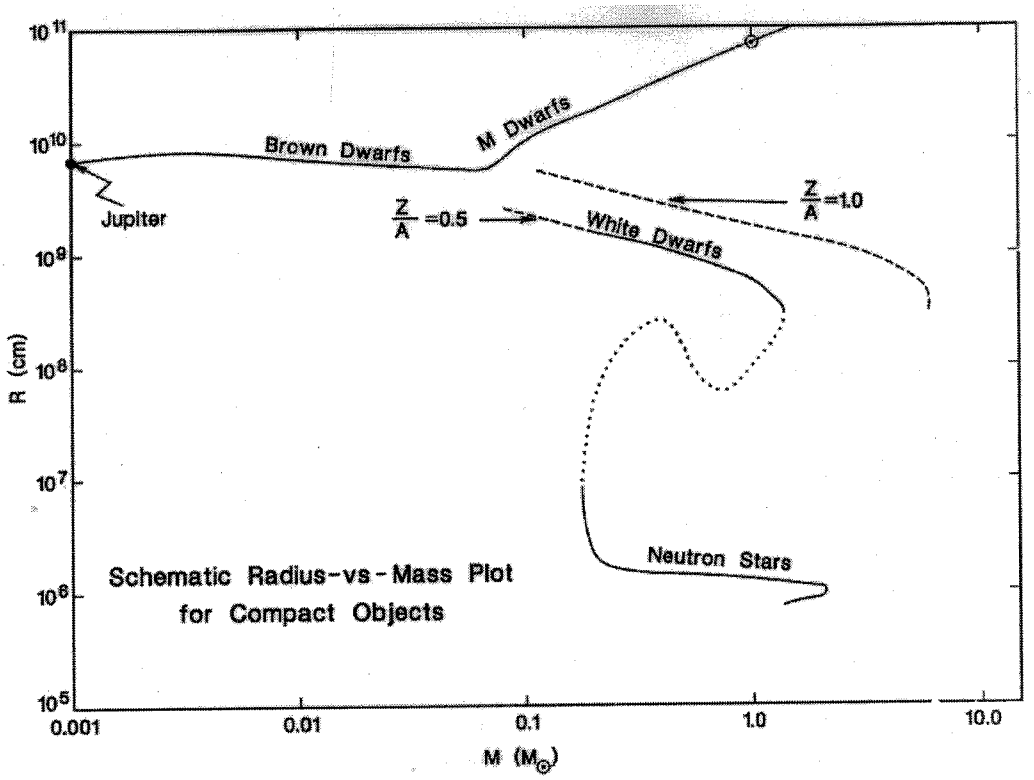

Figure 1.1 Mass versus radius. This plot shows that brown dwarfs have a roughly constant radius as a function of mass. This is important because it makes $T_{\rm eff}$ a function only of luminosity. If $T_{\rm eff}$ is observable then an object can be classified as a brown dwarf or star based on its $T_{\rm eff}$ or luminosity. (See Figure 1.2.) Courtesy A. Burrows. From Burrows and Liebert (1993).

brown dwarfs form out of interstellar gas cloud collapse. This distinction is problematic because there is no simple observable of the birth process. In the case of brown dwarf companions of stars, one might expect the orbit to be rather eccentric about the central star, while the orbit of a planet might be roughly circular (Black 1997). However, as reviewed by Lissauer et al. (1999), planets formed in circumstellar disks can be in highly eccentric orbits.

We propose a new definition of planets as objects for which no nuclear fusion of any kind takes place during the entire history of the object. (As far as we know, the only other attempt to define the term "planet" in the literature is that of Basri and Marcy

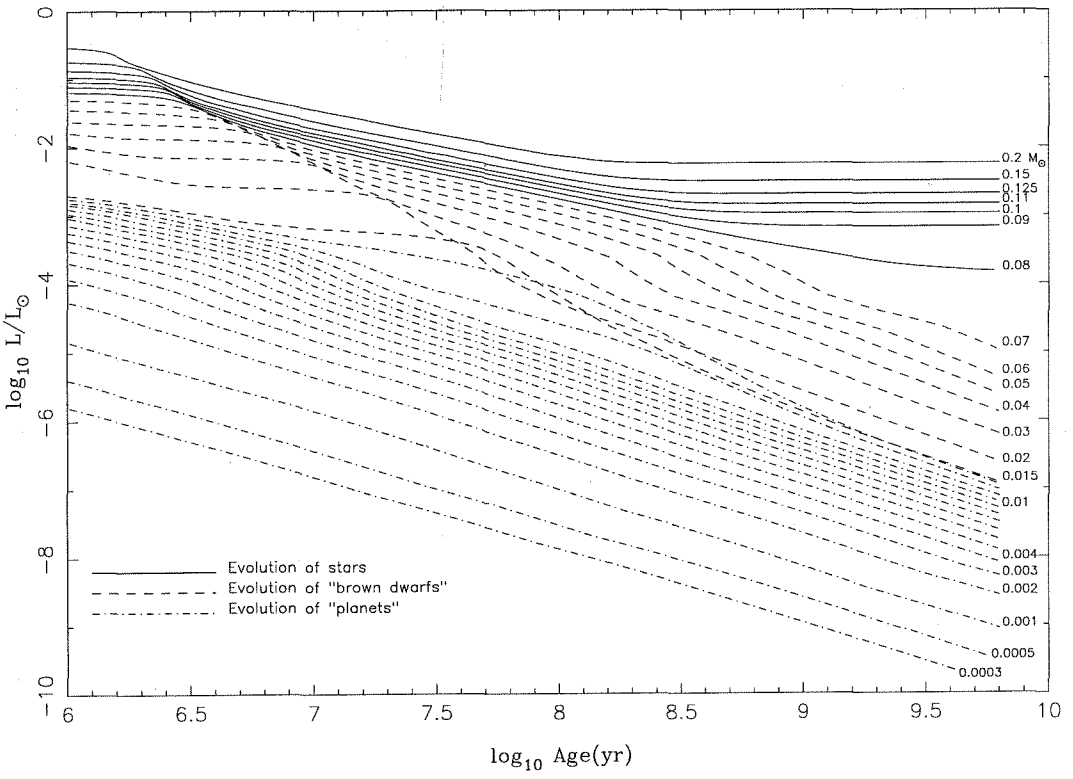

Figure 1.2 Cooling curves for objects with masses between 0.2 and 0.0003 $M_\odot$ from Burrows et al. (1997). Stars, objects above 0.075 $M_\odot$, eventually reach a constant luminosity, whereas brown dwarfs and planets continue to cool throughout their existences. The first knee on the higher mass curves indicates the time when deuterium fusion ends and ceases to be a source of energy. The second knee indicates where grain formation begins. This results in a sudden cooling of the objects. Burrows et al. have called objects below 13 M_J planets only because they never engage in deuterium fusion (see §1.1.2). It is important to note that the minimum luminosity for a star is 10^{-4} $L_\odot$ which corresponds to $T_{\rm eff} = 1800$ K. Courtesy A. Burrows.

(1997), which suggested a scheme similar to the one presented here. Though Burrows et al. (1997) use this same classification scheme, they present it as a purely semantic definition only for the purposes of their paper and do not advocate its replacement of the standard formation-motivated definition. We do.) According to Burrows et al. (1997), objects (at solar metallicity) with masses between 0.08 and 0.013 $M_\odot$ fuse deuterium when they are young. Deuterium undergoes fusion reactions at lower temperatures than hydrogen, primarily because the reaction $\mathrm{D}(p,\gamma)^3\mathrm{He}$ is extremely

rapid, being driven by the electromagnetic force. In contrast, the pp chain, driven by the weak nuclear force, is much slower and therefore less efficient, requiring higher temperatures. A plot of the luminosity evolution of objects between 0.2 and 0.0003 $M_{\odot}$ (Fig. 1.2) illuminates this issue. The very highest mass objects, stars, start out bright but eventually reach an equilibrium luminosity at the right side of the plot. The lower curves, for brown dwarfs and planets, continue to drop in luminosity past 10^{10} yr. The first knee in the upper curves of Fig. 1.2 indicates the age at which deuterium fusion ends, having completely depleted the deuterium fuel. However, for masses below 0.013 $M_{\odot}$, the curves are devoid of this knee because the objects are not even capable of fusing deuterium. These objects are planets. With these precise definitions, planets, brown dwarfs and stars occupy a hierarchy based on their internal physics. Stars fuse hydrogen in equilibrium, brown dwarfs do not fuse hydrogen in equilibrium but do fuse deuterium for some portion of their evolution and planets never fuse anything. Table 1.1 provides a summary of this hierarchy.

TABLE 1.1 SUMMARY OF DEFINITIONS OF STAR, BROWN DWARF AND PLANET

Object Type	Mass ($M_{\odot}$)	H Fusion	D Fusion	Contains Li	Contains D
Star	0.1 – 0.075	sustained	evanescent	no	no
Brown Dwarf	0.075 – 0.065	evanescent	evanescent	yes[†]	no
Brown Dwarf	0.065 – 0.013	never	evanescent	yes	no
Planet	< 0.013	never	never	yes	yes

This table gives the principal salient properties that distinguish stars, planets and brown dwarfs. Masses given here assume the objects have solar metallicity. [†]Brown dwarfs in the 0.075 – 0.065 $M_{\odot}$ range have lithium abundances which are age dependent.

Another justification of these definitions comes from the untested theoretical notion that deuterium fusion and convection, which may lead to magnetic fields and thus mass outflows, might halt the accretion process as these low-mass objects form (Shu et al. 1987). This process would then place the lower limit on the mass of

an object formed in isolation (not in a circumstellar disk) at 0.013 $M_\odot$, because a lower mass object could continue to accrete mass until it exceeded this limit when deuterium burning, and consequently mass outflow, would ensue. Thus, planets could not form the way stars and brown dwarfs do. However, if confirmed, this would be an outcome of the definition, not the overriding principle.

1.1.3 Observational Identification of Brown Dwarfs

There are three principal methods for confirming that a candidate brown dwarf is, in fact, substellar.[†]

Luminosity-Temperature Relation

The definitions presented above have direct consequences for the observations of brown dwarfs, stars and planets. The most obvious distinction between stars and brown dwarfs is illustrated in the cooling curves mentioned above (Fig. 1.2). An object of solar metallicity below 10^{-4} $L_\odot$ cannot be a star, regardless of its age. Intrinsic luminosity, L, is an observable only for objects with known distances. A good, but less sensitive and yet more practical, surrogate for luminosity is effective temperature, $T_{\rm eff} = (L/4\pi R^2\sigma)^{1/4}$, where σ is the Stefan-Boltzmann constant, because, as we demonstrated above, R is essentially constant for objects below the HBML (except very low-mass planets, where only the Coulomb force is important; see Fig. 1.1). Spectral synthesis models are complete enough at this point that comparison of spectra with the models constrains $T_{\rm eff}$ to better than 10% in most cases. A luminosity of 10^{-4} $L_\odot$ corresponds to $T_{\rm eff} = 1800$ K. The cooling curves show that a 0.013 $M_\odot$ brown dwarf reaches this temperature at an age of approximately 100 Myr.

[†] In our discussion of the observations of brown dwarfs we discuss only directly detected objects. For this reason we do not include substellar objects discovered in radial velocity studies. (See Marcy et al. 1999.)

Therefore, this technique for identifying brown dwarfs only works for relatively old and cool objects.

Lithium

Distinguishing young, hot brown dwarfs and planets from stars is easiest with the "lithium test."

The lithium test as proposed by Rebolo et al. (1992) relies on the fact that objects without hydrogen fusion retain their initial lithium abundances forever. This is a direct result of one of the nuclear fusion reactions: $^7\mathrm{Li}(p,\alpha)^4\mathrm{He}$. This reaction effects the complete destruction of lithium in the cores of very low-mass stars in 50 Myr and in brown dwarfs with masses between 0.08 and 0.065 $M_\odot$, which have short lived hydrogen fusion reactions, in 50 to 250 Myr (D'Antona and Mazzitelli 1994, Bildsten et al. 1997). Below 0.065 $M_\odot$ brown dwarfs retain their initial lithium abundances forever because they never host any hydrogen fusion reactions.

Theoretical models show that brown dwarfs and very low-mass stars are fully convective. Thus, the elemental abundances in the core where the putative fusion reactions happen are reflected on the convective timescale in their observable atmospheres. The convective timescale for a brown dwarf is on the order of decades but scales proportional to $L^{1/3}$. In contrast the evolutionary timescale is 6 to 8 orders of magnitude larger (Burrows and Liebert 1993, Bildsten et al. 1997), so core abundances can be assumed identical to atmospheric abundances.

Fig. 1.3 (from Rebolo et al. 1996) shows lithium abundance measurements as a function of $T_{\rm eff}$ for objects in the Pleiades. G and K stars have cosmic lithium abundances, but once $T_{\rm eff}$ reaches the M dwarf regime, the lithium abundance plummets for the reasons explained above. Below 3000 K, young brown dwarfs, such as PPl 15, Teide 1 and Calar 3 (described below), have measurable lithium abundances.

An interesting outcome of the lithium test is that one can accurately determine

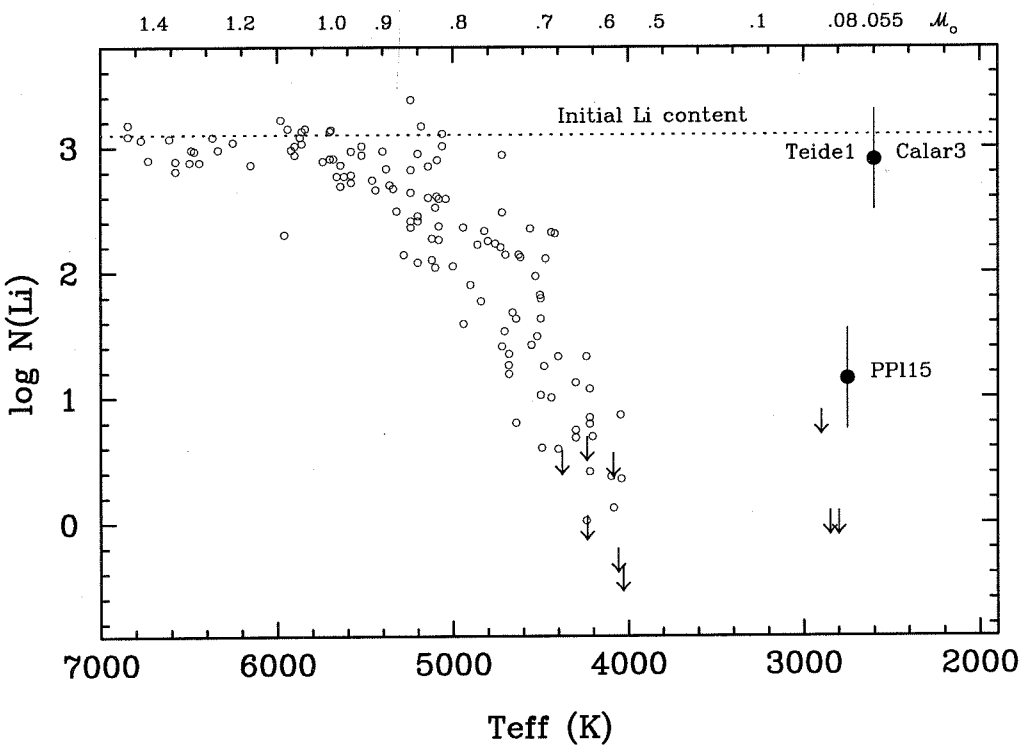

Figure 1.3 Lithium abundance versus $T_{\rm eff}$ for stars and brown dwarfs in the Pleiades. This plot shows how the presence of lithium in a low-temperature object can be used to establish its classification as a brown dwarf. The G and K dwarfs have lithium, but M dwarfs do not, because they are fully convective and the hydrogen fusion reactions destroy lithium. Brown dwarfs contain lithium because they do not support fusion reactions. PPl 15, Teide 1 and Calar 3, members of the Pleiades star cluster, are the first brown dwarfs confirmed in this manner. Courtesy of M. Zapatero-Osorio, from Rebolo et al. 1996.

the age of an open cluster by finding the "lithium depletion boundary," which is an imaginary line that separates faint objects without lithium from slightly fainter objects with lithium. This is demonstrated in Fig. 1.4 for the Pleiades (Stauffer et al. 1998). After 250 Myr, this boundary remains indefinitely at 0.065 $M_\odot$. In older clusters, the brightest objects with lithium will have a mass of 0.065 $M_\odot$, which can be used with the measured luminosity to place the object in a well-constrained part of Fig. 1.2. Objects above the HBML deplete their lithium within 100 Myr, so as long as the cluster being studied is older than 100 Myr, all of the cool objects in the

cluster which show lithium absorption must be brown dwarfs.

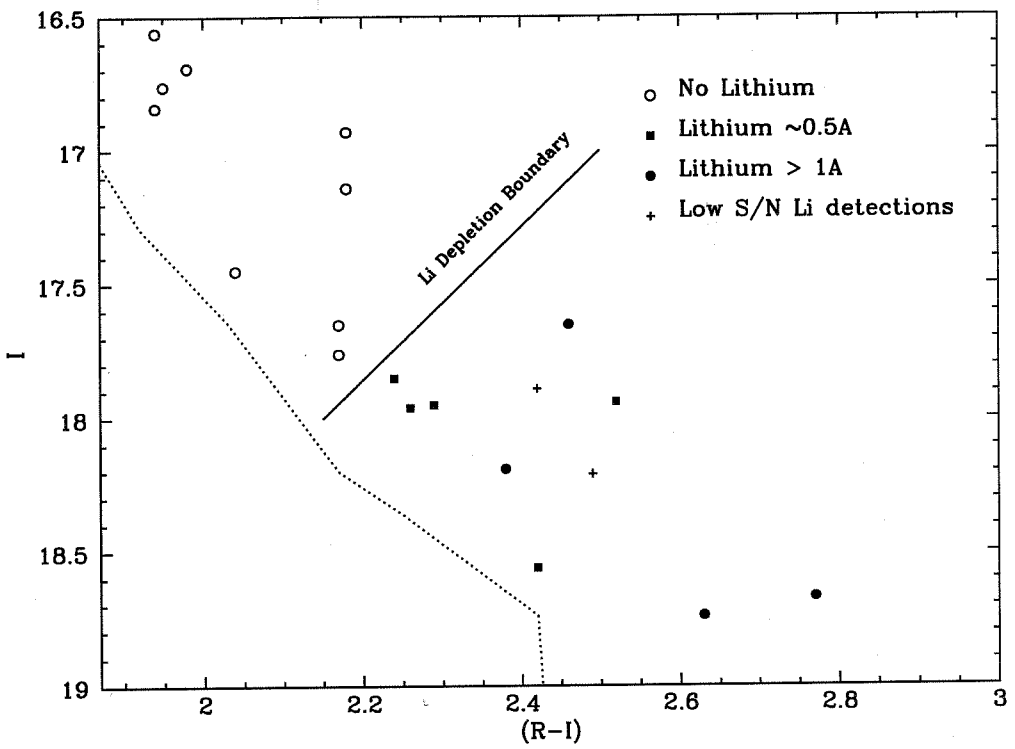

Figure 1.4 Color-magnitude diagram for very low-mass stellar and brown dwarf Pleiades members with available spectra capable of detecting the lithium 6708 Å doublet at equivalent widths greater than 0.5 Å. The dotted line is an empirical main sequence at Pleiades distance. The location of the "lithium depletion boundary" is indicated by the solid line and is used to determine a precise age for the cluster of 125 ± 8 Myr (Stauffer et al. 1998).

Fig. 1.4 demonstrates the application of this technique to determine the age of the Pleiades. The lithium depletion boundary is indicated by a line perpendicular to the zero-age main sequence and is defined by extensive spectroscopic observations of all the Pleiads near the line. (See §1.2.1 and 6.1 for more discussion.)

Molecules

Once a brown dwarf cools to $T_{\rm eff} = 1500$ K, lithium begins to form molecules and the Li I spectral signature weakens (Pavlenko 1998, Burrows and Sharp 1998). Fortunately a new diagnostic becomes available. Below 1500 K, chemical equilibrium between CO and CH_4 strongly favors CH_4 (Tsuji 1964, Fegley and Lodders 1994, Burrows and Sharp 1998). CH_4 has a number of extremely strong absorption features in the range of 1 to 5 μm. As a result, the spectroscopic detection of methane means that the effective temperature of the object must be below 1500 K, requiring that it be less massive than the HBML (§1.1.3). Ammonia forms at slightly lower temperatures than 1000 K and a host of more exotic species appear at even cooler temperatures. See Burrows et al. (1999) for a more complete discussion of this progression. These spectral signatures allow observers to classify brown dwarfs by $T_{\rm eff}$. In §1.2 and 1.3 we deal with this subject in greater depth.

Deuterium

Distinguishing brown dwarfs from planets, as defined here, involves a search for deuterium. The deuterium abundances of several planets in the solar system have been measured. (See, for example, Krasnopolsky et al. 1997.) In brown dwarfs, deuterium should be depleted to unmeasurable quantities, even in their atmospheres because convection causes a complete reflection of the core abundances in the atmosphere, as we reasoned in §1.1.3. Spectroscopic signatures of deuterium include absorption lines of HDO with numerous features between 1.2 and 2.1 μm (Toth 1997) and possibly CH_3D with strong features at 3.7 and 4.4 μm (Noll 1993, Krasnopolsky et al. 1997) in the 1 to 8 μm region. This proposed classification scheme is only hampered by the current state of technology, in that spectra of the known extrasolar "planets" indirectly detected through radial velocity studies (Marcy et al. 1999) cannot be obtained

yet.

Caveat: Dust

As brown dwarfs cool, theory predicts that dust will form in the atmosphere. Even some cool main-sequence stars seem to contain dust (Jones and Tsuji 1997). Dust formation occurs at the ridge in Fig. 1.2 at approximately 10^{-4} $L_{\odot}$ (1800 K). As the dust forms, the luminosity drops more precipitously. Below this ridge, a progression of species with important features in the near IR appears. These species will have two effects: (1) weakening of the molecular absorption features and (2) reorganization of the broadband spectral energy density toward a black body spectrum.

1.1.4 Observational History

Ever since Kumar's pioneering work, astronomers have searched for brown dwarfs primarily because they were regarded as "Terra incognito."

Some of the initial discussions of brown dwarfs suggested that they could be the "missing" matter implied by the dynamics of the galaxy. For example, simple extension of the Salpeter initial mass function (IMF), in which $dN/dM \propto M^{-2.35}$, to brown dwarf masses suggests that brown dwarfs ought to outnumber stars by two or three orders of magnitude. Whether an appreciable percentage of the dark matter is brown dwarfs or planets is still the subject of some debate. Most researchers agree that based on the microlensing experiments of MACHO (Alcock et al. 1998), most of the dark matter is not made of brown dwarfs. However, by adopting unusual parameters, it is still possible to construct galactic models consistent with the MACHO results and with more than 50% of the dynamical mass in brown dwarfs (Kerins and Wyn Evans 1998).

From 1984 through 1994 approximately 170 refereed papers were written on brown

dwarfs. By the end of 1996 that number doubled, and based on current publication rates, 1998 alone will see approximately 170 more papers submitted. This sudden explosion in observational and theoretical results was due to the discovery in late 1995 of Gliese 229B, the first cool brown dwarf detected (described in §1.3 and Chapters 2 and 3), and the confirmation of lithium in the brown dwarf candidate PPl 15 in early 1996 (and in Teide 1 and Calar 3 slightly later). The sustained publication rate is largely due to new large scale surveys which are now turning up brown dwarfs by the dozen. These dramatic successes, however, were preceded by several decades of unsuccessful searches and two conferences whose proceedings are punctuated with the wreckage of disproven brown dwarf candidates and steady improvements in theoretical work.

In 1985, when the first conference solely devoted to brown dwarfs was held at the George Mason University (Kafatos et al. 1986), a new breed of infrared and optical detectors had enabled the first searches designed to detect brown dwarfs directly. No brown dwarfs were found, however, and in retrospect this is because of a lack in sensitivity. The basic strategies behind these early searches are imitated to this day. One can look for brown dwarfs in isolation or as companions of nearby stars. Isolated brown dwarfs can be found in all-sky surveys or smaller surveys of star clusters. Companion searches employ techniques to prevent the bright nearby star from washing out the faint companion.

In 1987 the results of the Infrared Astronomical Satellite (IRAS), launched in 1984 to survey the entire sky at far infrared wavelengths, were presented. One of the principal goals of this satellite mission was to find brown dwarfs. None was detected (Beichman 1987).

The first direct searches for brown dwarf companions of nearby stars were coincident with the development of sensitive electronic infrared photodetectors. Probst (1983) used a single pixel device on NASA's Infrared Telescope Facility (IRTF) to

search for infrared excess around nearby white dwarf stars. The search was sensitive to companions within 15 arcsec of the stars. Probst targeted white dwarf stars because they are intrinsically fainter than main sequence stars, so that any infrared excess would be easier to detect. No brown dwarfs were detected.

Using the same single pixel detector, McCarthy et al. (1985) applied the technique of speckle interferometry. This technique uses rapid exposures to compensate for the blurring effects that the turbulent atmosphere has on astronomical images. In principle this permits the detection of a companion fainter and closer to the primary star than is possible in a standard direct image. McCarthy et al. (1985) reported a faint companion of the red dwarf, vB 8. Their results suggested that this object had a luminosity of about $10^{-5}\ L_{\odot}$. However, the putative companion was never detected again and remains an irreproducible result.

Forrest et al. (1988), using a 32×32 pixel InSb array on the IRTF, found several stellar companions of red dwarfs in the solar neighborhood, but still uncovered nothing faint enough to be considered a brown dwarf.

In 1988, Becklin and Zuckerman, who extended the work of Probst (1983) to survey nearby white dwarfs for faint companions, found the object known as GD 165B. GD 165B has a temperature of 1800 K (Jones et al. 1994), and until 1995 was the best candidate brown dwarf known. Subsequent spectroscopy by Kirkpatrick et al. (1998) has demonstrated that GD 165B has no lithium and is therefore either a star right at the HBML or a high mass brown dwarf a few Gyr old.

Henry and McCarthy (1990) conducted a search for infrared companions of the stars within 8 pc of the sun using the speckle interferometry technique and an array of pixels. Although they found no brown dwarfs, their sensitivity was somewhat limited, reaching a maximum of 7.5 magnitudes of difference between the central star and the faintest object detectable (Henry et al. 1992). For reference, Gliese 229AB (a red dwarf-cool brown dwarf system) has a contrast of over 10 magnitudes in the near

infrared (Matthews et al. 1996; see §1.3 and 3.1).

Substantial gains in detecting stars of lower and lower mass had been made by the next conference on brown dwarfs, held in Garching (see Tinney 1995 for proceedings). However, still no definitive brown dwarfs were presented. Determinations of the mass function presented at this meeting suggested that brown dwarfs are extremely rare, but, in retrospect, the surveys used were still not sensitive enough (D'Antona 1995).

During the course of a coronagraphic survey of nearby stars, Nakajima et al. (1995; §2.1) reported the discovery of an object with the same proper motion as Gliese 229. At a distance of 5.7 pc from the Sun, the inferred intrinsic luminosity of the companion, Gliese 229B, is 6.4 $\times 10^{-6}$ $L_{\odot}$ (Matthews et al. 1996; §3.1). Spectroscopy of this object revealed deep methane features and implied a temperature below 1200 K (Oppenheimer et al. 1995, §2.2; 1998, §3.2). Although many astronomers had become inured to brown dwarf announcements which were retracted months later, the spectrum of Gliese 229B is sufficiently distinctive that, when shown briefly at the 9th "Cool Stars, Stellar Systems and the Sun" conference in Florence, Italy (1995), it was unanimously taken as proof that the object was indeed a brown dwarf.

Parallel to the searches for companion brown dwarfs, several searches for isolated brown dwarfs were conducted between 1989 and 1995. The first CCD deep imaging surveys of the Pleiades believed to have reached below the HBML were those of Jameson and Skillen (1989, hereafter JS89) and Stauffer et al. (1989, hereafter S89). These initial surveys only covered very small portions of the cluster: JS89 imaged just 225 square arcmin and identified seven objects as likely Pleiades brown dwarfs, while S89 surveyed 1000 square arcmin and identified just four brown dwarf candidates. Subsequent analysis indicated that due to an error in the photometric calibration, only one of the JS89 objects was faint enough to be a possible Pleiades brown dwarf (Stringfellow 1991; Stauffer et al. 1994).

After the lithium test was proposed in 1992, several attempts to apply it to brown

dwarf candidates in the Pleiades revealed no lithium (Martín et al. 1994, Marcy et al. 1994). This was largely because the Pleiades is older than these studies presumed, so they selected candidates that were not faint enough. By obtaining a spectrum of a fainter object, PPl 15 (a Pleiades brown dwarf candidate identified by Stauffer et al. 1994), Basri et al. (1996, hereafter BMG) made the first detection of lithium in a brown dwarf candidate. Rebolo et al. (1996, hereafter R96) soon after detected lithium in two other Pleiades brown dwarf candidates, Teide 1 and Calar 3.

By the beginning of 1996 the first brown dwarfs had been found, and in March 1997 a conference was held in Tenerife, Spain (Rebolo et al. 1998), where the wealth of positive observational results was a direct testament to the sudden change in the field. We separate our discussion of successful observations of brown dwarfs into two sections, one on isolated brown dwarfs (§1.2) and the other on brown dwarf companions of nearby stars (§1.3). We also recommend the useful reviews by Kulkarni (1998), Allard et al. (1997), Hodgkin and Jameson (1997).

1.2 Isolated Brown Dwarfs

The principal reason for studying isolated brown dwarfs is to acquire a complete census of objects with masses below the HBML (i.e., to measure the mass function). The relative number of brown dwarfs of a given mass compared to the number of higher mass objects has important implications for star formation theories. Indeed, the eventual mass of an object formed out of an interstellar cloud fragment would seem to be entirely independent of the HBML, so that objects with masses well below the HBML ought to form out of interstellar cloud fragmentation (Burkert and Bodenheimer 1993; Shu et al. 1987). Observations of star formation regions in which very low mass clumps of gas exist certainly suggest that brown dwarfs can form out of this process (Pound and Blitz 1995). Measuring the mass function would determine

whether there is a lower limit to the mass of an object formed like a star and not in a circumstellar disk.

Because brown dwarfs cool, and a given brown dwarf can have a huge range of luminosities over its lifetime, making a complete census of them is greatly simplified by examining a sample of the same age. In such a sample, mass will be solely a function of luminosity, which is directly observable as discussed in §1.1.3. By far the best means to find a population of brown dwarfs with the same age is to identify low luminosity members of well-studied open clusters where, in principle, the age, distance and metallicity should be known accurately.

Surveys for field brown dwarfs, outside stellar associations, require immense sky coverage because of the intrinsic faintness of the brown dwarfs, which effectively limits the volume of space that the surveys probe. For example a 1000 K brown dwarf is detectable by the new near infrared all-sky surveys (2MASS and DENIS; see below) out to a distance of only about 6 pc.

Critical to both types of survey is the certification that a given object is a brown dwarf. The principal method for this is the lithium test. However, as the surveys probe fainter and fainter limits, certification through the molecular features described in §1.1.3 will become equally important.

1.2.1 Brown Dwarfs in Open Clusters and Star Forming Regions

Brown dwarf candidates are identified in photometric surveys based on their lying above the zero age main sequence (Fig. 1.4). To confirm that they are in fact cluster members (and not reddened, background stars) requires accurate proper motion measurements or accurate radial velocity measurements. However, to date at most one of the likely cluster brown dwarfs has a sufficiently accurate proper motion (Rebolo

et al. 1995). The lithium test has therefore provided the primary means to confirm the substellar nature of the young brown dwarf candidates.

TABLE 1.2 NEARBY CLUSTERS ($d < 200$ PC)

Cluster Name	Distance (pc)	Age (Myr)	No. of Known Members	Area on Sky Sq. Deg.
Ursa Major	25	300	25	20
Hyades	46	600	550	100
Coma	80	500	50	20
Pleiades	130	125	800	25
IC 2602	155	30	125	10
IC 2391	160	30	100	8
Praesepe	170	600	800	25
Alpha Perseus	175	75	350	30

The clusters listed here are those which can practically be searched for brown dwarf members. The Pleiades age is based on the lithium depletion boundary, which is 25 to 60% higher than the age determined from the upper main sequence turnoff, but is probably more accurate. The other clusters's ages are based on the upper main sequence turnoff. However, Alpha Perseus's age agrees with its lithium depletion age.

The Substellar Mass Population of the Pleiades

The Pleiades is the richest, nearby open cluster. (See Table 1.2.) For a nominal age of 100 Myr (Meynet et al. 1993), objects at the HBML are predicted to have effective temperatures of about 2500 K, corresponding to spectral class M6 V on the main sequence. Because of the cluster's proximity to the Sun (Table 1.2), these brown dwarfs should be detectable with modern optical CCDs. The cluster half mass radius is $\sim$2 pc, and the tidal radius is about 16 pc (Raboud and Mermilliod 1998; Pinsonneault et al. 1998). The areas on the sky corresponding to circles with these radii are 2.5 and 150 square degrees, respectively. This is important because it indicates that it is necessary to search a large area to sample a significant portion of the cluster. Because the Hyades is three times closer, it is spread over a much larger area on the sky than the Pleiades. For these reasons, the Pleiades has been

the principal hunting ground for isolated brown dwarfs.

Since 1989, at least 10 deep imaging surveys of the Pleiades other than those described in §1.1.4 have been conducted. A summary is provided in Bouvier et al. (1998). By using redder filters and more sensitive, larger format CCDs, these surveys have been able to reach lower inferred mass limits and cover larger portions of the cluster. A conservative assessment of the current surveys suggests that at least 40 substellar members of the Pleiades have now been identified (Fig. 1.4).

Using the "lithium depletion boundary" described above, BMG and R96 estimated the age of the Pleiades at about 120 Myr with PPl 15 and HHJ 3 (Hambly et al. 1993), the faintest Pleiad without lithium, defining the boundary. However, Basri and Martín (1998) subsequently discovered that PPl 15's luminosity was over-estimated because it is an approximately equal mass, short-period binary, with each component being about 0.7 mag fainter than the composite and having a mass of approximately 0.06 $M_{\odot}$. PPl 15 is the first brown dwarf binary system found.

Spectra of 10 additional Pleiades brown dwarf candidates have recently allowed Stauffer et al. (1998) to define the lithium depletion boundary in the Pleiades to ± 0.1 mag and thus to derive an age for the cluster of $\tau \sim 125 \pm 8$ Myr (Fig. 1.4). By coincidence, at this age the lithium depletion boundary corresponds to 0.075 ± 0.005 $M_{\odot}$, and therefore all Pleiades members fainter than the lithium depletion boundary are brown dwarfs (Ventura et al. 1998, Chabrier and Baraffe 1997). The faintest Pleiades candidates identified to date have masses on the order of 0.035 $M_{\odot}$ (Martín et al. 1998).

Zapatero-Osorio et al. (1997) and Bouvier et al. (1998) have used their surveys to estimate the Pleiades mass function in the substellar regime. Both groups obtain slightly rising mass functions for the range $0.045 \leq \mathrm{M} \leq 0.2$ $M_{\odot}$, with $\mathrm{dN/dM} \propto \mathrm{M}^{-1.0}$ and $\mathrm{M}^{-0.7}$, respectively. However, the relatively small fraction of the cluster that has been surveyed to date make these estimates fairly uncertain.

Brown Dwarfs in Other Open Clusters

Basri and Martín (1999) have reported a lithium detection for the faintest known member of the α Persei open cluster (and non-detection of lithium in one or two brighter, probable members), thus allowing them to place the age of the cluster between 60 and 85 Myr (Table 1.2).

Two deep imaging surveys of Praesepe (see Table 1.2) have been conducted (Pinfield et al. 1997; Magazzù et al. 1998). Magazzù et al. report one object in their survey with I $\sim$ 21 and a spectral type of about M8.5, which would indicate a mass near the substellar limit if the object is indeed a Praesepe member and if the cluster age is as expected ($\sim$600 Myr).

The deepest survey of the Hyades to date is that provided by Leggett and Hawkins (1988) and Leggett et al. (1994). The faintest objects in this survey may also be approximately at the substellar mass boundary; however, no spectra for the faintest candidates have yet been reported.

Brown Dwarfs in Star Forming Regions

Brown dwarfs in star forming regions (age $<$ 1 Myr) will be much more intrinsically luminous than those in the open clusters discussed above and should be easier to discover. However, it is in fact more difficult to "certify" that any given object is substellar in a star forming region than in an open cluster. First, the "lithium test" is of limited value at this age because all low mass stars should still have their original lithium abundance. However, as Basri (1998) points out, if a candidate object lacks lithium it can be discarded as a member of the star forming region. Second, the theoretical isochrones for young, low mass objects are quite uncertain. Thus, determining the ages of these objects is difficult. Even if the age can be determined, the intrinsic luminosity of a candidate object is difficult to measure because of uncertainties in

extinction parameters for these star forming regions.

However, based on the existing models and using the Pleiades as a reference, Basri (1998) has argued that any object with spectral type M7 or later must be a brown dwarf if it contains lithium. This is because stars more massive than the HBML deplete lithium before they can cool to the M7 effective temperature (i.e., before they reach the zero-age main sequence). Brown dwarfs on the other hand can cool to the M7 spectral type when they are much younger than the stars and still retain their lithium.

Luhman et al. (1997) have identified an apparent brown dwarf member of the ρ Ophiuchus star forming region based on its spectral type of M8.5. This object was originally thought to be a foreground star (Rieke and Rieke 1990); however, the new data indicate that it is much more likely to be a member of the cluster (in particular, it has very strong Hα emission and relatively low surface gravity). Comeron et al. (1998) have identified 3 other members of this region with spectral classes $>$ M7, based on new data with the ISO satellite and spectroscopy by Wilking et al. (1998).

Luhman et al. (1998) have also obtained spectra for a large number of faint candidate members of the star forming region IC348, and have identified three good brown dwarf candidates—two with spectral type M7.5 and one with spectral type M8.

1.2.2 Brown Dwarf Members of the Field Population

The search for isolated brown dwarfs in the field has also seen dramatic progress in the past 2 years. The primary sources of the newly discovered field brown dwarfs are the wide-field, near-IR imaging surveys DENIS and 2MASS; however, a number of objects have also been identified using other techniques.

Brown Dwarfs from DENIS and 2MASS

DENIS (DEep Near-Infrared Survey) obtains simultaneous images at I, J and K of the southern sky to limiting magnitudes of 18.5, 16 and 14.0 (3σ), respectively. Based on the photometry of previously identified very-low mass stars, the DENIS project uses a color criterion of I−J > 2.5 to select "interesting" objects, with the most interesting objects being those with colors like that of GD165B. The DENIS search contains no color criteria to distinguish analogs of Gliese 229B.

The DENIS team has reported about 5 objects with GD165B colors after analyzing only 500 square degrees. Optical spectra have been obtained for three of those objects, with one of them showing a strong lithium absorption feature (Delfosse et al. 1997; Tinney et al. 1997; Martín et al. 1997). All of these objects have spectra in the 0.8 μm region similar to that of GD165B. The lithium feature in combination with the very late spectral type for DENIS-P J1228.2−1547 indicate that this object is undoubtedly a brown dwarf. No lithium has been detected in two of the objects with very late spectral types. They could be old substellar objects in the mass range 0.065 to 0.075 $M_{\odot}$.

2MASS (Two-Micron All-Sky Survey) obtains simultaneous images at J, H and K of the entire sky to limiting magnitudes of 17, 16.5 and 15.5 (3σ), respectively. Digitized scans of the E or N plates from the Palomar Sky Survey are used to derive R or I magnitudes for objects detected in the infrared. 2MASS uses color criteria of J−K > 1.3 and R−K > 6, or J−K < 0.4 to select brown dwarf candidates, with the latter criterion being designed to find analogs of Gliese 229B (see §1.3).

More than a dozen candidates from 420 square degrees have had spectroscopic follow-up observations (Kirkpatrick et al. 1998). Six of these objects have extremely late spectral type and show lithium absorption, and thus are substellar; an approximately equal number of objects are similarly late but do not show lithium. None of the objects observed spectroscopically show methane in their spectra, and none have

been found with colors similar to those of Gliese 229B.

Considering the small fraction of the sky analyzed so far, it appears likely that 2MASS and DENIS will eventually provide a list of hundreds of field brown dwarfs. Due to the correlation of age, mass, effective temperature and luminosity, it is inevitable that this sample of brown dwarfs will favor relatively young objects with masses not far below the HBML.

The spectra of the coolest DENIS and 2MASS objects are sufficiently different from previously known objects that a new spectral class must be defined. Kirkpatrick (1997) and Martín et al. (1997) have suggested use of the letter L for this class. Kirkpatrick et al. (1998) have begun to define this class through the weakening of TiO bands to later types, the presence of resonance lines of alkali metals—in particular potassium, rubidium and cesium, with these lines becoming extremely strong at later types—the presence of other molecular species such as CrH, FeH and VO, and the absence of methane. One brown dwarf, Gliese 229B (§1.3), does not fit in the L class because it is several hundred degrees cooler than the coolest L dwarf. Another spectral class must be created once Gliese 229B analogs are discovered.

Other Field Brown Dwarfs

Two field brown dwarfs have been identified from proper motion surveys. The first of these, Kelu-1, was identified as part of a survey of 400 square degrees of the southern sky using deep Schmidt plates (Ruiz et al. 1998). Kelu-1 has a spectrum similar to GD165B's and has lithium in absorption and Hα in emission. At K = 11.8, Kelu-1 is comparatively very bright (and hence presumably quite nearby), and so is a good target for detailed study.

The other field brown dwarf identified via proper motion is LP 944−20, originally cataloged as a high proper motion object by Luyten and Kowal (1975). It was rediscovered in a search for very red objects by Irwin et al. (1991) and identified as

a very late-type M dwarf by Kirkpatrick et al. (1997). Tinney (1998) subsequently showed lithium was present with an equivalent width of about 0.5 Å. LP 944−20 has a measured parallax from which the intrinsic luminosity can be derived. Tinney used the inferred luminosity of 1.4×10^{-4} $L_{\odot}$ combined with an estimate of the lithium abundance to derive a mass estimate of 0.06 ± 0.01 $M_{\odot}$ and an age of about 500 Myr.

One other possible field brown dwarf has been identified from a deep photographic RI imaging survey by Thackrah et al. (1997). The object, 296A, was selected because it was quite bright ($I \sim 14.5$) and reasonably red ($R-I \sim 2.5$). Spectroscopy revealed a spectral type of M6 and a lithium absorption equivalent width of about 0.5 Å. These features suggest that it could be a Pleiades age star at the HBML.

1.3 Companion Brown Dwarfs

Searching for brown dwarf companions of nearby stars is attractive mainly because it is the most effective way to identify the coolest (lowest luminosity; see §1.1.3) objects. The principal difficulty in this is the scattered light of the primary star. There are several techniques to circumvent this difficulty. First, one can search at the longer wavelengths, where the contrast between the brown dwarf and the star is lowest. Second, one can search for companions of white dwarf stars where the contrast is very small because of the intrinsic faintness of the star. Third, the use of a coronagraph artificially suppresses the starlight with a series of optical stops (Nakajima et al. 1994).

1.3.1 Gliese 229B

A large survey of nearby stars using a coronagraph (with a tip-tilt image motion compensator) was carried out at the Palomar 60-inch telescope. This proved successful

when Nakajima et al. (1995; §2.1) showed that the star Gliese 229 has a companion with a luminosity of less than 10^{-5} $L_{\odot}$. The discovery image of Gliese 229B is shown in Fig. 1.5 with a subsequent image taken by the Hubble Space Telescope (Golimowski et al. 1998; §3.3). The impact of this discovery was far-reaching, not only did it validate the immense effort of the astronomers who persisted in working on brown dwarfs despite all the non-detections, but it also excited considerable interest among planetary scientists, partly because of the fact that Gliese 229B is orbiting a nearby star, but also because its spectrum (Oppenheimer et al. 1995, §2.2; 1998, §3.2) looks remarkably like Jupiter's, with major features due to water and methane. Methane dissociates at temperatures between 1200 and 1500 K, a fact which further implies the extremely low luminosity of Gliese 229B.

Matthews et al. (1996, §3.1) made photometric measurements of Gliese 229B from r band at 0.7 μm through N band at 12 μm. These data account for between 75 and 80% of the bolometric luminosity of the brown dwarf (depending on the model used for the unmeasured flux). The observed luminosity is $(4.9 \pm 0.6) \times 10^{-6}$ $L_{\odot}$, implying a bolometric luminosity of 6.4×10^{-6} $L_{\odot}$ and an effective temperature of 900 K assuming the brown dwarf radius is 0.1 $R_{\odot}$, as was argued in §1.1.1.

Allard et al. (1996) and Marley et al. (1996), using the photometry of Matthews et al. (1996, §3.1) and the spectrum from Oppenheimer et al. (1995, §2.2) constrained the mass of Gliese 229B between 0.02 and 0.055 $M_{\odot}$ by fitting non-gray atmosphere models. The mass is so uncertain because (1) the age of Gliese 229B is unknown and could be from 0.5 to 5 Gyr based on the spectrum of Gliese 229A and (2) the gravity has not been accurately measured.

Geballe et al. (1996) obtained a high resolution spectrum of Gliese 229B in the 1 to 2.5 μm region (see Fig. 3.10) and showed that there are hundreds of very fine spectral features due to water molecules. These may be the most gravity sensitive features in the spectrum (Burrows et al. 1997) and with higher resolution spectra the

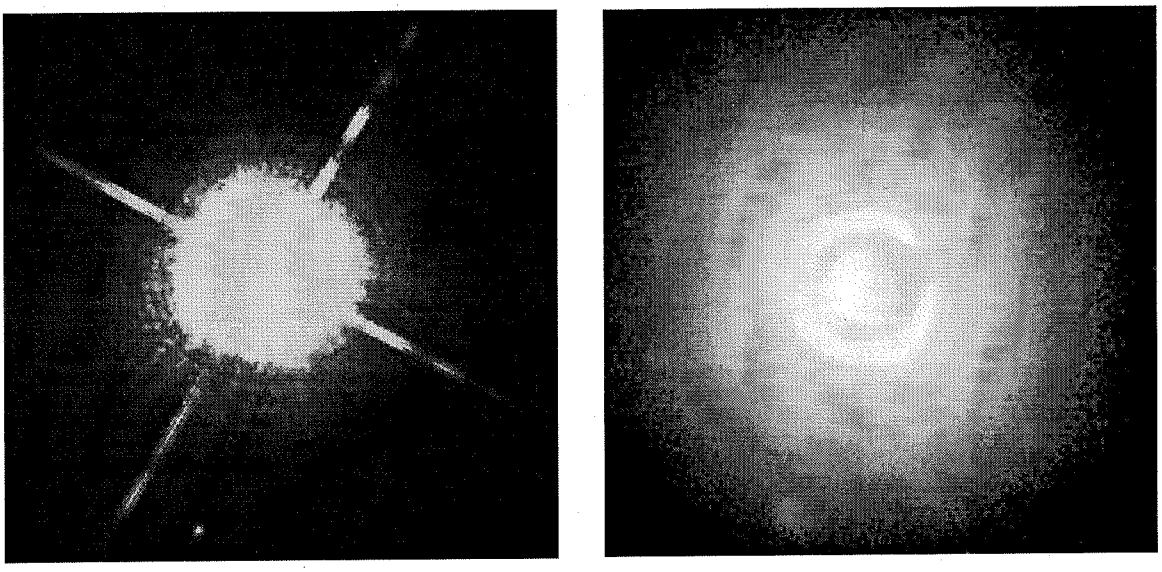

Figure 1.5 Two images of the Gliese 229 system. The left panel shows a direct image from HST's WFPC2. The brown dwarf is at the bottom left of the image. The right panel shows the discovery image from the Palomar 60 inch telescope fitted with a coronagraph. The coronagraphic stop is visible, obscuring most of the light from the primary star. The stop is 4 arcsec in diameter and is semi transparent. The brown dwarf is visible in the bottom left of the image. Both images are oriented with N up and E to the left and are approximately 17″ on a side.

gravity of Gliese 229B may be constrained to within 10%.

Another important conclusion of the Matthews et al. (1996, §3.1) paper is that the photometry indicates a complete lack of silicate dust in the atmosphere of the brown dwarf. Fig. 1.6 (from Matthews et al. 1996; also Fig. 3.3, §3.1) is a plot of the photometric measurements, along with a model spectrum from Tsuji et al. (1996b) and three black body curves assuming the brown dwarf has a radius of 0.1 $R_{\odot}$ and is at 5.7 pc. The model spectrum has no dust included in the calculation. By adding even a minute quantity of silicate dust, Tsuji et al. (1996b) find that the spectrum no longer fits the photometric data. In contrast, the L dwarfs of Kirkpatrick et al. (1998) and the spectrum of GD 165B (Jones et al. 1994; Jones and Tsuji 1997) appear to be considerably affected by the presence of dust.

Oppenheimer et al. (1998, §3.2) confirmed these conclusions with a high signal-to-noise spectrum of Gliese 229B (shown in Fig. 1.7 and 3.7) in the near infrared but also reported a smooth, almost featureless spectrum in the optical (0.85 to 1.0 μm) region that could not be fitted by any of the models. An optical spectrum was also obtained from the Hubble Space Telescope (HST) by Schultz et al. 1998. There is excellent overall agreement between the Keck and the HST spectra. However, the HST spectrum lacks the resolution and sensitivity to reveal the fine features seen in the Keck spectrum (Fig. 1.7) and discussed here.

The fact that the optical spectrum is smooth (Fig. 1.7) and that the water band at 0.92 μm is shallower than expected (Allard et al. 1997) indicates that there may be an additional source of continuum opacity not previously discussed by theorists. Indeed, Griffith et al. (1998) show that a haze of photochemical aerosols might be responsible for the relative smoothness of this part of the spectrum. These aerosols may be activated by ultraviolet radiation from Gliese 229A (known to flare from time to time). (A possible test of this conjecture is that field brown dwarfs with effective temperatures near 900 K should not have these aerosols in their atmospheres since they have no nearby source of incident ultraviolet radiation. See Griffith et al. 1998.)

This problem of whether silicate dusts, sulfides, hazes or even polyacetylenes appear in the atmospheres of objects below the HBML remains a subject of debate. It is, however, extremely important because dust can have a substantial effect upon the emergent spectrum. The issue of whether a parent star can cause photochemical reactions that greatly affect the spectra of its companions has implications for planet and brown dwarf searches. Indeed, the design of new searches and instruments will need to take heed of this work. In the case of Gliese 229B, a spectrum in the 5 to 12 μm region might yield some answers because incident ultraviolet radiation can also produce certain organic molecules, such as C_4H_2, with spectral features in the mid-infrared, as have been observed in spectra of Titan (Griffith et al. 1998; Khlifi et

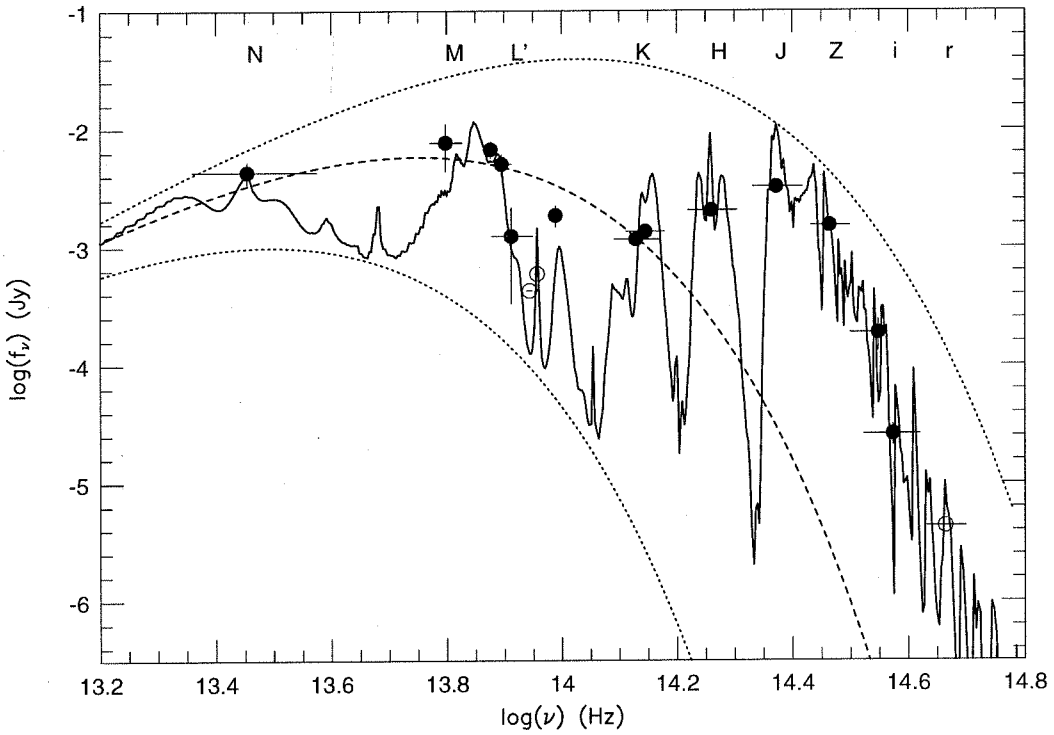

Figure 1.6 Photometric measurements of Gliese 229B (from Matthews et al. 1996). The photometry shown here represents 75 to 80% of the bolometric luminosity ($6.4 \times 10^{-6}\ L_\odot$) of the brown dwarf and demonstrates that the atmosphere is devoid of dust grains that affect the infrared spectrum. The solid circles represent actual measurements. Where no error bars are visible, the errors are smaller than the size of the circles. The open circles represent measurements that give only upper limits on the photometry. The solid line is a dust-free model spectrum from Tsuji et al. (1996b). The long-dashed line indicates a black body spectrum for $T_{\rm eff} = 900$ K, the estimated value for Gliese 229B. The dotted curves are black body spectra for $T_{\rm eff} = 500$ K (bottom) and 1700 K (top).

al. 1997; Raulin and Bruston 1996).

Noll et al. (1997) reported the detection of a feature due to carbon monoxide in the 4 to 5 μm spectrum of Gliese 229B (Fig. 1.7). Confirmed by Oppenheimer et al. (1998, §3.2), this feature shows that carbon monoxide exists in non-equilibrium abundances. At 900 K, the balance between CO and CH_4 strongly favors CH_4. Convection must, therefore, dredge up appreciable quantities of CO from deeper, hotter parts of the atmosphere.

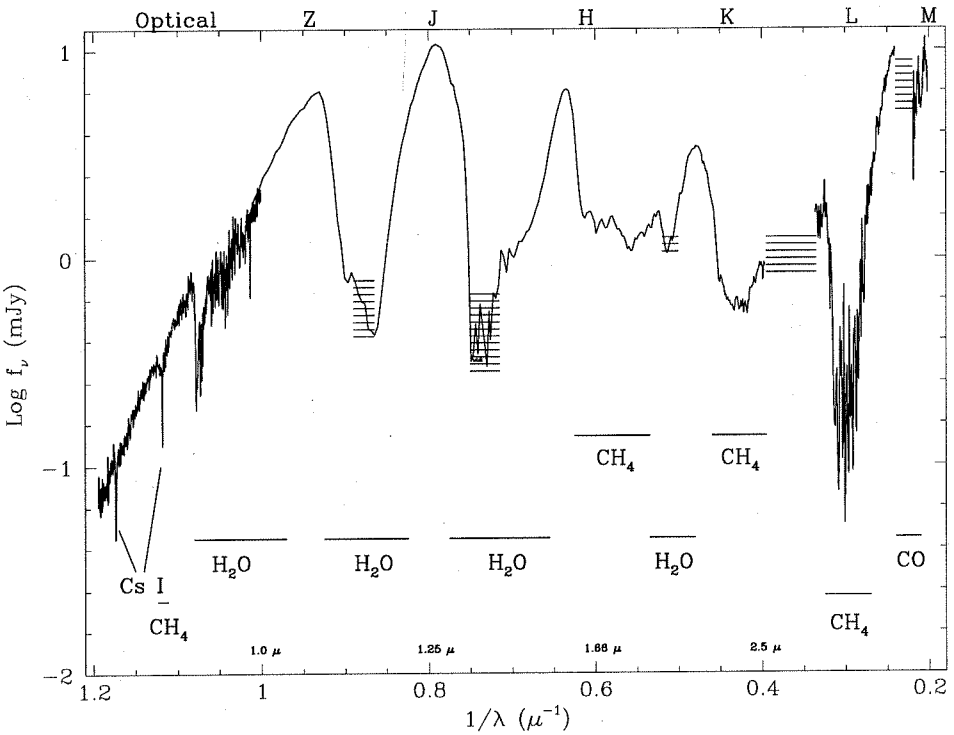

Figure 1.7 The spectrum of Gliese 229B from 0.8 to 5.0 μm. The principal absorption features are, as indicated, from water and methane, which is not present in stellar atmospheres. Additional features due to cesium and carbon monoxide are also marked. The relative smoothness of the 0.8 to 1.0 μm region indicates the presence of an unpredicted continuum opacity source. (From Oppenheimer et al. 1998.)

However, Oppenheimer et al. (1998, §3.2) suggested that the convection cannot be efficient even deeper where species such as VO and TiO ought to be present because there are no spectral signatures of these constituents. VO and TiO are observed in all of the late M and L-type dwarfs. This may indicate that cool, old brown dwarfs are not fully convective, but rather have an inner radiative zone below the outer convective layer as the models of Burrows et al. (1997) show.

In Fig. 1.7 several absorption features due to neutral cesium are indicated. Oppenheimer et al. (1998, §3.2) argued that this should be the last of the neutral atomic species present in atmospheres as one proceeds toward lower and lower temperature.

Of all the known elements, cesium has the lowest ionization potential, so at temperatures well above Gliese 229B's it is ionized and its signature is hidden in the extremely faint ultraviolet regions of the spectrum. In addition, it, along with the other alkali metals, is less refractory than the more familiar stellar atomic species (Al, Mg, Fe) and so it survives in atomic form to lower temperatures. Indeed, its presence also in some of the L dwarf spectra (Kirkpatrick et al. 1997) shows that it exists for effective temperatures from 1800 K to below 900 K. Oppenheimer et al. (1998, §3.2) suggest that neutral cesium, along with the other alkali metals, be used as an indicator of effective temperature for brown dwarfs.

Other than Gliese 229B, no other brown dwarfs have been confirmed as companions of stars. Oppenheimer et al. (1999b, §4) have surveyed all of the northern stars within 8 pc and found only one substellar companion. That survey was sensitive to objects up to 4 magnitudes fainter than Gliese 229B with separations from the star between 3 and 30 arcsec. The survey implies a star-brown dwarf binary frequency of less than 1%, although more than one specimen is needed to make this statement significantly meaningful. Several other searches are underway, however, including that of Krist et al. (1998) with the Space Telescope. It seems clear from the lack of numerous brown dwarf companions that hundreds or thousands of stars must be surveyed before a substantial population of these elusive objects can be studied in detail.

Chapter 2

Discovery of the Cool Brown Dwarf Gliese 229B

In 1994 and 1995 we observed the star Gliese 229 and found a cool brown dwarf orbiting it. This companion brown dwarf was unlike any star previously seen. In fact, it bears more resemblance to the planet Jupiter than anything else in the sky.

We presented the discovery of Gliese 229B in two papers, reproduced here in §2.1 and §2.2. Since publishing this work, we followed-up the discovery with an intensive campaign to observe Gliese 229B at as many wavelengths as possible. That work is presented in Chapter 3. Some of the later work has shown previous results to be slightly incorrect. The versions of the papers presented here have been corrected, or, in cases where a correction was not appropriate, a footnote has been added to prevent the propagation of misinformation. The results of the papers presented here supercede the previously published papers due to these corrections and some additions in Chapter 3.2.

2.1 Discovery of a Cool Brown Dwarf†

Tadashi Nakajima, Ben R. Oppenheimer, Shrinivas R. Kulkarni

Palomar Observatory 105-24, California Institute of Technology, Pasadena, CA 91125, USA

David A. Golimowski

Dept. of Physics and Astronomy, The Johns Hopkins University, Baltimore, MD 21218, USA

Keith Matthews

Palomar Observatory 105-24, California Institute of Technology, Pasadena, CA 91125, USA

and

Samuel T. Durrance

Dept. of Physics and Astronomy, The Johns Hopkins University, Baltimore, MD 21218, USA

Abstract

Brown dwarfs are starlike objects with masses less than 0.08 $M_\odot$, which are unable to sustain hydrogen fusion in their interiors (Kumar 1963; Tartar 1986; Stevenson 1991; Burrows and Liebert 1993). They are very hard to detect, as most of the energy of gravitational contraction is radiated away within $\sim 10^8$ yr, leaving only a very low residual luminosity. Accordingly, almost all searches for brown dwarfs have been directed towards clusters of young stars—a strategy that has recently proved successful (Basri et al. 1996; Rebolo et al. 1995). However, there are only modest observable differences between young brown dwarfs and very low-mass stars, making it difficult to identify young brown dwarfs without appealing to sophisticated models (Magazzù et al. 1993). Older brown dwarfs should have a more distinctive appearance, and if they are companions to nearby stars, their luminosity can be determined unambiguously. Here we report the discovery of a probable companion to the nearby star Gliese

†This section is an updated version of Nakajima et al. (1995). It is identical, except that a few mistakes in the original have been corrected.

229, with no more than a tenth the luminosity of the least luminous hydrogen burning star. We conclude that the companion, Gliese 229B, is a brown dwarf with a temperature of less than 1200 K and a mass 20 to 50 times that of Jupiter.

Three years ago, we initiated a search for brown dwarf companions to stars less than 15 pc away (Nakajima et al. 1994). Our strategy utilizes the precisely known distances to these stars to determine accurately the total luminosity of any discovered companions. In all models of low-mass stars, the lowest luminosity of any hydrogen burning star is $L_{min} \gtrsim 10^{-4}\ L_{\odot}$ (Burrows and Liebert 1993). Brown dwarfs of age 10^9 yr have luminosities well below L_{min} and are therefore clearly distinguishable from low-mass stars (Stevenson 1991). Consequently, we have begun the "Palomar-Byr" survey, a survey of all nearby stars with ages of about one billion (10^9) yr. These stars have either small space motion (Leggett 1992) or have active coronas (as inferred from copious Hα (Hawley 1995) or X-ray emission (Pallavicini 1989)), both of which are indicators of stellar youth. The survey comprises both optical coronagraphic imaging and infrared direct imaging of the stars.

During the last year, we observed about one hundred stars of this sample. Preliminary analysis of the data revealed a very intriguing proper motion companion to the nearby star, Gliese 229 also known as HD 42581 or LHS 1827. Its spectral type is M1V with $M_V = 9.3$ and a parallax of $0''.1749 \pm 0''.0045$ or a distance of 5.7 pc (Leggett 1992; see Gliese and Jahreiss 1991 for further details). This star was selected from a list of stars with known low space motion (Leggett 1992). Based on its kinematics it has been classified as a "young" disk star, age approximately 10^9 yr old. However, the star exhibits Hα absorption with an equivalent width of 0.5Å (Gizis 1997). All of the M1 stars in the Pleiades (age $\sim 10^8$ yr) show Hα in emission. However, some stars with $M_V > 9.5$ in the Hyades (age $\sim 8 \times 10^8$ yr) show Hα absorption even as strongly as Gliese 229 (Reid et al. 1995). This suggests that Gliese

229 is probably as old as the Hyades and the kinematics make it unlikely that the object is older than the Sun.

We observed Gliese 229 with the Johns Hopkins University's Adaptive Optics Coronagraph (Golimoski et al. 1992) at the Cassegrain focus of the Palomar 60-inch telescope on the nights of 27 and 29 October 1994 UT. A compact source, hereafter Gliese 229B, was detected $7\farcs78 \pm 0\farcs1$ from Gliese 229 at a southeasterly position angle, $PA = 163° \pm 1°$. Here PA is measured from north through east (Fig. 2.1). Exposures in three different bandpasses, Thuan–Gunn r, i, and z, showed that the object was very red (Fig. 2.2). Infrared data of Gliese 229B in the J, H, K_s and K bandpasses were obtained at the Hale 200-inch telescope on the nights of 14 and 15 September 1995 UT. During 3-8 October 1995 UT Gliese 229B was observed again with the Adaptive Optics Coronagraph (AOC) at the Palomar 60-inch telescope. During this run, we also observed the field centered on the star, θ_1 Ori. This field has a number of stars with well determined positions (Hirschfeld and Sinnot 1995) with respect to θ_1 Ori. These observations enabled us to derive the pixel scale ($0\farcs118$ pixel^{-1}) and also determine the orientation of the CCD (Charge Coupled Device) detector attached to the AOC. The orientation was as expected: the CCD columns were oriented north-south to within 0.1°.

The infrared image (Fig. 2.1) showed an object at the position of Gliese 229B. The r-band AOC images contain six stars, excluding Gliese 229, spread over the field of view of one square arcminute. We compared the relative positions of these stars in the 1994 and 1995 images. We found that there was very little change in the pixel scale but that the 1994 image was rotated $1\fdg8 \pm 0\fdg2$ with respect to the 1995 image. This comparison also yielded an empirical measure of the centroiding root-mean-square error, $\sigma \sim 1$ pixel in each axis. The occulting disk had a small enough transmission that we could satisfactorily centroid on Gliese 229. From 1994 to 1995, we found that Gliese 229 had moved, with respect to the six field stars, by 0.3 ± 1

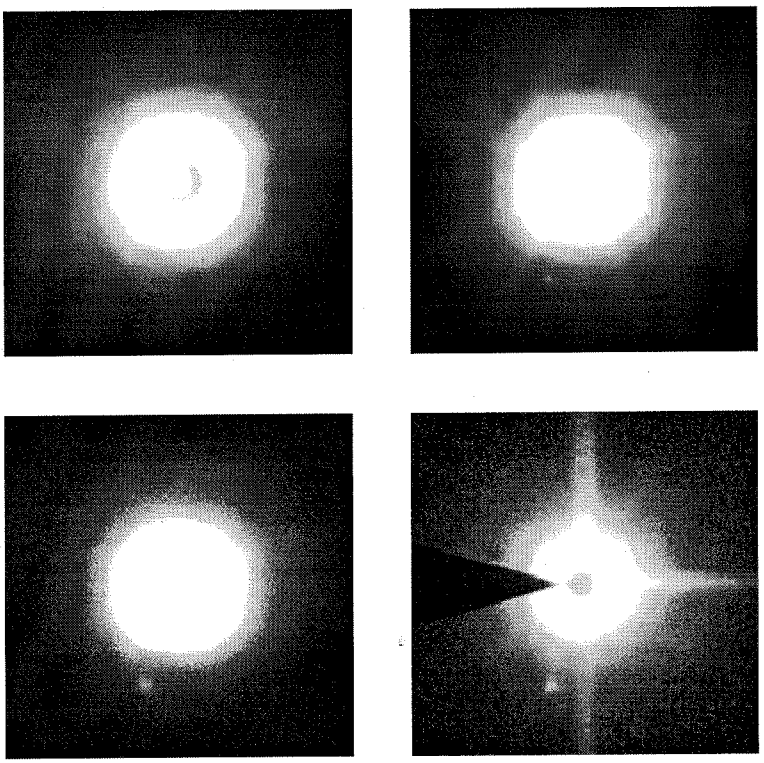

Figure 2.1 Optical and infrared images of Gliese 229. Each field of view is $25'' \times 25''$, with north up and east to the left. Upper left: r-band image. Upper right: i-band image. Bottom left: z-band image. Bottom right: K_s-band image. The logarithm of the data is displayed in all four panels. The brown-dwarf companion Gliese 229B is located $7\farcs6$ to the SSE of Gliese 229A. The r, i, and z images were obtained on epoch 1994.82 with the Adaptive Optics Coronagraph (AOC) and the Palomar 60-inch telescope. The AOC contains an image stabilizer for improved resolution and a pupil apodizer for suppression of light diffracted by the telescope aperture (Golimoski et al. 1992). The K_s image was obtained on epoch 1995.70 at the Hale 200-inch telescope. The infrared camera, located at the $f/70$ Cassegrain focus, contains reimaging optics and a Santa Barbara Research Corporation InSb detector. The secondary mirror used signals from a nearby field star to reduce image wander. A cryogenically cooled occulting disk masked Gliese 229A. The triangular support for this disk is seen at the left of the K_s image.

pixel to the east and 4.5 ± 1 pixel to the south. This is consistent with the known proper motion of Gliese 229, $0''.72$ yr^{-1} and PA $= 191°$ (Gliese and Jahreiss 1991). Gliese 229B is not detected in the r-band AOC image but is easily detected in the z-band image. Unfortunately, only two of the six field stars are seen in this image. With respect to these, Gliese 229B had moved 0 ± 1.5 pixel to the east and 3.7 ± 1.5 pixel to the south. Thus within the errors, it appears that Gliese 229B is a common proper motion companion of Gliese 229. It is appropriate to refer to Gliese 229 as Gliese 229A.

Our argument of companionship is based on two measurements, obtained about one year apart. It is certain that Gliese 229B is not a distant object since it has a measurable proper motion. It is conceivable, though improbable, that Gliese 229B is a foreground object, unrelated to Gliese 229A. Fortunately, this issue can be resolved through observations. Specifically, measurement of the parallax (easily possible with the Hubble Space Telescope) of Gliese 229B is the most definitive way to confirm companionship (see §3.3.4).

In order to undertake further observations (e.g., long-slit spectroscopy), it is necessary to obtain the precise offset of Gliese 229B with respect to Gliese 229A. This is best done using the infrared data rather than the AOC data for the following reason. At optical wavelengths, the contrast (C) defined as the ratio of the brightness of Gliese 229A to Gliese 229B is extremely large (at wavelength, $\lambda \sim 0.65$ μm, $C > 10^6$; $\lambda \sim 0.80$ μm, $C = 4 \times 10^5$; $\lambda \sim 0.9$ μm, $C \sim 8 \times 10^4$). For this reason, we have to use a coronagraph in order to image Gliese 229B and Gliese 229A simultaneously. However, spatial variations in the transparency across the occulting disk will bias the determination of the centroid of Gliese 229A but not that of Gliese 229B. An additional complication is that the point spread function varies across the coronagraphic field of view. The situation is far more favorable at infrared wavelengths where $C \sim 60$ and thus direct imaging techniques can be used. From a number of

short and long exposures we find that Gliese 229B is located $7''.69 \pm 0''.1$ from Gliese 229A at $PA = 162° \pm 1°$. The pixel scale and the orientation of the infrared camera are extremely well determined and known to be very stable.

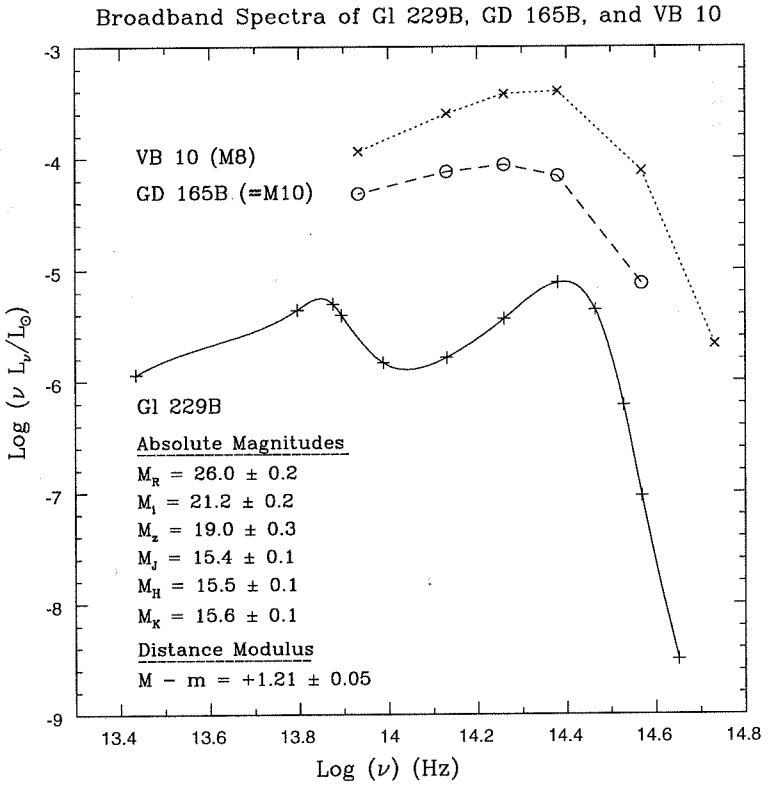

Figure 2.2 Broadband spectra of Gliese 229B, GD 165B and vB 10. The ordinate is the logarithm of νL_ν where ν is the frequency and L_ν the luminosity per unit frequency. The spectral band in which most of the energy emerges is best indicated by this quantity. The observed magnitudes of Gliese 229B are $r > 22.1$ (a 10σ upper limit), $i = 20.0 \pm 0.2$, $z = 17.8 \pm 0.3$, $J = 14.6 \pm 0.1$, $H = 14.7 \pm 0.1$, $K = 14.6 \pm 0.1$ and $K_s = 14.7 \pm 0.1$. The solid line is a cubic spline interpolation of the observed points. The data for GD 165B and the late M dwarf, vB 10, are obtained from Jones et al. (1994). Gliese 229B is remarkable for both its low luminosity and peaked spectral energy distribution. Additional points on this plot which did not appear in Nakajima et al. (1995) are from the more accurate photometry of Matthews et al. (1996). See §3.1.4.

The magnitudes of Gliese 229B are given in Fig. 2.2.[1] The total (or bolometric) luminosity L can be obtained by integrating the broadband spectrum shown in

[1]The point plotted here for r band is from the HST photometry presented in §3.3.4.

Fig. 2.2. This integration yields $L \sim 4.9 \times 10^{-6} L_{\odot}$. It is possible that there is considerable emission at frequencies smaller than the lowest measured frequency at K band. However, this method overestimates the total emission due to the presence of opacity between the observed bands. For these reasons, an accurate estimation of the total emission requires guidance from models of brown dwarf atmospheres. These models are still in their infancy, and they critically rely on effective temperature, $T_{\rm eff} = (L/4\pi R^2 \sigma)^{1/4}$, where R is the radius and σ is the Stefan-Boltzmann constant. For brown dwarfs, $R \sim 0.1\ R_{\odot}$ (Stevenson 1991; Burrows and Liebert 1993). We obtain $T_{\rm eff} = 900$ K for Gliese 229B. Only the models of Tsuji et al. (1995) are applicable to such a low $T_{\rm eff}$. They predict $\mathrm{K - L'} = 2$ for the observed $\mathrm{J - K} = 0.15$ and $T_{\rm eff} \sim 1000$ K. Incorporating the predicted L' and extrapolating the low frequency tail with a Rayleigh–Jeans formula, we obtain $L \sim 6.4 \times 10^{-6}\ L_{\odot}$.[2]

The definition of a brown dwarf depends on its mass being below 80 M_J. However, with the data at hand, it is not possible to determine the mass of Gliese 229B from dynamical considerations (Henry and McCarthy 1993). However, according to models of low-mass stars (Burrows and Liebert 1993), the luminosity of the lowest mass star is $L_{min} \gtrsim 10^{-4}\ L_{\odot}$. This is about equal to the luminosity of GD 165B (Zuckerman and Becklin 1992; Tinney et al. 1993). Unfortunately, the mass of this object is unknown. It is certainly on the threshold of the star-substellar boundary. The red dwarf with the lowest determined dynamical mass is GJ 1245C, $M = 0.074 \pm 0.013\ M_{\odot}$ (Henry and McCarthy 1993). The luminosity of this star is about $5 \times 10^{-4}\ L_{\odot}$. For Gliese 229B, we make the the conservative assumption of $L < 10^{-5}\ L_{\odot}$ which is more than an order of magnitude smaller than the luminosity of either of these two objects. Thus we conclude that Gliese 229B is certainly a brown dwarf. Below we argue that the peculiar broadband spectrum of Gliese 229B

[2]These numbers have been modified from those in Nakajima et al. (1995). Those were determined to be erroneous because of incomplete subtraction of the scattered light from Gliese 229A (Matthews et al. 1996; §3.1.4).

constitutes an independent line of reasoning that supports this conclusion.

We now use brown dwarf cooling models to estimate the mass of Gliese 229B. According to these models (Burrows and Liebert 1993), the luminosity of a brown dwarf older than 10^8 yr is

$$L = 3.4 \times 10^{-6}\ L_\odot\ t_9^{-1.3}\ (M/20M_J)^{2.64},$$

where t_9 is the age of the brown dwarf in billions of years, M is the mass of the brown dwarf, and M_J is the mass of Jupiter. Thus we infer a mass of $\sim 20\sqrt{t_9}\ M_J$. Earlier we argued that t_9 is of order unity. Even if t_9 is as high as 6, the estimated mass is still below the maximum mass for brown dwarfs. All this discussion assumes that Gliese 229A and Gliese 229B are coeval.

The broadband spectrum of Gliese 229B is unlike that of any known star or for that matter any known celestial object. Specifically, the infrared color is blue whereas the optical color is extremely red (Fig. 2.2). The spectral energy distribution peaks at J band, $\lambda \sim 1.25\ \mu$m. This is indeed predicted by recent models of brown dwarf atmospheres (Tsuji et al. 1995; Allard and Hauschildt 1995). This phenomenon is reproduced by all models regardless of the details of the input molecular opacities. At high pressures and low temperatures, characteristic of atmospheres of brown dwarfs, H_2O and CH_4 are formed abundantly and these molecules essentially limit the transmission to the near infrared band of 1 to 2 μm. Even in this band, CH_4 ensures that the dominant window is the J band. The cool temperature results in very little emission below 1 μm. Thus, these two effects conspire to produce a peak at J band. We argue that the peculiar broadband spectrum provides additional evidence that Gliese 229B is a cool brown dwarf. Elsewhere (Oppenheimer et al. 1995; §3.2.9), we report the detection of strong methane absorption in the spectrum of this object which provides the definitive proof that Gliese 229B is a cool object, $T_{\rm eff} < 1200$ K.

We end with some suggestions and speculations. First, searches for isolated brown

dwarfs should take advantage of the peculiar colors such as those we see in Gliese 229B. Specifically, the searches should not use infrared colors alone as a discriminant but compare optical flux to any infrared flux. Second, the projected separation of Gliese 229B is 44 astronomical units, which is about the distance from the Sun to Pluto. Thus the orbital motion of Gliese 229B should be $0\farcs1\ \mathrm{yr}^{-1}$. Observations with the Hubble Space Telescope will easily measure this (§3.3.4). Newly commissioned infrared interferometers have sufficient precision that the mass of Gliese 229B can be determined over the next few years, provided that the orbit is circular.[3]

[3]This turned out to be impossible because none of the interferometers in existence can observe objects with a declination of $-21°$.

2.2 First Spectrum of the Cool Brown Dwarf Gliese 229B[†]

B. R. Oppenheimer, S. R. Kulkarni, K. Matthews & T. Nakajima

Palomar Observatory 105-24, Caltech, Pasadena, CA 91125

Abstract

We present the first spectroscopic measurements of a cool brown dwarf, Gliese 229B. This spectrum in the near infrared has absorption features due to methane much like those of Jupiter. These features are not seen in any star. The presence of methane indicates that the surface temperature of Gliese 229B is below 1000 K. Features attributed to water vapor also indicate that Gliese 229B is much cooler than any known star.

Stars like our sun fuse hydrogen into helium and in the process produce energy, most of which appears as light. Current stellar models agree that objects less massive than 0.08 $M_\odot$ cannot sustain hydrogen fusion (Kumar 1963; Stevenson 1991; Burrows and Liebert 1993). (Here, the sun is denoted by the symbol $\odot$ and $M_\odot$ is the mass of the sun.) Such objects are the so-called "brown dwarfs." When they are young ($\lesssim 10^8$ yr) they contract relatively rapidly and the gravitational binding energy released makes these objects quite luminous. As they age, they rapidly cool and grow dim, becoming increasingly harder to detect. At even lower masses, there exist giant planets, the only examples of which are the giant outer planets of the solar system, including Jupiter (mass $M_J \sim 10^{-3}\ M_\odot$). According to theory, the objects in the mass range 1 to 100 M_J have similar characteristics. All of them have fully convective interiors[4] and have thin radiative atmospheres which radiate mostly between

[†]Previously published in Oppenheimer et al. (1995).

[4]This is no longer believed. In fact, the discovery of a thin, detached radiative shell below the photosphere of Jupiter was demonstrated by Guillot et al. (1994). Burrows et al. (1997) extended the argument to the brown dwarf regime and demonstrated that, in fact, most brown dwarfs are not

bands of molecular absorption. In addition, they all have about the same radius, $R \sim 0.1\ R_\odot$. Despite these similarities, brown dwarfs and giant planets are thought to form differently. It is believed that planets condense within a protoplanetary disk. In contrast, brown dwarfs are thought to form like stars through direct condensations of interstellar gas.

There are at least two different reasons why the study of brown dwarfs, especially cool brown dwarfs, excites considerable attention. First, astronomers would like to find these objects which lie in the unexplored mass range between stars and planets. Though these objects were predicted some 30 years ago (Kumar 1963), the lack of unambiguous specimens has been a major stumbling block in this field. Second, planetary scientists would like to study the atmospheres of cool brown dwarfs to understand how they are related to the atmospheres of planets. Such understanding is critical in the search for other planetary systems.

The emergent spectrum of radiation from a condensed object depends on the chemical composition, the surface gravity and the effective surface temperature, $T_{\rm eff}$. Here $T_{\rm eff}$ is defined by the relation $\sigma T_{\rm eff}^4 = L/4\pi R^2$, where L is the luminosity and σ is the Stefan-Boltzmann constant. The minimum luminosity of hydrogen fusing stars (the so-called main sequence stars) is $10^{-4}\ L_\odot$ (Stevenson 1991; Burrows and Liebert 1993). Thus, for these stars, $T_{\rm eff} \gtrsim 1800$ K. This is about equal to the temperature of GD 165B (Zuckerman and Becklin 1992), the coolest condensed object known until the discovery of Gliese 229B (Nakajima et al. 1995). As discussed above, old brown dwarfs do not generate nuclear power and thus can achieve very low $T_{\rm eff}$.

At the low temperatures characteristic of planets and old brown dwarfs, molecules

fully convective. In §3.2.9 (adapted from Oppenheimer et al. 1998) we show observational evidence for this structure.

and possibly dust are readily formed. Molecules have a large number of energy levels and this drastically complicates detailed modeling of their atmospheres. To date, there exist no detailed models for $T_{\rm eff}$ below 2000 K (Tsuji et al. 1995; Allard and Hauschildt 1995)[5]. However, predictions do exist. For example, below $T_{\rm eff}$ of 1000 K, most of the carbon is predicted (Tsuji 1964) to reside in methane, CH_4. In contrast, the cool, late-type stars (with $T_{\rm eff} > 1800$ K) have no methane. Their carbon resides mainly in CO which has a distinctive appearance in spectra of these stars.

Observations of cool objects are crucial to any further progress in this field. As Stevenson (1986) remarks in a review of high mass planets and brown dwarfs, "The biggest challenges for the future lie not in theory but in observations: we need more than two colors. We need spectra. . . . Refinement of the theory does not seem to be a compelling task until this happens."

Here we report the first near infrared spectroscopic observation of a cool brown dwarf, Gliese 229B (Nakajima et al. 1995). This object has the same proper motion as that of Gliese 229 and is thus most likely a companion of Gliese 229 (hereafter Gliese 229A). Nakajima et al. (1995) obtained broadband photometric measurements from which they deduce $L \lesssim 10^{-5}\ L_{\odot}$. This is ten times smaller than the minimum luminosity of any main sequence star. Nakajima et al. concluded that Gliese 229B is a cool ($T_{\rm eff} \lesssim 1200$ K) condensed object. At the present time, we are unable to determine the origin of this object. For simplicity we will refer to Gliese 229B as a brown dwarf (as opposed to a large planet).

IR spectra were obtained at the $f/70$ Cassegrain focus of the Hale 200-inch telescope using a grism spectrograph and an infrared camera consisting of reimaging optics and a 256×256 pixel Santa Barbara Research Corporation InSb detector. For

[5]This has changed drastically since the spectroscopic studies of Gliese 229B, which provided necessary data on the low temperature objects to which models could finally be compared. See, for example, Burrows et al. (1997), Fegley & Lodders (1996), Allard et al. (1996).

all observations reported here, a focal slit of 0.″5 by 32″ was used. The appropriate orders of the spectrum dispersed by the grism were selected with interference filters: Z (0.95 – 1.11 μm), J (1.15 – 1.40 μm), H (1.49 – 1.81 μm), and K (1.95 – 2.55 μm). For each of the spectra, the resolution was $\lambda/\Delta\lambda \sim 150$. The detector pixel size was 0.″125 in the spatial dimension and one quarter of the resolution in the spectral dimension.

Spectra of Gliese 229B were obtained in the K and H bands on the night of 14 September 1995 UT and in the Z, J, H, and K bands on the following night. We also obtained spectra of Jupiter for comparison. For atmospheric transmission calibration, G dwarf stars were observed at air masses similar to those of Gliese 229B and Jupiter. For wavelength calibration, we observed the bright planetary nebula NGC 7027.

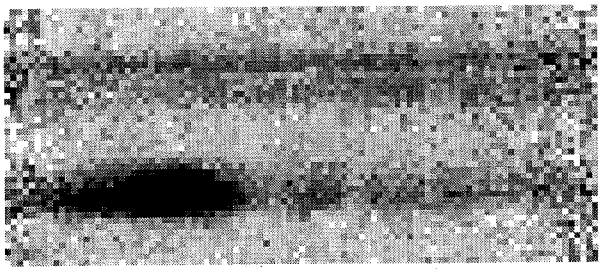

Figure 2.3 Typical spectral image of Gliese 229B in the H band. The vertical dimension covers 5.″4 west along the slit. The upper dark stripe is the spectrum of the light from Gliese 229A diffracted by the telescope spider and the lower dark stripe is the spectrum of Gliese 229B. Clearly, these two stripes do not overlap. Thus there was no confusion regarding whether the one dimensional spectra were in fact correct extractions from these spectral images. The wavelength coverage is from 1.5 μm (left) to 1.8 μm (right). The diffracted light from Gliese 229A is separated by 2.″4 from the light of Gliese 229B. The spectrum of Gliese 229A, a cool star of spectral type M1, is almost flat through the H band, while that of Gliese 229B strongly peaks just below 1.6 μm. This spectral feature of Gliese 229B distinguishes it from any previously known hydrogen burning star.

When obtaining the spectrum of Gliese 229B, we oriented the long axis of the slit east-west to minimize the contamination of light from Gliese 229A diffracted by

the secondary mirror support. Data obtained with the star at three different positions on the slit allowed us to remove time-varying sky contributions by subtracting consecutive images. We then divided the data by the spectral image of the G star HR 683 which was uniformly scanned along the slit by tilting the secondary. For Jupiter we used HR 6269. In addition, for Gliese 229A we subtracted the adjacent sky in order to remove atmospheric emission features, and obtained a spectral image (Fig. 2.3). This image demonstrates that the spectra of Gliese 229A and Gliese 229B are well separated, and there can be no mistake by which we might have extracted a combination of the two spectra. By summing the data along the spatial dimension, we created one-dimensional spectra. Next, we removed the blackbody shape of the G star. The absolute flux calibration of the Gliese 229B spectrum involved (i) the removal of the blackbody shape of the G star used, (ii) the normalization of the flux density to the photometry of Nakajima et al. (1995) and (iii) the assumption that Gliese 229B has a radius of 0.1 $R_{\odot}$ and is 5.7 parsecs distant. The result, then, is the flux density at the surface of Gliese 229B. The assumptions in step (iii) have no effect upon the shape of the spectrum (Fig. 2.4).

The spectrum of Gliese 229B is different from any of the spectra of late M stars, including GD 165B (see Figure 1 of Jones et al. 1994), but similar to that of Jupiter. The striking features in the Gliese 229B spectrum are the absence of any signal in one half (1.62 – 1.80 μm) of the H band and one half (2.25 – 2.40 μm) of the K band. However, these features are seen in Jupiter's spectrum (Fig. 2.4). In Jupiter, the H-band absorption is primarily attributed (Danielson 1966) to strong CH_4 bands and the K-band depression is due to CH_4 and also collisionally induced absorption by molecular hydrogen. The similarity of the H-band spectra of Gliese 229B to that of Jupiter is a clear indication that methane is present in Gliese 229B. Some similar features are observed in the dusty envelopes surrounding the bright asymptotic giant branch (AGB) stars. However, Gliese 229B has a large proper

motion (Nakajima et al. 1995). If it were an AGB star, with an intrinsic luminosity typical of such stars, Gliese 229B would lie outside the galaxy and would be moving at a relativistic speed.

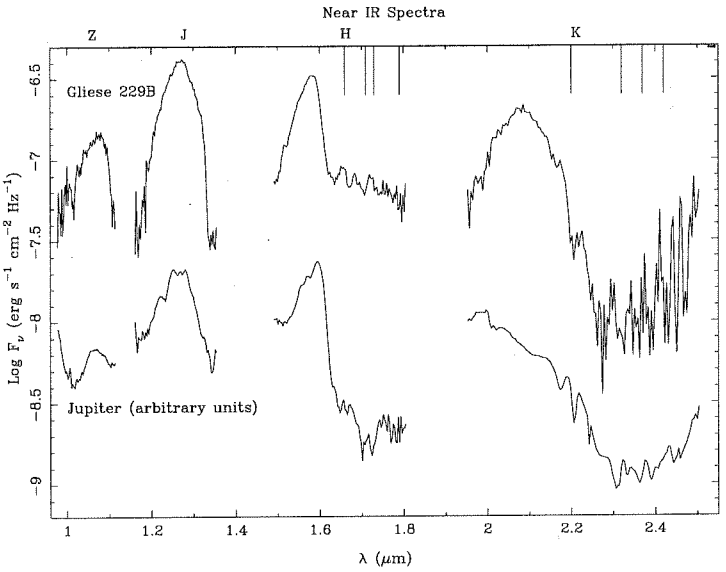

Figure 2.4 Near-infrared spectra of Gliese 229B and Jupiter. The spectra of Jupiter are positioned vertically simply for ease of comparison. The spectral resolution is 150. The vertical bars at the top of the plot indicate the locations of CH_4 absorption features at 1.66, 1.71, 1.79, 2.20, 2.32, 2.37 and 2.4 μm. The flux density is scaled to the values presumed at the surface of the brown dwarf.

A deep absorption feature at 1.34 μm is seen in the spectrum of Gliese 229B. Such a feature is also seen in all cool stars and GD 165B and is attributed to an H_2O absorption band. Jones et al. (1994) argued that the depth of this absorption feature, defined as R_{H_2O}, the ratio of flux in the band 1.286 – 1.303 μm to the flux in the band 1.338 – 1.356 μm, is inversely related to $T_{\rm eff}$. GD 165B has absorption much deeper than all the M stars and thus the largest value of $R_{H_2O} \sim 1.9$. R_{H_2O} for Gliese 229B is ~ 10. Jones et al. (1994) also pointed out that the slope of the spectrum in the range 2.05 – 2.15 μm is inversely proportional to $T_{\rm eff}$. The slope for Gliese 229B is more than an order of magnitude larger than that for GD 165B.

Tsuji (1964), on the basis of chemical equilibrium considerations, has argued that

for atmospheres with $T_{\rm eff}$ less than 1000 K almost all of the carbon is in the form of CH_4 rather than in CO. This explains why CH_4 is seen in Jupiter but not in any main sequence star. The presence of CH_4 in Gliese 229B is an independent indication that $T_{\rm eff}$ for Gliese 229B is less than 1000 K. Further support for this conclusion comes from the extreme values of the two spectral diagnostics described above. These imply that Gliese 229B is indeed a cool brown dwarf, with $T_{\rm eff} \lesssim 1000$ K.

Our upper limit on $T_{\rm eff}$ is based purely on chemical thermodynamics and molecular excitation physics. In contrast, Nakajima et al. (1995) used broadband photometric data and the assumption that Gliese 229B is at the distance of Gliese 229A to estimate that $T_{\rm eff} \lesssim 1200\ K$. Our upper limit on $T_{\rm eff}$ lends strong credence to the idea that Gliese 229A and Gliese 229B constitute a binary system at a distance of 5.7 parsecs.

Chapter 3

Detailed Study of Gliese 229B

3.1 Photometry: Spectral Energy Distribution[†]

K. Matthews, T. Nakajima, S. R. Kulkarni and B. R. Oppenheimer

Palomar Observatory, 105-24, Caltech, Pasadena, CA 91125

Abstract

Infrared broadband photometry of the cool brown dwarf Gliese 229B extending in wavelength from 0.8 to 10.5 μm is reported. These results are derived from both new data and reanalyzed, previously published data. Existing spectral data reported have been rereduced and recalibrated. The close proximity of the bright Gliese 229A to the dim Gliese 229B required the use of special techniques for the observations and also for the data analysis. We describe these procedures in detail. The observed luminosity between 0.8 and 10.5 μm is $(4.9 \pm 0.6) \times 10^{-6}$ $L_\odot$. The observed spectral energy distribution is in overall agreement with a dust-free model spectrum by Tsuji et al. for $T_{eff} \approx 900$ K. If this model is used to derive the bolometric correction, the best estimate of the bolometric luminosity is 6.4×10^{-6} $L_\odot$ and 50% of this luminosity lies between 1 and 2.5 μm. Our

[†]Previously published in Matthews et al. (1996).

best estimate of the effective temperature is 900 K. From the observed near-infrared spectrum and the spectral energy distribution, the brightness temperatures (T_B) are estimated. The highest, T_B = 1640 K, is seen at the peak of the J band spectrum, while the lowest, $T_B \leq$ 600 K, is at 3.4 μm, which corresponds to the location of the fundamental methane band.

3.1.1 Introduction

Earlier, we reported the discovery of a cool brown dwarf, Gliese 229B. It is assumed to be a companion of the nearby star Gliese 229A because they exhibit common proper motion (§2.1; Nakajima et al. 1995, hereafter N95). In §2.1, we presented broadband photometry of the brown dwarf between 0.65 and 2.2 μm and estimated the bolometric luminosity ($L_{bol} < 10^{-5}$ $L_\odot$) and the effective temperature ($T_{eff} < 1200$ K). In a second paper, we presented the near-infrared (1.0 to 2.5 μm) spectrum of Gliese 229B, and reported the first detection of methane absorption bands (Oppenheimer et al. 1995; §2.2).

Here we report narrow-band imaging photometry of Gliese 229B between 3 and 4 μm and broadband aperture photometry of Gliese 229A and Gliese 229B at 2.2 (K), 3.7 (L'), 4.8 (M), and 10.5 μm (N). Due to the large flux ratios between, and the small angular separation of, Gliese 229A and Gliese 229B, considerable effort was made to minimize the influence of the diffracted and scattered light of Gliese 229A on the photometry of Gliese 229B. We describe the observations and data reduction in §3.1.2 and §3.1.3, respectively. The near-infrared magnitudes (J, H, K, K_s) reported in N95 were found to be in error because of incorrect accounting for the diffracted light of Gliese 229A. The near-infrared, low-resolution spectral data reported in §2.2 were also reanalyzed and recalibrated (§3.1.3). In §3.1.4, we discuss the spectral characteristics of the photospheric emission of Gliese 229B and estimate the bolometric luminosity with the aid of model spectra by Tsuji et al. (1995, 1996a).

3.1.2 Observations

The journals of observations of Gliese 229A and Gliese 229B are given in Tables 3.1 and 3.2. The near-infrared photometry at Z, J, H, K_s, and K is reported in §2.1. The near-infrared spectroscopy is reported in §2.2. The new observations are discussed below.

TABLE 3.1 JOURNAL OF OBSERVATIONS AND PHOTOMETRY OF GLIESE 229A

Date 95 UT (1)	Band (2)	λ range (μm) (3)	Telescope (4)	Instrument (5)	Mode (6)	mag (7)	flux (Jy) (8)
23 NOV	K	2.02–2.43	H200	Photometer(InSb)	Chop	3.9	17.0
23 NOV	L'	3.37–4.01	H200	Photometer(InSb)	Chop	4.0	6.4
23 NOV	M	4.47–5.08	H200	Photometer(InSb)	Chop	4.0	3.8
9 & 22 NOV	N	8.0–13.1	H200	Bolometer(Ge)	Chop	3.9	1.02

Col. (4): H200 = the Hale 200-inch telescope. Col. (5): Both D-78 and NIRC employ SBRC InSb 256×256 arrays. Col. (8): 1 σ error in flux density is estimated to be ± 10%, unless given explicitly.

3.8 μm Observations

The observations at 3.8 μm were made in photometric conditions on the Hale 200-inch telescope on 11 October 1995 UT using the same equipment (D78, a camera similar to NIRC which is described below) that was used for the observations on 14 September 1995 (§2.1, §2.2). The only difference in the observational technique was that the chopping secondary was used to move the focal plane on the sky and that only the central 8″× 8″, (64 × 64 pixels) portion of the detector was read out. A single observation consisted of the following steps:

1. Six 68 millisecond frames were added into the image buffer.

2. The chopper moved the focal plane 5″ West on the sky and six 68 millisecond frames were added into the sky buffer. The chopper then moved the focal plane 5″ East back to the original position.

TABLE 3.2 JOURNAL OF OBSERVATIONS AND PHOTOMETRY OF GLIESE 229B

Date 95 UT (1)	Band (2)	λ range (μm) (3)	Telescope (4)	Instrument (5)	Mode (6)	mag (7)	f_ν (mJy) (8)
14 SEP	Z	0.95–1.11	H200	D-78	Stare	15.3	1.5
14 SEP	J	1.15–1.40	H200	D-78	Stare	14.2	3.2
14 SEP	H	1.49–1.81	H200	D-78	Stare	14.3	2.0
14 SEP	K_s	1.99–2.32	H200	D-78	Stare	14.3	1.3
14 SEP	K	1.9–2.4	H200	D-78	Stare	14.4	1.2
23 NOV	K_l	2.02–2.43	H200	Photometer(InSb)	Chop	14.5	1.0
6 OCT	3.08	3.03–3.13	KECK	NIRC	Stare	13.5	1.5 ± 0.2
6 OCT	3.31	3.28–3.34	KECK	NIRC	Stare	> 14.4	< 0.6
6 OCT	3.41	3.38–3.45	KECK	NIRC	Stare	> 14.7	< 0.4
23 NOV	L'	3.37–4.01	H200	Photometer(InSb)	Chop	13.4	1.1 ± 0.8
11 OCT	3.82	3.67–3.97	H200	D-78	Chop	11.8	5.0 ± 1.0
6 OCT	3.99	3.97–4.02	KECK	NIRC	Stare	11.4	6.6 ± 1.0
23 NOV	M	4.47–5.08	H200	Photometer(InSb)	Chop	10.9	7 ± 3
9 & 22 NOV	N	8.0–13.1	H200	Bolometer(Ge)	Chop	9.9	4.2 ± 0.9

Col. (4): H200 = the Hale 200-inch telescope. Col. (5): Both D-78 and NIRC employ SBRC InSb 256×256 arrays. Col. (8): 1 σ error in flux density is estimated to be $\pm$ 10%, unless given explicitly. The 3.08 λ range was incorrectly quoted in Matthews et al. (1996).

3. Steps 1 and 2 were repeated for 100 cycles.

4. The telescope was then moved 5″ East, and steps 1, 2, and 3 were repeated with the buffers interchanged.

5. The final image was formed by subtracting the two sky buffers from the sum of the two image buffers.

Gliese 229B was observed 5 times at 1.8 airmass by this procedure while the standard star HD 22686 (Elias et al. 1982) was observed twice at 1.7 airmass for 1 instead of 100 cycles.

Narrow-Band Imaging at the Keck Telescope

Gliese 229B was imaged through narrow-band filters in the 3 μm atmospheric window in late twilight and morning daylight of 6 October 1995 UT at the Keck Telescope

using NIRC (Matthews and Soifer 1994). The sky was photometric and the seeing at 3 μm was about 0.″5. The observations were unguided but of short enough duration that no tracking errors were noticed in the resulting images. The object images were obtained by summing a series of short integrations into a buffer and then the telescope was offset by 15″ North and a sky frame was obtained in the same manner. The standard star HD 22686 was measured, and then Gliese 299B was measured. Both were at similar airmass. In no case, did any of the six diffraction spikes produced by the secondary supports and segment gaps interfere with the image of Gliese 229B.

Observations by Aperture Photometer

Observations at N band were made on 9 and 22 November 1995 (UT) at the f/70, infrared Cassegrain focus of the Hale 200-inch telescope with a germanium bolometer (Infrared Laboratories, Tucson, AZ). The observations at the K, L' and M bands were obtained on 23 November 1995 UT using a photovoltaic InSb detector (SBRC, Santa Barbara, CA). Table 3.3 shows the details of the observations. The visual seeing estimated from the images displayed on the TV acquisition camera were 1.″5 during the N band observations and 1″ during the K, L' and M observations. Experience has shown that the seeing diameter at N band is about one half of that at visual wavelength on the Hale 200-inch telescope. The sky was photometric during all of the observations.

For all observations the focal plane aperture was 2.″0 in diameter and the chopping was East-West with a square wave of 50 Hz for the bolometer and 5 Hz for the InSb detector. The square wave had a peak-to-peak amplitude of 4.″8. This amplitude was chosen to be twice the right ascension distance from Gliese 229B to the secondary support diffraction spike from Gliese 229A. This configuration effectively nulled the contribution of the diffraction spike to the signal of Gliese 229B when chopping across the spike. The signal was demodulated with a lock-in amplifier using the chopper

TABLE 3.3 DETAILS OF APERTURE PHOTOMETRY

Date (95 UT)	Band	Object	τ (sec)	P (pair)	T_{int} (sec)	Airmass	Signal (DN/sec)
9 NOV	N	HR 2491	20	1	20	1.9	2.37×10^6
		Gliese 229A	20	4	80	1.9	1.81×10^4
		Gliese 229B	40	64	2560	1.8	26 ± 31
		Gliese 229A	20	4	80	1.8	2.02×10^4
		Gliese 229B	40	64	2560	1.8	58 ± 31
		Gliese 229I	40	64	2560	1.9	-4.5 ± 31
		Gliese 229A	20	2	40	1.9	1.83×10^4
		Gliese 229I	40	64	2560	2.2	28.5 ± 31
		Gliese 229A	20	2	40	2.4	1.77×10^4
		HR 2491	20	2	40	1.9	2.34×10^6
22 NOV	N	HR 2491	20	4	80	2.1	2.78×10^6
		Gliese 229A	20	4	80	2.0	2.03×10^4
		Gliese 229B	40	64	2560	1.8	111 ± 34
		Gliese 229A	20	6	120	1.8	1.90×10^4
		Gliese 229I	40	64	2560	1.8	2.4 ± 34
		Gliese 229A	20	4	80	1.9	1.62×10^4
		Gliese 229B	40	64	2560	2.0	113 ± 34
		Gliese 229A	20	4	80	2.2	1.46×10^4
		HR 2491	20	4	80	1.8	2.11×10^6
23 NOV	M	HR 2491	20	2	40	2.2	1.89×10^6
	L'	HR 2491	20	2	40	2.2	6.24×10^7
	L'	Gliese 229A	20	2	40	2.0	4.49×10^5
	M	Gliese 229A	20	2	40	2.0	1.37×10^4
	K	Gliese 229A	20	2	40	2.0	3.95×10^7
	K	Gliese 229B	80	2	160	1.9	4.35×10^3
	K	Gliese 229I	80	2	160	1.9	2.03×10^3
	K	Gliese 229B	40	2	80	1.9	5.23×10^3
	M	Gliese 229B	80	32	2560	1.9	28.5 ± 20
	M	Gliese 229A	20	2	40	1.8	1.40×10^4
	K	Gliese 229B	20	2	40	1.8	4.68×10^3
	M	Gliese 229B	40	64	2560	1.8	6.8 ± 20
	M	Gliese 229A	20	2	40	1.8	1.48×10^4
	K	Gliese 229B	20	2	40	1.8	4.87×10^3
	M	Gliese 229B	40	64	2560	1.8	31.0 ± 20
	M	Gliese 229A	20	2	40	1.9	1.31×10^4
	L'	Gliese 229A	20	2	40	1.9	4.36×10^4
	L'	Gliese 229B	80	8	640	1.9	79 ± 53
	K	Gliese 229B	20	2	40	2.0	4.30×10^3
	M	Gliese 229B	40	64	2560	2.1	28.8 ± 20
	M	Gliese 229A	40	2	80	2.3	1.06×10^4
	M	HR 2491	20	2	40	1.8	1.99×10^6

signal as reference. The output of the lock-in amplifier was converted to pulses by a voltage-to-frequency converter and integrated by a digital counter. A time of τ seconds of data were taken at one telescope position, after which the beams were switched by moving the telescope East or West by 4.″8 and another τ seconds of data were taken. The difference between these two integrations constitutes a measure of the signal, called a pair. The East-West order was then reversed and the process was repeated so that an even number (P) of pairs was obtained in all cases. See Table 3.3 for values of P and τ.

During all observations, a TV autoguider on an offset guider stage was used to obtain and preserve centering of the objects in the focal plane aperture. The offset guider has an astrometric uncertainty of less than 0.″1 peak amplitude when used to offset between objects. The guider also corrected for the change in the differential refraction of the atmosphere between the guide star at 0.7 μm and the infrared source. For Gliese 229B observations we used a guide star located 19 arcsec East and 70″ North from Gliese 229A.

The above is standard procedure for observations with an infrared photometer. The fast chopping and beam switching removes slowly varying sky and instrument contributions. In addition, in order to measure the possible contribution of scattered light from Gliese 229A to Gliese 229B we performed a series of observations centered on a position inverted about Gliese 229A. This point, hereafter Gliese 229I, is located at 2.″4 West and 7.″3 North of Gliese 229A. For Gliese 229I, we beam switched in a manner identical to that used for Gliese 229B.

In Table 3.3 we purposely present the raw data (with no corrections applied) to demonstrate the stability and consistency of the observations which were made with an unusually small focal plane aperture and near a very bright source, Gliese 229A. In Table 3.3, for those measurements with no listed uncertainties, the dominant cause of variation is due to fluctuations in the seeing; for those cases, the uncertainty is

estimated to be ± 10%. The total range in airmass correction is a maximum of ± 5% in the M band and is about one half that in the other bands for both the standard (HR 2491, see below) and Gliese 229A. However, the airmass correction requires an accurate knowledge of the spectrum of the object. The spectrum of Gliese 229B is quite complicated (see §3.1.3). For simplicity, we assume an airmass correction for Gliese 229B to be the same as that of the other stars.

The reduced photometric data are shown in Tables 3.1 and 3.2. The uncertainties, where shown, are derived from the nightly average of the statistical fluctuations within each individual measurement. There is no evidence that the noise, exclusive of seeing variations, varied over a night's measurements.

The standard star HR 2491 (Sirius; Neugebauer 1995) was measured both immediately before and after each night's observations of the Gliese 229 system. The observations were conducted in a manner identical to that used for Gliese 229 including the use of an offset guide star. HR 2491 was too bright to measure in the K band, so its measurement at L' plus the known stable ratio of system response to flux in the K band to that in the L' band was used to derive the K band magnitudes of Gliese 229A and Gliese 229B. In the case of the K band measurement of Gliese 229B only, the data in Table 3.3 are derived from the flux measured at the position of Gliese 229B with the flux measured at the Gliese 229I position subtracted; this reduces the raw value by about one half. It should be noted that discrepancy of this K result from that reported in N95 led us to reanalyze the imaging data reported in N95. §2.1 contains the reanalyzed numbers.

The ratio of the signal at Gliese 229I to Gliese 229A forms a good estimate of the contribution of the scattered light from Gliese 229A to the signal measured at Gliese 229B. Seeing improves and the strength of the diffraction spikes decreases with increasing wavelength. Thus, the scattered light contributions are expected to decrease with increasing wavelength. An upper bound to the scattered light, at longer

wavelengths, is given by the measured signal of Gliese 229A multiplied by the ratio of the K signal of Gliese 229I to Gliese 229A. The total error is due to both this scattered light and also measurement errors. The ratios of the expected scattered light contribution to the measurement error are 0.43 at L', 0.07 at M, and 0.06 at N. For this reason, no attempt was made to measure Gliese 229I at M, and the measurement at N of Gliese 229I, 0.5 $\pm$ 1.0 mJy, was not included in that of Gliese 229B. The measurement at L' is clearly uncertain. It is included as a check on the narrow-band measurements and shows that there is no truly bright emission feature between them.

3.1.3 Reduction of Imaging and Spectroscopic Data

Revision of the Near-Infrared Magnitudes

In the lower right panel of Fig. 2.1, a K_s (2.15 μm) image of Gliese 229B is shown. At this wavelength, the brightness ratio of Gliese 229A to Gliese 229B is $\approx 10^4$. In the case of infrared imaging, Gliese 229A is occulted by a focal plane disk, but there is no special Lyot stop to suppress diffracted light from the telescope edges and secondary mirror supports as the coronagraph used at optical wavelengths. In the initial reduction whose photometric results were reported in N95, DAOPHOT in IRAF was used to fit the point spread function of Gliese 229B in the presence of the wing of the point spread function of Gliese 229A. The large discrepancy between the K magnitude in N95 and that obtained by the aperture photometry described above, led us to reanalyze all the near-infrared imaging data. The photometry in §2.1 is identical to that presented in this section. Only the photometry in N95 is wrong. It was found that the new background subtraction procedure was adequate. In this reanalysis, we produced a flattened image by subtracting the image reflected about the vertical diffraction spike from the original image. As can be seen from Fig.

3.1, the dramatic difference between this flattened image and the image in Fig. 2.1 is striking. The new image is sufficiently flat so that accurate photometry can be obtained using APPHOT in IRAF. The revised magnitudes for the Z, J, H, K_s and K are given in Table 3.2.

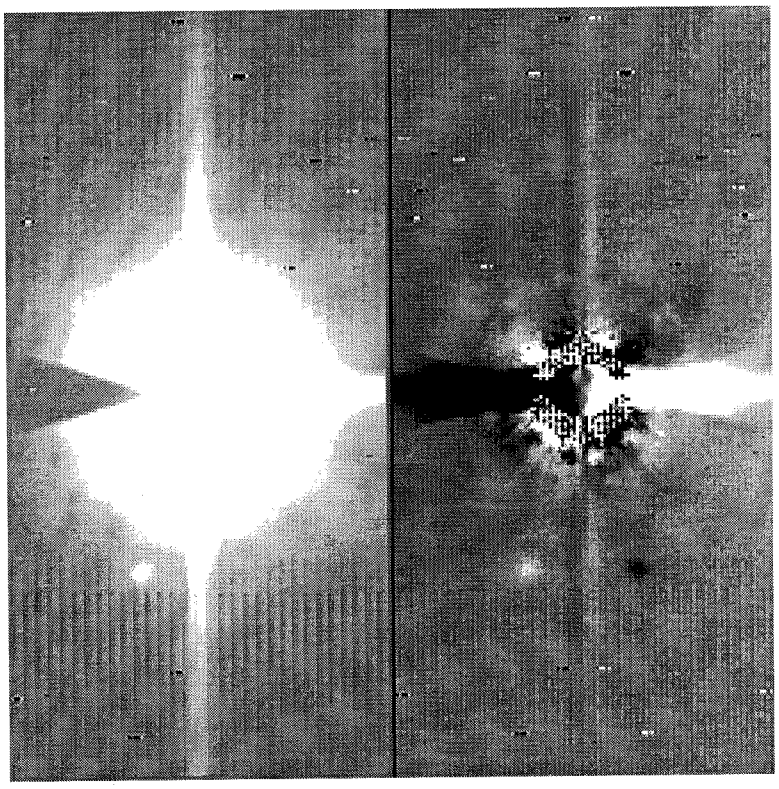

Figure 3.1 Left Panel: the K_s image used in N95. Right Panel: the left image subtracted from the same image after reflecting it along the vertical line. The stretch is ± 150 ADU. Note how flat the sky is, especially in the vicinity of Gliese 229B. Most photometry packages do not work well when the sky is not reasonably flat. We used the image on the right side to derive the photometry in the near-IR bands.

3 μm Narrow-Band Data Reduction

Narrow-band images at 3.08, 3.31, 3.41, and 3.99 μm obtained at the Keck Telescope were reduced differently from the broadband images obtained at the Hale 200-inch telescope. Because of the excellent seeing and low scattered light in the 3 μm region

at the Keck Telescope on Mauna Kea, the point spread function of Gliese 229B was hardly affected by the wing of Gliese 229A. However, vertical stripes were present in each image due to a readout electronics problem. This artifact was removed by shifting the image vertically and then subtracting the shifted image from the original. Gliese 229B was detected at 3.08 and 3.99 μm, but was not detected at 3.31 and 3.41 μm. For 3.31 and 3.41 μm, 1 σ upper limits of the fluxes are given in Table 3.2.

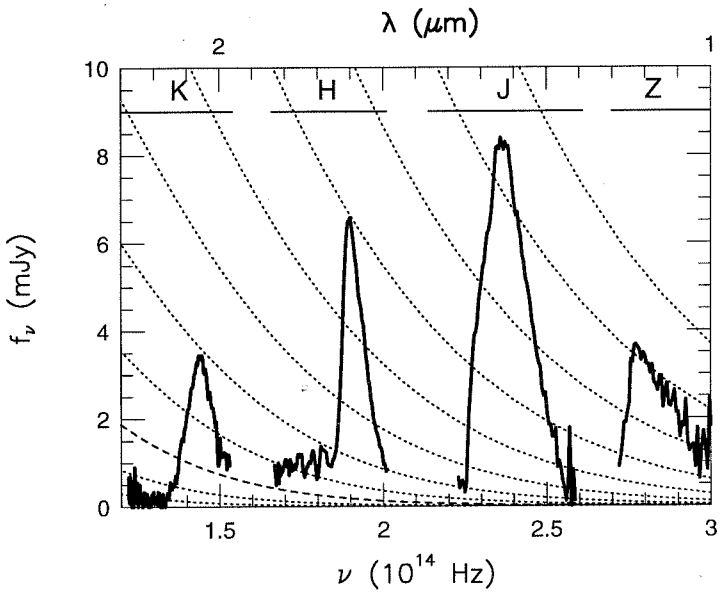

Figure 3.2 The observed near-infrared spectra of Gliese 229B (solid lines). The spectral resolution is $\nu/\Delta\nu \approx 150$. The width of each window in the Earth's atmosphere is indicated by the horizontal line just below the name of the window. Dashed lines indicate blackbody curves for T = 700 K (lower left) to 1700 K (upper right) plotted at an interval of 100 K. The long-dashed line is for T = 900 K, the estimated value of T_{eff} for Gliese 229B. Each blackbody curve was calculated assuming the radius, R = 0.1 $R_\odot$, and the distance, d = 5.7 pc, which are the assumed parameters for Gliese 229B. Each intersection of the spectrum and a blackbody curve indicates the brightness temperature (T_B) of that point of the spectrum. The highest, T_B = 1640 K, corresponds to the J band peak where the deepest layer in the atmosphere is exposed, while the lowest, T_B = 700 K, corresponds to the bottom of the methane absorption in K band where only the upper layer in the atmosphere is seen.

Reduction of the Near-Infrared Grism Spectra

Along with the imaging data obtained 14 September 1995 UT, we have reanalyzed the two-dimensional grism spectra obtained on 14 and 15 September 1995 UT. The observational procedures are briefly described in §2.2. Here we elaborate on the re-reduction and re-calibration of the spectra. In the spectral images, the spatial (slit) direction was placed along the y axis and the dispersion direction was along the x axis. In the original spectral image, the pixel-wise dispersion ($\Delta\lambda$/pixel) is a weak function of y. Using the strong emission lines seen in the spectrum of the bright planetary nebula, NGC 7027, this gradient of pixel-wise dispersion was estimated and each spectral image was rectified so that the pixel-wise dispersion became uniform along the y-axis. This procedure was performed before the column-wise subtraction of the OH airglow lines by the routine, BACKGROUND, in IRAF. The first order blaze wavelength of the grism is 6.6 μm, and the orders in individual bands are third in K, fourth in H, fifth and sixth in J, seventh and eighth in Z. The Z band spectra are thus obtained at angles well off the blaze angle. Consequently, the efficiency in the Z band is quite low. After eliminating bad pixels, one-dimensional spectra were extracted. For the calibration of atmospheric transmission, HR 1747 (G0V, $T_{\rm eff}$ = 5900 K) and HR 863 (G5V, $T_{\rm eff}$ = 5660 K) were used. G dwarfs are known not to have appreciable absorption or emission features at a resolution of about 150 in the near infrared. In the flux calibration, each raw spectrum divided by one of the two G star spectra was multiplied by the blackbody spectrum with corresponding $T_{\rm eff}$ normalized by the photometric data given in Table 3.2. The resultant near-infrared spectra of Gliese 229B are given in Fig. 3.2. The same spectra in a numerical form (ASCII file) can be obtained through the web page (http://astro.caltech.edu/$\sim$ bro/papers.html) or by contacting the author of this thesis. The revised spectra differ from those in Fig. 2.4 mainly in the flux calibration.

3.1.4 Discussion

Photospheric Emission of Gliese 229B

The near-infrared spectrum of Gliese 229B, presented in Fig. 3.2, can be characterized by deep absorption features of H_2O seen in the low-frequency side of Z, both sides of J, and the high-frequency halves of H and K. The other dominant features are absorption by CH_4 seen in the low-frequency halves of H and K. The fact that strong H_2O absorption features dominate the transmission by the Earth's atmosphere at these wavelengths must be accounted for in the determination of the total flux from Gliese 229B. In the Earth's cool atmosphere, only low-order rotational states of H_2O are excited, while in the warmer atmosphere of Gliese 229B, higher-order rotational states are also excited. Higher excitation of H_2O in the atmosphere of Gliese 229B results in much wider absorption bands. Thus it is expected that most of the emission from Gliese 229B will be observed by ground-based broadband photometry. In Table 3.4, we present, for each band, the absolute magnitude, corresponding flux in mJy if Gliese 229B were at the distance of 10 pc, and L_ν, the luminosity measured within the filter bandwidths. Here $L_\nu \equiv f_\nu 4\pi d^2 \Delta\nu$, where f_ν is the flux density at frequency ν, d is the distance to the source, 5.7 pc, and $\Delta\nu$ is the bandwidth of the band and given in Table 3.2. The total in-band observed luminosity (L_{obs}) is $(4.9 \pm 0.6) \times 10^{-6}$ $L_\odot$. The error estimate includes the error in Gliese 229A's parallax and uncertainties in the observations. If we assume that the radius of Gliese 229B, R(Gliese 229B), is 0.1 $R_\odot \approx R_J$, then $T_{eff} > 856$ K.

Comparison with Models and Bolometric Correction

We compare the atmospheric models of Tsuji et al. (1995, 1996a) with our data. Their models cover the wavelength range between 0.2 and 45 μm and their model for T_{eff} = 1000 K reproduces the observed spectral energy distribution (SED) reasonably well

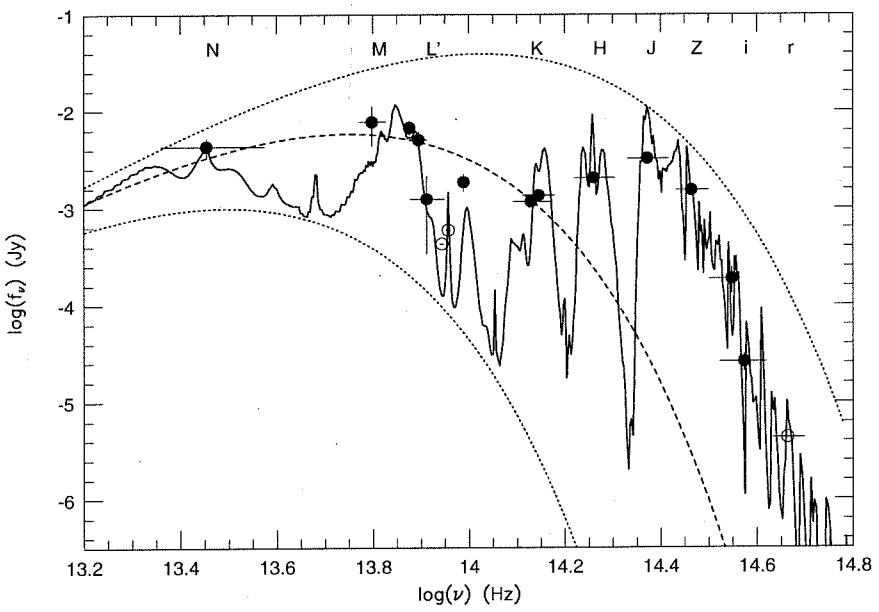

Figure 3.3 Comparison of broadband photometry with the model spectrum. Filled circles denote detections, while open circles indicate 1 σ upper limits. Horizontal bars attached to circles denote bandwidths, while vertical bars indicate 1 σ photometric errors. Locations of major bands are indicated by the letters. The solid line is the model spectrum for T_{eff} = 900 K by Tsuji et al. (1996a). Two short-dashed lines indicate blackbody curves for T = 500 K (bottom) and 1700 K (top). The long-dashed line indicates a blackbody curve for T = 900 K, the estimated value of T_{eff} for Gliese 229B. Non-detections through the narrow-band filters at 3.31 and 3.41 μm ($\log(\nu) \approx$ 13.95) indicate that the uppermost methane layer is cooler than 600 K. For the model spectrum and the blackbody spectra, R = 0.1 $R_\odot$ and d = 5.7 pc are assumed.

(Tsuji et al. 1996a). Tsuji has kindly provided us with his model spectra for T_{eff} = 800, 900, 1000, and 1200 K. These models give the following ratios of the luminosity that is contained in our observed bands to the bolometric luminosity (L_{obs}/L_{bol}): 0.76, 0.77, 0.78, and 0.80. Therefore L_{obs}/L_{bol} is rather insensitive to the effective temperature of the model. Using L_{obs}/L_{bol} = 0.77 for a bolometric correction, we obtain our best estimate of $L_{bol} = 6.4 \times 10^{-6}$ $L_\odot$. Again assuming R(Gliese 229B) = 0.1 $R_\odot$, we obtain T_{eff} = 913 K. The observed fluxes are compared with the model spectrum for T_{eff} = 900 K in Fig. 3.3 in which overall agreement is obviously seen.

Brightness Temperature and Depths of the Observed Atmosphere

The SED of Gliese 229B is significantly different from that of the blackbody for T_{eff} = 900 K. Due to deep H_2O and CH_4 absorption bands, the emergent flux is squeezed into the narrow windows through which hotter regions in the lower atmosphere are exposed. Fig. 3.2 presents the observed near-infrared spectrum with blackbody curves superimposed. Each intersection of the spectrum and a blackbody curve indicates the brightness temperature (T_B) of that portion of the spectrum. The highest, T_B = 1640 K, is seen at the peak within the J band spectrum ($\nu = 2.36 \times 10^{14}$ Hz). Fig. 3.3 shows the observed SED and the model spectrum with the blackbody curves similarly superimposed. Non-detections with the narrow-band filters at 3.31 and 3.41 μm ($\log(\nu) \approx 13.95$) indicate that the uppermost methane layer is cooler than 600 K.

TABLE 3.4 ABSOLUTE MAGNITUDES AND IN-BAND LUMINOSITIES OF GLIESE 229B

Band	Absolute Mag	f_ν(d=10pc) (mJy)	Luminosity ($L_\odot$)
Gunn r	> 23.3	< 0.0014	$< 3.0 \times 10^{-9}$
Gunn i	21.2	0.0084 ± 0.002	2.2×10^{-8}
Gunn z	19.0	0.061 ± 0.02	1.0×10^{-7}
Z	16.5	0.50	6.9×10^{-7}
J	15.4	1.1	1.5×10^{-6}
H	15.5	0.68	7.2×10^{-7}
K_s	15.5	0.44	2.9×10^{-7}
K	15.6	0.38	2.8×10^{-8}
3.08	14.7	0.5 ± 0.1	5.8×10^{-9}
3.31	>15.6	< 0.19	$< 1 \times 10^{-8}$
3.41	>15.9	< 0.14	$< 8 \times 10^{-9}$
L'	14.6	0.4 ± 0.3	1.6×10^{-7}
3.82	13.0	1.6 ± 0.3	3.1×10^{-7}
3.99	12.6	2.2 ± 0.3	6.3×10^{-8}
M	12.1	2.2 ± 1.0	6.1×10^{-7}
N	11.1	1.4 ± 0.3	5.9×10^{-7}

Lines 1, 2 and 3: Data from §2.1. Col 3: Flux density if Gliese 229B were placed at 10 pc.

3.2 Spectroscopy: Inside the Brown Dwarf†

Ben R. Oppenheimer, Shrinivas R. Kulkarni, Keith Matthews

Palomar Observatory 105-24, California Institute of Technology, Pasadena, California 91125

and

Marten H. van Kerkwijk

Institute of Astronomy, University of Cambridge, Madingly Road, Cambridge, CB3 0HA, UK

Abstract

We present a spectrum of the cool (T_{eff} = 900 K) brown dwarf Gliese 229B. This spectrum, with a relatively high signal-to-noise ratio per spectral resolution element ($\gtrsim$ 30), spans the wavelength range from 0.837 μm to 5.0 μm. We identify a total of four different major methane absorption features, including the fundamental band at 3.3 μm, at least four steam bands, and two neutral cesium features. We confirm the recent detection of carbon monoxide (CO) in excess of what is predicted by thermochemical equilibrium calculations. Carbon is primarily involved in a chemical balance between methane and CO at the temperatures and pressures present in the outer parts of a brown dwarf. At lower temperatures, the balance favors methane, while in the deeper, hotter regions, the reaction reverses to convert methane into CO. The presence of CO in the observable part of the atmosphere is therefore a sensitive indicator of vertical flows. The high signal-to-noise ratio in the 1 μm to 2.5 μm region permits us to place constraints on the quantity of dust in the atmosphere of the brown dwarf. We are unable to reconcile the observed spectrum with synthetic spectra that include the presence of dust. The presence of CO but lack of dust may be a clue to the location of the boundaries of the outer convective

†Previously published in Oppenheimer et al. (1998).

region of the atmosphere: the lack of dust may mean that it is not being conveyed into the photosphere by convection, or that it exists in patchy clouds. If the dust is not in clouds, but rather sits below the outer convective region, we estimate that the boundary between outer convective and inner radiative layers is between 1250 and 1600 K, in agreement with recent models.

3.2.1 Introduction

Gliese 229B is the first substellar object outside the solar system with an effective temperature, T_{eff}, well below 1800 K, the minimum T_{eff} for stars, found using direct imaging techniques (§2.1; Nakajima et al. 1995). Other substellar companions have been inferred to exist through indirect techniques (Wolszczan & Frail 1992; Mayor & Queloz 1997; Butler et al. 1997). The astrophysical nature of all these objects can only be understood in detail through spectroscopic studies. Unfortunately, current technology precludes the spectroscopic study of any of these objects, except Gliese 229B. Interestingly, the spectrum of a gaseous, substellar object is primarily determined by its effective temperature, and secondarily by its surface gravity and composition (Burrows et al. 1997; Burrows et al. 1996). Thus, the spectrum of Gliese 229B is expected to resemble the spectra of some of the less massive, but similarly hot, giant planets found in the radial velocity studies.

Here we present the spectrum of Gliese 229B with high signal-to-noise ratio from 0.837 μm out to 5 μm. Gliese 229B emits approximately 65% of its emergent flux in this wavelength region. An effort like this can perhaps be seen as a precursor to extrasolar planet studies or an extension of the work of hundreds of planetary scientists who have studied and modeled the atmospheres of the planets orbiting the Sun. In addition, these observations also give extremely interesting insights into the atmospheric physics of brown dwarfs, including the atmospheric dynamics. Our now

detailed set of observations can be compared with recent models.

Observations and Data Reduction

All observations reported here were made at the Keck Telescopes. At these telescopes, a major problem in observing Gliese 229B is the presence of diffraction spikes from Gliese 229A. The image of a star produced by one of the Keck telescopes has six diffraction spikes spaced every 60° around the center of the image. These spikes are produced by both the secondary support vanes and the primary mirror's segment gaps. The spikes are fixed with respect to the horizon. In celestial coordinates, the position angle of any spike is the paralactic angle plus an integer multiple of 60° (see right-top panel of Fig. 3.4). As a result, the spikes rotate as the star transits the sky. Useful spectra of Gliese 229B could only be obtained when the diffraction spikes of the very much brighter Gliese 229A were $\geq 15°$ away from the position angle of Gliese 229B. This reduced the time during which it was possible to observe Gliese 229B to 1.5 hours just after transit. Since Gliese 229B is not visible on the slit-viewing camera, we set up on Gliese 229A and applied a blind offset from there (7.″78 at position angle 161.°3; Nakajima et al. 1995).

3.2.2 Optical Data

We observed Gliese 229B using the Keck I telescope on 21 January 1996 (UT) with the Low Resolution Imaging Spectrometer (LRIS; Oke et al. 1995). We made three exposures of 1800 s duration each, using a Tektronix 2048 × 2048 pixel CCD with 24 μm pixels. We used the 1200 line mm^{-1} grating, blazed at 750 nm to cover the wavelength region of 847 to 973 nm at 0.06 nm pixel^{-1}. A 1″ slit, corresponding to 4.65 pixels, gave a spectral resolution of about 0.3 nm. The slit was placed East-West for all of the LRIS observations. An OG570 filter suppressed the second order

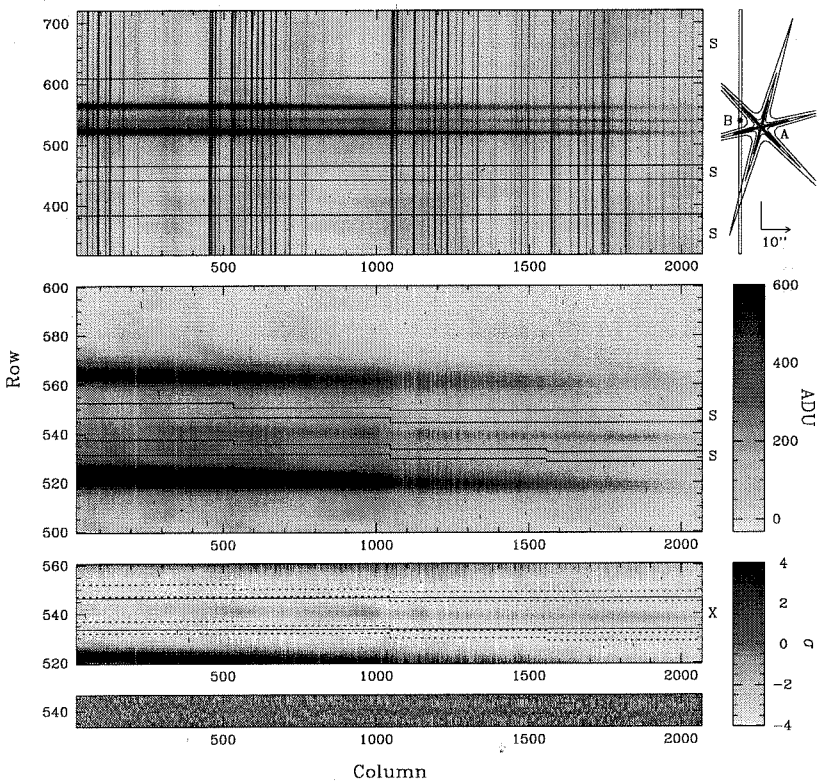

Figure 3.4 Reduction of the optical spectra. In the top panel, one of the spectral images (a 900 s integration) is reproduced, after only bias subtraction and division by a normalized flat-field. The whole spectral range is shown (blue to the left and red to the right), but not the full length of the slit. The grey scale is linear between -30 and 600 ADU (the gain is $2.2\,e^-\,ADU^{-1}$). A schematic view of the slit region of the spectrograph is also shown, with Gliese 229B in the slit, and A nearby with six diffraction spikes. Spectra of three of the spikes can be seen in the image. In the middle panel, the data is shown after removing telluric sky emission, as determined from fitting third-degree polynomials at every column in the regions marked 'S' to the right of the top panel. The contribution of scattered and diffracted light of Gliese 229A at the position of B was determined by fitting second-degree polynomials at every column in the two small regions marked 'S' to the right of the middle panel. The corrected data is shown in the third panel. The absorption due to steam bands, near column 1000, is clearly seen. The spectrum was extracted from the region indicated by the two solid lines, marked 'X' at the right-hand side. The fluxes weighted according to a spatial profile (see text) are used to extract the data. The residual after extracting the data is shown in the bottom panel in units of standard deviations, to show that the extraction is accurate. The scale in the Y direction is the same as that of the third panel. The grey scale is linear between -4σ and 4σ, as indicated.

spectrum.

On 6 February 1997 (UT), three more 900 s LRIS exposures were taken in the middle of the interval when the diffraction spikes were more than 15° away. The set-up was the same, except that the instrument had been moved to Keck II, and we used a new, more efficient 831 line mm^{-1} grating, blazed for a wavelength of 810 nm, covering the wavelength range 837 to 1024 nm at 0.09 nm $pixel^{-1}$. With the 1″ slit, the resolution was about 0.4 nm. On both nights the seeing was generally sub-arcsecond ($\sim$ 0.″8) and a few thin cirrus clouds sailed about in the sky. The spectra from these two observations were combined by smoothing the higher resolution spectrum to the 0.4 nm resolution and adding them. Full details on the reduction technique follow.

The spectral data were reduced using MIDAS and programs running in the MIDAS environment. The presence of Gliese 229A's diffraction spikes in the spectral images required special care during the reduction. The approach we used is illustrated in Fig. 3.4. The top panel shows a typical spectral image, after bias-subtraction and flat-field correction. First we removed the telluric emission lines (mostly OH). For this purpose, a third-degree polynomial was fitted through every column in regions free of stellar light (indicated by 'S' on the right-hand side of the panel).

The subtraction of the strongest sky lines is not always satisfactory (see second panel of Fig. 3.4). Most likely, this results from the fact that interference fringing in the CCD is not corrected adequately for the sky emission lines, as the response of a given pixel to monochromatic light is different from the response to the continuum emission from the flat-field lamp. The resulting structure over a column has a relatively large scale, however, and is mostly removed in the next step, in which the scattered and diffracted light from Gliese 229A is subtracted by fitting a second-degree polynomial to two small regions adjacent to the spectrum of Gliese 229B (see Fig. 3.4). As the spectra are not aligned perfectly, these regions are chosen slightly differently for different parts of the chip.

One-dimensional spectra were extracted using a scheme similar to the "optimal extraction" technique of Horn (1986), in which an average stellar profile along the slit is created to estimate the total flux from each pixel in a given column. All estimates are combined using weights inversely proportional to the square of each pixel's formal uncertainty (determined from the read noise and Poisson noise in the raw data). In the lower panel of Fig. 3.4, we show the difference between the raw data and the extracted data (in standard deviations). It is apparent that the extraction is quite accurate, since very little structure remains. We also extracted the spectrum of Gliese 229A with the same technique, after removing the contribution from Gliese 229B from the image. This allows us to verify that no contamination from Gliese 229A remains in Gliese 229B's spectrum. Indeed Fig. 3.9 shows that none of the features in A are present in the spectrum of B.

Wavelength calibration employed argon and krypton/mercury arc spectra taken after the series of exposures. For the 1200 line mm^{-1} spectra, only 7 lines were available, but they were quite evenly spread over the wavelength range. A fit to these lines's positions with a third-degree polynomial left a root-mean-square residual of 0.023 pixel. For the 831 line mm^{-1} spectra, 11 lines were used (achieving an rms of 0.03 pixel), but none of these were longward of 970 nm. However, a comparison of the locations of OH airglow lines in our spectral images with the wavelengths given by Osterbrock et al. (1997) shows that the wavelength calibration is accurate to better than 0.1 nm everywhere on the spectrum. For removal of telluric water vapor lines as well as relative flux calibration, we used spectra of Feige 34 (sdO; $V = 11.2$; Massey & Gronwall 1990), taken after Gliese 229B at similar airmass. The final absolute flux calibration was achieved using the photometric results in Matthews et al. (1996).

3.2.3 Infrared Data

On the nights of 8 and 9 February 1997 (UT) we obtained the Z, J, H, K, L and M band spectra using the Near-Infrared Camera (NIRC; Matthews and Soifer 1994) at the Cassegrain focus of the Keck I telescope. These spectra were obtained in several stages using the grism mode of the camera. The camera permits recording of low-resolution spectra in the Z, J and H bands simultaneously, then the H and K bands and finally the L and M bands. The "ZJH" region was obtained in 10 exposures of 40 s of "on-source" exposure time. After every 40 s exposure, we shifted the telescope 15.″6 North and took a 40 s long "sky" frame. The slit was placed East-West, as it was during the LRIS observations. This produced pairs of "on-source" exposures taken right before corresponding "sky" exposures. The distance 15.″6 was chosen so that we would be sampling exactly the same sky background relative to the primary star (Gliese 229A), but on the opposite side of the star. This seemed to be the optimal way to remove the point-symmetric background.

We used the grism with 150 line mm^{-1} and a slit 4.5 pixels wide (0.″675) to obtain the "ZJH" spectrum. Blocking filters were in place so that only light from the Z, J and H bands reached the detector. The H band spectrum was obtained a second time in a series of 22 more 40 s exposures (plus 22 corresponding sky exposures) in which the H and K spectra were recorded. In these spectra, the 120 line mm^{-1} grism was in place with corresponding blocking filters as well. The weather was clear and photometric and the seeing was 0.″7 on both nights.

The L and M band spectra were slightly trickier to obtain. As far as we know this work represents the first time the Keck telescope has been used for 3 to 5 μm spectroscopic observations. As a result we had to ascertain which electronics settings were optimal and what readout times and integrations were necessary. As shown by the results presented here, NIRC is fully capable and rather sensitive in these wavelength bands.

All of the spectral images contained both Gliese 229A and B, due to the diffraction spikes of A. Data reduction involved the following steps. For each "on-source" frame (which entailed the coaddition by the NIRC electronics of 1000 individual array readouts) we subtracted the "sky" frame immediately following. We then extracted spectra from bars ten pixels in width across the slit of both Gliese 229B and A. Gliese 229B's spectral signature was quite detectable in the single, "sky-subtracted" images. The extraction technique involved the "optimal extraction" method in which the pixels are summed in the spatial direction but weighted according to the signal in each pixel. The technique is similar to that used for the optical data, and it leads to a significant improvement in signal-to-noise ratio over simple addition. To make sure the sky background and particularly any contamination from A were not present in our final spectrum, we subtracted the corresponding "optimally extracted" spectrum ten pixels to either side of the spectral region of B.

We removed the instrumental response by dividing the extracted spectrum by the extracted spectrum of a calibrator star. In the case of the Z, J, H and K bands this calibrator was SAO 175039, a G8 star which smoothly approximates a black body spectrum through this wavelength region, except for a few hydrogen absorption lines which we edited out by linear interpolation. In the case of the L and M bands, we used Gliese 229A, an M1V star, which is quite flat in the region redward of 2 μm. (For L and M spectra of other early M dwarfs, see Berriman & Reid 1987 or Tinney et al. 1993.) Ideally one should use a calibrator star such as a bright F or G type star. However, the use of A is sufficient in this case. Absolute flux calibration involved matching the flux density in the spectrum with the photometric measurements of Matthews et al. (1996).

The wavelength calibration of the infrared data involved a simple method. We used the edges of the filter bands, clearly visible in the calibrator star spectra, to determine the wavelengths of the edges of each segment of the spectrum. The 50%

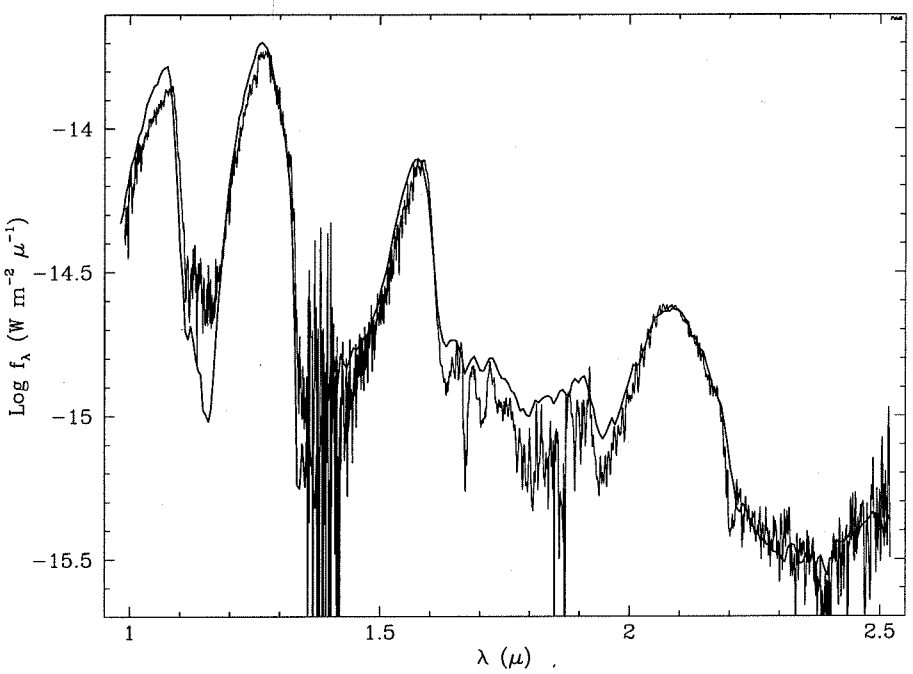

Figure 3.5 The Keck NIRC spectrum of Gliese 229B (lower resolution) compared with the UKIRT CGS4 spectrum (higher resolution). The agreement between the two spectra is good except in the 1.6 to 2 μm region and the 1 to 1.1 μm region. The discrepancies are, however, no more than 10% of the signal, and are most likely due to small differences in wavelength calibration and possibly to atmospheric dispersion, which could put some of the flux at the blue end of the UKIRT spectrum just outside the slit. This would explain the fact that the discrepancies are mostly on the blue end of the spectrum. Alternatively, there may be minor residual contamination from Gliese 229A in our spectrum. The UKIRT spectrum is taken from Geballe et al. (1996).

transmission points of the bands are known to an accuracy of 10 nm. With these "edge wavelengths" known, we linearly interpolated to determine the wavelength for each pixel across the spectrum. This introduces errors on the scale of 1 nm.

Finally, we added all of the extracted, calibrated spectra together.

Fig. 3.5 compares our 1 to 2.5 μm spectrum with the higher resolution spectrum of Geballe et al. (1996). The plot shows that there is good agreement between the spectra. The differences, which are most pronounced in the 1 to 1.1 μm and the 1.6

to 2 μm regions, amount to no more than 10% of the signal. These discrepancies are attributable to possible minor contamination from Gliese 229A in the 1.6 to 2.0 μm region of our spectrum as well as some minor differences in wavelength calibration. Alternatively, the Geballe et al. (1996) spectrum might have been affected by atmospheric dispersion, causing some of the bluer wavelengths to be slightly reduced in brightness since some of the blue light would have been blocked by the slit. In Geballe et al. (1996) it is shown that the small features in the brighter parts of the spectrum are almost entirely real and correspond closely to known absorption lines in water. Our spectrum is unable to resolve these features. However, the agreement between the spectra is an excellent confirmation of the data, as well as an indicator that our reduction method works and has no major contamination from scattered light from Gliese 229A.

Fig. 3.6 shows the relative instrumental response of NIRC with the 60 line mm^{-1} grism in the L band plotted along with our spectrum of Gliese 229B. The absorption band at about 3.4 μm is due to the resin inside NIRC. This resin is applied to the surface that will become the grating. Then a master grating is pressed against the resin so that an imprint of the grating is left in the resin, which subsequently dries and becomes the "replicant" grating used in NIRC. The instrumental transmission curve is simply the extracted spectrum of Gliese 229A, which, as we mentioned above, is flat in this region. The final spectrum of B shows none of the features due to this instrumental response.

3.2.4 The Spectrum

The complete spectrum is presented in Fig. 3.7, with the most important features labeled. The 1 to 2.5 μm part of this spectrum has been discussed in detail in Oppenheimer et al. (1995) and Geballe et al. (1996). Hence we concentrate on the new short and long wavelength parts. In the latter we find the fundamental methane

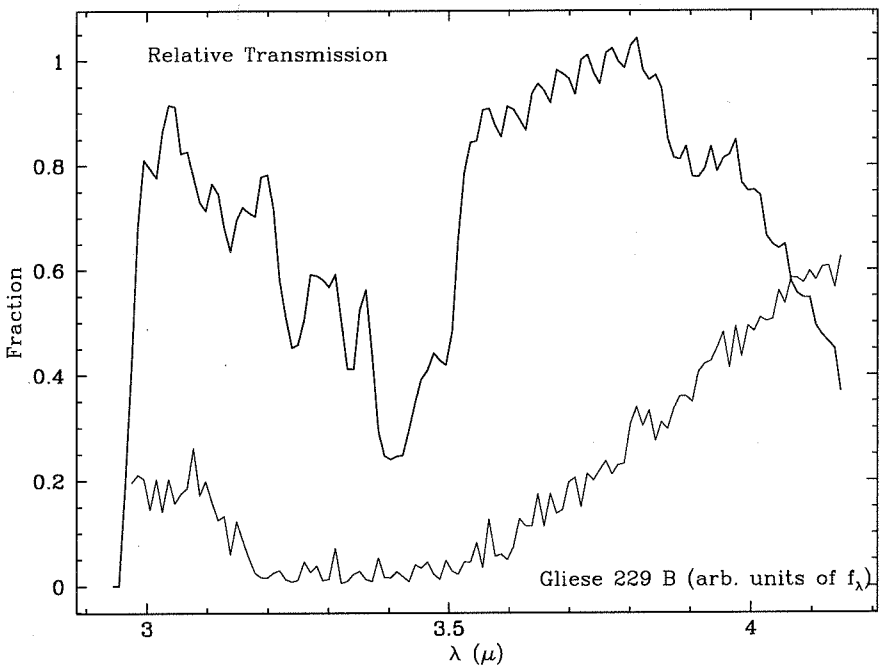

Figure 3.6 The relative instrumental transmission of NIRC through the L band (heavy line) and the f_λ of Gliese 229B (lighter line). The large variations in the instrumental transmission are due to the resin that forms the rulings on the grism in NIRC. See §3.2.3 for a more detailed discussion.

band at 3.3 μm, and an interesting small feature in the M band which we attribute to CO, in confirmation of the claims of Noll et al. (1997; see section 3.2.7). In the optical part, shown enlarged in Fig. 3.8, there are two prominent atomic lines due to cesium, a very weak feature caused by methane and a strong steam band. These are all discussed in detail in the following sections.

Before discussing the detailed parts of the spectrum it is useful to compare the spectrum of Gliese 229B with spectra of some of the lowest mass stars. Fig. 3.9 shows the optical part of the spectrum compared with that of vB 10 and LP 944−20, which were studied by Kirkpatrick et al. (1997). Note the distinct absence in Gliese 229B of any of the molecular absorption features due to refractory elements, such as VO and

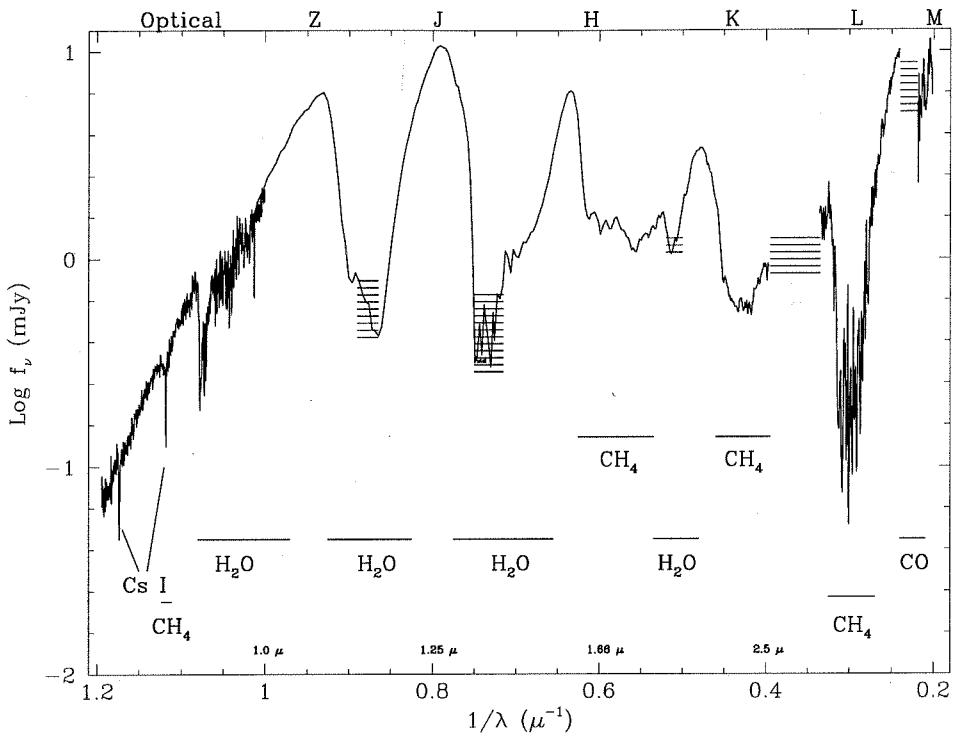

Figure 3.7 The spectrum of Gliese 229B from 0.84 to 5 μm. Major opacity sources are indicated. Regions with horizontal bars correspond to wavelengths where the atmosphere is too opaque to permit collection of useful data from the ground. Along the top of the plot are indicated the filters corresponding to the various wavelength bands.

TiO. Also the steam feature is far deeper and more exaggerated in Gliese 229B. In contrast to the stars, Gliese 229B seems smooth blueward of the steam feature, with the exception of the two neutral cesium lines and a possible faint methane feature. (See §3.2.9 and §3.2.5 for a detailed discussion.)

Fig. 3.10 compares Gliese 229B's near IR spectrum with those of GD 165B and vB 10 again. The comparison spectra are reproduced here courtesy of H. R. A. Jones and appeared in Jones et al. (1994). The huge swings in flux density in Gliese 229B are not to be found in either star. In particular, this figure shows the great importance that methane has on Gliese 229B's spectrum, causing drastic drops in the flux density

at 1.6 and 2.2 μm.

The water bands at 1.1 and 1.4 μm are also vastly deeper in Gliese 229B than in the stars. More specifically, the water band at 1.4 μm is about 2.5 times deeper in Gliese 229B than it is in GD 165B. Some of these differences may be magnified by the presence of dust in GD 165B and vB 10. Dust serves to smooth out spectra such as these, and it has recently come to light that dust is quite important in the spectra of some very low mass stars (Jones & Tsuji 1997). (See §3.2.8.)

Interesting comparisons can be made of the Gliese 229B spectrum with that of Jupiter. Although the spectrum of Jupiter is due to reflected sunlight throughout the wavelengths discussed here, there exist many similarities. We discuss these in the sections below where appropriate.

What follows is a detailed explanation of various aspects of Gliese 229B which can be addressed with the data presented in this paper.

3.2.5 Methane

Our spectrum in the 3 to 4 μm region shows an extremely large absorption feature (Fig. 3.7). We attribute this to the fundamental methane absorption band, which has been observed in planets and moons in the solar system. Noll (1993) detected an interesting spike in the spectrum of Jupiter at 3.52 μm. Other researchers have also noticed this feature (Drossart et al. 1996). We do not see this feature in our spectrum of Gliese 229B. Drossart et al. (1996) attribute this feature to reflected solar light emerging between what is actually two important methane features. The principal reason we cannot comment on the presence of this feature in Gliese 229B is that the signal-to-noise ratio in this part of the spectrum is exceedingly low. For that reason the depth of this band cannot be determined from this data.

Another formerly undetected band of methane presented here is the faint band in the 0.89 μm region. This band, which is quite prominent in the reflectance spectra of

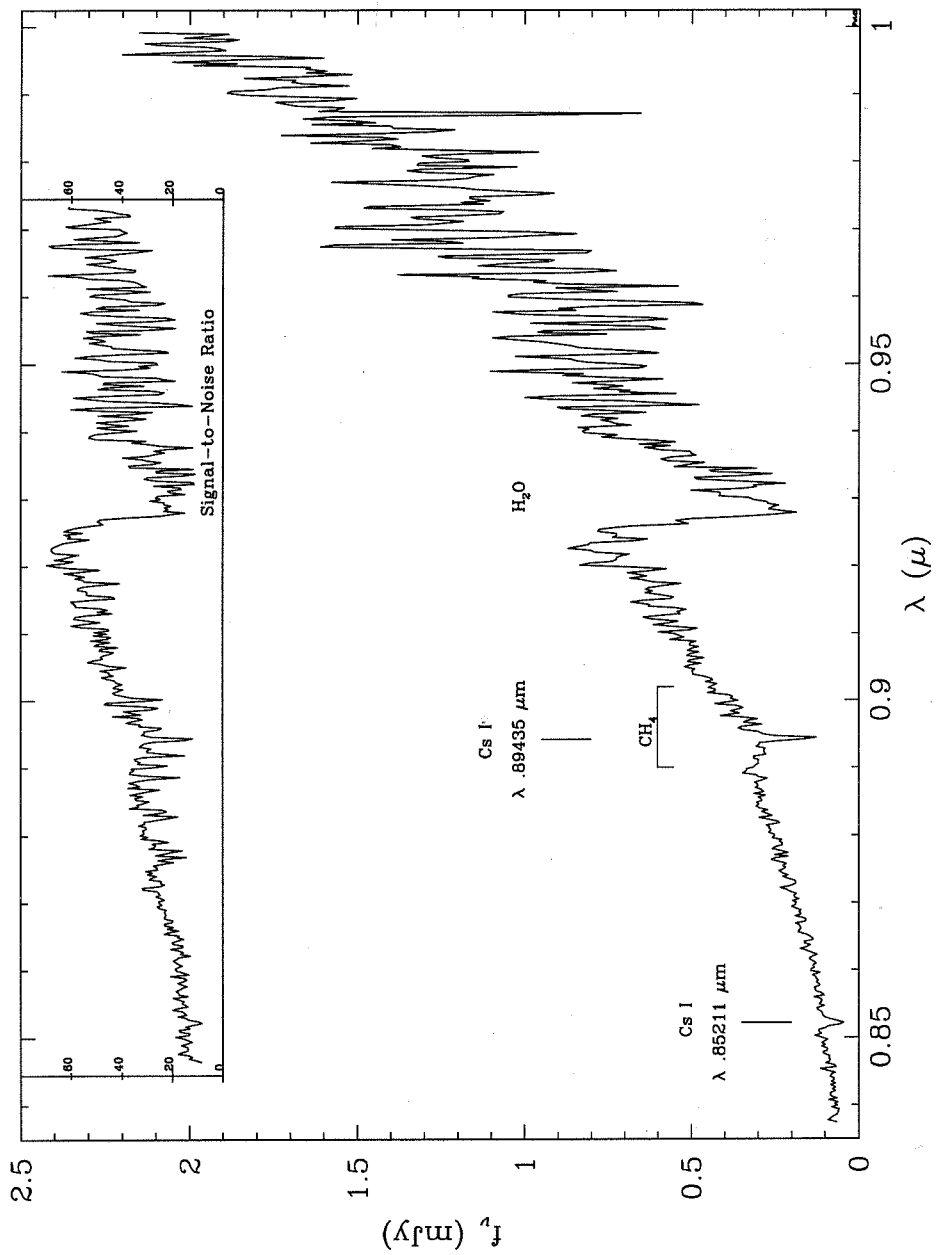

Figure 3.8 The spectrum of Gliese 229B from 0.837 to 1.0 μm. Important absorption features are labeled. The upper panel is a graph of the signal-to-noise ratio through the central region of the spectrum. The redward end of the spectrum degrades considerably in signal-to-noise ratio because of the decreasing sensitivity in the CCD. The seemingly noisy long-wavelength end of this spectrum contains what are largely real features. The dips in signal-to-noise ratio near 0.88 μm are due to telluric emission lines.

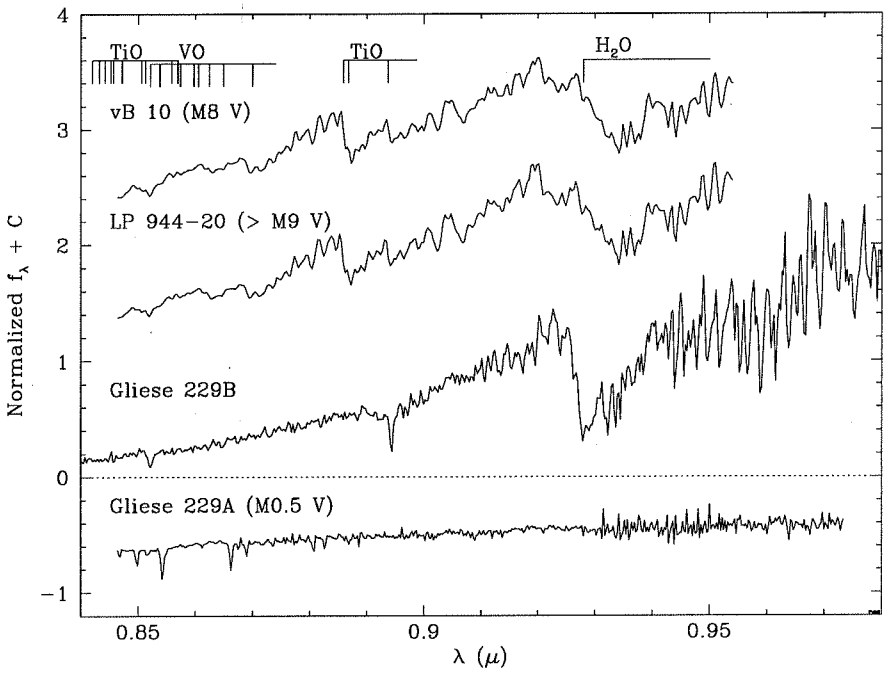

Figure 3.9 The optical spectrum of Gliese 229B compared with spectra of two of the least massive stars known, vB 10, an M8 V star, and LP 944−20 whose spectral classification is $\gtrsim$ M9 V according to Kirkpatrick et al. (1997). These spectra are presented here courtesy of J. D. Kirkpatrick and appeared earlier in Kirkpatrick et al. (1997). The values of C are 1.0 for LP 944−20 and 2.0 for vB 10. Line locations, with the exception of Cs and CH_4, are from Kirkpatrick et al. (1991).

Jupiter, Saturn, Titan, Uranus and Neptune, has been shown by Karkoschka (1994) to be strongly dependent upon the effective temperature. Large differences in the depth of the band are apparent in the spectra he presents. This is important because the temperature dependence of the absorption coefficient for methane is poorly known. Examination of the results in Karkoschka (1994) show that this band should be extremely weak at high temperatures, such as the 900 K temperature of Gliese 229B. Thus, the weakness of this feature is expected.

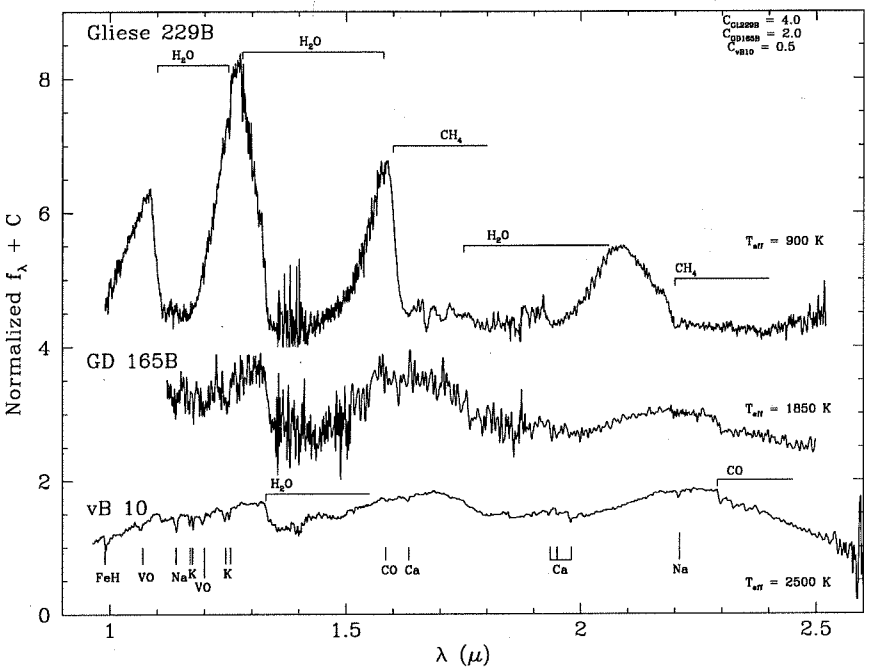

Figure 3.10 The near IR spectrum of Gliese 229B compared with spectra of vB 10 and GD 165B. The IR spectrum is that of Geballe et al. (1996) and is used because it matches the resolution of the other two spectra which appear courtesy of H. R. A. Jones and were first published in Jones et al. (1994). The importance of methane in the spectrum of Gliese 229B is best demonstrated in this figure. The distinct drop-off in flux density at 1.6 and 2.2 μm are features not to be found in stellar spectra. The water bands at 1.1 and 1.4 μm are also grossly magnified in strength in Gliese 229B. The absorption line identifications for vB 10 are from Jones et al. (1994).

3.2.6 Water

Water is by far the most important source of non-continuum opacity in Gliese 229B. (Continuum opacity comes, as indicated by models, from H^-, H_2^- and H_2 collision induced absorption; Burrows et al. 1997.) In models of Gliese 229B, the absorption between the near IR filter bands (which are naturally defined by telluric water absorption) are broad and deep. This is highly beneficial. It means that the majority of the flux from Gliese 229B and any similar objects, such as extrasolar giant planets, will

pass through the earth's atmosphere (Matthews et al. 1996), and that brown dwarf or extrasolar planet studies are not hindered by this telluric absorption.

Geballe et al. (1996) showed that the narrow features in the 2.0 to 2.2 μm region correspond closely to the opacity of water. Saumon et al. (1996) have shown that a measurement of the surface gravity of Gliese 229B could be made using these very fine water features.

The optical spectrum (Fig. 3.8) shows many narrow features redward of 0.925 μm. These are essentially all real features and are a result of the complex structure of the water molecule (F. Allard, private communication). In principle one can conduct an analysis of these water features similar to that in Meadows & Crisp (1996), in which the thermal structure of the atmosphere of Venus was deduced. However, this entails modeling of line profiles and spectral synthesis with detailed radiative transfer models, which our group is unable to do at present. Unfortunately, the models for Venus cannot be used because Gliese 229B (presumably) has no rocky surface underlying its atmosphere. In the case of Venus, the surface has a profound impact on the radiative processes in the atmosphere (Meadows & Crisp 1996).

3.2.7 Carbon Monoxide

The first vibration-rotation band (1-0) of CO is centered near 4.7 μm. Motivated by a paper by Fegley & Lodders (1996), which discussed the importance of the detection of CO, we measured the 3 to 5 μm spectrum of Gliese 229B presented here. Since then, the presence of CO in the atmosphere of Gliese 229B has been reported by Noll et al. (1997; hereafter NGM). NGM, using spectral data in the 4.7 μm region, claim to detect the expected increase in flux density in the center of the 1-0 vibration-rotation band. Though the noise in their data was appreciable, the detection is clear and the model spectrum they generated agrees well with the data.

Our data confirm their result, as can be seen in Fig. 3.11, where we have reproduced NGM's Fig. 3.5 (courtesy of Mark Marley), showing their data and model, but with our data overdrawn. Their model fits the observations best with a mole fraction, q, of qCO = 200 ppm (parts per million) and a brown dwarf radius of 8×10^4 km (which affects the flux density as well as the model's adiabat). We have scaled the flux density of the NGM data by a factor of two to match the flux density we measured in Matthews et al. (1996). The uncertainty on each of the points in our data is approximately 2/3 the uncertainty in the data of NGM. Our data fit the model extremely well, even in regions where the NGM data do not.

NGM state that the sudden break at 4.82 μm in their spectrum is due to incorrect removal of a telluric line. Indeed, we do not see this feature in our spectrum.

As NGM discuss, one does not expect CO to be present in the atmosphere of Gliese 229B in thermochemical equilibrium. Fegley & Lodders (1996) computed models of the thermochemical equilibrium abundances of many molecules for a pressure temperature profile of Gliese 229B from Marley et al. (1996). They found that only at a temperature of about 1400 K would one expect the mole fraction of CO to equal that of CH_4. At 1250 K CO is about 10 times less abundant. At the 900 K isotherm one would expect the abundance of CO to be almost 10^{-4} times that of CH_4. In the atmospheres of Jupiter and Saturn, the $qCO/qCH_4 = 1$ boundary is much deeper (Fegley & Lodders 1994). The only explanation for the presence of CO in the photosphere of Gliese 229B is that it is not in thermochemical equilibrium. This seems to require convection which would bring measurable quantities of CO up from the deeper and warmer parts of the atmosphere. The convection need not necessarily reach all the way to 1400 K. Even if it extended into the 1250 K region, substantial quantities of CO could be pulled up into the outer atmosphere (Fegley & Lodders 1994, Fegley and Lodders 1996).

This indicates that the outer convective region of Gliese 229B is at least as deep

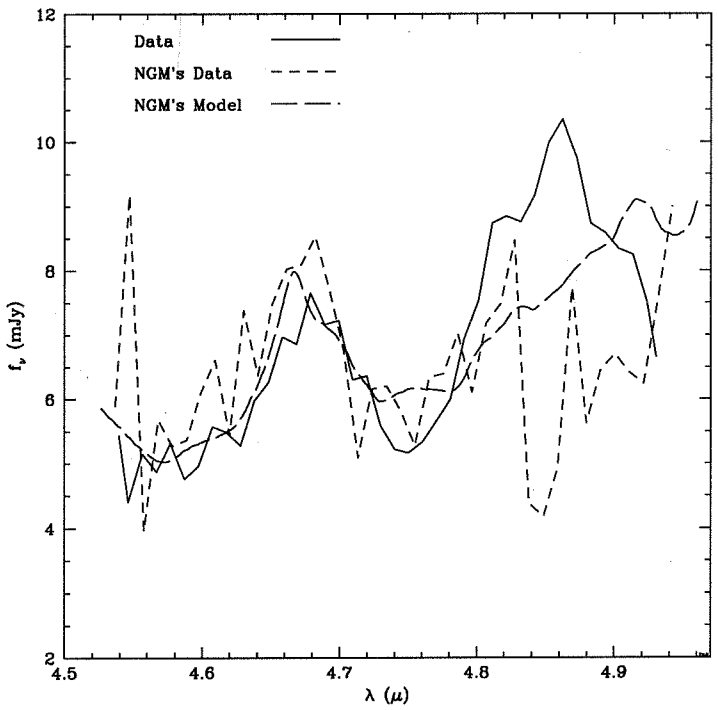

Figure 3.11 Expanded view of the spectrum of Gliese 229B between 4.5 and 5.0 μm. The solid line represents the data presented in this paper, while the short-dashed line comes from Noll et al. (1997), as does the model spectrum represented by the long-dashed line. Typical uncertainties in our data points are about 2/3 those of Noll et al. (1997), which are on the order of $\pm$ 1 mJy. Our data confirm the detection of carbon monoxide in Gliese 229B's atmosphere. The peak at 4.67 μm is due to a gap in the middle of the 1-0 vibration-rotation absorption band of CO. The model uses a mole fraction of qCO = 200 ppm and a brown dwarf radius of 80000 km. The feature at 4.85 μm in the Noll et al. (1997) data is due to incorrect removal of a telluric line. Their data and model appear courtesy of K. Noll, T. Geballe and M. Marley.

as the 1250 K isothermal surface. Recent models by Burrows et al. (1997) found that an object like Gliese 229B has an outer radiative region, followed as one progresses inward by a thin convective region which spans a temperature range depending upon the mass and effective temperature. Below this thin outer convective region lies another radiative region which extends in almost all of the models to a depth where

the temperature is about 2000 K. Inside this inner radiative region is a final convective region which reaches to the core of the brown dwarf. This concept of shells of alternating convective and radiative regions seems to be in agreement with the observations made here. The CO might form easily in the outer convective shell, which can reach to temperatures of over 1250 K, and get dredged up to the observable part of the atmosphere. To make this more clear, one must consider the presence of dust in the spectrum of Gliese 229B.

3.2.8 Dust

The issue of dust in Gliese 229B has been the subject of some discussion, particularly among the modelers of brown dwarf and planet atmospheres (e.g., Marley et al. 1996, Tsuji et al. 1996b, Allard et al. 1996). At some point in the near future, the application of a detailed theory of the cloud microphysics (such as appears in Rossow 1978) may be possible. For now, we restrict ourselves to a somewhat more qualitative discussion.

Metallicity of Gliese 229B is important to any discussion of its dust content. At this time we have no direct measurement of the metallicity of Gliese 229B. However, the two measurements of the metallicity of Gliese 229A are [M / H] = $+0.15 \pm 0.15$ (Mould 1978) and [Fe / H] = -0.2 ± 0.4 (Schiavon et al. 1997), which are both consistent with solar metallicity (within the error bars). If Gliese 229B formed the way planets are thought to form, out of a circumstellar disk surrounding the nascent Gliese 229A, it may be that the metallicity of the brown dwarf is higher than that of its sun, as is the case for the outer planets of the solar system. In this case, one would expect to see even more dust (Burrows et al. 1997). On the other hand, if Gliese formed out of the collapse of an interstellar cloud, the way Gliese 229A presumably formed, the metallicities should be identical. This is important because of the apparent lack of dust influences in the spectrum, as we discuss below.

Jones & Tsuji (1997) have demonstrated that dust plays an extremely important role in the spectra of the very lowest mass stars. Looking at progressively cooler stars, Jones & Tsuji (1997) find that dust increases in importance past the spectral classification M6. The evidence for this is that the prominent TiO and VO bands that define late M type spectra suddenly seem to reduce in strength past the M6.5 V spectral type. This cannot be reconciled with dust-free models of late type stars, which show increasing strengths of the TiO and VO bands until the bottom of the main sequence (Allard and Hauschildt 1995). Furthermore, Tsuji et al. (1996a) have shown that GD 165B's spectrum can only be explained with the presence of large quantities of dust. It may be that past the M6.5 V spectral type stars do not all appear the same: some may be rather dusty, while others may not. This might be due to differences in metallicity and in details of the stars's weather patterns. Observational support for such differences comes from the diversity of spectra observed by Kirkpatrick et al. (1997).

The results of Jones & Tsuji (1997) would lead one to expect that a substellar object such as Gliese 229B would be even more affected by dust. However, based on the photometry of Gliese 229B (as reported by Matthews et al. 1996), Tsuji et al. (1996b) concluded that dust does not play a role in determining the spectral energy distribution. From our high signal-to-noise ratio spectral data through the deepest parts of the methane absorption bands, we can more quantitatively compare the observed spectrum with a range of spectra calculated with differing quantities of dust. We find that the spectrum presented here cannot be reconciled with any of the dusty models that Tsuji et al. (1996b) computed. Even the least dusty model of Tsuji et al. (1996b) does not fit the observed spectrum. For instance, the observed factor of 10 drop in flux density in the K band matches only the dust free models of Tsuji et al. (1996b). The dusty models of Tsuji et al. (1996b) show a pronounced dampening of this methane absorption band.

The question that now arises is "Where is the dust that is expected to be present in the brown dwarf?" We see two possibilities. The first, suggested by Tsuji et al. (1996b), is that the lack of dust is only apparent; the dust, which one expects from thermochemical considerations, is present but in clouds in the photosphere with a small covering fraction. This would presumably be an observably testable suggestion. One could look for variability in the absorption bands of Gliese 229B. In the various spectral images we have taken at Keck and Palomar, we found no evidence for variability greater than 10% on time scales from several minutes to two days and over a one year baseline in the 1.6 μm methane absorption band, the depths of which are easily detected in a single 40 second exposure on Keck. Whether the presence of clouds would produce a 10% or larger effect is not clear. However, this is probably a viable explanation.

Another possible reason for the lack of dust is that it sits deep within the atmosphere below the outer convective region in an inner radiative region (first predicted in planets by Guillot et al. 1994, and predicted to exist in brown dwarfs by Burrows et al. 1997), so that it is not blown back up into the photosphere through convection. The presence of this inner, detached radiative zone is essentially due to a coincidence of the minimum in the predominant H_2 collision induced absorption and the peak of the emergent black body spectrum (Burrows et al. 1997). The model adiabats for a surface gravity of $g = 3 \times 10^4$ cm s^{-1} are shown in Fig. 3.12 and appear courtesy of A. Burrows. These plots show where the temperature gradient falls below the adiabatic value (heavy, solid curve) and where it is equal to the adiabatic temperature gradient (dashed curve). The photosphere is also indicated in this plot by the large solid dot on each curve. It is interesting to note that the photospheric pressure is approximately 1 bar. However, the locus of this point is somewhat deceptive because of the large range of brightness temperatures displayed in the spectrum (Fig. 3.3). In the optical, where the brightness temperature is closer to 1400 K, the

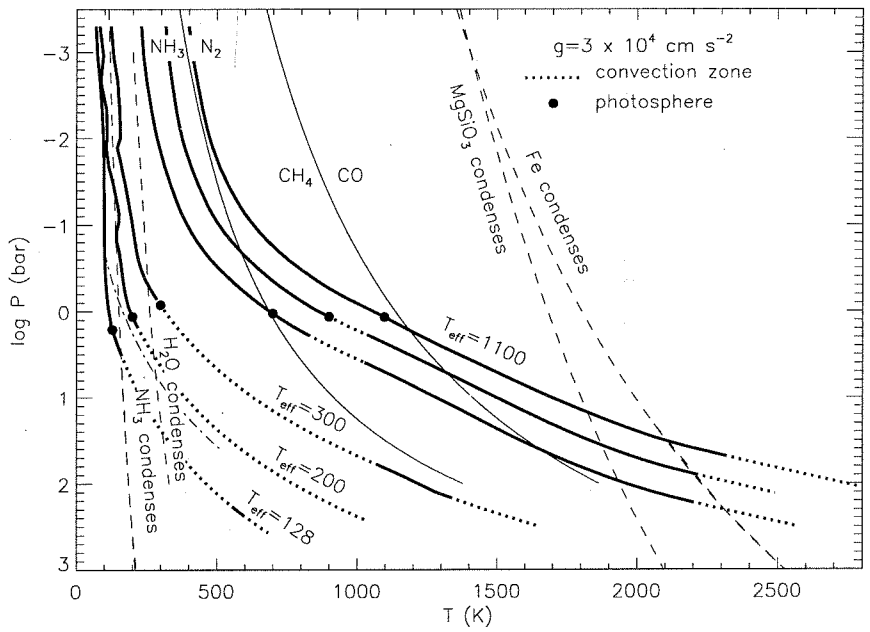

Figure 3.12 Temperature-pressure profiles for brown dwarfs with $g = 3 \times 10^4$ cm s^{-1}, from Burrows et al. (1997). The curves indicate the radiative (solid, heavy lines) and convective (heavy, dotted lines) zones. The appearance of a detached radiative zone below the photosphere (which is indicated approximately by the solid dot on each curve) may play a role in which chemical species are visible in the emergent spectrum. To illustrate this condensation curves are shown to illustrate which species are important in this parameter space. Courtesy A. Burrows.

corresponding pressure is almost 10 bar, while in the depths of the methane features, where the temperature is as low as 500 K, the pressure is approximately 0.1 bar. This range of pressures affects the thermochemistry visible in the emergent spectrum. We believe that the spectroscopy presented here provides support for the existence of this structure apparent in the models. There are several points we can raise in support of this idea.

We argued above (§3.2.7) in confirmation of Noll et al. (1997) that there is an appreciable quantity of CO visible in the spectrum of Gliese 229B, and that this is many orders of magnitude higher than the amount expected from thermochemical equilibrium. We further argued that this can be the result of convection in the brown

dwarf's atmosphere. This seems to imply that the convective region of the brown dwarf must extend at least to a depth where CO is abundant. Fegley & Lodders (1996) showed that the CO to CH_4 phase transition ought to happen at around 1400 K and a pressure of about 10 bars in Gliese 229B. As mentioned above, it is possible that the CO we observe comes from a lower temperature where it exists but in smaller relative quantities. Thus it could perhaps come from as low a temperature as 1250 K, where the mole fractions of CO and CH_4 differ by a factor of 10. We already know, though, that the dust forms at much higher temperatures than this. By far the most abundant refractory elements are Fe, Mg, Si and Al. These form Al_2O_3 (corundum) in the late M dwarf regime, Fe clusters at 2000 K (Fegley and Lodders 1996), and $MgSiO_3$ (enstatite) at 1600 K (Tsuji et al. 1996a, Sharp & Huebner 1990).

This may indicate where the boundary between the outer convective and inner radiative regions of the brown dwarf are. Specifically, the boundary must be at a temperature above 1250 K, to permit dredging of substantial quantities of CO into the cooler regions, and yet cooler than 1600 K, where enstatite forms. If the outer convective region extends deeper and hotter than 1600 K, then the condensation and falling or raining rate of enstatite must be much faster than the convective wind speed, so that the enstatite and other types of dust never reach the outer atmosphere. This process would be similar to the falling of rain droplets in the Earth's convective and stormy atmosphere. Rain falls despite the convection. Presumably one could model this process to answer the question raised in this paragraph. If the dust is below the outer convective region in a radiative region, clouds are not needed to reconcile the observations with theory.

According to Marley et al. (1996) and Marley (1997), theoretical temperature versus pressure curves for Gliese 229B show that the atmospheric structure becomes adiabatic at approximately 1600 K and 10 bars of pressure. This is consistent with our suggestion above, that the outer convective/inner radiative boundary is between

1250 and 1600 K. It is also consistent with the new models by Burrows et al. (1997) shown in Fig. 3.12.

If this is true, then one would predict that objects at some temperature below the 1800 K of GD 165B will begin to show the effects of dust less and less. Indeed, the expectation is that the much hotter brown dwarfs will exhibit dust in their spectrum. The possibly-close proximity of the radiative-convective boundary in Gliese 229B to the formation temperature for enstatite suggests that a brown dwarf even slightly hotter than Gliese 229B might show some effects of dust in its spectrum. Thus, one should see a progressive decrease in the importance of dust through the range of effective temperatures from 1800 to 900 K. Alternatively, below a certain temperature, the photosphere may become dust free. This could happen if convection is unable to bring the dust back into the photosphere because it just rains out of the convective region.

It is entirely possible, however, that the type of internal structure we discuss here is largely model dependent. For example, additional, as-yet-unidentified opacity sources inside the brown dwarf atmosphere could upset or even drastically change the conclusions of the models that there are inner radiative and convective zones.

As a final note on the dust in Gliese 229B, we remark upon the smooth-looking parts of the optical spectrum. This may be due to a haze of exotic types of dust not yet identified with extremely fine particle size, but this requires additional work on behalf of the modelers (M. Marley, F. Allard, personal communication).

3.2.9 Cesium

Of the alkali metals (Li, Na, K, Rb, Cs and Fr), only lithium, sodium, potassium and rubidium have been known to play an important role in low-mass star spectra (Kirkpatrick et al. 1997; Basri & Marcy 1995 and references therein). Recently, Tinney (1997) found cesium absorption lines in spectra of several very low-mass stars.

This completes the set of alkali metals one would expect to find in such stars.

The reason the alkali metals are important is that they have very low ionization potentials: from 5.390 eV for Li to 3.893 eV for Cs (Letokhov et al. 1987). These are the lowest ionization potentials for any of the elements. As a result, in most stellar atmospheres they are ionized and would only be visible in an ultraviolet spectrum, a wavelength region never used to classify M dwarfs. As one considers stellar atmospheres of cooler and cooler temperatures, the neutral alkalis begin to appear, with Cs appearing only in the very coolest atmospheres. Continuing this progression through cooler atmospheres, as one crosses into the brown dwarf regime, these metals should begin to form molecules. Thus, they would again disappear from the optical to near IR spectra.

In the case of Gliese 229B, the two strongest cesium lines are present. (See Fig. 3.8.) The other alkali metals have their strongest lines blueward of the shortest wavelength we were able to measure. (Li is at 670.8 and 812.6 nm; Na is at 589.5 and 589.0 nm; K is at 769.9 and 766.5 nm and Rb is at 794.8 and 780.0 nm.) Unfortunately we are unable to use the lines for a reliable calculation of the abundance of cesium in Gliese 229B. This is because there exist to date no curve of growth models for these absorption lines.

The cesium lines present in the optical region of the spectrum of Gliese 229B comprise the principal doublet of cesium. The line at 852.1 nm corresponds to a transition of the solitary valence electron from the 6 $^2S_{\frac{1}{2}}$ state to the 6 $^2P_{\frac{3}{2}}$ state. The other line at 894.3 nm corresponds to the transition from 6 $^2S_{\frac{1}{2}}$ to 6 $^2P_{\frac{1}{2}}$. (This notation follows the standard spectroscopic notation convention, $^{2S+1}L_J$.) Kirkpatrick (private communication) has found the same two cesium lines in a new spectrum of GD 165B, as well. These are by far the strongest lines of cesium. The next strongest line at 917.2 nm is several times weaker than either of these and is not visible in Gliese 229B.

An important question to answer is "At what temperatures can we expect these alkali metals to form molecules?" This question, which requires thermochemical equilibrium calculations, has been thoroughly addressed for planet sized objects like Jupiter by Fegley & Lodders (1994). Their thermochemical equilibrium calculations would lead one to believe that none of the alkali metals should be visible in the spectrum of Jupiter, because they ought to have formed molecules already. Indeed, in Jupiter, one expects CsCl to dominate over Cs even at temperatures as high as 2000 K. (The brightness temperature in the region of the Cs lines in Gliese 229B is approximately 1300 K.) However, it is not entirely correct to use the calculations for Jupiter when discussing Gliese 229B. The adiabat for Gliese 229B places a given temperature at a substantially lower pressure. A. Burrows (personal communication) believes that the turnover from Cs to CsCl in Gliese 229B happens around 1500K. However, until the full calculations are carried out, reconciling the theory with this detection of atomic Cs cannot happen. It is possible that one merely expects the deep Cs lines we see, but if they are not compatible with thermochemical equilibrium, it is possible that some quantity of Cs is being convected into the observable atmosphere much the way the CO is, as we described in §3.2.7. The thermochemical equilibrium calculations could also lead to an important temperature diagnostic for brown dwarfs and very low-mass stars. By observing which alkali metals exist in atomic form, one could determine the temperature of a given object through comparison with the thermochemical equilibrium calculations.

These considerations also have implications for the so-called lithium test for brown dwarfs. It may be that the lithium test, in which one attempts to detect atomic lithium in the candidate brown dwarf (Rebolo et al. 1992; Magazzù et al. 1993), might only be meaningful for the highest temperature brown dwarfs. The temperature at which lithium becomes LiOH determines this. For the case of the Jupiter adiabat, this is well above 2000 K (Fegley & Lodders 1994). The field would benefit from new

thermochemical equilibrium calculations using the adiabats found for Gliese 229B (Marley et al. 1996; Burrows et al. 1997).

3.3 Astrometry: Orbital Motion[†]

David A. Golimowski

Department of Physics and Astronomy, The Johns Hopkins University, Baltimore, MD 21218

Chris J. Burrows

Space Telescope Science Institute, 3700 San Martin Drive, Baltimore, MD 21218

Astrophysics Division, Space Science Department, European Space Agency

Shrinivas R. Kulkarni, Ben R. Oppenheimer

Palomar Observatory, 105–24, California Institute of Technology, Pasadena, CA 91125

and

Robert A. Brukardt

Department of Physics and Astronomy, The Johns Hopkins University, Baltimore, MD 21218

Abstract

Three-epoch observations of the M1V + brown dwarf system Gliese 229AB using the Hubble Space Telescope's Wide Field and Planetary Camera 2 (WFPC2) are reported. Relative astrometric measurements spanning one year confirm the common proper motion of the pair and reveal the first evidence of orbital motion. The radial and azimuthal components of Gliese 229B's relative motion are $-0''.087$ and $+0''.049$, respectively, indicating an elliptical orbit rather than an inclined circular orbit. The absolute WFPC2 magnitudes of Gliese 229B are $M_{1042} = 16.37$, $M_{814} = 20.76$, and $M_{675} = 24.60$, assuming a distance of 5.774 pc. The detection of Gliese 229B through the F675W bandpass is the first reported at R band wavelengths. The measured flux through F1042M ($\lambda_c \approx 1$ μm) is well matched by the latest models of dust-free, brown dwarf photospheres by Tsuji et al. These models severely overestimate the broadband fluxes shortward of 0.8 μm,

[†]Previously published in Golimowski et al. (1998)

however, which indicates that a strong source of optical continuum opacity exists in the photosphere of Gliese 229B. A search for fainter companions to Gliese 229A in the Planetary Camera was negative to limiting absolute magnitudes of $M_{1042} \approx 19$ and $M_{814} \approx 24.5$ beyond 7″ of Gliese 229A. Non-detection limits for the Wide Field Cameras are 1.5 magnitudes greater than those for the Planetary Camera.

3.3.1 Introduction

Brown dwarfs are compact objects with masses below the minimum mass required for stable hydrogen burning. Nakajima et al. (1995; hereafter N95, reproduced in §2.1) reported the first unambiguous discovery of a cool brown dwarf, Gliese 229B, from a coronagraphic survey of nearby stars with ages $\sim$ 1 Gyr. N95 identified Gliese 229B as a common proper motion companion of the nearby star Gliese 229 (HD 42581, LHS 1827; $V = 8.14$; spectral type M1V; hereafter Gliese 229A). The near-infrared spectrum of Gliese 229B shows strong absorption by CH_4 and H_2O (Oppenheimer et al. 1995, reproduced in §2.2; Geballe et al. 1996) and resembles the reflection spectra of the giant outer planets in our solar system.

Using observed broadband fluxes from 0.8 to 10.5 μm and a distance to Gliese 229A of 5.7 pc, Matthews et al. (1996; hereafter M96, reproduced in §3.1.4) derived a bolometric luminosity of $\sim 6.4 \times 10^{-6}$ $L_\odot$ for Gliese 229B, well below the minimum luminosity for hydrogen-burning stars ($L_{\rm min} \approx 10^{-4}$ $L_\odot$; Burrows and Liebert 1993). Assuming a radius for Gliese 229B equal to that of Jupiter (Burrows and Liebert 1993), M96 obtained $T_{\rm eff} \approx 900$ K. At this effective temperature, the brown dwarf's atmosphere is expected to be composed primarily of H_2, H_2O, CH_4, and N_2 (Tsuji and Ohnaka 1995; Fegley and Lodders 1996). Thus, the strong CH_4 absorption first noted by Oppenheimer et al. (1995) supports the $T_{\rm eff}$ derived by M96. Spectral models of cool brown dwarfs predict that Gliese 229B has a dust-free photosphere

(Tsuji et al. 1996b) and an effective temperature of 900 to 1000 K (Allard et al. 1996, Marley et al. 1996). This temperature range implies a mass of 0.03 to 0.055 $M_\odot$ for a likely age of 1 to 5 Gyr (Allard et al. 1996, Marley et al. 1996). Optical spectra of Gliese 229B indicate an absence of TiO and VO, commonly associated with metal-rich M dwarfs, suggesting that Ti and V have condensed and settled as dust in the lower atmosphere (Oppenheimer 1997, Schultz et al. 1998, Oppenheimer et al. 1998). Recent near-infrared spectra reveal CO in greater abundance than expected for equilibrium with CH_4 at $T_{\rm eff} \approx 900$ K, possibly because of convective mixing from warmer layers of the upper atmosphere (Noll et al. 1997, Oppenheimer et al. 1998). Such mixing is observed in Jupiter's atmosphere (Noll et al. 1988) and may provide clues about the formation and internal structure of Gliese 229B.

In this paper, we present the results of three-epoch observations of Gliese 229B using the Wide Field and Planetary Camera 2 (WFPC2) aboard the *Hubble Space Telescope* (*HST*). These observations comprise four *HST* orbits granted by the Director of the Space Telescope Science Institute (STScI) from his discretionary observing time. Using the high astrometric accuracy of *HST*, we confirm that Gliese 229AB is a common proper motion pair and report the first evidence of orbital motion. We also present optical broadband photometry of Gliese 229B, including the first measurement in the R bandpass. Finally, we provide limits on the brightness of other possible companions located beyond $0\farcs25$ from Gliese 229A.

3.3.2 Observations and Data Reduction

Observations of Gliese 229AB were performed on UT 17 November 1995, UT 26 May 1996, and UT 11 November 1996 using WFPC2. Gliese 229A was acquired at the approximate center of the Planetary Camera (PC), providing a $33\farcs5 \times 33\farcs5$ field of view (FOV) centered on the star. Telescope roll angles of 328° (epochs 1 and 3) and 148° (epoch 2) were selected so that the position angle of Gliese 229B (PA

= 163°; N95) would not coincide with the diffraction spikes or the charge overflow from the saturated image of Gliese 229A. Data from the three Wide Field Cameras (WFCs) were also obtained, providing partial coverage of the circumstellar field up to 2′ from Gliese 229A.

First-epoch images were recorded through three broadband filters: F675W (WFPC2 *R*), F814W (WFPC2 *I*), and F1042M ($\lambda_c \approx 1$ μm) (Burrows et al. 1995). To guarantee accurate astrometry of Gliese 229AB, unsaturated images of each component were obtained by recording sets of four short (1.6 s) and two long (300 s) exposures through F1042M. Between the exposures of each set, the pointing was offset in successive steps of 0.″2275 (5 PC pixels) along the rows and columns of the CCD. These offsets ensured that neither cosmic-ray events nor defective pixels would skew the image centroids. Similarly, two-exposure sets of 0.11, 5, and 400 s were recorded through F814W. These sets permitted inspection of the circumstellar field with varying sensitivity beyond 0.″25 from Gliese 229A. One 500 s exposure through F675W was also obtained, completing the two-orbit time allocation. For the 0.11, 1.6, and 5 s exposures, a gain of 14 e^- DN^{-1} was used to minimize detector saturation by Gliese 229A. For the longer exposures, a gain of 7 e^- DN^{-1} was used to enhance sensitivity to faint field sources. During the exposures longer than 1.6 s, the pixels in the PC's serial register were continually clocked to minimize the effect of charge overflow.

Second-epoch observations of Gliese 229AB were conducted with the telescope rolled 180° from the first-epoch roll angle. Gliese 229A was acquired $\sim 3''$ from the nominal first-epoch pointing. At this roll angle, the FOV of each WFC was diametrically opposite Gliese 229A from its corresponding first-epoch FOV. Because of the asymmetric focal-plane configuration of the WFPC2 CCDs (Burrows et al. 1995), approximately 20% of the total WFC FOV was imaged in both the first and second epochs. Sets of two 1.6 s exposures and two 300 s exposures were recorded through

F1042M, and two 400 s exposures were obtained with F814W. (The F814W exposures produced images of distant field stars needed for astrometric measurements of Gliese 229AB.) As before, pointing offsets of 0.″2275 were performed along each CCD axis between the exposures of each set.

Third-epoch images were obtained with the telescope rolled at the same angle used during the first-epoch observations. Gliese 229A was acquired $\sim$ 0.″4 from the nominal first-epoch pointing. Although the sequence of exposures was intended to be the same as that used during the second epoch, a miscommunication during observation planning resulted in a sequence of exposures through F1042M identical to that used during the first epoch. No exposures through F814W were obtained. The consequences of this miscommunication are discussed in §3.3.3.

The data were flux calibrated using the Space Telescope Science Data Analysis System (STSDAS) software and the calibration reference files recommended by the *HST* data archive for each epoch. The images of each exposure set were shifted by 5 PC pixels in each axis to a common registration coinciding with the nominal telescope pointing. The shifted images then were combined to produce a single image devoid of cosmic-ray or "hot-pixel" artifacts. The final images represented the average of their constituent exposures after rejection of pixel values at least 3σ above the mean value at that location. For the single F675W image, artifacts were identified by visual inspection.

Subtraction of Gliese 229A's point-spread function (PSF) from the vicinity of point sources in the PC field was performed using the NOAO IRAF task IMSURFIT. Bivariate Legendre polynomials were fit to the PSF outside a circular aperture encompassing each source and lying within a 25 $\times$ 25-pixel subimage centered on that source. The fitted surfaces were then subtracted from the subimage, providing noiseless removal of the PSF. Image centers and fluxes of each source were determined by averaging individual measurements of each from the PSF-subtracted subimages

created from polynomial fits of varying order.

The astrometric and photometric measurements for all sources in the WFPC2 FOV were obtained using conventional methods of aperture photometry. The image centers were determined using an image centroid algorithm in which only those pixels having intensities above the mean intensity of the photometry aperture are used (Da Costa 1992). The centroids were then transformed to distortion-free coordinates using the STSDAS task METRIC (Gilmozzi et al. 1995). The measured fluxes were converted to instrumental magnitudes by applying the aperture corrections and synthetic zero points defined by Holtzman et al. (1995a, 1995b) for the WFPC2 photometric system. In the WFPC2 system, Vega has $m \approx 0$ through all broad- and medium-band WFPC2 filters. This system differs significantly from the standard STScI magnitude system (STMAG), in which an object with a constant F_λ spectrum and $m = 0$ has a monochromatic flux of $F_\lambda = 3.63 \times 10^{-9}$ erg cm^{-2} s^{-1} Å^{-1}.

3.3.3 Results

Figure 3.13 shows $9\farcs1 \times 13\farcs7$ sections of the long-exposure F1042M, F814W, and F675W images of the Gliese 229 system obtained on UT 17 November 1995. The logarithms of the pixel intensities are displayed to reduce image contrast. The fields have been rotated counterclockwise by 13° so that north is up and east is to the left. Evident in the images are the diffraction spikes caused by the *HST*+PC secondary-mirror spider and the charge overflow from the saturated pixels near Gliese 229A. The source located to the south-southeast of Gliese 229A is the same object identified by N95 as the brown-dwarf companion, Gliese 229B. The image sections have been normalized to the same brightness at a distance of 30 pixels ($1\farcs4$) from Gliese 229A to emphasize the redness of Gliese 229B at optical wavelengths. Despite the logarithmic display, Gliese 229B is barely detectable in the F675W image.

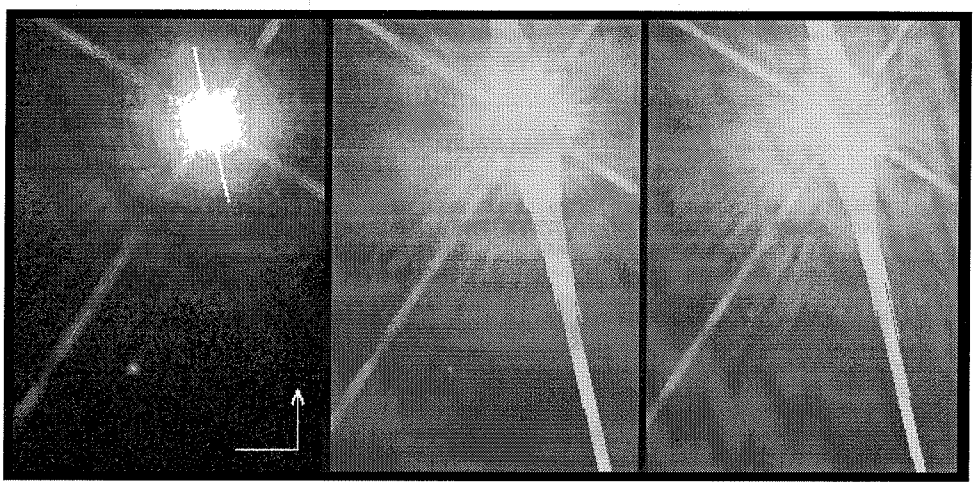

gure 3.13 Images of Gliese 229AB obtained on UT 17 November 1995 using the *HST* Planetary mera. The panels are 9.″1 × 13.″7 sections of two combined 300 s exposures through F1042M (left),) combined 400 s exposures through F814W (middle), and one 500 s exposure through F675W ght). The logarithms of the pixel intensities are presented to reduce image contrast. The fields e been rotated counterclockwise by 13° so that north is up (indicated by the compass arrow) and t is left. Gliese 229B is located 7.″761 from Gliese 229A at a position angle of 163.°55. The panels e been normalized to a common brightness 30 pixels (1.″4) from Gliese 229A to emphasize the ness of Gliese 229B at optical wavelengths. Although barely detectable in the right panel, Gliese)B is imaged through F675W with SNR = 5.

ıotometry of Gliese 229B

ble 3.5 lists the fluxes and WFPC2 magnitudes for Gliese 229AB in the F1042M, 14W, and F675W bandpasses measured for each epoch. The equivalent STScI magudes are listed for sake of comparison. The values for Gliese 229B were obtained ng the average PSF-subtracted subimages described in §3.3.2 and the photometric ibration technique of Holtzman et al. (1995a). The uncertainties in the fluxes repreıt the combined effects of read noise, photon noise, PSF-subtraction error, flat-field ıccuracy (1% on small scales), and zero-point uncertainty ($\lesssim$ 2%). The measured xes of Gliese 229B through F1042M and F814W are consistent with the Gunn z d i measurements reported by N95 (and tabulated by M96) and are up to five times ›re certain. The detection of Gliese 229B through F675W is the first ever reported

at R band wavelengths (N95). The WFPC2 colors of Gliese 229B measured from the first-epoch images are $m_{675} - m_{814} = 3.84 \pm 0.24$ and $m_{814} - m_{1042} = 4.39 \pm 0.06$.

The F1042M fluxes measured for Gliese 229AB are invariant from epoch to epoch. However, the F814W fluxes of Gliese 229B measured in epochs 1 and 2 do not agree within the computed uncertainties. The lack of temporal and chromatic correlation between these measurements discourages the notion that Gliese 229B is photometrically variable. The discrepancy is more likely attributable to the photometric performance of WFPC2 and the flux calibration of the data. Holtzman et al. (1995a, 1995b) reported that the WFPC2 CCDs have substandard charge-transfer efficiency, which may cause absolute photometric errors as large as 4% depending on the brightness and location of the source and background signal. Moreover, small changes in the detective efficiency of the PC can occur in the days or weeks between the calibration and science observations. For example, the fluxes measured from the images calibrated shortly after each observation by the STScI data pipeline (Leitherer et al. 1995) differed by 3 to 4% from those measured from images recalibrated later using better suited calibration data. Although these instrumental and calibration errors cannot be precisely quantified, their combined uncertainty probably exceeds the 1% required to bring the discrepant F814W fluxes into accord.

Relative Astrometry of Gliese 229B

The motive for choosing three observational epochs spaced six months apart was to compute explicitly and independently the proper motion and parallax of Gliese 229B. With these parameters, the brown dwarf's bolometric luminosity and companionship with Gliese 229A could be verified. This task required the presence of distant background stars in the PC FOV against which the motion of Gliese 229B could be measured. No such stars appeared in the 300 s images through F1042M,

but five faint (> 20 mag) stars did appear in the 400 s images through F814W. Unfortunately, because of a miscommunication during observation planning, no F814W images were recorded during the third epoch. Consequently, independent derivations of Gliese 229B's proper motion and parallax were unobtainable. Nevertheless, astrometric measurements relative to Gliese 229A were obtainable and permitted a reliable assessment of Gliese 229B's nature as a binary companion.

To determine accurately the position of Gliese 229B relative to Gliese 229A, the image centroids of each were computed using the 1.6 and 300 s exposures through F1042M. Because the signal-to-noise ratio (SNR) of each source's image is large (see Table 3.5), the accuracy of the centroid as a position estimator is limited not by photon noise, but by telescope pointing, background subtraction, image distortion, and the accuracy of the centroid algorithm itself. Variations of Gliese 229A's centroid measured from the individual 1.6 s images showed that the rms error of the interexposure pointing offsets was at most 0.03 pixel along each axis of the PC. Thus, the centroids measured from the combined 1.6 and 300 s images were unaffected by pointing error and jitter. Measurements of Gliese 229B's centroid from the final background-subtracted subimages described in §3.3.2 varied by $\lesssim 0.01$ pixel (rms), indicating an insensitivity to the order of the bivariate-polynomial fit. Gilmozzi et al. (1995) characterized the geometric image distortion caused by the WFPC2 optics and derived equations of transformation between measured image centroids and orthogonal coordinate systems for each WFPC2 camera. They computed an rms error between actual and transformed coordinates of $\lesssim 0.11$ PC pixel. Monet (1992) estimates the accuracy of the image centroid algorithm to be ~ 0.1 pixel. Combined in quadrature, these uncertainties amount to an actual image-center error of ~ 0.16 PC pixel.

Any measured changes in the position angle of Gliese 229AB between epochs are limited in accuracy by the uncertainty of *HST's* roll-angle offset between visits.

This uncertainty may be quantified by examining the positions of fixed background stars in the WFPC2 images. The five background stars appearing in the F814W PC images are useful for determining the angular offset of the PC between epochs 1 and 2. Although no background stars appeared in the F1042M PC images, 51 stars were imaged by the three WFCs in epochs 1 and 3. These 51 stars may be used to determine the angular offset of the PC between epochs 1 and 3 *only if* the offsets of the PC and WFCs are consistently identical. If so, the 25 stars appearing in that 20% of the WFC FOV imaged in both epochs 1 and 2 also may be used to improve the offset statistics generated by the five stars in the PC images.

To compute the roll-angle offsets between epochs, the position angles of all pairs of background stars imaged in each camera were computed from their distortion-corrected centroids (Gilmozzi et al. 1995) and then differenced from the position angles of the same star-pairs imaged in different epochs. The differences were then weighted by the product of the fluxes of the star-pairs and averaged to produce a mean angular offset between epochs for each camera. The resultant offsets are shown in Table 3.6. The uncertainties reflect the rms deviation of the individual offsets measured for the star-pairs imaged in the respective cameras. (Note that the star-pairs imaged by WF2 during epochs 1 and 2 appeared in WF4 during epochs 2 and 1, respectively. Stars imaged by WF3 in epochs 1 and 2 were not reimaged in epochs 2 and 1, respectively.) The resultant offsets for epochs 1 and 2 are the same, within uncertainties, for the PC and the WFCs. Similar agreement is seen among the resultant offsets measured for epochs 1 and 3 using the three WFCs, so the average of these offsets may be confidently applied to the third-epoch PC images.

Using an image scale of $0\farcs04554$ pixel^{-1} for the PC (Holtzman et al. 1995b), a first-epoch *HST* roll angle of $328\fdg00 \pm 0\fdg07$ (determined from the PA_V3 image-header keyword and a guide-star position error of $1''$), and the average roll-angle offsets from Table 3.6, we find that Gliese 229B lay at the following separations and

TABLE 3.5 WFPC2 PHOTOMETRY OF GLIESE 229AB

Object	Filter	Exp. (s)	Date (UT)	F_λ (erg cm^{-2} s^{-1} Å^{-1})[b]	F_ν (Jy)[b]	Magnitude[a] STMAG	WFPC2	Error[b]	SNR[c]
Gliese 229A	F1042M	1.6	17 Nov 1995	$(3.844 \pm 0.086) \times 10^{-12}$	13.38 ± 0.30	7.438	5.481	±0.024	862
			26 May 1996	$(3.851 \pm 0.086) \times 10^{-12}$	13.40 ± 0.30	7.436	5.479	±0.024	607
			11 Nov 1996	$(3.869 \pm 0.087) \times 10^{-12}$	13.47 ± 0.30	7.431	5.474	±0.024	862
Gliese 229B	F1042M	300	17 Nov 1995	$(5.08 \pm 0.18) \times 10^{-16}$	$(1.77 \pm 0.06) \times 10^{-3}$	17.14	15.18	±0.04	35
			26 May 1996	$(5.19 \pm 0.15) \times 10^{-16}$	$(1.80 \pm 0.05) \times 10^{-3}$	17.11	15.16	±0.03	56
			11 Nov 1996	$(5.09 \pm 0.16) \times 10^{-16}$	$(1.77 \pm 0.06) \times 10^{-3}$	17.13	15.18	±0.03	45
	F814W	400	17 Nov 1995	$(1.77 \pm 0.06) \times 10^{-17}$	$(3.76 \pm 0.13) \times 10^{-5}$	20.78	19.57	±0.04	37
			26 May 1996	$(1.90 \pm 0.05) \times 10^{-17}$	$(4.04 \pm 0.10) \times 10^{-5}$	20.70	19.49	±0.03	68
	F675W	500	17 Nov 1995	$(8.57 \pm 1.71) \times 10^{-19}$	$(1.28 \pm 0.26) \times 10^{-6}$	24.07	23.41	$^{+0.24}_{-0.20}$	5

Notes to Table 3.5

[a] Magnitudes are based on synthetic zero points given by Holtzman et al. (1995a) for the STScI and WFPC2 photometric systems. Zero points are defined for a 0.″5 radius aperture.

[b] Uncertainties include read noise, photon noise, background-subtraction error, calibration accuracy, and instrumental effects (see text).

[c] SNR = signal-to-noise ratio; based on read noise, photon noise, and background-subtraction error only.

position angles from Gliese 229A:

17 Nov 1995: $7''.761 \pm 0''.007$ @ $163°.55 \pm 0°.10$

26 May 1996: $7''.720 \pm 0''.007$ @ $163°.69 \pm 0°.10$

11 Nov 1996: $7''.674 \pm 0''.007$ @ $163°.91 \pm 0°.10$

The change in the relative position of Gliese 229B between epochs 1 and 3 ($0''.100 \pm 0''.013$) is $\sim 50\sigma$ less than the annual proper motion of Gliese 229A ($0''.727 \pm 0''.001$ yr^{-1}; ESA 1997). Since the parallactic motion of both objects over 0.98 yr is nearly zero, we concur with N95 that Gliese 229A and B exhibit common proper motion. Barring the unlikely scenario that the pair are comoving but not gravitationally bound, we conclude that the monotonic motion of Gliese 229B relative to Gliese 229A tabulated above is orbital in nature.

TABLE 3.6 ROLL-ANGLE OFFSETS BETWEEN EPOCHS

		Roll-angle offset	
Camera[a]	Filter	Epoch 2 – Epoch 1	Epoch 3 – Epoch 1
PC1	F814W	$179°.86 \pm 0°.02$	—
WF2	F814W	$179°.87 \pm 0°.03$	—
	F1042M	$179°.93 \pm 0°.06$	$359°.86 \pm 0°.03$
WF3	F1042M	—	$359°.84 \pm 0°.03$
WF4	F814W	$179°.88 \pm 0°.06$	—
	F1042M	—	$359°.87 \pm 0°.03$
Average		$179°.88 \pm 0°.02$	$359°.86 \pm 0°.02$

Notes to Table 3.6

[a] Camera with which star-pairs were imaged during Epoch 1.

Search for Fainter Companions

The large SNR of the F1042M and F814W images of Gliese 229B demonstrates the usefulness of WFPC2 for seeking faint companions to nearby stars. Schroeder & Golimowski (1996) assessed the PC's ability to detect such companions and formulated an algorithm that systematically identifies point sources embedded in the PC's complex PSF. They determined that this algorithm can locate a faint source anywhere within the circumstellar field provided that the source's brightness is at least 10σ above the local background. We applied this search algorithm to the PC images of Gliese 229AB to identify any fainter companions in the system and to establish an upper limit to the brightness of any undetected companions.

Because the same field was imaged by the PC in all three epochs, the search algorithm was applied to the first-epoch F1042M and F814W images only. The search space was centered on Gliese 229A and spanned the entire PC FOV except for those regions vignetted by the shadow of the WFPC2 pyramid (Burrows et al. 1995) or saturated by the excess charge from Gliese 229A's image. Because the excess charge flows predominantly along the columns of pixels, the inner radial limit of the search varied with azimuth. The minimum search radii (oriented perpendicular to the charge overflow) were $\sim 0\farcs25$ for the 300 s F1042M image and $\sim 1\farcs25$ for the 400 s F814W image. The 5 s F814W image was also examined to provide search coverage of the region $0\farcs25$ to $1\farcs25$ from Gliese 229A in that bandpass. The dashed curves in Figures 3.14 and 3.15 show the azimuthally averaged profiles of Gliese 229A from the long-exposure F1042M and F814W images, respectively. The profiles were sampled over 5×5 pixel arrays in radial steps of $0\farcs5$ and azimuthal intervals of 30°. Care was taken to avoid the diffraction spikes, charge overflow, and Gliese 229B. The solid curves trace the detection limits for point sources having four pixels equal to 10σ above the local background. In each figure, the location and brightness of Gliese 229B is plotted as a point of reference. The figures demonstrate that F1042M is the

better bandpass for seeking Gliese 229B-like objects within 4″ of Gliese 229A, while F814W is more suitable for searching beyond this angular distance.

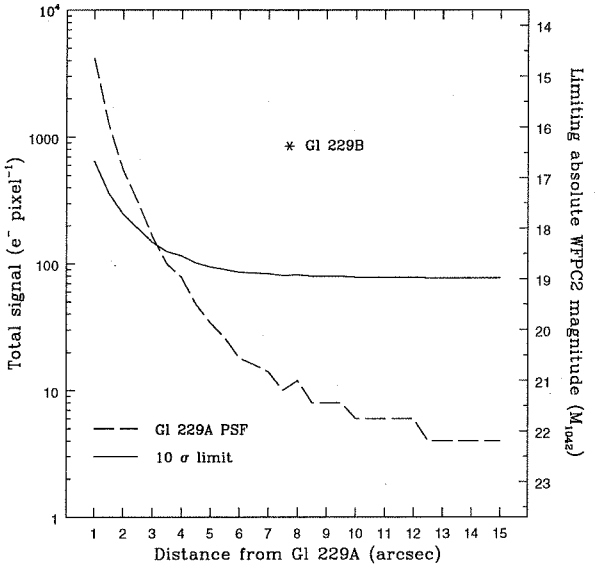

Figure 3.14 Signal and absolute magnitude detection limits for faint companions to Gliese 229A imaged in the PC through F1042M. The dashed curve shows the azimuthally averaged image profile of Gliese 229A. The solid curve traces the detection limits for point sources having four pixels equal to 10σ above the local background. The location and brightness of Gliese 229B is plotted for reference.

The search algorithm identified six astronomical sources (excluding Gliese 229B) in the F814W image and none in the F1042M image. The six sources in the F814W image consisted of five faint ($20.5 < m_{814} < 22.5$) stars (one of which was binary) and one bright ($m_{814} \approx 18$) galaxy. These six sources also appeared in the F675W image; none were redder than $m_{675} - m_{814} = 1.5$. None of the sources exhibited proper motion greater than 0.″02 (0.5 pixel) between epochs 1 and 2, so all were deemed to be distant background objects.

Because the background signal in the WFC images was mostly devoid of scattered light from Gliese 229A, visual inspection alone was sufficient for identifying sources with SNR $\gtrsim 5$. We computed the fluxes and distortion-free centroids of all WFC sources with F1042M and F814W fluxes brighter than SNR $= 5$ (*i.e.*, $m_{1042} < 19.2$

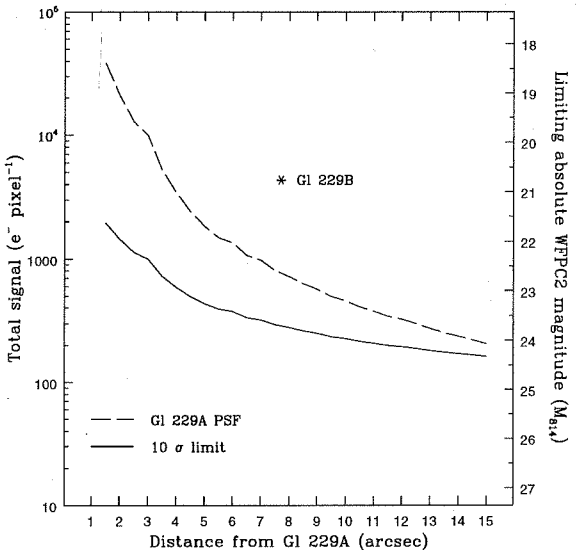

Figure 3.15 Signal and absolute magnitude detection limits for faint companions to Gliese 229A imaged in the PC through F814W. The curves have the same meaning as those in Fig. 3.14.

and $m_{814} < 24.7$) that appeared in at least two epochs or bandpasses. These selection criteria permitted identification of widely-separated companion candidates from their colors or proper motions. We identified 174 sources, of which 159 are point like (presumably stars) and 15 are galaxies. Figures 3.16 and 3.17 show the color–magnitude diagrams of all the point sources identified in the WFPC2 FOV during any two epochs. The distribution of colors in each figure is consistent with interstellar reddening at a galactic latitude of –18°. No source is sufficiently red to be considered a very-low-mass companion candidate. Moreover, none of the WFC sources exhibits any significant proper motion.

In summary, we detected no other potential companions to Gliese 229A brighter than (1) the 10σ limits depicted in Figure 3.14 for the PC images, and (2) $M_{1042} = 20.4$ or $M_{814} = 25.9$ in the WFC images.

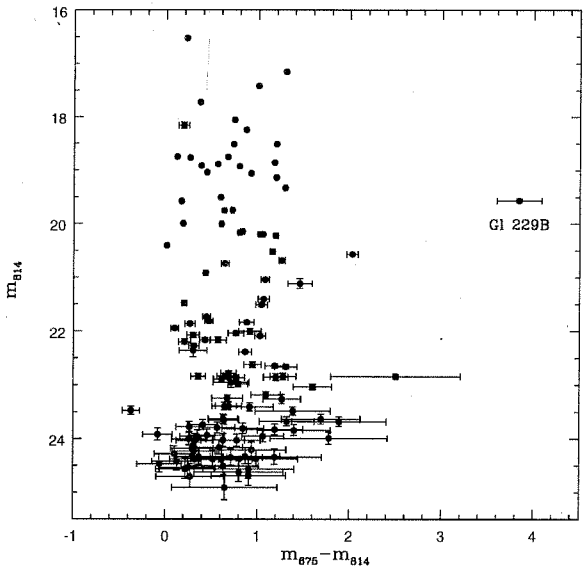

Figure 3.16 Color–magnitude diagram of all point sources identified in the WFPC2 FOV during any two epochs. Plot of m_{814} versus $m_{675} - m_{814}$. Gliese 229B is plotted for reference. No other source is sufficiently red to be considered a very-low-mass companion candidate. Moreover, none of the other sources exhibits common proper motion with Gliese 229AB.

3.3.4 Discussion

Using a parallax of $0\farcs17319 \pm 0\farcs00112$ for Gliese 229A (ESA 1997) and the first-epoch images, we compute for Gliese 229B absolute WFPC2 magnitudes of $M_{1042} = 16.37 \pm 0.04$, $M_{814} = 20.76 \pm 0.04$, and $M_{675} = 24.60^{+0.24}_{-0.20}$. Thus, Gliese 229B is the least luminous object beyond our solar system ever imaged at optical wavelengths. The broadband flux ratios measured from the same images are $f_{1042}/f_{814} = 28.7$ and $f_{814}/f_{675} = 20.7$. Since the interval between the pivot wavelengths of F814W and F1042M is about 1.75 times that between F675W and F814W, the average flux from Gliese 229B in these bandpasses increases $\sim 28\%$ more rapidly between F675W and F814W than it does between F814W and F1042M.

Tsuji et al. (1996b) and M96 have shown that the broadband fluxes from 0.8 to 10 μm reported by M96 are well fit by model spectra of dust-free, brown

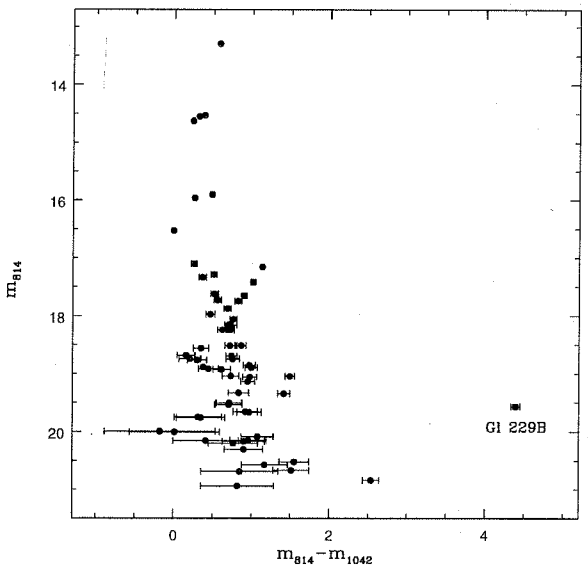

Figure 3.17 Color–magnitude diagram of all point sources identified in the WFPC2 FOV during any two epochs. Plot of m_{814} versus $m_{814} - m_{1042}$.

dwarf photospheres with $T_{\rm eff}$ = 900 and 1000 K. Tsuji has kindly provided us with two sets of his revised dust-free models for $T_{\rm eff}$ = 900 and 1000 K. The sets are distinguished by the inclusion (model A) or exclusion (model C) of opacity from TiO and VO. Both sets of models include some transitions of H_2O and CH_4. We compare our WFPC2 measurements to Tsuji's model spectra in Figure 3.18. Both model-C spectra match the measured F1042M flux well, but they severely overestimate the fluxes observed through F675W and F814W. Although absorption by TiO and VO is absent from the observed optical spectrum of Gliese 229B (Oppenheimer 1997, Schultz et al. 1998, Oppenheimer et al. 1998), the model-A spectra are significantly better matches to the F675W and F814W fluxes. Schultz et al. (1998) noted a similar overestimation of Gliese 229B's optical flux in the model spectra of Allard et al. They surmised that the emergent flux shortward of 0.8 μm is strongly absorbed by dust grains suspended in the photosphere. Oppenheimer et al. (1998), however, have reported that the near-infrared spectrum of Gliese 229B

cannot be reproduced by any of the dusty-photosphere models of Tsuji et al. (1996b). Because these models consider the effects of only the most abundant species of dust, it remains to be seen whether this dilemma can be resolved by the inclusion of condensates from less abundant refractory elements.

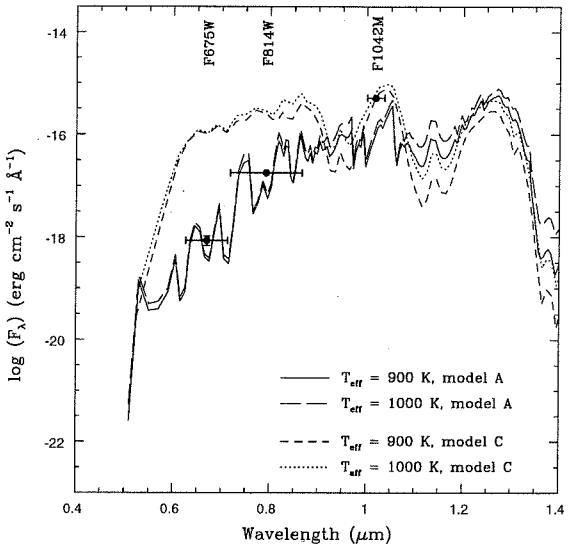

Figure 3.18 Comparison of measured WFPC2 broadband fluxes with models of dust-free, brown dwarf photospheres by Tsuji et al. Optical spectra are shown for brown dwarfs with solar metallicity, $\log(g) = 5$, and $T_{\rm eff} = 900$ and 1000 K at a distance of 5.774 pc. The spectra are grouped according to the inclusion (model A) or the exclusion (model C) of opacity from TiO and VO. (Neither molecule is observed in the actual optical spectrum of Gliese 229B.) All models include some transitions of H_2O and CH_4. The model-C spectra match the measured F1042M flux well, but severely overestimate the observed fluxes through F675W and F814W. These fluxes are better matched by the model-A spectra, which indicates that a strong source of optical-continuum opacity exists in the photosphere of Gliese 229B.

Although the spectral energy distribution of Gliese 229B has been studied extensively in the last two years, the question concerning Gliese 229B's formation as a binary or a planetary companion remains unanswered. Boss (1996) has suggested that orbital eccentricity may resolve this question, since binary stars usually have elliptical orbits (Duquennoy and Mayor 1991) and planets form with nearly circular orbits. The one-year span of our observations is insufficient for computing Gliese

229B's orbit, but its eccentricity can be constrained from our astrometry and Kepler's Laws. The semi-major axis, a, of a Keplerian orbit is

$$a = \left(\frac{2}{r} - \frac{v^2}{\mu}\right)^{-1} \tag{3.1}$$

where $r = |\mathbf{r}(t)|$ and $v = |\mathbf{v}(t)|$ are the separation and velocity of the orbiting body at time t. The quantity μ equals $G(m_1 + m_2)$, where G is the gravitational constant and m_1 and m_2 are the component masses. For bound orbits, $a \geq 0$. The eccentricity, e, of a bound orbit is

$$e = \sqrt{\left(1 - \frac{r}{a}\right)^2 + \left(\frac{u}{na^2}\right)^2} \tag{3.2}$$

where $u = \mathbf{r} \cdot \mathbf{v}$, and $n = \sqrt{\mu/a^3}$ (Danby 1988).

Equations 3.1 and 3.2 cannot be solved uniquely without knowing Gliese 229B's motion along the line of sight, but a and e can be constrained from the observed motion in the plane of the sky. Gliese 229B's motion between epochs 1 and 3 was $0\farcs100 \pm 0\farcs013$, of which $-0\farcs087 \pm 0\farcs010$ (1.91 ± 0.23 pixels) was radial motion and $+0\farcs049 \pm 0\farcs019$ (1.07 ± 0.42 pixels) was azimuthal motion. Assuming a mass of 0.57 $M_\odot$ for Gliese 229A (Henry and McCarthy 1993), we have computed lower limits to the kinetic (T) and potential (U) energies of Gliese 229B from its projected position and velocity between these epochs. We find that $T_{\rm min}/U_{\rm min} \approx -0.34$, which strongly supports (though does not prove) a bound orbit. Figures 3.19 and 3.20 depict the loci of a and e, respectively, for such orbits, based on Gliese 229B's average position and velocity between epochs 1 and 3, varying values of Gliese 229B's line-of-sight position and velocity, and an estimated mass for Gliese 229B of 0.045 $M_\odot$. From these parameters, we compute $a \gtrsim 32$ AU, a period $P = \sqrt{4\pi^2 a^3/\mu} \gtrsim 236$ yr, and $e \gtrsim 0.25$. (For the six-month intervals between epochs 1 and 2 and epochs 2 and 3, $e \gtrsim 0.07$ and 0.45, respectively.) Although this eccentricity may imply a binary rather

than planetary origin for Gliese 229B, a verdict based solely upon the small-sample statistics of known planetary orbits is questionable at best.

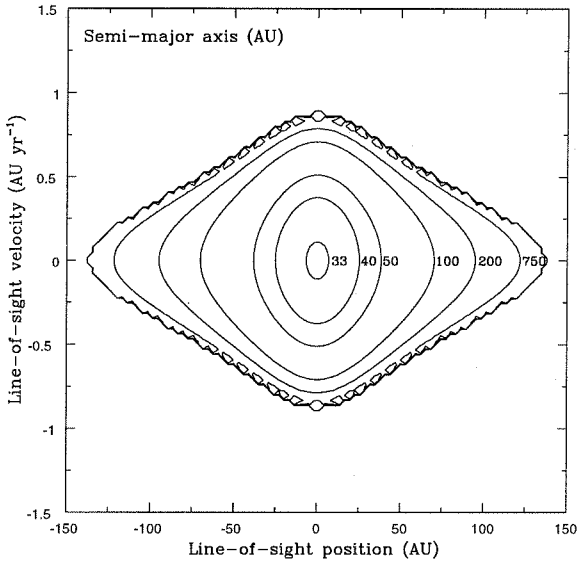

Figure 3.19 Loci of semi-major axes consistent with bound Keplerian orbits and the observed motion of Gliese 229B between epochs 1 and 3. The parameters are shown as functions of the line-of-sight position and velocity of Gliese 229B relative to the the plane of the sky. The heavy contours reflect the boundaries between bound and unbound orbits. We compute $a \gtrsim$ 32 AU, $e \gtrsim$ 0.25, and $P \gtrsim$ 236 yr for Gliese 229B, assuming masses of 0.57 $M_\odot$ and 0.045 $M_\odot$ for Gliese 229A and B, respectively.

The theory and observation of brown dwarf atmospheres are in their adolescence. At this time, we cannot accurately predict the F1042M and F814W fluxes of brown dwarfs older or less massive than Gliese 229B. Therefore, we cannot with certainty interpret the limiting magnitudes of our search for fainter companions in terms of age or mass limits. Rough estimates are possible, however, if assumptions are made about the the behavior of the optical spectra of older or less-massive brown dwarfs. Burrows et al. (1997) have made the first theoretical predictions of the infrared colors and absolute magnitudes of brown dwarfs with $T_{\rm eff} \lesssim 1300$ K. They present an M_J versus $J - K$ diagram showing the theoretical isochrones of brown dwarfs with ages

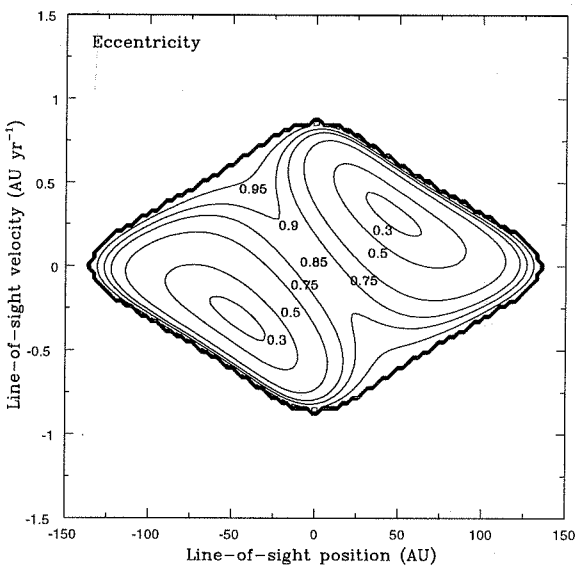

Figure 3.20 Loci of eccentricities consistent with bound Keplerian orbits and the observed motion of Gliese 229B between epochs 1 and 3. The parameters are shown as functions of the line-of-sight position and velocity of Gliese 229B relative to the the plane of the sky. The heavy contours reflect the boundaries between bound and unbound orbits. We compute $a \gtrsim$ 32 AU, $e \gtrsim$ 0.25, and $P \gtrsim$ 236 yr for Gliese 229B, assuming masses of 0.57 $M_\odot$ and 0.045 $M_\odot$ for Gliese 229A and B, respectively.

0.5, 1, and 5 Gyr (Figure 20 of Burrows et al. 1997). If we assume that M_{1042} scales proportionally to M_J (not an unreasonable assumption given their model spectra), then the asymptotic limit of the 10σ-detection curve in Figure 3.14 corresponds approximately to mass detection limits of 10, 15, and 33 $M_{\rm Jup}$ for brown dwarfs of age 0.5, 1, and 5 Gyr, respectively. Likewise, the mass detection limits corresponding to $M_{1042} = 20.4$ for the WFCs are about 7, 10, and 23 $M_{\rm Jup}$ for brown dwarfs of age 0.5, 1, and 5 Gyr, respectively. Although the F814W magnitude limits are deeper than those for F1042M, the F814W flux from brown dwarfs drops with decreasing $T_{\rm eff}$ more rapidly than the F1042M flux. Consequently, F814W may be less sensitive than F1042M to old or low-mass brown dwarfs.

Chapter 4

The 8 Parsec Survey

Abstract

We present the technique and results of a survey of stars within 8 pc of the Sun with declinations $\delta > -35°$ (J2000.00). The survey, designed to find faint companions with no color bias, consists of optical coronagraphic images of the $1'$ field of view centered on each star and infrared direct images with a $32''$ field of view. The images were obtained through the optical Gunn r and z filters and the infrared J and K filters. The survey achieves sensitivities up to four absolute magnitudes fainter than the coolest known brown dwarf, Gliese 229B. However, this sensitivity varies with the seeing conditions, the intrinsic brightness of the star observed and the angular distance from the star. As a result we tabulate sensitivity limits for each star in the survey. We used the criterion of common proper motion to distinguish companions and to determine their luminosities. In addition to the brown dwarf Gliese 229B, we have identified 6 new stellar companions of the sample stars. Since the survey began, accurate astrometric parallax measurements for most of the stars have become available. As a result some of the stars we originally included should no longer be included in the 8 pc sample. In addition, the 8 pc sample is incomplete at

the faint end of the main sequence. We assess the sensitivity of the survey to stellar companions and to brown dwarf companions of various masses and ages.

4.1 Introduction

In 1992 a brown dwarf companion search began at Palomar with the initiation of a collaboration between T. Nakajima and S. Kulkarni at Caltech and D. Golimowski and S. Durrance at Johns Hopkins. The Hopkins group brought the Adaptive Optics Coronagraph (AOC; Golimowski et al. 1992) to Palomar to be fitted on the 60" Telescope. The first results of this collaboration are given in Nakajima et al. (1994), which entailed a search for companions of high galactic latitude stars. Companions were distinguished from background stars through statistical arguments based on the distribution of point sources as a function of angular separation from the stars. In 1994, the work expanded to a new sample of nearby stars which were believed to be young. A short description of this sample is contained in Nakajima et al. (1995; §2.1). This sample was biased toward young stars in an attempt to discover brown dwarf companions, with the assumption that younger brown dwarfs would be easier to detect because they should be brighter (§1.1). The first success of this collaboration was the discovery of a faint companion of the star Gliese 105A (Golimowski et al. 1995). The first success of the young star survey was the discovery of the cool brown dwarf Gliese 229B (Nakajima et al. 1995; Oppenheimer et al. 1995; §2).

Following the discovery of Gliese 229B, we decided that it was of paramount importance to conduct a volume-limited survey for companions. If we continued to pursue the biased sample and found no more brown dwarfs, we would have little to say about the prevalence of companion brown dwarfs.

For this reason, in late 1994 we began a survey of all the Northern ($\delta > -35°$)

stars within 8 pc of the Sun to search for brown dwarf companions. Because all of the known stars within 8 pc have measurable proper motions, our survey was designed to find common proper motion companions. We thus observed each star at multiple epochs, if point sources other than the star appeared in the field of view. This permitted us to discern companions simply by measuring the relative offset between the star and the putative companions at each epoch. The common proper motion criterion distinguishes this survey from previous searches for brown dwarfs because it is intrinsically unbiased by color or other theoretical notions of what a brown dwarf should look like. (See §1.3 for a description of the history of brown dwarf searches.) The common proper motion criterion is the most physically rigorous short-term method for finding companions. (Longer term methods include orbital motion measurements and common parallax measurements, which eliminate the minute possibility that two objects within an arcminute of each other might exhibit common proper motion and yet be physically unassociated.)

This survey is also distinguished from others because it represents the first use of adaptive optics techniques in the study of nearby stars. With our tip-tilt observations dating back to 1992, we greatly predate any other such searches. At the time of this writing, the use of higher order adaptive optics systems is becoming widespread in these sorts of studies (e.g., Delfosse et al. 1998b). The combination of adaptive optics and coronagraphy, and the use of both infrared and optical bandpasses made the search effective.

To achieve our goal of a volume-limited survey, we assembled a sample of stars which appear in the Third Catalog of Nearby Stars (Gliese and Jahreiss 1991) and have parallaxes greater than $0\farcs125$. The completeness of this sample has been the subject of debate. (See, for example, Reid and Gizis 1997.) We address this issue in depth in §4.2 where we also present an updated catalog of the stars within 8 pc.

The observations are explained in detail in §4.3, and a complete description of the

sensitivity limits is presented in later sections.

4.2 The 8 pc Sample

4.2.1 Culling the Catalog

When we began our survey the best list of stars within 8 pc of the Sun was a subset of the Third Catalog of Nearby Stars (Gliese and Jahreiss 1991; CNS3). The subsequent releases of the Hipparcos Main Catalog (ESA 1997) and the Yale Catalog of Trigonometric Parallaxes (van Altena et al. 1995) provide important sets of data that modify the census of stars within 8 pc. Ultimately the two new catalogs moved some stars out of, and others into, the 8 pc sample. These catalogs also added a few stars to the sample, which were not in the CNS3. The Hipparcos Catalog did not add any unknown stars to the 8 pc sample because trigonometric parallaxes were only obtained for previously cataloged stars. However, Hipparcos did measure 7 stars in 5 systems whose parallaxes had never before been measured and which place them within 8 pc. The Yale Catalog adds no new stars to the catalog but does provide astrometric parallaxes for 37 stars within 8 pc which were not measured by Hipparcos. This reduces the number of stars in our sample whose parallaxes are simply inferred from photometry. These so-called photometric parallaxes involve measurements of the colors of a given star. The colors determine the spectral class of the star and, thus, its absolute luminosity. From the absolute luminosity, the distance modulus is calculated. These photometric parallaxes are notoriously erroneous because the luminosity class of a given star, which is unobservable through photometry alone, can drastically affect the implied distance. In addition, unknown multiplicity of such stars can affect the parallax implied by photometry. In the new catalog we assemble here, only 6 stars are included based on photometric parallaxes. These are the only stars

within 8 pc in the CNS3 which were not measured astrometrically by the Hipparcos or the Yale surveys.

Pursuant to this discussion we have created a new catalog of stars within 8 pc of the Sun. We believe this comprises the most complete census of the 8 pc volume to date. In our catalog we combine all the stars within the CNS3, Hipparcos and Yale catalogs which have parallaxes greater than $0''.125$. The three catalogs are fully cross-correlated and for each entry in our database we have up to three different parallaxes, although only the most accurate is listed in the catalog presented here. Precedence for inclusion in the final catalog is given to the Hipparcos measurement which is generally more accurate than the Yale measurement (except in the case of star systems Gliese 185AB and Gliese 644ABCD, where the Yale parallax is more accurate). For six of the stars neither Yale nor Hipparcos measurements exist. These stars have photometric parallaxes listed in the CNS3 and we have included them to be as inclusive as possible.

To be certain that we have included all the known subordinate stellar and substellar objects associated with these stars, we conducted a search of the literature. Two papers (Delfosse et al. 1998b, Reid and Gizis 1997) in particular provided new companions, some of which have been resolved and some of which were detected through radial velocity studies. Our catalog is not biased in any way as to whether a given companion has been visually resolved. A complete census must be free of these considerations. Therefore, we include all of the companions mentioned in Reid and Gizis (1997) and most of those in Delfosse et al. (1998b). We believe that our final catalog is complete to-date because we have used all of the available resources and studies of the nearby stars.

Our sample includes, therefore, 163 stars, one brown dwarf (Nakajima et al. 1995) and one indirectly detected planet (Delfosse et al. 1998a). These entities are arranged in 111 star systems, 29 of which are double, nine of which are triple, one of which is

quadruple and one of which is quintuple.

Table 4.1 lists all the star systems in the 8 pc sample described above. In this table we give a single entry for every object known within 8 pc. For multiple systems, entries are grouped together and indicate the separation of the subordinate components, along with other vital data. The table is arranged in order of decreasing parallax in milliarcseconds (mas). The "Source Code" field in each entry indicates where the parallax measurement comes from. The motivation for this arrangement of stars stems from the need for a consistent catalog of stars within 8 pc of the Sun to which objects can be added easily without disrupting the previously cataloged objects. (Previous catalogs, for example, had to get around this difficulty by simply renaming every star in the catalog or by adding clumsy decimals to the naming scheme whenever a new star was found. Here we list several of the multitude of names for each of the stars but maintain the organization by parallax.) This is needed in the coming years as the effort to identify nearby stars with planets grows. Future space missions such as the Space Interferometry Mission and the Next Generation Space Telescope have distinct goals which include expanding the census of objects within 8 pc of the Sun. The flexibility of this new catalog of stars within 8 pc allows for this along with the ability to add companions of any type to the catalog. Companions of stars are indicated by capital Roman letters after the parallax and generally are given in the order in which the components are discovered. An implicit A is given to every principal star in each star system. However, the A is only used if at least component B has been discovered. For convenience we give HD, Durchmusterung, CNS3 or other names for the stars if they are available. This permits easy identification of the stars in astronomical databases.

TABLE 4.1. THE 8 PC SAMPLE

Parallax	Position (J2000.00)		μ (mas)		V	CNS3	Durch.	Other	SMA	Source
(mas)	RA (^{h} ^{m} ^{s})	Dec. ($^\circ$ $'$ $''$)	RA	Dec.	(^{m})	Name	No.	Name	(AU)	Code
549.01	17:57:48.50	+04:41:36.2	−797.84	10326.93	9.54	Gl 699	BD+04 3561	G140−024		HHH
419.10	10:56:22.46	+07:00:27.6	−3846.7	−2693.5	13.46	Gl 406		G045−020		YYY
392.40	11:03:20.19	+35:58:11.6	−580.20	−4767.09	7.49	Gl 411	BD+36 2147	G119−052		HHH
379.21A	06:45:08.92	−16:42:58.0	−546.01	−1223.08	−1.44	Gl 244A	BD−16 1591			HHH
379.21B					8.44	Gl 244B			19.7	HHC
373.70A	01:39:01.74	−17:56:58.5	3316.8	584.8	12.52	Gl 65A		G272−061		YYY
373.70B					12.56	Gl 65B			5.1	YYY
336.48	18:49:49.36	−23:50:10.4	637.55	−192.47	10.37	Gl 729				HHH
316.00	23:41:56.69	+44:09:34.5	84.6	−1614.8	12.27	Gl 905		G171−010		YYY
310.75	03:32:55.84	−09:27:29.7	−976.44	17.97	3.72	Gl 144	BD−09 697			HHH
299.58	11:47:44.40	+00:48:16.4	605.62	−1219.23	11.12	Gl 447		G010−050		HHH
289.50A	22:38:37.25	−15:17:07.1	2379.8	2219.2	12.32	Gl 866A		G156−031		YYY
289.50B						Gl 866B		G156−031 B	1.2	YY
289.50C						Gl 866C		G156−031 C	0.3	YY
287.13A	21:06:53.94	+38:44:57.9	4155.10	3258.90	5.20	Gl 820A	BD+38 4343			HHH
285.42B	21:06:55.26	+38:44:31.4	4107.40	3143.72	6.05	Gl 820B	BD+38 4344		85.2	HHH
285.93A	07:39:18.12	+05:13:30.0	−716.57	−1034.58	0.40	Gl 280A	BD+05 1739			HHH
285.93B					10.7	Gl 280B			15.9	HHC
280.28A	18:42:46.69	+59:37:49.4	−1326.88	1802.12	8.94	Gl 725A	BD+59 1915	G227−046		HHH
284.48B	18:42:46.90	+59:37:36.6	−1393.20	1845.73	9.70	Gl 725B		G227−047	48.5	HHH
280.27A	00:18:22.89	+44:01:22.6	2888.92	410.58	8.09	Gl 15A	BD+43 44	G171−047		HHH
280.27B					11.06	Gl 15B		G171−048	155.0	HHC
275.80	08:29:44.30	+26:46:01.4	−1139.0	−605.6	14.81	GJ 1111		G051−015		YYY
274.17	01:44:04.08	−15:56:14.9	−1721.82	854.07	3.49	Gl 71	BD−16 295			HHH
269.05	01:12:30.64	−16:59:56.3	1210.09	646.95	12.10	Gl 54.1		G268−135		HHH
263.26	07:27:24.50	+05:13:32.8	571.27	−3694.25	9.84	Gl 273	BD+05 1668	G089−019		HHH
249.52A	22:27:59.47	+57:41:45.1	−870.23	−471.10	9.59	Gl 860A	BD+56 2783	G232−075		HHH
249.52B					9.85	Gl 860B			9.5	HHY
242.89A	06:29:23.40	−02:48:50.3	694.73	−618.62	11.12	Gl 234A		G106−049		HHH
242.89B					14.6	Gl 234B			4.2	HHC

TABLE 4.1. THE 8 PC SAMPLE (CONT.)

Parallax	Position (J2000.00)		μ (mas)		V	CNS3	Durch.	Other	SMA	Source
(mas)	RA (^{h} ^{m} ^{s})	Dec. ($^\circ$ $'$ $''$)	RA	Dec.	(^{m})	Name	No.	Name	(AU)	Code
235.24A	14:49:32.61	−26:06:20.5	−1389.70	135.76	11.72	Gl 563.2A	CD−2510553			HHH
221.80B	14:49:31.76	−26:06:42.0	−1421.60	−203.60	12.07	Gl 563.2B			5.4	HHH
234.51	16:30:18.06	−12:39:45.3	−93.61	−1184.90	10.10	Gl 628	BD−12 4523	G153−058		HHH
227.90A	12:33:16.37	+09:01:16.1	−1797.5	220.7	12.44	Gl 473A		G012−043		YYY
227.90B					13.04	Gl 473B			5.4	YYY
227.45	03:22:05.50	−13:16:43.8	−112.94	−299.04	12.16			HIP 15689		HHH
226.95	00:49:09.90	+05:23:19.0	1233.05	−2710.56	12.37	Gl 35		G001−027		HHH
224.80	02:00:05.90	+13:00:34.2	1111.2	−1778.4	12.26	Gl 83.1		G003−033		YYY
224.00A	08:58:56.10	+08:28:28.0	329.1	−320.0	10.89	1405A		G041−014A		GCC
224.00B						1405B		G041−014B	0.5	GC
224.00C						1405C		G041−014C	3.2	GC
220.85	17:36:25.90	+68:20:20.9	−320.47	−1269.55	9.15	Gl 687	BD+68 946	G240−063		HHH
220.30	10:48:15.29	−11:21:30.5	616.2	−1525.2	15.60	1679				YYY
220.20A	19:53:56.51	+44:24:14.6	439.9	−583.8	13.41	GJ 1245A		G208−044		YYY
220.20B					14.01	GJ 1245B		G208−045	47.0	YYC
220.20C					13.41	GJ 1245C		G208−044 B	3.7	YYC
213.00	00:06:39.52	−07:34:18.5	−830.1	−1864.5	13.74	GJ 1002		G158−027		YYY
212.69A	22:53:16.73	−14:15:49.3	960.33	−675.64	10.16	Gl 876A	BD−15 6290	G156−057 A		HHH
212.69B	22:53:16.73	−14:15:49.3	960.33	−675.64		Gl 876B	BD−15 6290	G156−057 B	0.21	HH
206.94A	11:05:28.58	+43:31:36.4	−4410.79	943.32	8.82	Gl 412A	BD+44 2051	G176−011		HHH
206.94B					14.40	Gl 412B		G176−012	190.0	HHC
205.22	10:11:22.14	+49:27:15.3	−1361.55	−505.00	6.60	Gl 380	BD+50 1725	G196−009		HHH
204.60	10:19:36.23	+19:52:10.7	−503.2	−52.9	9.40	Gl 388	BD+20 2465	G054−023		YYY
202.69	17:29:36.25	+24:39:14.7	97.33	348.92	11.39			HIP 85605		HHH
198.24A	04:15:16.32	−07:39:10.3	−2239.33	−3419.86	4.43	Gl 166A	BD−07 780			HHH
198.24B					9.52	Gl 166B	BD−07 781	G160−060	507.5	HHC
198.24C					11.17	Gl 166C			44.5	HHC
198.00A	22:46:48.50	+44:19:50.6	−772.3	−464.0	10.06	Gl 873A	BD+43 4306			YYY
198.07B	22:46:49.73	+44:20:02.4	−704.66	−459.39	10.29	Gl 873B	BD+43 4305	G216−016	167.4	HHH

TABLE 4.1. THE 8 PC SAMPLE (CONT.)

Parallax	Position (J2000.00)		μ (mas)		V	CNS3	Durch.	Other	SMA	Source
(mas)	RA (^{h} ^{m} ^{s})	Dec. ($^\circ$ $'$ $''$)	RA	Dec.	(^{m})	Name	No.	Name	(AU)	Code
196.62A	18:05:27.29	+02:30:00.4	124.56	−962.66	4.03	Gl 702A	BD+02 3482			HHH
196.62B					4.20	Gl 702B			22.9	HHY
194.44	19:50:47.00	+08:52:06.0	536.82	385.54	0.76	Gl 768	BD+08 4236			HHH
191.86A	00:15:28.11	−16:08:01.7	728.18	−617.48	11.49	GJ 1005A		G158−050 A		HHH
191.86B						GJ 1005B		G158−050 B	3.9	HH
191.20A	08:58:12.21	+19:45:45.9	−873.5	−30.5	14.06	GJ 1116A		G009−038		YYY
191.20B					14.92	GJ 1116B			23.6	YYC
186.20	06:00:03.23	+02:42:15.6	229.2	−74.5	11.33	0999		G099−049		YYY
185.48	11:47:41.38	+78:41:28.2	743.21	480.40	10.80	Gl 445		G254−029		HHH
184.13	13:45:43.78	+14:53:29.5	1778.46	−1455.52	8.46	Gl 526	BD+15 2620	G063−053		HHH
182.15	20:52:33.02	−16:58:29.1	−306.70	30.78	11.41			HIP 103039		HHH
181.36A	04:31:11.52	+58:58:37.5	1300.21	−2048.99	10.82	Gl 169.1A		G175−034		HHH
181.36B					12.44	Gl 169.1B		G175−034	46.6	HHC
181.32	06:54:48.96	+33:16:05.4	−729.33	−399.31	9.89	Gl 251		G087−012		HHH
177.46	10:50:52.06	+06:48:29.3	−804.40	−809.60	11.64	Gl 402		G044−040		HHH
175.72	05:31:27.40	−03:40:38.0	763.05	−2092.89	7.97	Gl 205	BD−03 1123	G099−015		HHH
173.41	19:32:21.59	+69:39:40.2	598.43	−1738.81	4.67	Gl 764	BD+69 1053			HHH
173.19A	06:10:34.62	−21:51:52.7	−137.01	−714.06	8.15	Gl 229A	BD−21 1377			HHH
173.19B						Gl 229B			48.8	HH
172.78	05:42:09.27	+12:29:21.6	1999.05	−1570.64	11.56	Gl 213		G102−022		HHH
170.26A	19:16:55.26	+05:10:08.1	−578.86	−1331.70	9.12	Gl 752A	BD+04 4048	G022−022		HHH
170.26B					17.52	Gl 752B			521.6	HHC
169.90	08:12:41.57	−21:33:11.6	37.0	−706.0	12.10	Gl 300				YYY
169.32A	14:57:28.00	−21:24:55.7	1034.18	−1725.60	5.72	Gl 570A	BD−20 4125			HHH
163.63B	14:57:26.54	−21:24:41.5	987.05	−1666.81	8.01	Gl 570B	BD−20 4123		107.5	HHH
163.63C	14:57:26.54	−21:24:41.5	987.05	−1666.81		Gl 570C			0.8	HH
168.59	07:44:40.17	+03:33:08.8	−344.87	−450.84	11.19	Gl 285		G050−004		HHH
167.99A	00:49:06.29	+57:48:54.7	1087.11	−559.65	3.46	Gl 34A	BD+57 150			HHH
167.99B					7.51	Gl 34B			71.00	HHC

TABLE 4.1. THE 8 PC SAMPLE (CONT.)

Parallax	Position (J2000.00)		μ (mas)		V	CNS3	Durch.	Other	SMA	Source
(mas)	RA (^{h} ^{m} ^{s})	Dec. ($^\circ$ $'$ $''$)	RA	Dec.	(^{m})	Name	No.	Name	(AU)	Code
167.51	23:49:12.53	+02:24:04.4	995.12	−968.25	8.98	Gl 908	BD+01 4774	G029−068		HHH
167.08A	17:15:20.98	−26:36:10.2	−473.69	−1143.93	4.33	Gl 663A	CD−2612026			HHH
167.08B	17:15:20.98	−26:36:10.2	−473.69	−1143.93	5.11	Gl 663B			74.0	HHC
167.56C	17:16:13.36	−26:32:46.1	−479.71	−1123.37	6.33	Gl 664	CD−2612036		6390.0	HHH
164.70	17:47:51.02	+70:53:46.3	−1246.0	1083.2	14.15	GJ 1221		G240−072		YYY
163.51	14:34:16.81	−12:31:10.4	−357.50	595.12	11.32	Gl 555	BD−11 3759			HHH
163.00	05:01:57.60	−06:56:42.0	−541.8	−551.3	12.1	0855				GCC
162.50	12:13:25.87	+10:15:43.5	−92.8	−14.7	5.85	1922	BD+11 2440			YYY
162.00A	07:36:25.00	+07:04:44.0	203.0	−290.0	13.22	1201A		G089−032 A		GCC
162.00B					13.22	1201B		G089−032 B	3.5	GCC
161.77A	17:46:14.41	−32:06:08.3	−77.62	−270.12	11.39			HIP 86963A		HHH
161.77B	17:46:12.63	−32:06:12.8	−49.82	−319.82	10.49			HIP 86963B	155.0	HHH
161.77C	17:46:14.41	−32:06:08.3	−77.62	−270.12				HIP 86963C	<0.1	HH
161.59A	09:14:22.79	+52:41:11.8	−1533.58	−562.80	7.64	Gl 338A	BD+53 1320	G195−017		HHH
159.48B	09:14:24.70	+52:41:11.0	−1551.30	−656.25	7.70	Gl 338B	BD+53 1321	G195−018	102.0	HHH
160.06A	23:31:52.18	+19:56:14.1	554.40	−62.61	10.05	Gl 896A	BD+19 5116	G068−024		HHH
160.06B					12.4	Gl 896B			25.8	HHC
160.06C						Gl 896C			<0.1	HH
160.06D						Gl 896D			<0.1	HH
159.52	15:19:26.82	−07:43:20.2	−1224.55	−99.52	10.57	Gl 581	BD−07 4003	G151−046		HHH
158.17A	17:12:07.89	+45:39:57.5	325.96	−1591.73	9.31	Gl 661A	BD+45 2505	G203−051		HHH
158.17B					9.96	Gl 661B			4.4	HHY
157.24A	07:10:01.83	+38:31:46.1	−439.68	−948.36	11.65	Gl 268A		G087−026		HHH
157.24B						Gl 268B			0.1	HH
156.30	14:56:38.58	−30:10:33.6	−482.5	−835.7	17.05	2363				YYY
156.00	13:07:04.30	+20:48:38.0	−71.7	−39.8	12.58	GJ 2097				GCC
155.00	05:55:09.37	−04:10:04.6	534.7	−2316.1	14.45	Gl 223.2		G099−044		YYY
153.96A	16:55:28.75	−08:20:10.8	−829.34	−878.81	9.02	Gl 644A	BD−08 4352			YHH
153.96B	16:55:28.75	−08:20:10.8	−829.34	−878.81	9.69	Gl 644B			1.4	YHY
153.96C	16:55:31.75	−08:23:38.8	−829.34	−878.81	16.78	Gl 644C			1765.0	YHC
153.96D	16:55:28.75	−08:20:10.8	−829.34	−878.81		Gl 644D			0.1	YHH
153.96E	16:55:25.23	−08:19:21.3	−813.47	−895.23	11.73	Gl 643			557.8	HHH

TABLE 4.1. THE 8 PC SAMPLE (CONT.)

Parallax	Position (J2000.00)		μ (mas)		V	CNS3	Durch.	Other	SMA	Source
(mas)	RA (^{h} ^{m} ^{s})	Dec. ($^\circ$ $'$ $''$)	RA	Dec.	(^{m})	Name	No.	Name	(AU)	Code
153.24	23:13:16.98	+57:10:06.1	2074.37	294.97	5.57	Gl 892	BD+56 2966			HHH
152.90	12:18:54.77	+11:07:41.4	−1285.0	203.5	13.79	GJ 1156		G012−030		YYY
151.93	16:25:24.62	+54:18:14.8	432.29	−170.71	10.13	Gl 625		G202−048		HHH
150.96	11:00:04.26	+22:49:58.7	−426.31	−279.94	10.03	Gl 408		G058−032		HHH
149.26A	14:51:23.38	+19:06:01.7	152.81	−71.28	4.54	Gl 566A	BD+19 2870			HHH
149.26B					6.97	Gl 566B			32.7	HHC
148.29A	21:29:36.81	+17:38:35.8	1008.09	376.21	10.33	Gl 829A		G126−004A		HHH
148.29B						Gl 829B		G126−004B	0.5	HH
146.30	08:12:03.21	+08:44:41.3	1172.2	−5077.4	12.83	Gl 299		G050−022		YYY
145.27	22:56:34.81	+16:33:12.4	−1033.21	−283.33	8.68	Gl 880	BD+15 4733	G067−037		HHH
143.45A	17:18:57.18	−34:59:23.3	1149.24	−90.80	5.91	Gl 667A	CD−3411626			HHH
143.45B					6.27	Gl 667B			5.0	HHY
143.45C					10.24	Gl 667C			34.0	HHC
141.95	20:53:19.79	+62:09:15.8	1.08	−774.24	8.55	Gl 809	BD+61 2068	G231−019		HHH
138.72A	02:36:04.89	+06:53:12.7	1806.27	1442.50	5.79	Gl 105A	BD+06 398	G073−070A		HHH
138.72B	02:36:14.20	+06:52:06.0	1806.27	1442.50	5.82	Gl 105B		G073−071	1588.0	HGY
138.72C	02:36:04.89	+06:53:12.7	1806.27	1442.50		Gl 105C	BD+06 398B	G073−070B	28.8	HH
138.30	23:35:14.37	−02:24:12.6	789.1	−846.2	14.69	GJ 1286		G157−077		YYY
138.29	10:28:55.55	+00:50:27.6	−602.32	−731.87	9.65	Gl 393	BD+01 2447	G055−024		HHH
137.84A	17:09:31.54	+43:40:52.9	333.92	−278.02	11.77	2708A		G203−047A		HHH
137.84B						2708B		G203−047B	3.0	HH
137.50	18:19:02.56	+66:11:06.1	470.2	−408.7	13.46	2897		G258−033		YYY
135.30A	00:24:41.30	−27:08:52.8	−53.5	611.7	15.42	GJ 2005A				YYY
135.30B						GJ 2005B			7.39	YY
135.30C						GJ 2005C			14.80	YY
134.40	22:23:07.54	−17:37:01.1	291.4	−721.3	13.25	3517				YYY
134.04	00:48:22.98	+05:16:50.2	758.04	−1141.22	5.74	Gl 33	BD+04 123			HHH
133.91	01:42:29.76	+20:16:06.6	−302.12	−677.40	5.24	Gl 68	BD+19 279			HHH
132.60	18:07:30.80	−15:58:14.2	−563.1	−351.9	13.64	GJ 1224		G154−044		YYY
132.42	02:44:15.51	+25:31:24.1	864.77	−367.17	10.55	Gl 109		G036−031		HHH
132.40A	01:08:16.39	+54:55:13.2	3421.44	−1599.27	5.17	Gl 53A	BD+54 223			HHH
132.40B					11.	Gl 53B			4.8	HHC

TABLE 4.1. THE 8 PC SAMPLE (CONT.)

Parallax	Position (J2000.00)		μ (mas)		V	CNS3	Durch.	Other	SMA	Source
(mas)	RA (^{h} ^{m} ^{s})	Dec. ($^\circ$ $'$ $''$)	RA	Dec.	(^{m})	Name	No.	Name	(AU)	Code
132.10	06:01:11.30	+59:35:00.2	−144.3	−818.4	11.71	998		G192−013		YYY
131.12	13:29:59.79	+10:22:37.8	1128.00	−1074.30	9.05	Gl 514	BD+11 2576	G063−034		HHH
130.94	22:56:24.05	−31:33:56.0	330.53	−159.86	6.48	Gl 879	CD−3217321			HHH
130.08	22:57:39.05	−29:37:20.1	329.22	−164.22	1.17	Gl 881	CD−3019370			HHH
129.54	17:25:45.23	+02:06:41.1	−580.47	−1184.81	7.54	Gl 673	BD+02 3312	G019−024		HHH
129.40A	05:02:28.42	−21:15:23.9	−141.55	−221.74	8.31	Gl 185 A	BD-21 1051			YHH
129.40B						Gl 185 B			9.5	YH
128.93	18:36:56.34	+38:47:01.3	201.02	287.46	0.03	Gl 721	BD+38 3238			HHH
128.80	06:59:32.00	+19:19:55.4	835.4	−895.9	14.83	GJ 1093		G109−035		YYY
128.28	18:05:07.58	−03:01:52.7	570.14	−332.59	9.37	Gl 701	BD−03 4233	G020−022		HHH
127.99	10:12:17.67	−03:44:44.4	−152.93	−242.90	9.26	Gl 382	BD−03 2870	G053−029		HHH
126.00	13:31:46.70	+29:16:36.0	−227.7	−159.5	11.95	2128		G165−008		GCC
125.62	20:30:32.05	+65:26:58.4	443.25	284.06	10.54	Gl 793		G262−015		HHH
125.00	05:56:23.69	+05:20:46.9	−479.4	−940.9	14.11	GJ 1087		G099−047		YYY

Notes to Table 4.1

The coordinates are given in the J2000.00 equinox and epoch, meaning that they include the proper motion and precession. Source Codes: G: Gizis (1997), C: CNS3, H: Hipparcos, Y: Yale. The three characters correspond to parallax, position and V band magnitude respectively and are meant to indicate where the listed value comes from.
SMA means semi−major axis and is derived from the projected separation if the companion is visibly detected or the radial velocity orbital solution (Reid and Gizis 1997). Positions for companions are only given if grossly different from the primary star position or if needed for identification purposes (i.e., to establish which star the companion is closest to in a multiple star system).

4.2.2 Completeness of the 8 pc Catalog

It is important before describing the observations we undertook to estimate how complete our catalog of star systems within 8 pc is.

The simplest way to assess this involves extrapolating the number of stars within 5 pc to the volume of the 8 pc sample. This sort of analysis was conducted by Henry et al. (1997). In their estimation, the CNS3 is complete for stars with $M_V < 11$ all the way out to 10 pc, although the majority of the incompleteness is in the far-less-studied Southern sky ($\delta < -35°$). Their computation involves taking the densities of stars of various absolute magnitudes in the 5 pc volume in the CNS3 (widely used as a benchmark for complete stellar samples) and multiplying by the ratio of the volumes due to increasing the radius of the sample. The 5 pc sample in the CNS3 contains 53 stars with $\delta > -35°$, so we would expect about 217 stars in the 8 pc sample. Considering the fact that we assemble here 163 stars, and that the Poisson error on these numbers is large (53 ± 7, and 217 ± 14), this implies that our catalog is complete to approximately 75% (assuming the stellar densities within 5 pc are correct). Any incompleteness is most likely among the very faintest stars (white dwarfs and late M dwarfs), because they are less likely to have been measured and studied in depth in large scale stellar surveys. In addition, many of the nearby stars were found through large-scale proper motion surveys. Some stars may therefore be missing from the nearby star sample because they have very small proper motions.

Reid and Gizis (1997) argue that the CNS3 is complete to $M_V < 14$ for $\delta > -30°$ within 10 pc. $M_V = 14$ corresponds to the spectral type M4.5. These considerations permit us to conclude that our sample is complete at least to the spectral type M5, and possibly even fainter. We conservatively claim that the sample is 75% complete and believe that the missing stars are all later than M5 in spectral type.

4.3 Observations

In pursuit of our goal to image and study brown dwarf companions of stars in our sample, we conducted observations of 107 of the 111 star systems (96% of the sample) in optical and near infrared wavelengths. The observations employed two different imaging instruments, the AOC attached to the Palomar 60" Telescope and the Cassegrain Infrared Camera fitted to the Palomar 200" Hale Telescope.

4.3.1 Common Proper Motion

We imaged each of the stars at least twice in order to discern faint objects within 30″ of each star which display the same proper motion as the stars themselves. Our decision to use the common proper motion criterion was motivated by the plethora of models of brown dwarfs at the time the survey began. These models painted often conflicting depictions of the colors or spectra that brown dwarfs ought to exhibit. (See Burrows and Liebert 1993 for a comprehensive review of the state of these models at about the time that our survey began.) We decided that instead of relying upon one of the models and designing a survey that looked for colors that that model predicted, we would use a more basic physical argument for finding cool companions. In contrast, numerous other surveys examined large fields of view and excluded objects as possible brown dwarfs based on their infrared colors. (See Hawkins 1998 for an up-to-date review of these sorts of searches.) Unfortunately, most of these were unsuccessful partly because the color criteria excluded certain types of brown dwarfs, such as the low-temperature variety.

The technique we employ here is explained through example in Fig. 4.1. This figure shows four z band coronagraphic images of the star Gliese 105A (138.72AC). The first two images are magnified portions of the region immediately around the star. These two images were taken a year apart and show a faint second object

with the same proper motion. The star moves $2''.2$ yr^{-1} permitting extremely easy discrimination between common proper motion companions and background stars. This is demonstrated in the bottom two images, which are larger portions of the same images. In these two, one can clearly see that the two stars to the West do not share the proper motion of the star. We reported this common proper motion companion in the paper by Golimowski et al. (1995).

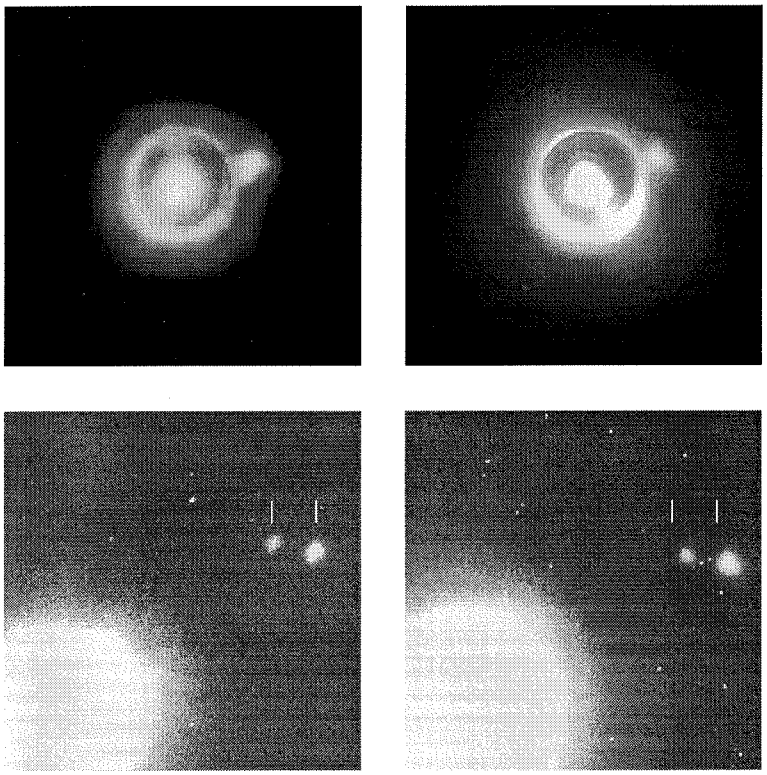

Figure 4.1 Images of Gliese 105AC (138.72AC). The top two panels are magnified portions of the lower panels. These images were taken in the z band in October 1994 (left) and October 1995 (right). North is up and East is to the left. The star has moved over $2''.2$ between these two epochs and yet the fainter object maintains the same offset from the star in the top panels. This makes it a common proper motion companion. The seeing was better than $0''.6$ in the images, and the astigmatism (which has since been fixed) of the 60" telescope is apparent. The pixel size is $0''.117$. The top images measure $16''$ on a side. The lower images are $40''$ on a side. The two white tick marks in the lower left panel serve to mark the positions of the two field stars in 1994. In the lower right panel they are placed in the same location to clearly show that the field stars have moved relative to the central star (which is placed in the same location in the two panels).

The error in the measurement of the centroid of a stellar image on a CCD is approximately the angular size of the image divided by the signal-to-noise ratio. (There is a correction factor if the pixel size is much smaller than the image size, but this amounts to a 0.6% correction in this survey. This is because we require every star to be imaged in 1″ seeing or better.) In our survey we combine several measurements of each star to improve upon this standard astrometric limit, by combining n measurements. The effective signal-to-noise ratio of the combined measurement is improved by the factor $n^{-1/2}$. At each epoch we have at least two images. With at least two epochs per star, the value of n for most stars is greater than four. The average value of n for all the stars in the survey is eight. This means that the average centroid error for sources detected at the 5 σ level is 0.″07. All of the stars in our sample exhibit proper motions greater than 0.″07 yr^{-1}. Thus we are capable of discerning background objects from common proper motion companions with these observations. In most cases, the proper motions are actually substantially larger than 0.″07 yr^{-1} and the requirement on the astrometric errors is far less stringent than 0.″07.

4.3.2 Optical Observations

Optical coronagraphic images of the survey stars were obtained during 25 separate observing runs on the Palomar 60" Telescope between September 1992 and April 1999. These images were obtained with a Tektronix 1024 × 1024 pixel CCD camera binned in a 2 × 2 pattern (0.″117 pixel^{-1}) attached to the back-end of the AOC. This device consists of a standard Lyot coronagraph (Lyot 1939) fitted behind a tip-tilt mirror which uses the occulted star as a guide star. The tip-tilt correction provides substantial gains in image resolution on the Palomar 60" Telescope because, there, the majority of the atmospheric disruption of the stellar wavefront resides in tip-tilt energy or, equivalently, image motion. We routinely obtained images with resolutions of 0.″7 and on six of the observing runs we obtained images at 0.″45 resolution. The

images were taken through the Gunn r and z filters, with additional images taken through the i band if a companion were found. In almost all cases the CCD was exposed for 1000 s. However, for the stars whose magnitude is $V < 6$, we were forced to take shorter exposures and to sum these to produce a final image with a 1000 s exposure time. The AOC on the 60" telescope was incapable of guiding on stars fainter than $V \sim 13.5$. For this reason we were unable to observe 13 of the sample stars in the optical. We had to rely upon the infrared observations of these stars to discern companions. These stars are indicated by the words "too faint" in Table 4.2.

The AOC's focal plane coronagraphic stop is slightly transparent. This permits an accurate measurement of the position of the star in the CCD image. (Without the transparent stop, pinpointing the star would have been impossible because the pupil plane stop eliminates the diffraction spikes of the star.) We used coronagraphic stops $4\farcs2$ in diameter for most observations, except in the case of the brightest stars where an $8\farcs4$ diameter stop was used. We claim no sensitivity to faint companions under the stops. However, equal brightness binaries were sometimes resolved under the masks (e.g., Fig. 4.10).

If a set of r and z band images failed to reveal any sources in the field of view other than the star, we would not reobserve the star. Table 4.2 lists the dates of all the observations of each star in the sample. In all cases we attempted to acquire images with seeing better than $1\farcs0$. Seeing worse than this strongly degraded our sensitivity (§4.4). In all cases we were able to obtain such images at least once for each of the stars observed, and at least twice for those stars with possible companions (i.e., with any other point source in the field of view).

Data reduction involved the subtraction of a bias frame from each of the science images, division by a flat field image obtained using the 60" dome and a flat field lamp, and the removal of cosmic rays (easy to identify in these images because of the very small plate scale). The images were then inspected by eye. In most cases

this was sufficient to ascertain whether common proper motion companions were present. However, for the stars whose proper motions are small, additional work was required to distinguish field stars from common proper motion objects. Because the central occulting mask of the coronagraph was somewhat transparent, we were able to centroid the light of the survey star to ascertain its position in the images. Simple centroiding of the other point sources yielded pixel locations as well. These were converted into angular separations in arcseconds by using the observing run's plate scale and detector orientation. These were determined with the astrometric calibrator fields as explained in §4.3.4.

4.3.3 Infrared Observations

Direct infrared images of each of the sample stars were obtained with the D78 Cassegrain Infrared Camera on the Palomar 200" Telescope during 15 observing runs between May 1995 and March 1999. We allowed the stars to saturate the central part of the 256 × 256 InSb array ($0\farcs125$ pixel^{-1}). The field of view in these images was approximately $32\farcs$ The position of the star can be determined to sub-pixel accuracy by fitting lines to the diffraction spikes and ascertaining their intersection. Our imaging technique entailed the use of the J and K filters with two types of exposure through each filter. The first type involved a total of five coadds of 1 s exposure time. These images were meant to reveal close binaries with a dynamic range on the order of five to eight magnitudes (depending on the seeing). The second type of exposure used five coadds of 10 s. These exposures were designed to detect fainter companions outside of a $3''$ radius from the star. In each case a sky frame was taken immediately after the data image was acquired. The sky frame was taken in the same manner as the data image, but with the telescope pointed $50''$ to the N or E. In some cases we changed this distance because of the presence of a rather bright source in the sky frame.

As with the optical observations, if no objects other than the star appeared, we would not observe the star a second time. In addition the seeing requirement of $\leq 1''.0$ for the infrared observations was identical to that for the optical images (see above).

The data reduction for the infrared images involved the subtraction of the sky frame from the "on-source" frame. Subsequent division by a flat field (acquired from the twilight sky during each observing run) permitted the more detailed examination of the images. As with the optical data, usually visual inspection of the images was enough to discern common proper motion companions. In cases where more accurate measurements were necessary, we needed to pinpoint the location of the survey star. This could not be done through centroiding because all of the stars's images were saturated. Fortunately, we could use the diffraction spikes in the infrared images (absent in the optical images because of the pupil plane apodizing mask in the coronagraph). By fitting the unsaturated parts of the two diffraction spikes with perpendicular lines, we were able to localize the star with an accuracy of better than a third of a pixel. (We confirmed this through short unsaturated exposures of some of the fainter stars in the sample while the telescope was guided on a field star. The low frequency tip-tilt system on the f/70 secondary mirror of the 200" telescope guides with an accuracy of better than $0''.03$ over 20 min.) This stellar position on the detector was then used, along with centroids of the light from putative companions, to compute offsets between the objects. These were converted into angular offsets in arcseconds by using the plate scale as described in §4.3.4.

4.3.4 Astrometric Calibration

In order to obtain the highly accurate astrometric measurements of the offsets between the central star and its putative companions, we made observations of calibration fields at each observing run. These fields contained six to ten stars whose relative positions are extremely accurately known. We used these fields to determine that

TABLE 4.2. LIST OF OBSERVATIONS OF THE 8 PC SAMPLE

Para. (mas)	V (^{m})	Dates of AOC Observations	Dates of Infrared Observations
549.01	9.54	9/92; 4/94	8/96; 7/97
419.10	13.46	2/97; 4/97	12/96
392.40	7.49	4/94	12/96
379.21	-1.44	11/96; 1/98	10/96
373.70	12.52	10/94; 10/95b	8/96
336.48	10.37	6/95; 8/95; 10/95a; 6/96	8/96; 7/97
316.00	12.27	9/92; 8/95; 10/95a; 10/95b; 9/97	8/96; 7/97
310.75	3.72	10/95b	8/96; 11/97
299.58	11.12	1/93; 2/96; 4/97	12/96
289.50	12.32	6/95; 8/95; 9/97	9/95; 8/96
287.13	5.20	10/95b; 8/96	8/96
285.93	0.40	2/95; 11/96; 1/98	11/97
280.28	8.94	6/92; 8/96; 4/97	8/96; 7/97
280.27	8.09	10/95b; 9/97	8/96; 12/96; 8/97;
275.80	14.81	too faint	11/95; 12/96
274.17	3.49	10/95b; 11/96	11/95; 8/96; 8/97
269.05	12.10	8/95; 11/96; 9/97	9/95; 8/96;
263.26	9.84	2/95; 2/97	12/96; 11/97
249.52	9.59	10/95b; 8/96	11/95; 7/97
242.89	11.12	2/95; 12/95; 11/96	11/95; 10/96; 12/96
235.24	11.72		3/99
234.51	10.10	4/94; 4/97; 6/97	8/96; 7/97
227.90	12.44	1/93; 2/96; 4/97	12/96
227.45	12.16		3/99
226.95	12.37	9/92; 8/95	8/96; 12/96
224.80	12.26	8/95; 10/95a; 10/95b; 9/97	9/95; 11/95; 8/96; 10/96
224.00	10.89	2/95; 11/95; 11/96; 1/98; 3/98	12/96; 3/98; 12/98
221.80	12.07		3/99
220.85	9.15	6/95; 8/95; 9/97	8/96; 7/97
220.30	15.60	too faint	2/96; 12/96
220.20	13.41	9/92; 8/97	11/95; 8/96; 7/97; 8/97
213.00	13.74	9/97	10/96
212.69	10.16	10/93; 10/94; 8/95; 9/97	8/96; 7/97
206.94	8.82	4/94	2/96; 12/96
205.22	6.60	1/93; 4/97	2/96;
204.60	9.40	4/94; 2/95; 12/95	12/95; 12/96
202.69	11.39		3/99
198.24	4.43	2/96; 11/96; 9/97	10/96; 12/96;
198.00	10.06		
196.62	4.03	8/96; 8/97; 9/97	8/96

TABLE 4.2. (CONT.) LIST OF OBSERVATIONS OF THE 8 PC SAMPLE

Para. (mas)	V (^{m})	Dates of AOC Observations	Dates of Infrared Observations
194.44	0.76	10/95b	8/96
191.86	11.49	11/96; 9/97	12/96; 8/97
191.20	14.06	too faint	12/96; 3/98
186.20	11.33	12/95; 11/96; 1/98	10/96; 12/96; 11/97
185.48	10.80	2/97	12/96
184.13	8.46	1/93; 4/94; 4/97	12/96; 7/97
182.15	11.41		
181.36	10.82	11/96; 9/97	10/96; 12/96
181.32	9.89	11/96; 1/98	10/96
177.46	11.64	2/97; 4/97; 1/98	12/96
175.72	7.97	11/96; 1/98	12/96
174.23	9.02	8/96; 4/97	8/96; 7/97
173.41	4.67	8/96	8/96
173.19	8.15	10/94; 2/95; 10/95a	9/95; 11/95; 10/96; 12/96
172.78	11.56	11/96; 1/98	10/96; 12/96; 11/97
170.26	9.12	9/92; 6/96	8/96; 7/97
169.90	12.10	11/96; 1/98	12/96; 11/97
169.32	5.72	4/97	7/97
168.59	11.19	2/95; 11/95; 11/96; 1/98	12/95; 12/96; 11/97
167.99	3.46	11/96; 8/97	10/96; 8/97
167.51	8.98	9/92; 10/93; 11/96; 9/97	8/96; 8/97
167.08	4.33	4/97; 9/97	7/97; 6/98
164.70	14.15	too faint	3/98
163.51	11.32	6/93; 4/97	7/97
163.00	12.1	11/96	10/96; 12/96
162.50	5.85	4/97	12/96
162.00	13.22	1/98	12/95; 12/96
161.77	11.39		3/99
161.59	7.64	11/96	12/96
160.06	10.05	10/95a; 9/97	11/95; 8/96; 7/97
159.52	10.57	6/93; 4/94	7/97; 3/98
158.17	9.31	4/94; 9/97	8/96; 7/97
157.24	11.65	10/94; 11/95	11/95; 10/96
156.30	17.05	too faint	3/98; 6/98
156.00	12.58	4/97; 6/97	12/96
155.00	14.45	too faint	10/96; 12/96; 3/98
153.24	5.57	8/96; 11/96; 8/97	8/96; 7/97
152.90	13.79	4/97; 1/98	2/96; 12/96
151.93	10.13	4/97	7/97
150.96	10.03	2/97; 4/97; 1/98	12/96

TABLE 4.2. (CONT.) LIST OF OBSERVATIONS OF THE 8 PC SAMPLE

Para. (mas)	V (^{m})	Dates of AOC Observations	Dates of Infrared Observations
149.26	4.54	4/97	7/97
148.29	10.33	10/94; 8/96	8/96
146.30	12.83	11/96; 4/97	12/96; 11/97; 3/98
145.27	8.68	11/96; 9/97; 1/98	10/96; 7/97
143.45	5.91	8/97; 9/97	7/97; 6/98
141.95	8.55	6/93; 6/96; 11/96	8/96; 7/97
138.72	5.79	10/93; 10/94; 8/95; 10/95a	9/95; 10/96; 12/96; 8/97; 12/98
138.30	14.69	too faint	10/96; 10/97
138.29	9.65	4/94; 2/95; 11/96; 4/97; 1/98; 3/98	12/96
137.84	11.77		7/97
137.50	13.46	too faint	7/97
135.30	15.42	too faint	9/95; 8/96
134.40	13.25	9/97	7/97
134.04	5.74	10/93; 11/96	8/96; 12/96; 8/97
133.91	5.24	10/93; 8/96; 9/97	8/96
132.60	13.64	too faint	7/97; 6/98
132.42	10.55	10/95b; 2/97	8/96
132.40	5.17	8/96; 11/96; 8/97	12/96
132.10	11.71	11/96; 1/98	10/96; 12/96; 11/97
131.12	9.05	4/97	12/96
130.94	6.48	8/97	10/96; 7/97
130.08	1.17	11/96; 9/97	10/96
129.54	7.54	4/94; 4/97	8/96; 7/97
129.40	8.31	11/96; 1/98	10/96; 12/96; 11/97; 3/98; 3/99
128.93	0.03	9/97	7/97
128.80	14.83	too faint	10/96; 12/96; 11/97
128.28	9.37	8/97; 9/97	7/97; 3/98; 6/98
127.99	9.26		
126.00	11.95	6/95; 4/97; 6/97	2/96; 12/96; 7/97
125.62	10.54		3/99
125.00	14.11	too faint	10/96; 11/97

the astrometric distortion on the face of the CCD chip used in the AOC observations is smaller than 0.″01 over the whole chip. In the infrared observations the distortion is almost a full pixel near the edges of the array. This distortion is constant with time. Because we centered the stars in the same position on the infrared array at each observing run, the comparison of astrometric measurements is valid, despite this image distortion. We did not use relative astrometry measured on the infrared images in conjunction with other measurements made on the AOC images. For these reasons we applied no astrometric distortion correction in our measurements of relative offsets between stars.

For all of the infrared observing runs, the data were taken with the Cassegrain ring angle precisely set to place North up and East left on the array. This prevented complications in astrometric measurements that would arise from using arbitrary position angles of the array with respect to the cardinal directions.

For every AOC observing run we would observe whichever of the three astrometric calibration fields (listed in Tables 4.3, 4.4 and 4.5) was visible. In each case we would place the star shown in the center of each of Figs. 4.2, 4.3 and 4.4 in the center of the field of view. This star was used for guiding and rapid tip-tilt image motion compensation. From the images—500 s r band exposures—we were able to determine precisely the plate scale and the rotation of the CCD on the plane of the sky. We found that the plate scale was extremely stable in both instruments (despite the fact that the CCD camera used on the AOC was taken apart and reassembled twice between the starting and ending dates of the survey). The accurate positions of the stars in these fields are from Cudworth (1979) for M5, Cudworth (1976) for M15 and McCaughrean and Stauffer (1994) for the Trapezium.

Figs. 4.2, 4.3 and 4.4 show each of the three calibration fields and Tables 4.3, 4.4 and 4.5 give the positions of the stars used for the astrometric calibration.

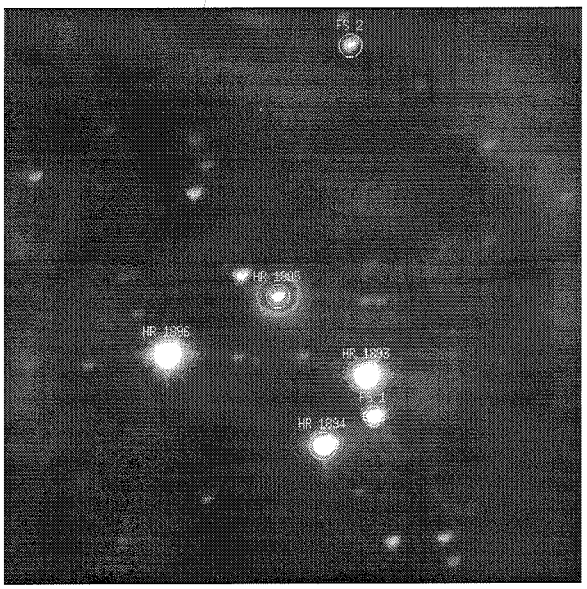

Figure 4.2 The Trapezium astrometric calibration field. The stars marked with circles and numbers are the stars listed in Table 4.3 and are the ones used to conduct the calibration. The image measures one arcminute on a side. North is down and East left.

TABLE 4.3. TRAPEZIUM CALIBRATION FIELD

Star	Position (J2000.00)	
Name	RA (^{h} ^{m} ^{s})	Dec ($^\circ$ $'$ $''$)
HR 1895	05:35:16.462	−05:23:23.03
HR 1893	05:35:15.821	−05:23:14.45
HR 1894	05:35:16.129	−05:23:06.96
HR 1896	05:35:17.248	−05:23:16.69
FS 1	05:35:15.768	−05:23:10.06
FS 2	05:35:15.953	−05:23:49.99

Notes: HR 1895 is the central, occulted star in the image. Position data are from McCaughrean and Stauffer (1994).

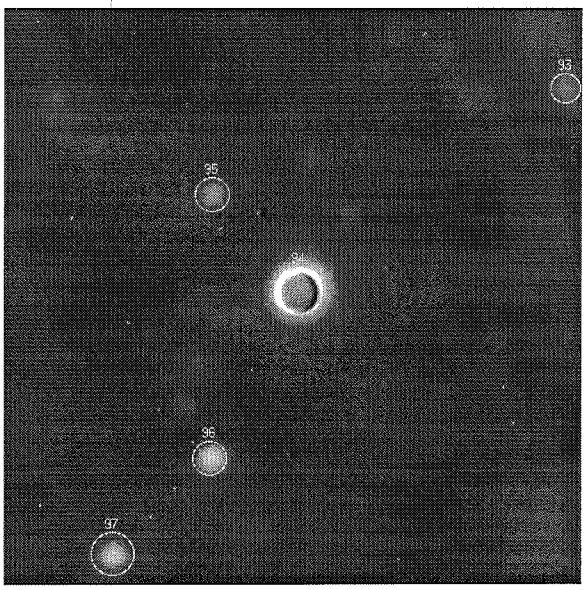

Figure 4.3 The M5 astrometric calibration field. The stars marked with circles and numbers are the stars listed in Table 4.4 and are the ones used to conduct the calibration. The images measure one arcminute on a side. North is left and East down.

TABLE 4.4. M5 CALIBRATION FIELD

Star	Position (B1950.00)	
Name	RA (^{h} ^{m} ^{s})	Dec ($^\circ$ $'$ $''$)
93	15:16:01.70	+02:11:31.7
94	15:16:03.14	+02:12:00.0
95	15:16:02.46	+02:12:09.6
96	15:16:04.36	+02:12:09.7
97	15:16:05.05	+02:12:20.3

Notes: Positions and numbering scheme are from Cudworth (1979). Star 93 is occulted and centered in the image.

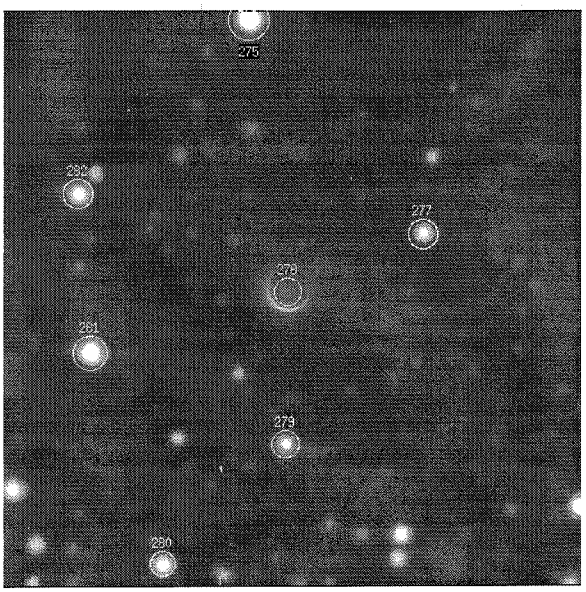

Figure 4.4 The M15 astrometric calibration field. The stars marked with circles and numbers are the stars listed in Table 4.5 and are the ones used to conduct the calibration. The image measures one arcminute on a side. North is left and East down.

TABLE 4.5. M15 CALIBRATION FIELD

Star	Position (B1950.00)	
Name	RA (^{h} ^{m} ^{s})	Dec ($^\circ$ $'$ $''$)
275	21:27:22.82	+11:55:33.6
277	21:27:24.40	+11:55:15.3
278	21:27:24.83	+11:55:30.2
279	21:27:25.93	+11:55:30.0
280	21:27:26.80	+11:55:43.5
281	21:27:25.24	+11:55:51.0
282	21:27:24.09	+11:55:52.1

Notes: Positions and numbering scheme are from Cudworth (1976). Star 278 is occulted and centered in the image.

4.4 Detection Limits for Each Star

Typically in imaging surveys assessing the sensitivity of the images and the survey as a whole simply involves a determination of the limiting magnitudes of the images. However, in this case the problem is somewhat more complicated.

The presence of the bright star in our images means that over much of the field of view the sensitivity is limited by the light of the star and not the sky background (or read noise as was the case for speckle interferometric surveys of these stars; Henry and McCarthy 1990). However, this survey extends into uncharted parameter space because the coronagraphic technique suppresses a substantial portion of the starlight. The image shown in Fig. 4.5 illustrates this with the Gliese 105 AC system.

We have measured the detection limits for each star in the survey as a function of angular separation from the central star. To do this we took the images of each star with $1''.0$ seeing or better—the acquisition of such images was a survey requirement (§4.3)—and inserted artificial point sources at an array of separations from the star. These artificial point sources were generated with appropriate Poisson noise statistics and angular sizes to match the seeing conditions. The magnitudes of these artificial stars (calibrated to the photometric standards used during the relevant observing run) were set so that each artificial star was just visible to the eye. From these magnitudes, the sensitivity curve is derived. An example of this is shown in Fig. 4.6.

From this procedure, we had a measurement of the faintest source visible at a set of about 10 to 15 radii from the star. Using a spline interpolation between these points, we derive the magnitude limit for r, z and J as a function of radius measured from the star. In each band we have individual curves of this nature for each central star in the survey. These curves are summarized in Figs. 4.7, 4.8 and 4.9, where we have displayed representative curves for various star brightnesses in each bandpass.

There are several important effects documented by the curves in Figs. 4.7, 4.8 and

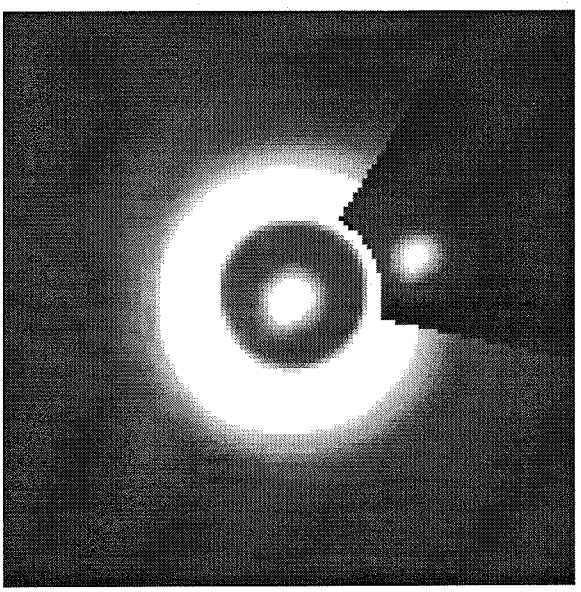

Figure 4.5 Image of Gliese 105AC. This image, taken through the i band in October 1993, shows only the inner $14\farcs5 \times 14\farcs5$ piece of the larger AOC image. North is up and East to the left. The occulting mask (somewhat transparent) is $4\farcs3$ in diameter and reveals the core of the star's seeing disk. Outside the occulted region, part of the seeing disk has been modeled and subtracted to make the companion stand out better. This is unnecessary in order to see the companion, however, as shown in Fig. 4.1. This image demonstrates the huge dynamic range possible with the AOC. Only $3\farcs3$ from a star with $i = 7.03^m$ we detected, with ease, a very low-mass star with $i = 12.6^m$ with a signal-to-noise ratio of several thousand. We could have detected a companion at this separation in this image as faint as 18.5^m, indicating a dynamic range of 11.5^m at $3\farcs3$. (From Golimowksi et al. 1995.)

4.9. The most obvious is that the z band imaging is the most sensitive, achieving a maximum dynamic range of 15.5 magnitudes at $10''$, while, in addition, even the brightest companions can be imaged inside the $5''$ radius. In comparison, the J band has no sensitivity at the $5''$ radius for the bright stars and only achieves a maximum dynamic range of 13 magnitudes. What is even more important is the large, slowly-eroding wing of the point spread function in the J band. The r and z bands do not have nearly as much of this broad wing primarily because of the pupil-plane stop in the coronagraph. This stop is designed specifically to depress the wings of the stellar point spread function.

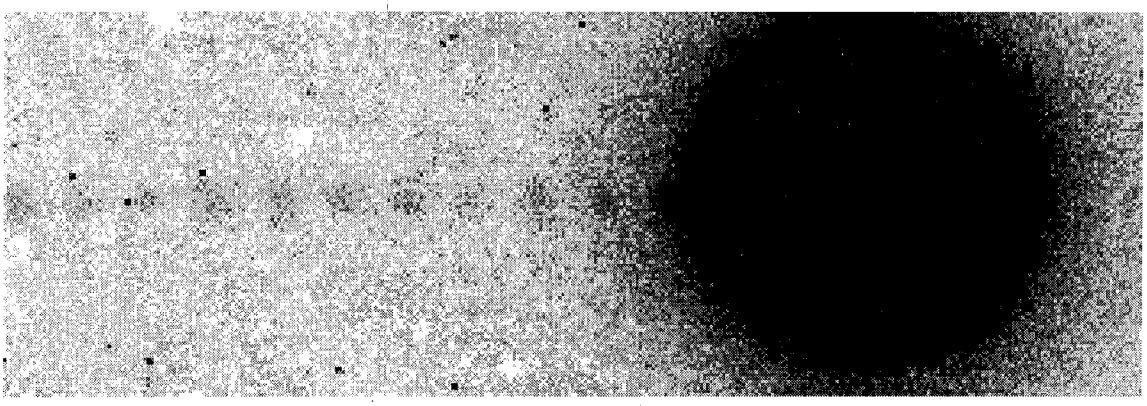

Figure 4.6 Example of the sensitivity curve determination technique. The images shown are part of a z band coronagraphic image of 998 (132.10). The artificial point sources are visible to the left of the star and are placed at regular intervals of 20 pixels. The grayscale stretch shows the lowest light levels, permitting visibility of the large-separation artificial sources while excluding the sources close to the star. The image measures approximately $40'' \times 10''$. The sensitivity curve derived from this image is the lowest one in Fig. 4.8.

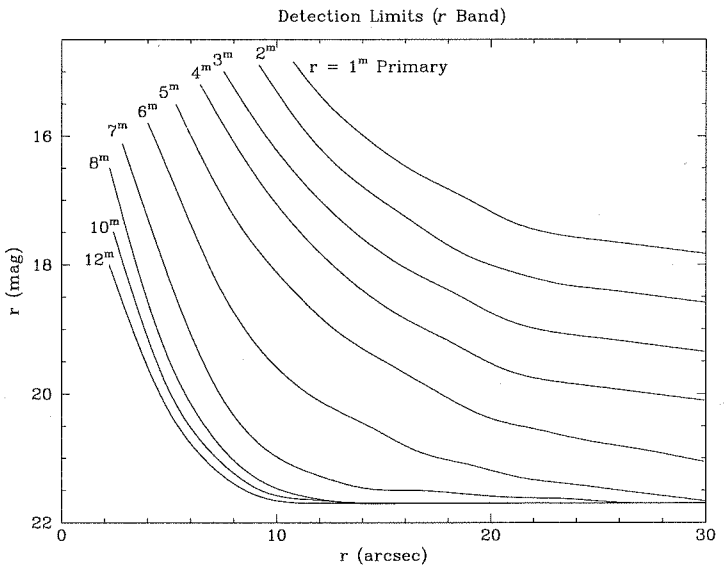

Figure 4.7 Sensitivity curves for r band showing magnitude limit as a function of separation (in arcseconds) from the star for star magnitudes ranging from 1^m to 12^m.

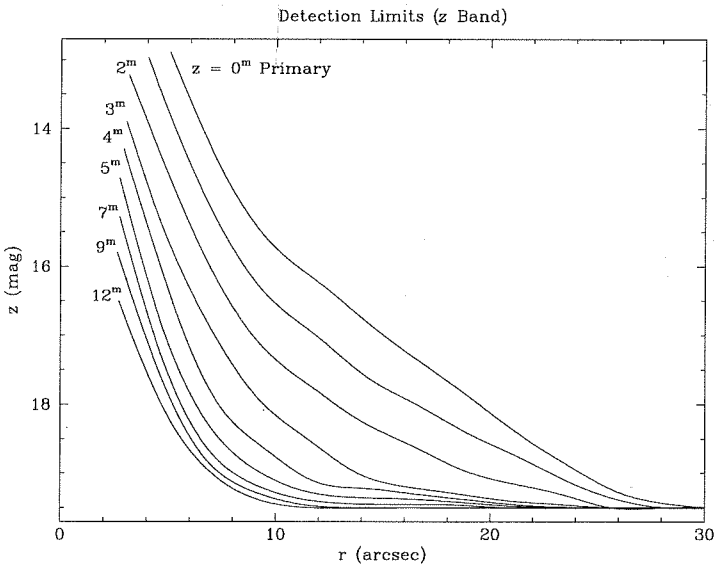

Figure 4.8 Sensitivity curves for z band showing magnitude limit as a function of separation (in arcseconds) from the star for star magnitudes ranging from 0^m to 12^m.

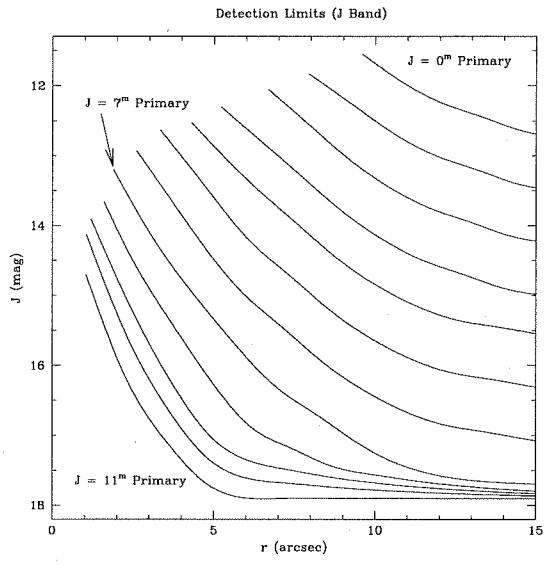

Figure 4.9 Sensitivity curves for J band showing magnitude limit as a function of separation (in arcseconds) from the star for star magnitudes ranging from 0^m to 11^m.

4.5 Detection Limits for the Survey

From the observational point of view, the curves in Figs. 4.7, 4.8 and 4.9 are the ultimate measure of the sensitivity of our survey. These curves parameterize the sensitivity for every star in the sample. However, it is of paramount importance to convert the information in Figs. 4.7, 4.8 and 4.9 into statements about the survey as a whole and in terms of physical, not observational, parameters. For example, can we safely claim with this data that for all the stars within 8 pc we would have detected *any* unknown stellar companions in orbits between 3 and 200 AU?

To address this issue, we use the curves found in the previous section to determine the number of surveyed stars for which we could have detected a companion of a given magnitude at a given separation. This information is expressed in terms of the fraction (or percentage) of the total number of stars imaged as a function of magnitude and physical separation in AU. To do this, we systematically went through the catalog of stars. For each star, we took the relevant sensitivity curve, as derived in the previous section, and converted the magnitude scale into absolute magnitudes, using the parallax of the star. We also converted the angular scale into physical separation in AU by dividing by the parallax in arcseconds. Then, we tested whether companions with a set of magnitudes in each band and a set of separations would be visible in our images. By doing this exercise for every star observed, we ended up with a tally of the number of stars, as a function of magnitude and separation, for which the analysis showed that a companion would be visible.

This analysis was done for each of the r, z and J bands. (The K band sensitivity curves are essentially identical to the J band curves so we did not independently conduct this analysis for K band.) The results are shown in Tables 4.6, 4.7 and 4.8.

The drop off in the survey sensitivity at large physical companion separations is due to the varying physical field of view caused by the distribution of parallaxes of

TABLE 4.6. PERCENTAGE OF SURVEY STARS WITH OBSERVATIONS SENSITIVE TO COMPANIONS OF ALL J MAGNITUDES

M_J	Separation (A.U.)									
	2.5	5	10	20	40	80	120	160	200	225
9.9	1	31	97	99	98	60	2	0	0	0
10.9	1	31	97	99	98	60	2	0	0	0
11.9	1	31	97	99	98	60	2	0	0	0
12.9	1	31	97	95	94	59	2	0	0	0
13.9	1	26	81	90	83	59	2	0	0	0
14.9	0	5	46	80	80	56	2	0	0	0
15.9	0	4	28	66	73	48	2	0	0	0
16.9	0	1	5	33	65	45	2	0	0	0
17.9	0	0	0	4	25	15	1	0	0	0
18.9	0	0	0	0	0	0	0	0	0	0

M_J is the absolute magnitude in J band. The line above the 11.9^m entry is meant to demarcate all stars (above the line) from cool brown dwarfs.

TABLE 4.7. PERCENTAGE OF SURVEY STARS WITH OBSERVATIONS SENSITIVE TO COMPANIONS OF ALL z BAND MAGNITUDES

M_z	Separation (A.U.)									
	2.5	5	10	20	40	80	120	160	200	225
11.5	0	1	29	100	100	97	84	60	26	13
12.5	0	1	29	100	100	97	84	60	26	13
13.5	0	1	26	83	99	97	84	60	26	13
14.5	0	1	25	75	99	97	84	60	26	13
15.5	0	1	25	67	98	97	84	60	26	13
16.5	0	0	20	59	92	95	84	60	26	13
17.5	0	0	3	28	83	95	83	60	26	13
18.5	0	0	1	8	67	94	83	59	26	13
19.5	0	0	0	0	9	67	66	52	25	12
20.5	0	0	0	0	0	0	0	0	0	0

M_z is the absolute magnitude in z band. The line below the 14.5^m entry demarcates all stars (above the line) from cool brown dwarfs.

TABLE 4.8. PERCENTAGE OF SURVEY STARS WITH OBSERVATIONS SENSITIVE TO COMPANIONS OF ALL r BAND MAGNITUDES

M_r	Separation (A.U.)									
	2.5	5	10	20	40	80	120	160	200	225
13.7	0	1	29	100	100	97	84	60	26	13
14.7	0	1	29	100	100	97	84	60	26	13
15.7	0	1	29	98	90	95	84	60	26	13
16.7	0	1	27	89	85	95	83	60	26	13
17.7	0	0	20	72	82	93	82	59	25	13
18.7	0	0	6	54	79	87	82	59	25	11
19.7	0	0	5	51	79	80	77	58	25	11
20.7	0	0	0	5	57	77	70	52	25	11
21.7	0	0	0	0	8	58	64	44	17	9
22.7	0	0	0	0	0	0	0	0	0	0

M_r is the absolute magnitude in r band. The line below the 16.7^m entry demarcates all stars (above the line) from brown dwarfs.

the stars in the survey. In the J band there is no sensitivity outside of 120 A.U., for example, because the field of view is $15''$ and the minimum parallax is 125 mas.

In Tables 4.6 through 4.8, we have drawn a horizontal line at the approximate absolute magnitude of a 0.08 $M_\odot$ star. All stellar companions must be brighter than the absolute magnitude indicated by the line. Brown dwarfs can be brighter than this line if they are young, but objects below this line must be brown dwarfs and not stars.

4.6 Sensitivity to Stellar Companions

We now extend the analysis from the previous section. Instead of discussing the survey sensitivity in terms of observational quantities, we relate those quantities to known properties of stars. This allows us to determine the ability of the survey to find stellar companions of the survey stars. A stellar companion at the minimum

mass for hydrogen burning (0.08 $M_\odot$; Burrows et al. 1997) has absolute magnitudes of $M_r = 17.4$, $M_z = 14.9$ and $M_J = 11.5$. These magnitudes are determined by averaging the photometry of several of the objects known to be at the minimum stellar mass (Henry and McCarthy 1993). We now use these measurements to make a single table showing the sensitivity to a minimum mass star in each of the bandpasses. The result is shown in Table 4.9.

TABLE 4.9. PERCENTAGE OF SURVEY STARS WITH OBSERVATIONS IN J, z AND r BAND SENSITIVE TO 0.08 $M_\odot$ STELLAR COMPANIONS

Band	Separation (A.U.)									
	2.5	5	10	20	40	80	120	160	200	225
J	1	31	97	99	98	60	2	0	0	0
z	0	1	25	72	98	97	84	60	26	13
r	0	1	27	89	82	95	83	59	26	13

What this table demonstrates is that the combination of the infrared and optical imaging permits the detection of any stellar companion at separations greater than 10 AU. We note that for the smaller separations, J band is most sensitive. z band is more sensitive than J band at the higher separations. This is primarily due to the drop in coverage at large separations in the J band (where the field of view is only 32″).

Indeed, we have detected six new stellar companions of these stars. These are described below.

4.7 New Companions

In the course of our observations we have discovered or confirmed seven new companions of nearby stars. Three of these stars, originally included in the 8 pc sample have

been removed from the sample because of new and more accurate trigonometric parallaxes. The new companions belong to the following systems: Gliese 105 (138.72), Giclas 089−032 (162.00), Gliese 229 (173.19), Giclas 041-014 (224.00), LP 476−207, LP 771−095 (LTT 1445) and LHS 1885 (Giclas 250−031). Only Gliese 229B is substellar. The last three in the list are no longer part of the 8 pc sample, which means that four of our new companions are in the 8 pc sample. Since Gliese 105AC (Fig. 4.1) and Gliese 229AB have been reported and described in detail elsewhere, we simply refer the reader to Golimowski et al. (1995) for Gliese 105AC and §2 and 3 (Nakajima et al. 1995; Oppenheimer et al. 1995, Matthews et al. 1996, Golimowski et al. 1998 and Oppenheimer et al. 1998) for Gliese 229AB. Below we describe the other companions.

4.7.1 Giclas 089−032 (162.00)

This star, with no trigonometric parallax measurement, is listed in the CNS3 with a photometric parallax of 162.00 mas and a spectral type of M 5. The Palomar survey has resolved the star into a binary of equal magnitude. It was noted as a double source with $0\farcs7$ separation in Henry et al. (1997), but they had no information to determine whether the two components were physically associated. In our coronagraphic images taken in January 1998, we resolve the two components under the semi-transparent focal plane mask. The short infrared images also barely resolve the components. With images taken between December 1995 and January 1998 and the known proper motion of the star, $0\farcs354$ yr^{-1}, we have ascertained that the two components exhibit the same proper motion, and no measurable change in relative offset during this time span. Fig. 4.10 shows several of our images. Our measured separation is $0\farcs73$.

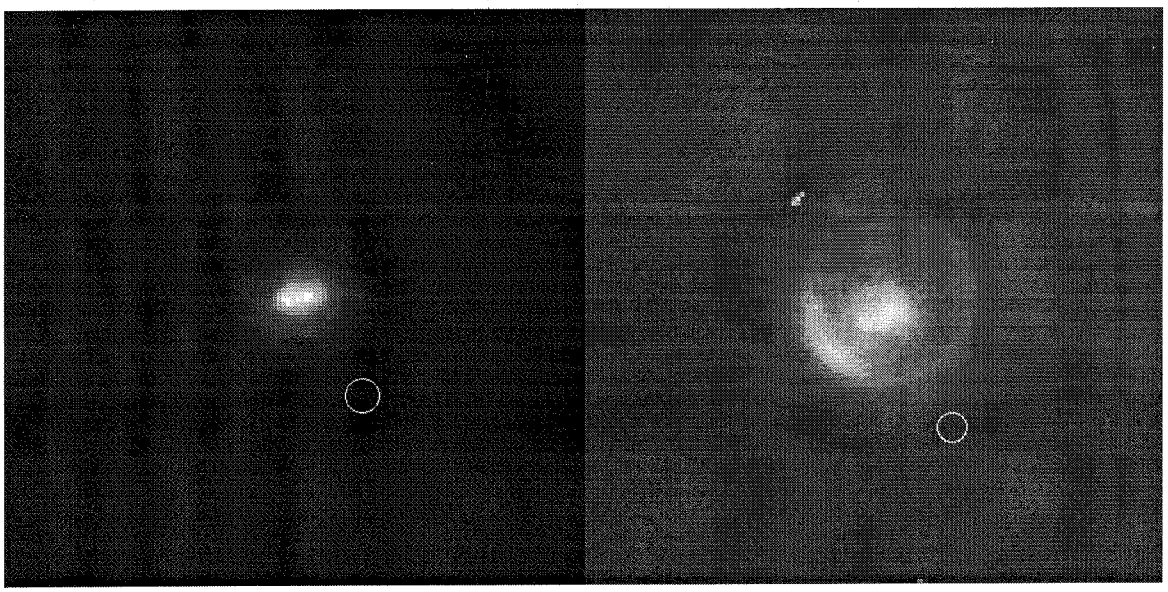

Figure 4.10 Images of Giclas 089−032 (162.00). This star has been resolved into two components. The left image is a 5 s K band image taken in December 1996. The components have a separation of 0.″75, and North is up with East left. The right panel is a 1000 s z band image taken in January 1998. North is 4.2° left of up and E 90° counterclockwise from there. The two components have been resolved through the semi-transparent coronagraphic mask (4.″3 in diameter). Here the components have a measured separation of 0.″71, consistent, within the 0.″05 error bars, with the infrared offset measured 1.1 years earlier. The star has a known proper motion of 0.″354 yr^{-1}. Thus this is a common proper motion pair. The circle in each panel indicates the size of the core of a single star's point spread function.

4.7.2 Giclas 041−014 (224.00)

Giclas 041−014 is a star with a photometric parallax of 224 mas. There is no trigonometric parallax measurement for this star. Reid and Gizis (1997) report that this object has a spectroscopic companion of approximately equal mass. Delfosse et al. (1998b) have determined the orbit of this companion (with a period of 7.6 days). However, Delfosse et al. also claim to have resolved a third component of the system with adaptive optics images. They determine a separation of 0.″62 and a difference of 0.5 magnitudes at K band. This star, which is listed in Table 4.1 as a binary, was included in our survey. We observed it eight times over the duration of this

project. Only two of our observations were capable of resolving this putative companion. Both observations were with the AOC in extremely good seeing conditions where the corrected image size was 0.″45 and 0.″50. We resolved the companion and measured offsets of 0.″47 in November 1996 and marginally resolved the companion at 0.″52 in March 1998. (The standard errors discussed in §4.3.4 apply to the November 1996 measurement. However, since we only marginally resolved the two components in March 1998, we suggest that the error on that measurement is ± 0.″1.) Despite the marginal resolution in March 1998, the expected change in relative offset of this star over this period of time is about 1.″ Thus, if it were a background object, we would have easily measured this large change in the offset. The magnitude difference in z band is approximately 1.6. Fig. 4.11 shows the November 1996 z and the March 1998 r band images. In the case of this star (all three components of which are included in Table 4.1), there was also a faint field star about 9″ to the NW. This star's relative offset between these epochs changed approximately 1″, consistent with the 0.″459 yr^{-1} proper motion.

4.7.3 LP 476−207

This M 4 star was given a photometric parallax of 142 mas in CNS3. The subsequent Hipparcos measurement of 31.20 mas places it well outside the 8 pc sample. Part of the reason that the photometric parallax is so incorrect must be due to the presence of the companion we have found. Even though this star is no longer in the 8 pc sample, it was in our original catalog, so we observed it. We found a common proper motion companion about 1 magnitude fainter in K band than the primary star. This companion is located 1.″03 from LP 476−207. The two images in Fig. 4.12 show a 5 s K band image from October 1996 and a 1000 s z band image from January 1998. The proper motion of this star is only 0.″0837 yr^{-1}, which is less than 1 pixel yr^{-1} in these images, but the 2.24 yr baseline permits easy identification of this fainter

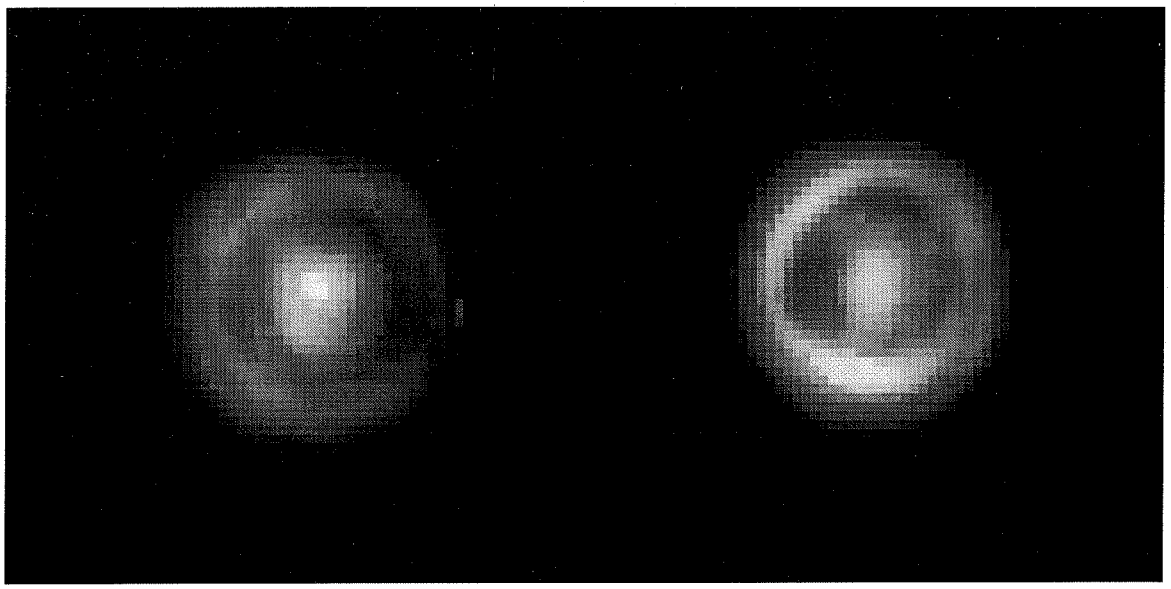

Figure 4.11 Images of Giclas 041−014. This star has been resolved into two components. The left image is a 1000 s z band image taken in November 1996. The components have a separation of $0\farcs47 \pm 0.05$. North is left and East up. The right panel is a 1000 s r band image taken in March 1998. North is left and East is up. The two components have been only marginally resolved here through the semi-transparent coronagraphic mask ($4\farcs3$ in diameter), the edge of which is visible because of the spillover of light from the stars. Here the components have a measured separation of $0\farcs52 \pm 0.1$, consistent, within the error bars, with the offset measured 1.25 years earlier. The star has a known proper motion of $0\farcs459$ yr^{-1}. Thus this is a common proper motion pair.

object as a common proper motion companion. Henry et al. (1997) also identified this star as double, without further information to determine that the two are physically associated. Delfosse et al. (1998b) have confirmed the results above, measuring an offset of $0\farcs97$ and a magnitude difference of 0.9 in the K band. However, because of the single epoch nature of their observation, they were unable to state with certainty that this was a physical companion of the star. Interestingly, they also reported the detection of an unresolved spectroscopic companion of the primary star.

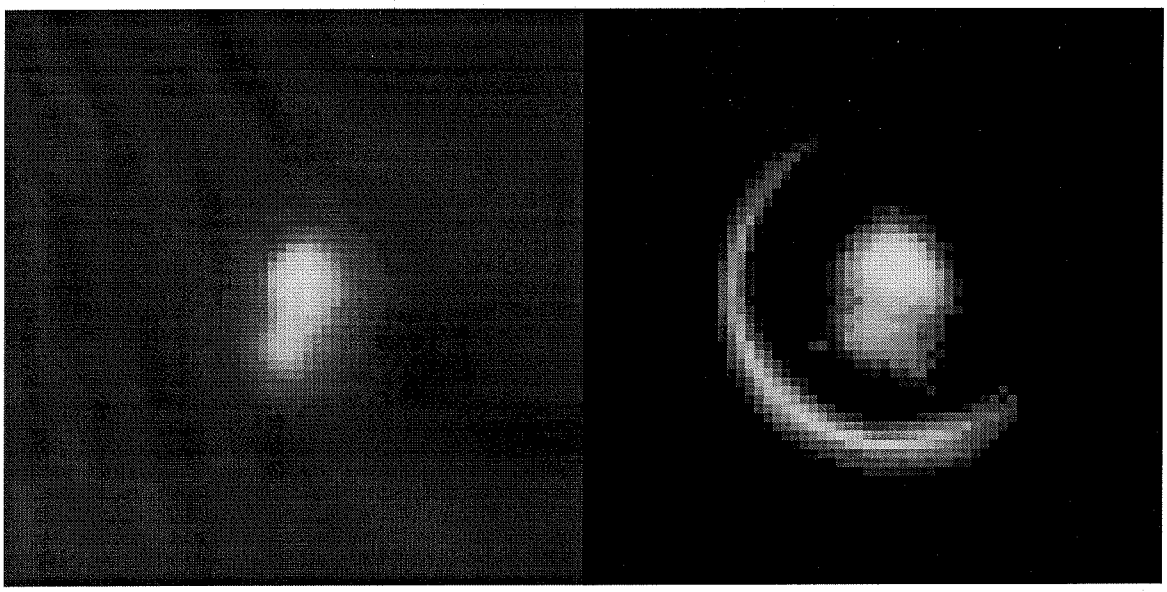

Figure 4.12 Images of LP 476−207. This star has been resolved into two components. The left image is a 5 s K band image taken in October 1996. The components have a separation of 1.″03. North is up and East is left. The right panel is a 1000 s z band image taken in January 1998. North is up and East is left. The two components have been resolved through the semi-transparent coronagraphic mask (4.″3 in diameter), the edge of which is visible because of the spillover of light from the companion. Here the components have a measured separation of 0.″99, consistent, within the 0.″05 error bars, with the infrared offset measured 2.24 years earlier. The star has a known proper motion of 0.″0837 yr^{-1}. Thus this is a common proper motion pair.

4.7.4 LP 771−095 (LTT 1445)

This star, along with LP 771−096, is a known binary, but we have found a third component which sits along the line between the two stars and which shares the proper motion of the binary. The CNS3 listed a photometric parallax of 131 mas, but the Hipparcos mission subsequently measured the trigonometric parallax at 92.97 mas. The proper motion of this star is 0.″4723 yr^{-1}, which makes identification of common proper motion companions easy within a single year. The stars LP 771−95 and 771−96 were both classified as M 3.5 by Gizis (1997), and the third component is approximately 1.2 magnitudes fainter than LP 771-095 in the K band. It has a separation of 1.″12 from LP 771−095. LP 771−096 is 7.″23 from LP 771−095. Fig.

4.13 shows two of the images we acquired of this system.

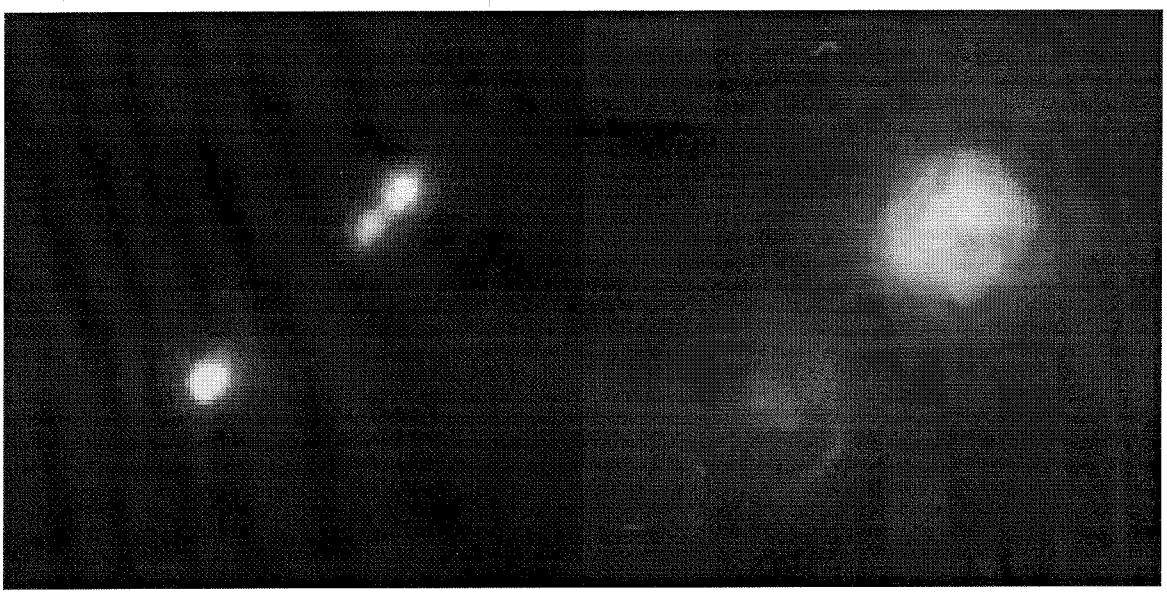

Figure 4.13 Images of LP 771−095 triple system. This star is a known binary (the two outer stars), but we have found a third stellar component of the system which shares the proper motion of the other two (LP 771−095 and LP 771−096). On the left is a 5 s K band image taken in October 1996. The components have a separation of 1.″12 and 7.″23 from the star LP 771−095, which is to the upper right in the images. North is up and East is left. The right panel is a 1000 s z band image taken in October 1995. North is up and East to the left. LP 771−096 is under the mask in this case. All three components are clearly visible. Unfortunately, the astigmatism of the Palomar 60" telescope is also apparent. In order to measure accurate astrometry on this image, we used only the light in the brightest part of the point spread function. Our astrometry matches that from the infrared images. The proper motion of the outer pair of stars has been measured to be 0.″4723 yr^{-1}. Thus this is a common proper motion triple system.

4.7.5 LHS 1885 (Giclas 250−031)

The CNS3 listed LHS 1885 with a photometric parallax of 129 mas. The Yale trigonometric parallax survey, however, measured a parallax of 87.4 mas, which removed it from our original sample of 8 pc stars. This M 4.5 (Gizis 1997) star was reported as double by Henry et al. (1997). We have found that the second component shares

the proper motion of the star. The second component is approximately 1.7 magnitudes fainter in the K band and is 1.″66 distant from the primary star. The proper motion of 0.″516 yr^{-1} permits identification of the common proper motion companion in less than a year. Fig. 4.14 shows two K band images taken in November 1995 and December 1996.

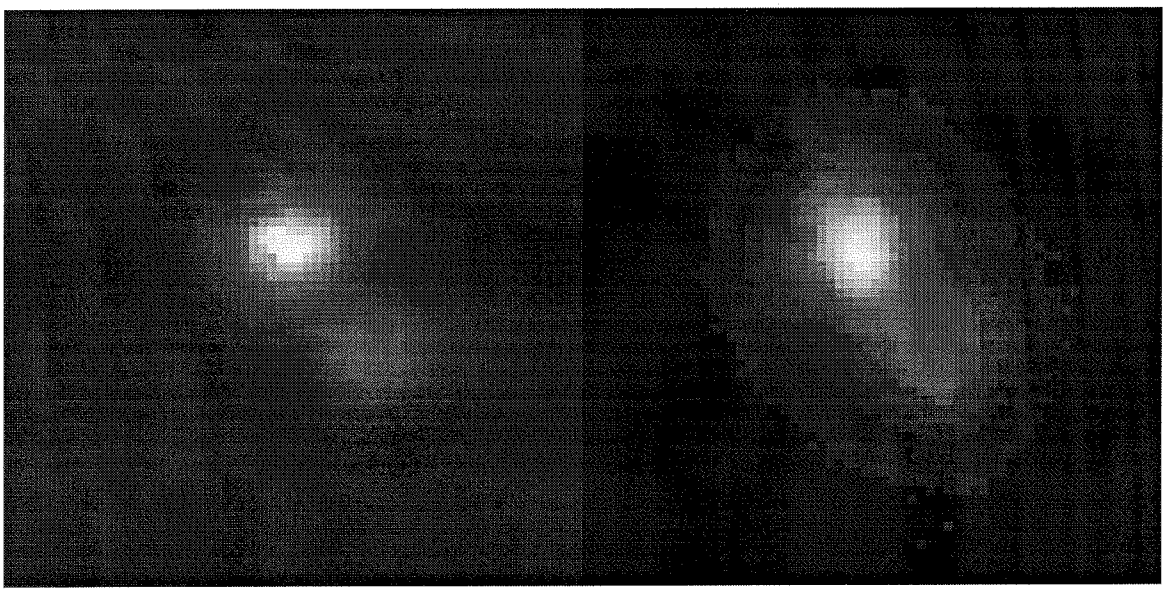

Figure 4.14 Images of LHS 1885. The second, fainter point source in these images is a common proper motion companion of LHS 1885, the brighter star. On the left is a 5 s K band image taken in November 1995. The components have a separation of 1.″65 and North is up with East left. The right panel is a 5 s K band image taken in December 1996. North is up and East is left. The separation measured from this image is 1.″68. The proper motion of LHS 1885 is 0.″516 yr^{-1}. Therefore, the fainter star is a common proper motion companion of LHS 1885.

4.8 Sensitivity to Brown Dwarf Companions

We now must expand the analysis from §4.6 to fainter levels and different colors: those of the brown dwarfs. Since only a handful of objects below $T_{\rm eff} = 1800$ K are known and only one with a temperature below 1000 K (see §1, 2 and 3), we must use these available objects as templates. The use of Gliese 229B photometry (Matthews et al.

1996; §3.1) permits the production of a table similar to Table 4.9. This is presented in Table 4.10.

TABLE 4.10. PERCENTAGE OF SURVEY STARS WITH OBSERVATIONS IN J, z AND r BAND SENSITIVE TO GLIESE 229B-LIKE COMPANIONS

Band	Separation (A.U.)									
	2.5	5	10	20	40	80	120	160	200	225
J	0	5	37	70	77	50	2	0	0	0
z	0	0	0	5	55	92	82	59	26	13
r	0	0	0	0	0	0	0	0	0	0

The contrast between Table 4.10 and 4.9 is quite dramatic. The survey has no sensitivity to cool brown dwarfs in the r band. This is principally because in this band the absolute magnitude of the template brown dwarf, Gliese 229B, is 24.6 (Golimowski et al. 1998; §3.3), while the images were limited to, at best, 21.7. The survey is most sensitive to brown dwarf companions in the z band at the wider separations and in the J band for separations $\leq$ 40 AU. This is due to the suppression of the broad wings of the point spread function by the pupil-plane coronagraphic stop. Brown dwarfs in orbits with separations between 50 and 100 AU would have been detected around more than 80% of the stars in the survey.

Ultimately we would like to express the sensitivity of the survey in terms of what the lowest mass brown dwarf we could possibly detect is. This is complicated by the fact that brown dwarfs cool. As such, a brown dwarf of a given mass will evolve through many magnitudes of brightness in a given bandpass over the timescale of several billion years (see §1). Unfortunately, the state of the art models which produce synthetic spectra, and thus color information, do not extend to the r band. However, the models of Burrows et al. (1997; personal communication) supply us with the magnitudes in the z and J bands for brown dwarfs of all masses (15 M_J to 70 M_J) for

two different ages, 1 and 5 Gyr. From this information we can convert the absolute magnitudes in Tables 4.7 and 4.6 into brown dwarf masses for each of the two ages, 1 and 5 Gyr. The results are shown in tabular and graphical form: Tables 4.11 through 4.14 and Figs. 4.15 through 4.18.

TABLE 4.11. PERCENTAGE OF SURVEY STARS WITH z BAND OBSERVATIONS SENSITIVE TO COMPANIONS OF BROWN DWARF MASS: AGE = 5 GYR

Mass	Separation (A.U.)									
(M_J)	2.5	5	10	20	40	80	120	160	200	225
70	0	1	25	67	98	95	84	60	26	13
65	0	0	20	59	93	95	84	60	26	13
59	0	0	4	34	92	95	84	60	26	13
51	0	0	3	28	83	95	83	60	26	13
45	0	0	3	28	82	95	83	60	26	13
39	0	0	1	8	67	93	83	59	26	13
35	0	0	0	1	28	86	82	59	26	13
34	0	0	0	1	24	79	76	59	25	13
33	0	0	0	0	0	0	0	0	0	0

Notes: Here, M_J is the mass of Jupiter.

TABLE 4.12. PERCENTAGE OF SURVEY STARS WITH J BAND OBSERVATIONS SENSITIVE TO COMPANIONS OF BROWN DWARF MASS: AGE = 5 GYR

Mass	Separation (A.U.)									
(M_J)	2.5	5	10	20	40	80	120	160	200	225
70	0	5	39	77	77	52	2	0	0	0
60	0	4	28	65	73	48	2	0	0	0
50	0	1	9	46	68	46	2	0	0	0
45	0	1	5	33	65	44	2	0	0	0
40	0	1	1	16	50	42	2	0	0	0
35	0	0	0	4	25	17	1	0	0	0
34	0	0	0	0	0	0	0	0	0	0

Notes: Here, M_J is the mass of Jupiter.

TABLE 4.13. PERCENTAGE OF SURVEY STARS WITH z BAND OBSERVATIONS SENSITIVE TO COMPANIONS OF BROWN DWARF MASS: AGE = 1 GYR

Mass	Separation (A.U.)									
(M_J)	2.5	5	10	20	40	80	120	160	200	225
65	0	1	26	83	99	97	84	60	26	13
60	0	1	26	83	99	97	84	60	26	13
51	0	1	25	74	98	97	84	60	26	13
40	0	1	25	67	98	97	84	60	26	13
31	0	0	4	34	92	95	84	60	26	13
21	0	0	1	8	69	95	83	60	26	13
15	0	0	0	1	28	83	81	59	26	13
14	0	0	0	0	0	0	0	0	0	0

Notes: Here, M_J is the mass of Jupiter.

TABLE 4.14. PERCENTAGE OF SURVEY STARS WITH J BAND OBSERVATIONS SENSITIVE TO COMPANIONS OF BROWN DWARF MASS: AGE = 1 GYR

Mass	Separation (A.U.)									
(M_J)	2.5	5	10	20	40	80	120	160	200	225
70	1	30	96	94	94	59	2	0	0	0
60	1	30	91	90	83	59	2	0	0	0
50	1	18	64	83	81	58	2	0	0	0
40	0	5	46	80	78	56	2	0	0	0
30	0	4	28	66	74	49	2	0	0	0
25	0	1	9	46	71	46	2	0	0	0
20	0	1	5	31	64	44	2	0	0	0
16	0	1	1	16	48	42	2	0	0	0
13	0	0	0	0	0	0	0	0	0	0

Notes: Here, M_J is the mass of Jupiter.

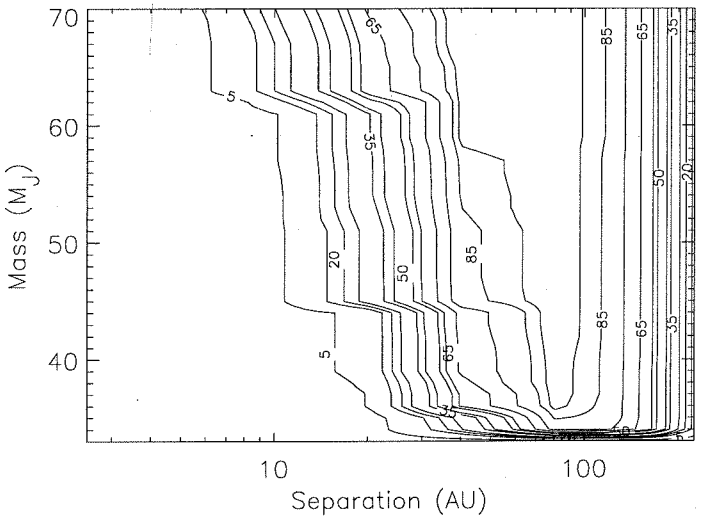

Figure 4.15 Brown dwarf mass vs. separation: Survey coverage in z, age 5 Gyr. This is a contour plot of an expanded form of the data presented in Table 4.11. It shows the survey sensitivity in z band as described in the text as a function of brown dwarf mass and orbital separation, assuming the age of the stars is 5 Gyr.

We should note that the two ages chosen here are meant to be representative of the ages of the sample stars. Assuming a constant star formation rate in the galaxy, the ages of stars in the disk would be evenly distributed between 1 and 5 Gyr.

Caveat

We must make an important qualification of the results of the computations described above. The conversion of z band magnitudes into masses is not ideal because as Burrows et al. (1997; personal communication) have noted, the synthetic spectra do not reproduce the observed spectrum of Gliese 229B in the wavelength range from 0.89 to 0.99 μm. While the general shape of the synthetic spectra is not far off, the flux density in this region is overestimated. The quantity of this overestimation is not entirely clear because the age of Gliese 229B is not well constrained (§2.1). The principal reason for the discrepancy between the observed and theoretical spectra lies in the exceedingly important question of how dust affects the spectra. In §1.6 and

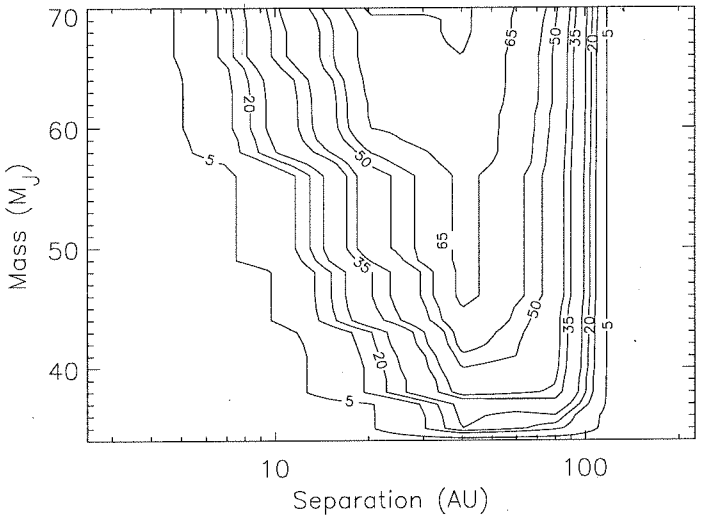

Figure 4.16 Brown dwarf mass vs. separation: Survey coverage in J, age 5 Gyr. This is a contour plot of an expanded form of the data presented in Table 4.12. It shows the survey sensitivity in J band as described in the text as a function of brown dwarf mass and orbital separation, assuming the age of the stars is 5 Gyr.

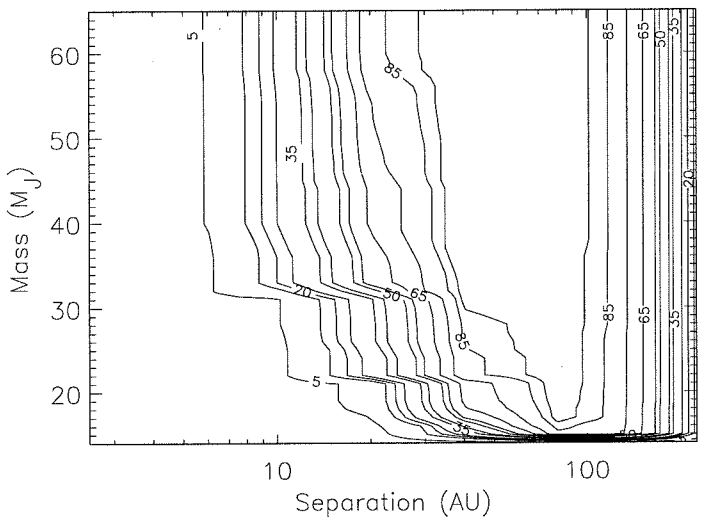

Figure 4.17 Brown dwarf mass vs. separation: Survey coverage in z, age 1 Gyr. This is a contour plot of an expanded form of the data presented in Table 4.13. It shows the survey sensitivity in z band as described in the text as a function of brown dwarf mass and orbital separation, assuming the age of the stars is 1 Gyr.

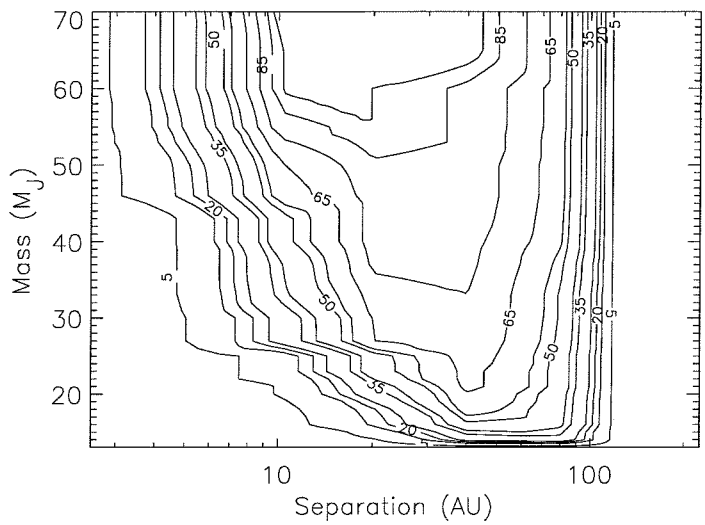

Figure 4.18 Brown dwarf mass vs. separation: Survey coverage in J, age 1 Gyr. This is a contour plot of an expanded form of the data presented in Table 4.14. It shows the survey sensitivity in J band as described in the text as a function of brown dwarf mass and orbital separation, assuming the age of the stars is 1 Gyr.

§3.3 we discuss this at length, but the question has not been answered adequately. (See also Griffith et al. 1998.) This problem is of vital importance to future searches for brown dwarf companions because dust can have a huge effect upon the spectral energy distribution of these low-mass objects. As an example of this, one need only compare the near infrared spectra of Gliese 229B and GD 165B, which are plotted simultaneously and to scale in Fig. 3.9. In this case, GD 165B is widely believed to contain large quantities of dust in its photosphere, whereas the spectrum of Gliese 229B seems mostly unaffected by dust at these wavelengths.

In addition, we do not separately evaluate the conversion between J magnitudes and mass and K band magnitudes and mass because the measurements in the two bands yields essentially identical masses. As we mentioned above (§4.6), the sensitivity curves for K band are the same as those for J band.

4.9 Discussion and Summary

What is becoming increasingly clear from the searches for field brown dwarfs, such as the Two-Micron All-Sky Survey (Kirkpatrick et al. 1998; personal communication), is that brown dwarfs greatly outnumber stars in the field population. It would seem to follow logically that many stars could have brown dwarf companions, if the formation mechanism for binary stars applies to star-brown dwarf systems. However, we have shown here that brown dwarfs seem to have a multiplicity fraction with stars far below the 30 to 40% observed for binary star systems with orbits between 40 and 100 AU (Reid and Gizis, 1997). In this separation range, we would have detected brown dwarfs more massive than 40 M_J, regardless of their age, around 80% of the survey stars.

The initial goal of this survey was to find brown dwarfs. However, because we found only one, and because our survey detection limits are complex functions of brightness, separation and age, placing constraints on possible mass and separation distributions of brown dwarf companions requires extensive Monte Carlo simulations. This is a rather complex problem which requires its own computational techniques. This work is currently in progress and will be published in a separate paper.

Here we present several simple statements which can be made with certainty.

1. This survey would have found all stellar companions of any type around 98% of the survey stars and between 3 and 30″ of the stars. Indeed in §4.7 we present 6 new stellar companions. This does not dramatically change the multiplicity fraction for the 8 pc sample.

2. Brown dwarfs more massive than 40 M_J, regardless of their age, would have been detected around 80% of the survey stars for separations between 40 and 120 A.U. Only one such object exists (Gliese 229B, at > 39 A.U.).

3. There has been no complete assessment of the population of brown dwarf

companions of the survey stars for separations outside 100 A.U. The most complete study to date has been that of Simons et al. 1996, but it did not cover the whole sample and turned up no new brown dwarfs. Our survey is insensitive to such wide separation binaries.

4. A more sensitive survey of the same stars in the sample presented here is necessary to obtain a complete census of brown dwarf companions in the solar neighborhood. This requires the suppression of scattered light from the primary stars (i.e. achieving a higher dynamic range) and an increase in the limiting magnitude of the sky-limited regions of the images. The next step in this sort of research is a full-scale, adaptive-optics-based survey, ideally with simultaneous infrared and optical imaging (because, as we demonstrated, the sensitivity in z band is extremely important).

4.9.1 Endnote

In §4.4 we addressed the issue of how sensitive the survey is as a whole and for individual stars. Ideally these calculations and observations should be gathered into a general statement about brown dwarf companions of nearby stars. This turns out to be a rather complex problem with a large and essentially unexplored parameter space. It is unexplored not only from the observational standpoint but essentially no research has been conducted on the theoretical aspects of the problem.

From the observational standpoint, the search for faint or low-mass companions of stars has only become practical in the past five to ten years. The two approaches to the problem—direct and indirect detection—have turned up positive results, but each has access to a different part of the parameter space. The parameter space is defined by mass of the companion and orbital separation. This seems simple enough, but as shown in the previous section the sensitivity of a direct observing campaign is not a constant through any region of this parameter space when the mass is below the "hydrogen burning limit." This is particularly true because brown dwarfs cool.

The cooling essentially introduces an additional parameter, the age. In the case of the indirect searches the sensitivity to mass is uninfluenced by age, but the parameter space is also explored in a non-uniform manner for a large sample of stars: it depends mainly upon the length of time over which the observations are scattered for each star. The point of this discussion is that the mass-separation parameter space is poorly sampled, and making direct comparisons between the direct and indirect observing methods is difficult because the overlap in parameter space is only now beginning to exist. The simplest comparison is shown in Fig. 4.19, where the mass-separation parameter space is shown with lines indicating sensitivity limits of various search techniques. The only imaging survey on the plot is that presented in this paper.

One of the most compelling features of Fig. 4.19 is the number of objects in the brown dwarf mass range at small separations. This seems to suggest that perhaps star systems with brown dwarfs favor small, or typically planetary, separations. What is certainly clear from our work is that the multiplicity fraction of brown dwarfs is far smaller than the 35 to 40% for stellar binary systems.

In light of this it is important to discuss the mass function. The mass function below the "hydrogen burning limit" has been the subject of heated debate and has always relied upon observational constraints rather than purely theoretical. In the past ten years it has become clear that the Salpeter mass function, which works for higher mass stars, does not apply to the very lowest mass stars. Recently, studies of open star clusters such as the Pleiades, which probe into the brown dwarf mass range, have begun to provide extensions of the mass function. (See, for example, Martín et al. 1998.) However, the masses of the objects discovered are generally not well-constrained because the theoretical models of these objects are not complete and unable to reproduce all of the observations. Other techniques for finding brown dwarfs in the field, such as the microlensing experiments, give accurate masses, but have found such a sparse number of objects in the brown dwarf mass range that

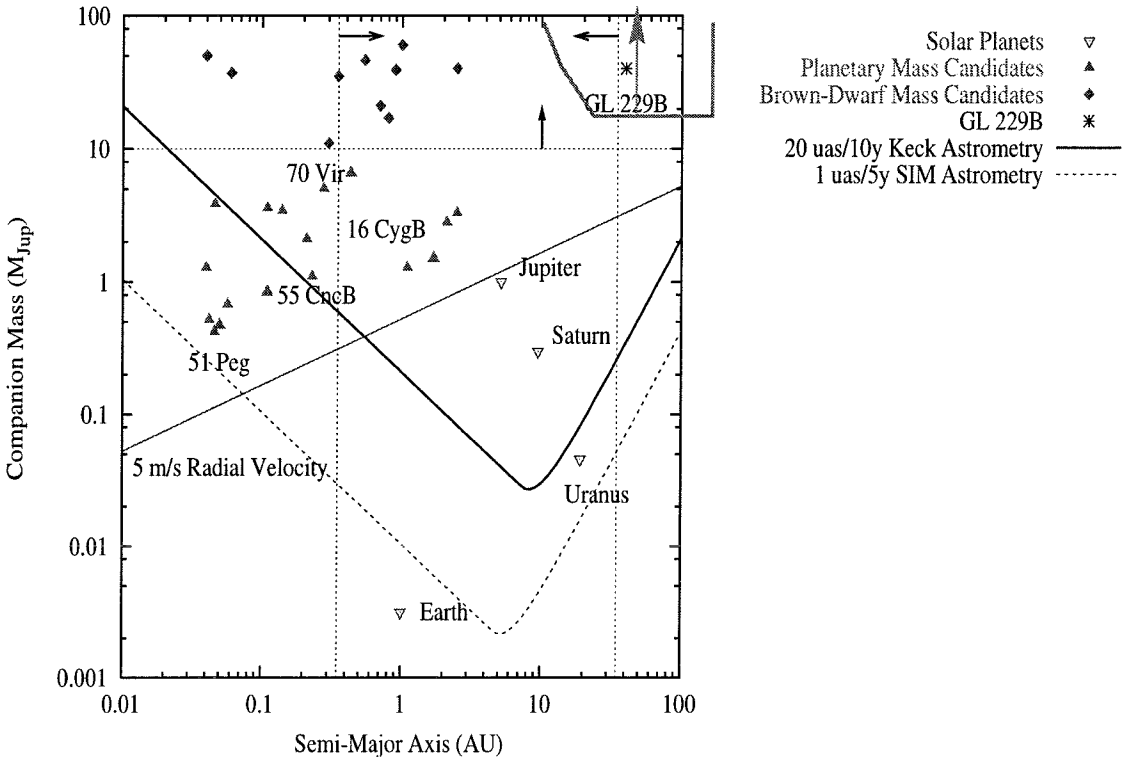

Figure 4.19 Mass-separation parameter space. This plot (courtesy A. Boden) shows the known substellar companions of stars discovered to-date. The major planets of the solar system are indicated with open triangles. Gliese 229B is represented by an asterisk. The planets found in radial velocity searches are represented by closed triangles and the brown dwarf candidates by diamonds. The curves indicate the detection limits of several techniques. The thin, straight line shows the 10 m s^{-1} limit of the current radial velocity searches. The two bent, thin lines show the predicted limits of astrometric searches with the Keck interferometer project (upper, solid curve) and the Space Interferometry Mission (lower, dashed curve). The limits of the survey presented here are shown by the heavy set of grey lines in the upper right. The dotted lines and accompanying arrows indicate the approximate region to be probed with Palomar or Keck adaptive optics imaging surveys. Our work represents the first direct imaging project to probe this parameter space.

the error bars on the implied mass distribution are large. A careful analysis of the MACHO results (Alcock et al. 1998) is presented by Chabrier and Méra (1998) and "clearly illustrates the difficulty to reach robust conclusions about the mass in the form of substellar objects in the central regions of the Galaxy, and more precisely, in the disk and the bulge, from present microlensing experiments." Indeed, Chabrier

and Méra cannot constrain the space density of brown dwarfs to a range smaller than an order of magnitude around 9×10^{-3} $M_{\odot}$ pc^{-3}.

A further complication of this problem stems from the observation, most recently by Reid and Gizis (1997), that the mass function for companions is actually different from the mass function of field stars. In their analysis of the 8 pc sample, they find that the distribution of the mass ratios of multiple systems has a significant peak near the ratio 0.95. In their estimation this excludes the notion that companions of stars come from the same mass function as solitary stars. For a survey of the nature presented here, this makes drawing conclusions about the various mass functions described above essentially irrelevant. It would be akin to trying to understand techno music by listening to classical violin concertos. There has been no study of companion mass functions in the brown dwarf regime. Furthermore, if the mass ratio distribution that Reid and Gizis (1997) find extends into the brown dwarf mass range, our survey excludes the most important set of stars to find brown dwarf companions of: we argued that the 25% incompleteness of our sample is all due to missing the very lowest mass stars within 8 pc. These are the ones that would be expected to have more brown dwarf companions.

Chapter 5

Related Work: Lithium in Very Low-Mass Stars in the Pleiades†

Ben R. Oppenheimer

Palomar Observatory, 105-24, California Institute of Technology, Pasadena, California 91125

Gibor Basri

Astronomy Department, University of California, Berkeley, CA 94720

T. Nakajima and S. R. Kulkarni

Palomar Observatory, 105-24, California Institute of Technology, Pasadena, California 91125

Abstract

High-resolution, Keck Telescope echelle observations from 630 nm to 850 nm of seven Pleiads with spectral types from M5 to M6.5 reveal rather rapid rotation, with an average $v \sin i \sim 52$ km s^{-1}, and chromospheric activity in Hα emission. The activity in these stars is not any stronger than that of other Pleiades low-mass stars, despite the expected high contrast of Hα with their cool photospheres and their rapid rotation. This shows that the "leveling off" of Hα equivalent widths previously noted in low-mass stars in young clusters is not related to the conventional rotation-activity

† Previously published in Oppenheimer et al. 1997b.

connection.

None of the stars previously categorized as brown dwarf candidates have lithium signatures in their spectra. They are, therefore, very low-mass stars and not brown dwarfs. However, two stars, HHJ 339 and HHJ 430, 1 and 2 magnitudes above the Pleiades zero-age main sequence, do show absorption due to Li I at 670.8 nm and in the subordinate feature at 812.6 nm. These two stars are also rotating very rapidly. These facts strongly suggest that these stars are rather young. Their proper motions and radial velocities agree with those measured for the Pleiades as a whole. We discuss various explanations for these stars, none of which is completely satisfactory. In one scenario they represent very late star formation in the Pleiades cluster (implying a huge range in the ages of Pleiads). This seems unpalatable given the lack of matter dense enough to form stars in the Pleiades at present. Another possibility is that these stars formed in a nearby, more recent star formation site and drifted into the Pleiades. Although the cluster recently passed through a clump of young Taurus stars, we do not see how it could "accrete" two of them. In our most feasible explanation, we posit that a cloud which was a member of the "Pleiades Supercluster" recently formed stars, which are now scattered between us and the Pleiades. HHJ 339 and HHJ 430 could be members of this group whose motion has now brought them near the older open star cluster.

5.1 Introduction

The Pleiades star cluster in Taurus is relatively nearby ($\sim$ 125 pc; Stauffer et al. 1994) and seems to be rather young ($\sim$ 100 Myr) (Patenaude 1978; Stauffer et al. 1989;

Basri et al. 1996). Because of these characteristics, it is an ideal hunting ground for brown dwarfs, which are thought to be brighter and thus easier to detect when young. Also because of its youth and proximity, it provides an excellent opportunity to study faint, very low-mass stars. As a result some investigators have identified faint point sources in the Pleiades as very low-mass stars and brown dwarf candidates (Hambly et al. 1993, hereafter HHJ). These stars are usually identified as Pleiades members by examination of their space motion, and their proper placement in an HR diagram (implying roughly the right distance). The stars in the Pleiades have fairly narrow distributions of proper motions and radial velocities. Therefore, stars in the direction of the Pleiades with space motions in agreement with these distributions are believed to be cluster members. This membership assertion is bolstered if the stars are chromospherically active (indicating youth), but the assertion remains statistical in nature.

Most researchers agree that the Pleiades cluster is between 70 and 130 Myr old. Though various papers have suggested that the stars might actually have a wide distribution of ages (Herbig 1962; Stauffer 1982; Stauffer 1984; HHJ), most of these claims have been adequately explained with inaccurate photometry and luminosity inflation due to unresolved companions of some of the stars (Stauffer et al. 1995). Some of the remaining spread of the main sequence could be due to cluster depth effects. At present, the general consensus is that the stars in the Pleiades are approximately coeval. The range of ages above primarily reflects controversy about the overall age of the cluster and not an age spread (Basri et al. 1996).

Several Studies (Steele et al. 1995; Steele and Jameson 1995; Stauffer et al. 1995; Basri et al. 1996; Basri and Marcy 1995) of some of the faintest low-mass Pleiades members, identified by HHJ as having the proper motion of the cluster, have revealed that many of these dim objects are, in fact, low-mass stars and not brown dwarfs. The so-called "lithium test" (Magazzù et al. 1991; Rebolo et al. 1992) has been

the primary method by which these brown dwarf candidates have been reclassified as low-mass stars. The essence of the lithium test is to search for absorption due to lithium in the spectrum of the candidate at issue. The presence of lithium in dim, very low-mass objects is an indicator either of extreme youth (as in the case of weak-line T Tauri stars (wTTS)) or of a mass below the minimum mass required for sustained hydrogen fusion in the object's core, or both. A nuclear reaction destroys the primordial lithium abundance in the least massive stars in ~100 Myr, and much faster in more massive stars. After several years of searching, Basri et al. (1996) finally found one faint object in the Pleiades with detectable amounts of lithium. This object, PPl 15, was identified by Stauffer et al. (1994). It is most likely a brown dwarf just below the mass necessary for sustained hydrogen fusion. Subsequently lithium has been confirmed in two Pleiades stars, Teide 1 and Calar 3, which are fainter than PPL 15 (Rebolo et al. 1996). These are certainly brown dwarfs.

Measurements of the chromospheric activity and the rotation velocities of low-mass Pleiades and Hyades stars (Stauffer et al. 1994; Stauffer et al. 1995; Basri and Marcy 1995) have shown that the empirical age-activity and age-rotation relations (Giampapa and Liebert 1986; Soderblom et al. 1993b) may not hold for stars later than M5. However, the paucity of observations has made it difficult to make definitive statements concerning these matters. These studies and others (Liebert 1995) conclude that the low-mass stars maintain rapid rotation for longer times than their more massive counterparts. The immediate explanation for this has been that these very low-mass stars have diminished magnetic braking (Barnes and Sofia 1996). It is not yet clear whether this is due to a reduction in magnetic flux, or a reconfiguration of the flux into smaller structures that are less efficient at braking. These issues are discussed in more detail by Basri and Marcy (1995).

5.2 Data Acquisition and Reduction

We observed the stars listed in Table 1 on the nights of 12, 13 and 15 October 1994 at the W. M. Keck 10m Telescope with the HIRES instrument (Vogt 1992). The only exception is that HHJ 339 was observed on the night of 23 November 1994. The total integration time for each star is listed in Table 1, along with the number of exposures represented by the integration time. We used the HIRES echelle spectrometer to capture fifteen orders of spectral data covering the range 630.0 nm to 850.0 nm. Gaps of approximately 4.5 to 5 nm, where no data were taken because of the limited size of the CCD chip, separate the orders. The Tektronix CCD chip measures 2048 pixels on a side. For every observation, we used a slit with a sky-projected width of $0\farcs861$ and a height of $14''$. This results in a resolution of $\lambda/\Delta\lambda = 45000$, or a $\Delta\lambda = 0.014$ nm at 630.0 nm and a $\Delta\lambda = 0.019$ nm at 850.0 nm. This resolution element corresponds to approximately 3 pixels. On each night the seeing was about $1''$ and fairly stable, and the weather conditions were clear.

Data reduction involved the following steps, using software kindly supplied by Jim McCarthy and Austin Tomaney. First, we subtracted bias frames from the spectral images. The bias frames exhibit two dimensional structure, so we felt that simple subtraction of a median value of the bias frame would be insufficient to remove the CCD bias. The spectral images were then divided by a "flat field" image which was created with a 3 second exposure using a quartz lamp illuminating the telescope's dome. From these "flattened" and bias-subtracted images, we then removed cosmic rays using a standard routine that searches for sharp spikes in the image and interpolates over these spikes. The automatic routine did not always remove all of the cosmic rays apparent to the eye, so in a few frames some additional interpolation was done manually. The curved spectral orders were traced out on exposures of the brighter stars. These tracings were assumed correct for the fainter stars, which would not have

been traced well by the routine due to the lack of signal. The tracing routine fits a Gaussian profile to the star light in the spatial dimension of each order along a third order polynomial in the dispersion direction. This accounts for the curvature of the orders.

Using this tracing, we then took a representative order for each star whose spectrum was to be extracted. In this order we summed about 200 columns. This allowed us to determine where in the order the actual signal from the star was and where the sky signal was. We assigned two ranges of pixels (about 15 pixels total) on either side of the star light in the representative order to be treated as sky light. Using these ranges, we were able to determine the contribution due to the sky background and to remove it. In this process, the signal in these two "sky apertures" was summed in the spatial direction. This sum was weighted according to the intensity of the signal. From this weighted average of all the sums across the slit, the sky profile over the entire slit was determined with a third order polynomial fit. Further, the night sky continuum was calculated by evaluating the median in the dispersion direction over 11 pixel increments. This median was then used to scale the sky profile previously determined. In the case where a night sky line was present (when the weighted sum across the sky regions of the slit was 5 σ above the sky continuum), the profile was scaled according to the weighted sum across the slit. In this way a two dimensional sky was calculated, and subtracted from, each order in the frame.

After the sky subtraction, a profile in the spatial direction was fitted to the remaining star signal in each order. The profile was a third, fourth or fifth order polynomial in the spatial direction for each column along each order fitted to a sum of between five and forty columns of data, depending on the strength of the signal. For weaker signals more columns of data were summed and lower order polynomials were fitted. For the brighter stars, such as HHJ 430, though, only five columns were needed to determine a profile accurately. Finally, using this profile, the data in each column

of each order were summed in the spatial direction and weighted according to the profile. This provides a so-called "optimal extraction."

There are several advantages to using such a complicated data extraction scheme. First, the tracing of orders takes into account the curvature of the orders. Other data extraction methods involve straightening the orders by resampling the data. This can introduce resampling noise if not done very carefully, which can degrade the signal-to-noise ratio of the final spectrum, significantly in the case of very faint stars. Second, the weighting of the sum in the spatial direction by a profile gives more weight to the brighter pixels. This also yields an improvement in signal-to-noise ratios compared with the simpler method of a straight, unweighted sum.

5.3 Observations

Measurements of each star's heliocentric radial velocity, as listed in Table 1, were made using the standard cross correlation technique using several regions of the spectra, including the area around the Hα emission feature and the order centered on 712.0 nm, in which lie some strong TiO absorption bands. These radial velocities are all relative to HHJ 36, which Stauffer et al. (1995) determined to be 5.2 km s^{-1} with an accuracy of $\pm$ 5 km s^{-1}. Based on the various measurements of each star's radial velocity, the error in the radial velocities is $\pm$ 5 km s^{-1}.

Steele & Jameson (1995) reported that HHJ 18 has excess opacity in the 800 to 900 nm region of its spectrum, unlike that of a normal M5.5 star. In the 50 nm of our spectrum in the blue half of this region, we cannot confirm this excess opacity. In fact, the spectrum appears almost identical to that of HHJ 16 (another M5.5 star) in this region.

TABLE 5.1. OBSERVED STARS AND DERIVED PARAMETERS

Star	Sp. Type	t_{int} (s)	N_{exp}	Hα W_λ	Ca I W_λ	K I W_λ	Rb I W_λ	Ti I W_λ	Li I W_λ [a]	Li I W_λ [b]	$v \sin i$	v_{rad}
HHJ 6	M6.5	11300	3	-7.2		4.0	0.5	0.6			50 ± 10	4.4
HHJ 10	M6	3000	1	-6.3		4.2					52 ± 5	9.3
HHJ 11	M5.5	5000	2	-6.9		3.6	0.5[e]	0.4			45 ± 5	5.1
HHJ 16	M5.5	3000	1	-8.9		3.6	0.7	0.6			45 ± 5	6.3
HHJ 18	M5.5	3000	1	-6.0		2.3	0.6[e]	0.7			60 ± 10	7.3
HHJ 19	M5.5	3000	1	-5.4		3.5	0.4[e]	0.7			55 ± 5	9.3
HHJ 36	M5	3000	1	-6.9	0.3	2.5	0.4	0.5			37 ± 5	5.2[c]
HHJ 339	M5	600	1	-10.4	0.4	2.1	[d]	0.4	0.9	[d]	58 ± 5	9.4
HHJ 430	M5	1000	1	-10.0	0.3	2.1	0.4[e]	0.3	0.7	0.2	65 ± 5	9.1

Notes to Table 5.1

[a] Li I 670.78 nm

[b] Li I 812.64 nm

[c] This measurement is from Stauffer et al. (1995).

[d] Not within the detector format.

[e] Possible chromospheric emission core.

All equivalent widths are given in units of Å and have measurement errors of about 10%. The radial and rotational velocities are listed in (km s^{-1}). The radial velocities are in the heliocentric reference frame and all have an error of ± 5 km s^{-1}. The Ca I line is at 657.280 nm. The K I line is at 769.898 nm. The Rb I line is at 794.760 nm. The Ti I line is at 842.650 nm. HHJ 339 also has a Ti I line at 843.498 nm with an equivalent width of 1.3Å. The spectral types come from Steele & Jameson 1995, except for HHJ 10, HHJ 11 and HHJ 339, which are our own and are based on careful comparison of these stars's spectra with those of the others in the sample.

5.3.1 Rotation and Chromospheric Activity

Measurements of each star's Hα equivalent width are also included in Table 1. There is no obvious correlation of these widths with any of the other derived parameters in the table.

We have measured the rotational velocities of the stars in our sample using methods similar to those expounded in Basri and Marcy (1995). The star we use as a slowly rotating template is LHS 292. Because the stars here are such rapid rotators, we found that several of the spectral regions used by Basri and Marcy (1995) were not as useful. We therefore concentrated on the CaH bands between 694 nm and 700 nm. Other orders were used primarily as confirmations of the values found there. Again we compared cross correlation functions against the slow rotator with the observations and with model spectra at different rotations. Very low signal-to-noise ratios compromised our accuracy in a couple of cases. Our measurements of $v \sin i$ are listed in Table 1, along with their accuracies. All of the stars are rotating at least as rapidly as 35 km s^{-1}, and they have an average rotational velocity of 52 km s^{-1}.

It is perhaps not surprising that all these stars are such rapid rotators. They are the low-mass extension of the rapidly rotating K dwarfs in the Pleiades (Stauffer and Hartmann 1987, Soderblom et al. 1993a). These M dwarfs are rapidly rotating in part because of "spin up" as they shrink toward the main sequence, and perhaps because they are fully convective. The "spin down" of higher mass stars may be initially confined to their convective envelopes. In contrast, the late M dwarfs must lose angular momentum throughout their structures. On the other hand, one might expect the observational effect of random inclination angles to produce a few apparently slow rotators, which are not present in our sample. It must be the case, therefore, that they are all rotating *very* rapidly. Low-mass stars show little evolution in Hα strengths from the Pleiades age to that of the Hyades (Stauffer et al. 1995), so it will be very interesting to pursue the rotational behavior of the very low-mass

Hyades stars.

5.3.2 Atomic Features

The depletion of lithium in a very low-mass star provides an excellent constraint on both its mass and its age. For a given mass, the lithium is predicted to be depleted at a well defined age (D'Antona and Mazzitelli 1994). Conversely, the minimum mass at which lithium is still detectable in a cluster provides an age for the cluster. Finally, when the cluster age is sufficiently large, the presence of lithium at the bottom of the main sequence signals detection of brown dwarfs. Basri et al. (1996) have already discussed the age of the Pleiades as found by the lithium test. Here, we have observed stars brighter than those considered by them. Such stars should all be depleted of lithium unless there were a substantial age spread in the cluster.

None of the stars we observed at the bottom of the main sequence shows lithium. This is consistent with the age suggested by Basri et al. (1996) and a minimal age spread. The luminosities of all our targets, along with the age from Basri et al. (1996), demand that they are very low-mass stars and not brown dwarfs. For ages less than the Basri et al. (1996) value of $\sim$ 120 Myr, the lack of lithium in these stars places an even stronger constraint that they are stars and not brown dwarfs. Fig. 5.1 is a color-magnitude diagram for the very low-mass stars in the Pleiades, with all the stars that have been tested for lithium labeled. Based on TiO band strengths estimated from moderate resolution spectra, Stauffer et al. (1995) argue that the true colors of HHJ 18 and HHJ 36 are considerably bluer than the published values. This is indicated by the arrows in Fig. 5.1. Stars in which lithium has been found are indicated with a diamond. The two stars which are not on the Pleiades main sequence do show lithium and are discussed in §5.4.

We have examined the behavior of a few atomic features as listed in Table 1. Because of the rapid rotation of the stars combined with a large number of blended

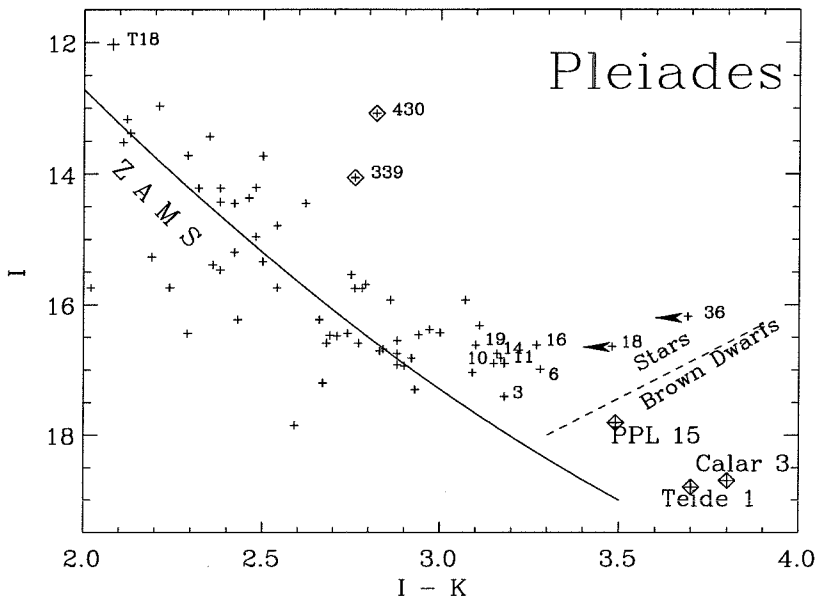

Figure 5.1 Color-Magnitude Diagram of the Pleiades showing all of the stars (labeled with their HHJ numbers) observed in various searches for lithium and the recently discovered lithium brown dwarfs. Stars with detected lithium have diamonds around them.

molecular lines, we do not feel the line strengths can be measured with accuracies better than about 10%. While HHJ 339 and 430 clearly have weaker lines than the others (and are the hottest), we do not see diagnostics at high resolution which clearly distinguish between M5 and M6. The best ordered behavior is found for K I: cooler stars using low resolution classification show a stronger line. We also checked the width of the K I features in HHJ 339 and 430, to see whether they are narrower than in other stars of the same spectral type that are closer to the main sequence (such as HHJ 36). There is a hint that this is so, but we are reluctant to make a strong statement because small differences in temperature can cause comparable effects. Basri et al. (1996) suggested that Rb I might serve a similar function, but our spectra are complicated by the possible presence of chromospheric emission cores

in the Rb I line in some stars.

5.4 Two Enigmatic Detections of Lithium

One of the most intriguing results of this investigation emerges from the observations of two brighter members of the HHJ sample, HHJ 339 and HHJ 430. These stars appear in pre-main sequence locations on the Pleiades HR diagram (see Fig. 5.1), which is curious in itself and is why we observed them. It could have meant that they are simply foreground stars with the same proper motion as the Pleiades. They have Hα strengths at the upper end of the equivalent widths seen for very low-mass Pleiads; the implied surface fluxes are even higher since the underlying continuum is brighter.

The unexpected result in our spectra, however, is the strong presence of lithium in both HHJ 339 and HHJ 430 (Fig. 5.2). Not only is the resonance line at 670.8 nm quite visible, but the subordinate line at 812.6 nm is also easily seen in HHJ 430. (In HHJ 339, the subordinate line sits in one of the dataless gaps between the spectral orders.) In both cases, the lithium strengths are similar to those found in wTTS. None of the published X-ray studies of the Pleiades have HHJ 430 in the field of view. However, HHJ 339 is in the recent ROSAT pointed observation of the Pleiades undertaken by Micela et al. (1996). They are only able to assign an upper limit to its X-ray luminosity of $\log L_X < 29.30$ erg s^{-1} because it lies 48.'1 away from the center of the field. This upper limit is not inconsistent with the typical X-ray luminosity of wTTS, which is $\log L_X \approx 28$ to 30 erg s^{-1}. In conclusion, these stars have essentially all the usual characteristics of wTTS.

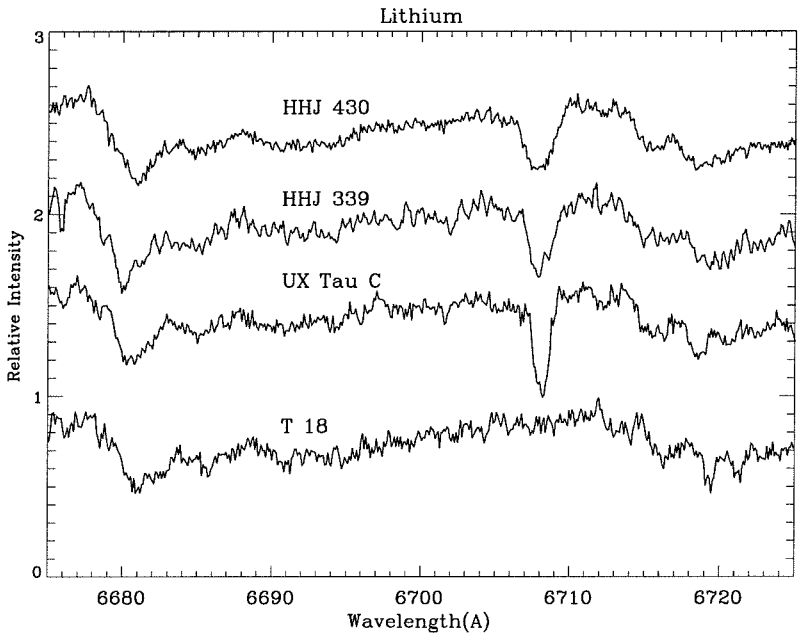

Figure 5.2 The 670.8 nm lithium resonance line in HHJ 339, HHJ 430 and UX Tau C, a well studied T Tauri star. For comparison, the same region of T 18's spectrum is also shown courtesy of J. R. Stauffer.

5.4.1 Are HHJ 339 and HHJ 430 Pleiads?

Although their proper motions are near the median for cluster members according to HHJ, it is conceivable that they could simply be foreground wTTS with the same proper motion. However, they could not be very much closer since they already sit in the proper place in the HR diagram to be on the pre-main sequence at the distance of the Pleiades. We argue below (§5.4.2) that these stars must be in their pre-main sequence phase in order to have retained lithium.

As an additional check, we carefully measured their radial velocities, since the Pleiades is not very different in radial velocity from field stars in that direction. Velocities found by us for our whole sample have a mean of 7.2 km s^{-1} and a standard deviation of 2.1 km s^{-1}. This is just as expected and in agreement with Basri et al.

(1996) and Stauffer et al. (1995). The stars HHJ 339 and HHJ 430 lie about one sigma above the mean velocity (with HHJ 11 similarly high).

Thus, the three traditional membership criteria—proper motion, radial velocity, and Hα strength—provide reasonable evidence that they are cluster members. As already mentioned, their luminosities and temperatures do not place them on the Pleiades main sequence, but are consistent with a pre-main sequence location. It is unlikely that binarity could cause them to occur as far from the main sequence as they do (in the absence of strange spectroscopic anomalies). Only a parallax measurement could make the membership assertion more certain.

We note that these two stars were first posited to be members of the Pleiades because they were seen to flare by Haro et al. (1982) who called them HCG 332 and HCG 509, instead of HHJ 339 and HHJ 430.

5.4.2 How Old Are HHJ 339 and HHJ 430?

We have taken three independent approaches to placing constraints on their mass and age. The first and third methods give upper limits to the masses and ages, while the second attempts to estimate these physical parameters directly.

Luminosity and Lithium Depletion

Our first method is to estimate the luminosity of the stars assuming they are in the cluster, and then to find the lowest mass and largest age at which lithium could still be undepleted at that luminosity. The bolometric luminosity can be estimated from colors, using bolometric corrections. We adopt a distance modulus for the Pleiades of 5.60. Stauffer et al. (1994) give a formula for estimating luminosity from the I magnitude. Applying this to HHJ 339 and HHJ 430 yields luminosities, $log(L/L_{\odot})$, of -1.69 and -1.36 respectively. Alternatively, one can use the K magnitude and

bolometric correction from Tinney et al. (1995). For $I - K$ colors of 2.88 and 2.94, the bolometric corrections are about $BC_K \sim 2.95$. This yields luminosities of -1.56 and -1.14 respectively. This offset in the methods was also seen by Basri et al. (1996). Taking the geometric mean of them, we adopt $log(L/L_\odot)$ of -1.63 and -1.25 for HHJ 339 and HHJ 430, respectively. We use the calculations of D'Antona and Mazzitelli (1994) to find at what mass and age lithium is beginning its depletion. Adopting the set of models that seems to match observed lithium depletions best (their Table 6), we find that HHJ 339 is likely to have a mass between 0.15 and 0.20 $M_\odot$ with an age between 10 and 30 Myr. For HHJ 430 the age is at most 20 to 30 Myr, with a mass of between 0.30 and 0.35 $M_\odot$. These estimates are upper limits on the ages and masses; so the stars could also be less massive and younger. The third method, described below, takes this analysis further.

For completeness, we consider whether these two stars could be foreground stars on the main sequence. In that case, they would have to be about one and two magnitudes closer which would lower their intrinsic luminosities so that, for both stars, $log(L/L_\odot) \approx -2.0$. Referring once again to the tables in D'Antona and Mazzitelli (1994), this would imply, because of the strong presence of lithium, that HHJ 339 and HHJ 430 are about 0.1 $M_\odot$ and must be younger than 25 Myr. Such young stars, however, must sit above the main sequence, contrary to the original supposition. This provides an additional, though less stringent, argument for cluster membership, since they are in fact in the pre-main sequence if at the distance of the cluster.

Theoretical Isochrones

The second method to determine the ages and masses of these stars is to try to place the stars directly onto evolutionary tracks and see what mass and age is implied. These have to be compatible with the observation of lithium. Here, the difficulty is in assigning an effective temperature based on colors (made more difficult by the stars's

not being on the main sequence). A lot of work has recently gone into this problem.

For example, Kirkpatrick et al. (1993) fit synthetic spectra of stellar atmospheres with observed spectra to determine a temperature scale for M dwarfs. Using this scale, we assign a temperature of 3250 ± 125 K to HHJ 430 and 339. Referring once again to the tables of D'Antona and Mazzitelli (1994), and the bolometric luminosities found above, we find that HHJ 339 can be between 0.05 and 0.15 $M_{\odot}$ with corresponding ages between two and ten million years. HHJ 430 can fall within the same mass range, but the age is constrained to be within 0.1 and 3 Myr.

These estimates are consistent with the upper limits derived above. (In addition, it was this sort of work which led Steele et al. (1993) to conclude that there was an age spread in the Pleiades, but the corrections in Steele and Jameson (1995) reversed those conclusions. No discussion of either HHJ 339 or HHJ 430 appears in either paper.)

These models assume that the evolving stars have solar metallicity, a reasonable assumption for the Pleiades.

Lithium Line Curves of Growth

Recently, a number of researchers have investigated the curves of growth of several lithium lines in very low-mass, pre-main sequence stars (Pavlenko et al. 1995 and references therein). This work greatly facilitates the assignment of abundances to line widths observed in stars. For the two stars at issue, the model atmosphere calculations of Pavlenko et al. (1995) give lithium abundances of $\log N(\mathrm{Li}) = 3.0 \pm 0.2$ for HHJ 339 and $\log N(\mathrm{Li}) = 2.6 \pm 0.3$ for HHJ 430. (Here, $\log N(\mathrm{H})$ is 12, and the cosmic abundance of lithium is assumed to be $\log N(\mathrm{Li}) = 3.2$.) These estimates assume that the stars have effective temperatures of between 3000 and 3500 K and the error estimates arise from allowing that the lithium can be in LTE or NLTE and that the stars may have chromospheres strong enough to affect the line widths. The theoretical

equivalent widths are relative to a "true" continuum, while ours are observational, which likely makes them systematically smaller. Thus, these abundances should be taken as lower limits.

From these derived lithium abundances, one can determine the ages of the stars based on the lithium depletion models used in the first attempt at constraining this parameter above. Using Table 6 of D'Antona and Mazzitelli (1994), and assuming that HHJ 339 and HHJ 430 have masses of between 0.1 and 0.3 $M_{\odot}$, our abundances, which are clearly not far below the assumed cosmic abundances, result in ages of 20 $\pm$ 10 Myr for both HHJ 339 and HHJ 430. Because lithium depletion happens rapidly, these ages are upper limits.

The conclusion of all three arguments is that these two stars are no older than 30 Myr, but could be as young as a few Myr.

5.4.3 How Can Young Stars Exist in a 100 Myr Cluster?

The rather startling implication of this analysis is that these two stars, which appear to satisfy cluster membership criteria, are as much as 100 Myr younger than the stars on the Pleiades main sequence. Taken at face value, this would imply that star formation has been going on for a very long time in this cluster, so that there exists a huge age spread in its members. Interestingly, Steele et al. (1993) had reached a similar conclusion (that stars existed from the upper main sequence turnoff age of the cluster down to less than 10 Myr). They did not discuss how star formation could persist in a cluster over such a long period of time. Furthermore, such lengthy periods of star formation are not compatible with the current consensus on the star formation process and the lifetimes of star-forming clouds (Leisawitz et al. 1989). Stauffer et al. (1995) and Steele and Jameson (1995) agree that this inferred age spread was due in part to an incorrect color conversion. However, the corrected photometry in Steele and Jameson (1995) does not remove the full spread in the MS observed in

the Pleiades color-magnitude diagram (see their Fig. 10), nor does it remove the age spread implied by the theoretical isochrones.

Instead, Steele and Jameson (1995) suggest, using quantitative arguments, that most of the spread can be explained by a binary main sequence situated about 0.75 mag above the MS, and of the same age. However, this cannot fully explain the distance from the MS at which a few of the stars lie, including HHJ 36 and HHJ 16 and especially HHJ 18. Steele and Jameson (1995) find an anomalous spectrum for HHJ 18, whereas Stauffer et al. (1995) and we do not. These stars lie on younger isochrones, but do not show lithium as HHJ 339 and HHJ 430 do. As mentioned above, we suspect that HHJ 18 and HHJ 36 are really bluer than indicated, and belong with the other main-sequence stars. It may also be the case that HHJ 36 is not a Pleiades star at all: Tinney et al. (1995) suggest that it does not have the correct proper motion, although HHJ claim it does. We conclude there is no good evidence for an "intermediate age" population which would be expected if the age spread was large.

It is interesting to note that the stars which Steele and Jameson (1995) identify as single lie predominantly blueward of their 70 Myr isochrone, suggesting an older age. Basri et al. (1996) point out that there is a discrepancy in the ages implied by the low-mass stars and by the high-mass stars in the cluster, in the sense that the low-mass stars seem generally older. They provide important, new support for the older, 100 Myr age, and note that convective overshoot in the cores of the massive stars could bring them into agreement with this older age. If one does not accept that argument, then there is still good evidence for a large age spread. In order that there be no evidence for an age spread greater than 10 Myr, one must accept their argument, and revised photometry or distances for the outlying stars mentioned above must bring them closer to the main sequence.

As a secondary argument against an age spread in the Pleiades, Stauffer et al.

(1995) plot Hα equivalent widths versus an ad hoc age indicator, the number of magnitudes a given star sits above the main sequence. They argue that because the stars with the youngest ages do not have the largest Hα equivalent widths, the age indicator is not correct and there is no evidence for an age spread. This argument is weak, however, because it is well-known that stars at such late spectral types have huge spreads in their Hα equivalent widths at various ages, from that of the Pleiades to that of the Hyades (600 Myr, see Stauffer et al. 1991).

In any case, the proposition that the Pleiades contains stars which formed both 120 and 20 Myr ago from the same ISM cloud is not one which is easily accepted (but would be very important if true). The stars in our sample imply that this is a possibility. In this context, however, it is surprising that there are no obviously intermediate-aged stars.

It seems rather unlikely that stars were born inside the Pleiades only a few to ten million years ago because there is no interstellar material in the Pleiades that is dense enough to form stars. The cluster is colliding with a cloud right now (White and Bally 1993 and Herbig 1996) which is the source of the reflection nebulosity the cluster is famous for, but it does not contain dense material. The knot discussed by Herbig (1996) is dense, but does not contain much mass. It is unclear whether it is capable of forming a star; even if it did, the star would not remain in the cluster because it has a different space motion. In both cases, these clouds are near the Pleiades now but were not a few million years ago. White and Bally (1993) and Herbig (1996) disagree about the motion of the interstellar material, but do not disagree that the Pleiades is moving through it. The Pleiades could have collided with a dense cloud 20 Myr ago, but it must have been essentially following the cluster in order to produce two stars with the cluster's space motion and location. In that case, it would probably be considered part of the original cluster material.

If one assumes, instead, that our two lithium stars did not form in a very late

bout of star formation within the Pleiades, how is it possible for such young stars to be apparent cluster members? The Pleiades sits in the midst of a rather complicated grouping of giant molecular clouds, those belonging to Gould's Belt and Taurus. For studies of the kinematics of this interstellar material, refer to, for example, White and Bally (1993) and Herbig (1996). Because of this, many clumps of star-forming clouds exist in rather close proximity to the Pleiades cluster. At the distance of 127 pc, a cloud 5° away could be as close as tens of parsecs. Furthermore, huge numbers of X-ray bright and lithium bearing stars (indicating ages of a few tens of Myr) have recently been discovered in this part of the sky distributed over tens of degrees (Neuhäuser et al. 1995a), some with radial velocities consistent with that of the Taurus clouds (Neuhäuser et al. 1995b).

To investigate this further, we consider the relative motions of the Pleiades and the Taurus clouds over the past 30 million years, the upper limit on the ages of HHJ 339 and HHJ 430. The Taurus clouds have been shown by Herbig (1996) to be moving with a relative radial velocity of about 10.5 ± 1 km s^{-1} and a relative proper motion of $2\farcs0 \pm 0\farcs4$ per century at a P. A. of $325° \pm 30°$relative to the Pleiades. This is determined by the radial velocity of the CO emission and the proper motions of various clumps of wTTS in the clouds. Furthermore, the Taurus clouds now lie at a distance of 150 ± 10 pc (Herbig 1996). This means that about 2 million years ago the Pleiades may well have passed directly through a star forming clump in the Taurus cloud. (See Fig. 5.4.)

Considering the interaction cross sections, it is essentially impossible that the Pleiades could have "captured" one, let alone two, of the young stars in this cloud. However, recent models of few-body systems by Sterzik and Durisen (1995) show that typical configurations of young stellar objects in star forming regions may eject stars from these regions, with 60% acquiring velocities greater than 3 km s^{-1}. Furthermore, their simulations also demonstrate that these stars can be ejected on time scales

much less than the evolution timescale of the newborn stars. Feigelson (1996) also promotes such a scheme, in which many star forming regions disperse some of their stars outside of their traditionally accepted boundaries, and suggests that it can explain the apparent deficit of wTTS older than a few million years in star forming regions. So perhaps HHJ 339 and HHJ 430 are examples of these "runaway" wTTS. For this to work, the stars must be ejected from the star forming clump at the same time that the Pleiades was passing through it. Furthermore, the stars have to be ejected with the same space motion as the Pleiades. This would be a remarkable coincidence if there were only one of these stars; it seems highly implausible that two would behave this way.

On the other hand, there *is* a set of pre-main sequence stars which have almost the same the space motion as the Pleiades. These are part of the "Pleiades supercluster," most recently discussed by Eggen (1995). Some of these objects are clearly above the main sequence, and many have strong stellar activity and show strong lithium lines. There is every reason to believe that they are much younger than the stars in the Pleiades cluster itself. In that sense, the supercluster does have a very large age spread. The only star discussed by Eggen (1995) which is similar to our lithium stars is the early M binary T 18. This is actually a member of the Pleiades cluster. Stauffer (private communication) has provided us with his spectrum of one component of T18 (Fig. 5.2); it clearly has depleted lithium to, at most, a small fraction of the abundance in our 2 HHJ stars, and is quite consistent with complete depletion. While it is slightly hotter (making the equivalent width of lithium for a given abundance smaller), this star does not present the same quandary as our stars in terms of being obviously very young. However, if it is at the distance of the cluster, it lies above the main sequence even after accounting for its binary nature (Fig. 5.1), unless it is really quadruple. Eggen (1995) points out that it is similar to a non–cluster member of the supercluster, HD155555C. The other (more massive) members of that triple

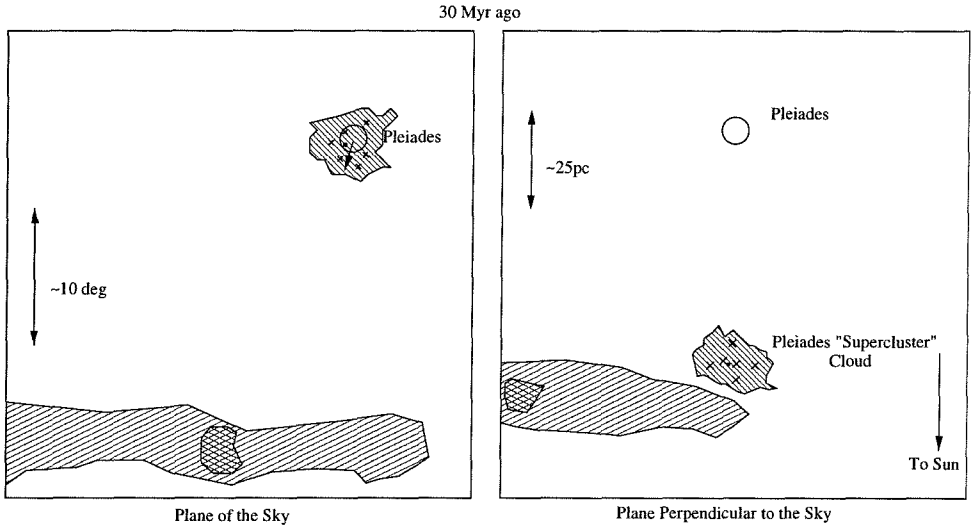

Figure 5.3 Schematic views of the Pleiades and Taurus clouds in both the plane of the sky and projected into a plane perpendicular to the sky. In all six panels of Figs. 5.3, 5.4 and 5.5, the Pleiades cluster is represented by a small circle. The x markers represent stars in the Pleiades "supercluster." In this scheme, these stars will increase in number and the clump will expand about their center of expansion (marked with a dot) as discussed in §5.4. HHJ 339 and HHJ 430 might come from such a population. The large shaded region represents the Taurus molecular cloud. Approximate scales are indicated. The arrows indicate the motion of the Pleiades relative to the Taurus clouds. This figure shows the region as it might have appeared 30 Myr ago. The darker shaded region is where the wTTS present in Figs. 5.4 and 5.5 will form. The shaded region encapsulating the x markers is meant to show that 30 Myr ago these stars were forming and a lot of gas must have been present. This figure is meant to illustrate a working hypothesis that explains the presence of HHJ 339 and HHJ 430 in the Pleiades. By no means are the locations and motions represented precise.

system show lithium (Martin and Bradner 1995) but the M star does not (consistent with an age of 30 Myr).

It is interesting that Yuan and Waxman (1977) claim that the motion of the supercluster as a whole may suggest an age of about 150 Myr, another indication for the larger-than-classical age proposed by Basri et al. (1996). Yuan and Waxman (1977) show that the actual motion of the cluster over its lifetime is complicated; it oscillates above and below the galactic disk plane. Determining through which clouds t may have passed is very difficult (particularly since they may not still be around).

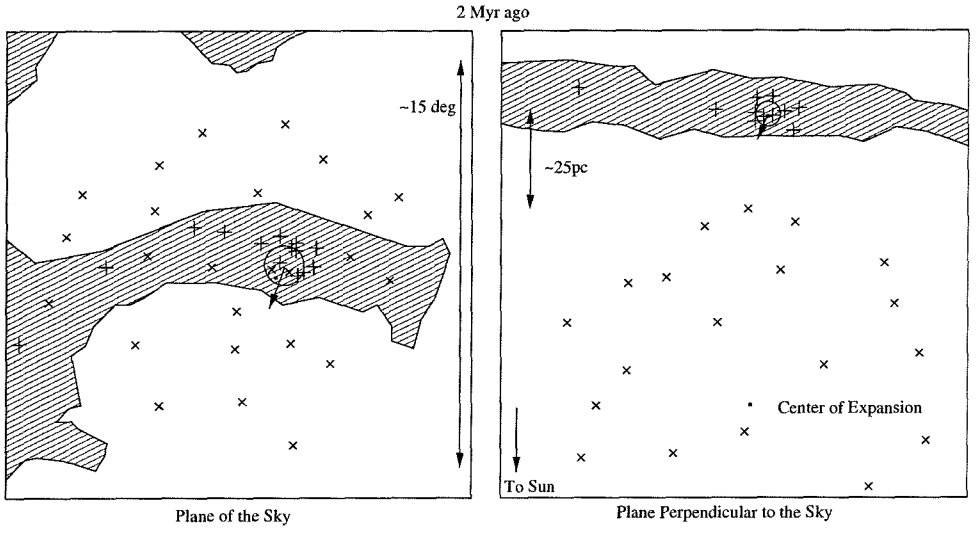

Figure 5.4 Schematic views of the Pleiades and Taurus clouds in both the plane of the sky and projected into a plane perpendicular to the sky. This figure shows the same region shown in Fig. 5.3 but at an epoch only 2 Myr ago, when the Pleiades passed through a region of star formation in the Taurus clouds. Pluses indicate wTTS which are known to exist at present. This figure is meant to illustrate a working hypothesis that explains the presence of HHJ 339 and HHJ 430 in the Pleiades. By no means are the locations and motions represented precise.

The young supercluster stars are not particularly puzzling, however, since they are not actually in the Pleiades cluster, but are merely streaming by us with a similar space motion (that of the supercluster). This space motion is not very different from the general solar neighborhood, so use of the supercluster concept is not crucial to our argument. One can imagine that there was a wide complex of vaguely related clouds which shared a general motion but formed stars at different times. This suggests our best hypothesis for what HHJ 339 and HHJ 430 might really be. Suppose a cloud in the supercluster complex (or simply with space motion sufficiently similar to that of the Pleiades) formed stars 20 to 30 Myr ago (Fig. 5.3). Its motion would be similar to the Pleiades. We suppose that its center of expansion now is in the direction of the cluster and roughly halfway between us and the Pleiades cluster. Suppose further that this cloud became unbound (as is usual) when it formed stars, and that they left

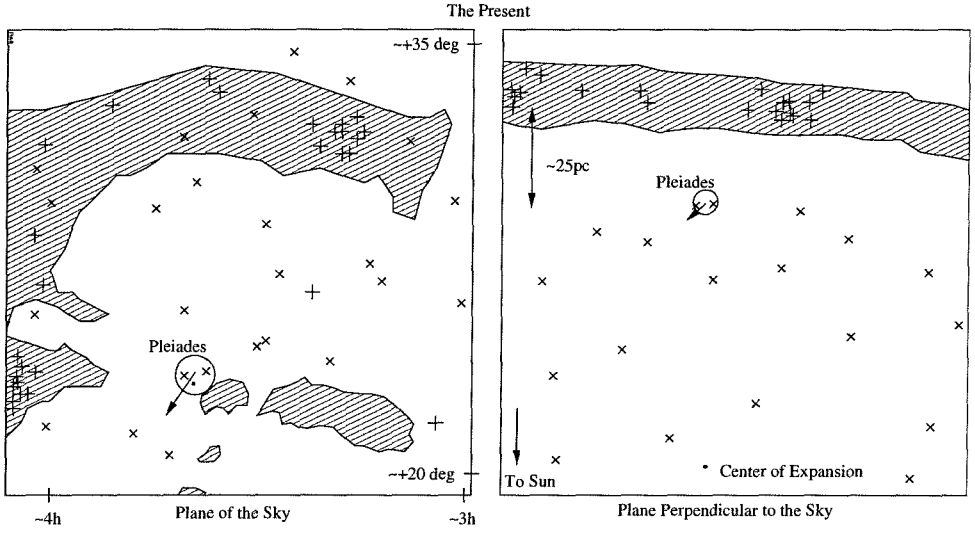

Figure 5.5 Schematic views of the Pleiades and Taurus clouds in both the plane of the sky and projected into a plane perpendicular to the sky. This figure shows the present epoch. Pluses again indicate approximate locations of known wTTS. In this set of panels, the Taurus clouds have the approximate shape that Ungerechts & Thaddeus (1987) found in CO emission.

with a velocity dispersion of 2 to 3 km s^{-1}.

The front edge of the expanding cloud of young stars would now be fairly close to us, explaining several of the nearby, young stars in Eggen (1995). These can be found as bright X-ray sources, with the correct space motion. The back side of the expanding cloud of young stars would now be approaching the Pleiades cluster, with radial velocities slightly higher than it (as our 2 stars display; Figs. 5.3, 5.4 and 5.5.) Presumably these stars have maintained this motion over their lifetimes, while bound cluster members with similar velocities are in orbits within the cluster. Members of this group would be harder to pick out of the field, unless a proper motion survey like that of HHJ were performed. Thus, we would predict that there are many other stars like HHJ 339 and HHJ 430, which have space motions similar to the Pleiades. Most of these should not be in the exact direction of the Pleiades nor at nearly its distance, but a few could be. It would then not be outrageously coincidental that these two stars appear to be in the cluster. Instead, this is an observational selection effect.

Indeed, Neuhäuser et al. (1995a) see a large population of X-ray bright late-type stars in the general direction of Gould's belt, most of which are far from any molecular clouds.

Our hypothesis can be tested three ways. First, if the kinematics of many of the cool, stellar X-ray sources in the general direction (up to tens of degrees away) of the cluster are studied, we would predict that a reasonable number of them would be considered part of the Pleiades supercluster. Second, if the detailed proper motion and parallax of HHJ 339 and 430 are studied (with HST, for example), we would not be surprised to find that they are really a little in front of the cluster and perhaps don't have exactly its space motion. Third, we would predict an excess of field stars closer than the Pleiades which show signs of youth (e.g., have lithium or rapid rotation) to be found in the general direction of Taurus and surrounding constellations, compared with other directions.

5.5 Conclusions

We have examined high resolution spectra of several of the faintest known stars in the Pleiades. None of them shows lithium, confirming that the lithium depletion limit and the region in the HR diagram inhabited by substellar objects occurs just faintward of them. The stars in our sample are very rapidly rotating and exhibit strong chromospheric activity, as evidenced by their Hα emission features. This chromospheric activity is not unusual for such stars. However, the fact that all of these stars are rapidly rotating shows that the previously noted (Stauffer et al. 1991) "leveling off" of Hα equivalent widths in young, very late-type stars is unrelated to a leveling off of rotational velocities. Given the current understanding of the rotational history of low mass stars, it is not surprising that these stars are all rapid rotators.

Two brighter stars, HHJ 339 and HHJ 430, exhibit lithium features and are clearly

young. We argue that these stars belong to the Pleiades cluster because of radial velocities, proper motions and HR diagram positions consistent with not only cluster membership, but also lithium depletion models. They were observed because they are apparently on the Pleiades pre-main sequence. The presence of lithium confirms that they are young. They must be some 50 to 100 Myr younger than most of the Pleiades stars. We discuss several explanations for this. One is that they represent very late star formation in the cluster, implying that stars have been forming in the Pleiades for a very long time. However, this explanation is problematic because the high density gas required for star formation is not present now, and stars of intermediate age are not obviously extant. As another explanation, the possibility that the cluster could have encountered a star-forming cloud recently enough to make these stars is also discussed; we argue that it would be difficult to arrange for the stars to have the right space motion unless the cloud had essentially always been related to the cluster.

We also consider the possibility that the stars formed in an unrelated cloud and then ended up as cluster members. Although it is conceivable that one such star might have escaped from a nearby star-forming cloud several million years ago, at the same time as the Pleiades passed by, and with the motion of the Pleiades, it is difficult to imagine two such stars being ejected in exactly the same direction and velocity at the same time.

On the other hand, there is a population of stars which are as young as our lithium stars and share the general space motion of the Pleiades. Our most plausible explanation of HHJ 339 and HHJ 430 is that they were born in this "supercluster." In this scheme, the star formation took place fairly recently at a location between the Sun and the Pleiades. Over the past few-to-tens of millions of years the nascent stars in this region became unbound and expanded such that these two stars, HHJ 339 and HHJ 430, can appear to be in the Pleiades. Since the "supercluster" exhibits the same space motion as the Pleiades, these two stars would appear to satisfy all the

usual membership criteria, except that they are unusually young. We do not advance this idea as clearly correct; it is just the most conservative explanation we could think of for these enigmatic stars.

Appendix A

The Palomar Deformable Mirror†

Ben R. Oppenheimer

Palomar Observatory, 105-24 California Institute of Technology, Pasadena, CA 91125

Dean Palmer, Richard Dekany, Anand Sivaramakrishnan

Jet Propulsion Laboratory, Spatial Interferometry Systems Group, Sec. 386

4800 Oak Grove Blvd., Pasadena, CA 91109

Mark Ealey, Thomas Price

Xinetics, Inc., 37 MacArthur Ave., Devens, MA 01433

Abstract

We present a study of the operating characteristics of the Xinetics Inc. deformable mirror and the driver electronics built by the Jet Propulsion Laboratory for Palomar Observatory's adaptive optics project. This mirror, the first of its type built by Xinetics Inc., contains 349 PMN actuators which control a 2 millimeter thick mirror surface coated with protected silver. Measurements are separated into static and dynamic categories. The static tests determine the unpowered figure of the mirror surface, the influence of solitary actuators on the mirror surface and how the actuators

†Previously published in *Adaptive Optics and Applications*, Proceedings of the SPIE, Vol. 3126, R. K. Tyson, R. Q. Fugate, eds. 1997.

move as a function of voltage applied, including considerations of hysteresis and creep. We have been able to flatten the mirror surface to an rms value of 19 nanometers. In the dynamic tests, we have resolved the motion of individual actuators whose voltages were changed at frequencies up to 1.5 kHz. The purpose of this study is to show that this deformable mirror has specific characteristics that must be determined in order to optimize its control.

A.1 Introduction

In 1994 the Jet Propulsion Laboratory (JPL) and the Palomar Observatory entered into an agreement allocating 25% of the 200 inch Hale Telescope observing time to JPL. In partial payment for this observing time, JPL would produce a major new instrument for the telescope. The decision was made that this would be an adaptive optics (AO) instrument, and that Cornell University (the third partner in time sharing of the 200 inch telescope) would construct a near infrared camera to be used in tandem with the AO instrument.

In 1995 the Jet Propulsion Laboratory began the AO project in earnest. The goal of the project is to produce diffraction limited images in the 1 to 2.5 μm wavelength range using natural guide stars. The AO system will mount at the f/15.6 Cassegrain focus of the telescope and includes a 16 $\times$ 16 sub-aperture Hartmann-Shack wavefront sensor and electronics to enable closed-loop operation at 500 Hz. Wavefront correction will be achieved with a tip-tilt mirror and a 349 actuator deformable mirror. Ultimately the system is designed to accommodate easily the addition of a laser beacon guide star. The system should be fully operational at the close of 1998.

This report details specific tests of the deformable mirror (DM) conducted at JPL between September 1996 and February 1997. The tests were designed to reveal

characteristics of the mirror in actual operation, which might affect the quality of wavefront correction. The tests can be broken into two groups: those dealing with the static figure of the mirror surface under the influence of the 349 actuators and those resolving the temporal behavior of the mirror.

The general finding was that the commonly-used simple picture of deformable mirrors—in which the mirror surface is assumed to be linear slopes between adjacent actuators—may not be a completely accurate model when compared to the actual mirrors, at least as evidenced by the one example studied here. The principal idea behind this study was that if we can understand how the mirror works in practice, we can adjust our control loop accordingly and improve wavefront correction.

First, we examined the specifications of the mirror and compared them with those specified by the manufacturer, Xinɛtics Inc.

A.2 Specifications of the DM

A.2.1 Xinɛtics's Acceptance Tests

The mirror surface is circular with a 5.850 inch clear aperture and a controllable surface with a 5.520 inch diameter. The casing is about 7.25 inches wide and the base is 8 inches deep. The optical axis of the mirror sits 6.125 inches above the bottom surface of the base, and the mirror is protected by a clear plastic cover. The mirror itself is a 2 mm thick face sheet of utralow expansion (ULE) glass silver coated on one side and attached to the actuators on the other. The actuators are attached to a base inside the casing. The mirror surface was extremely clean when it arrived at JPL, and it has remained so through this study.

The 349 lead magnesium niobate (PMN) actuators are arranged in a square grid pattern with a spacing of 7 mm. These actuators are meant to accept 0 to 100

V to deliver a mechanical stroke of at least 4 μm, with a maximum permissible difference of 2 μm between adjacent actuators. The influence of an actuator on its neighbor was found by Xinξtics to be 9 to 11% of the stroke of that actuator, and the hysteresis in actuator positioning should be less than 1%. Xinξtics states that the actuator frequency response is 4 kHz before it is attached to the mirror face sheet. This is the -3 dB frequency for an actuator connected to the Xinξtics driver electronics and moving through half of the full stroke of the actuator. The speed at which the actuators move is dependent upon their capacitance. In the original specifications before the mirror was manufactured this was meant to be 0.25 μF. However, the mirror that was delivered has actuators with an average capacitance of 1.6 μF. This will adversely affect the actuator movement speeds. Fortunately, though, the electronics were designed to exceed expectations, so this loss of a factor of 6 is accounted for and the actuators should respond quickly enough for our application. (See §A.4.1.)

The mirror surface is coated with "protected silver," an industry standard coating which gives greater than 95% reflectance from about 0.41 μm redward. This is needed because although the final result is a corrected near infrared wavefront, the wavefront sensing is done in the optical in the Palomar AO system (0.5 to 0.9 μm).

The acceptance tests run by Xinξtics Inc. found an average stroke of 5.31 μm with a standard deviation of 0.31 μm before they attached the mirror substrate. After attaching the mirror they measured the optical quality of the surface with no voltage applied to any of the actuators. "At a wavelength of 633 nm over the full aperture the peak-to-valley value of the surface is 0.54 λ (surface) with an rms value of 0.072 λ (surface) or $\lambda/14$ rms. Over the control aperture the peak-to-valley of the surface is 0.26 λ (surface) with an rms value of 0.063 λ or $\lambda/16$ rms."[1] All of these

[1]From *349 Channel Deformable Mirror for the Palomar Telescope: User's Manual, Program No. 5204* (Xinξtics Inc., 410 Great Road # A6, Littleton, MA 01460, (508) 486-0181), p. 7.

measurements are well within the specifications requested by JPL. The measurements we made are explained in the next two subsections. We find good agreement with the values quoted by Xinξtics.

A.2.2 Palomar AO Configuration of the DM

In the configuration used for the Palomar AO system, only the inner 241 actuators are addressed. This assigns every square of four adjacent actuators to one of the subapertures on the primary mirror. The actuators outside the inner 241 are "slaved" to those on the edge of the controllable region, so that they mimic exactly the voltages on the outer edge of actuators in the controllable region. (See Figure A.1.) Actuators within the shadow of the central obscuration of the primary telescope mirror are "slaved" in software.

The electronics that control the actuators were designed and built by Dean Palmer of JPL. They include a set of zener diodes arranged so that the difference in voltage between two adjacent actuators can be no more than 27.5 V. This prevents the accidental application of a large voltage difference between two actuators, which could result in ripping an actuator off the back surface of the mirror. The epoxy bond between the actuator and the mirror face sheet is apparently weaker than the face sheet itself, so this sort of damage will not render the mirror useless. Only the separated actuator would become useless. The electronics are connected to a high voltage power supply and to a computer which issues the commands to change the voltages on the actuators. Computer commands consist of the address of an actuator followed by an integer from 0 to 4095. Setting an actuator to 4095 results in the maximum voltage being applied to that actuator. This voltage is determined by the voltage gain potentiometer on the taxi receiver board and may be limited (or clipped) by the setting of the voltage limit potentiometer on the high voltage power supply. The high voltage power supply is nominally set at 100 V.

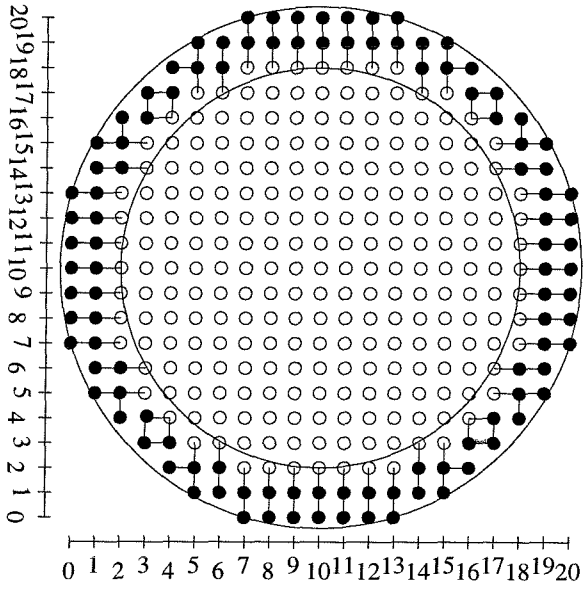

Figure A.1 A Map of the DM. Each actuator is indicated by a circle. The open circles are actuators addressable by the electronics. The closed circles are "slaved" actuators. They are connected to controllable actuators as indicated by the lines on the plot so that they always have the same voltage as the open circle actuator they are "slaved" to. The addressing scheme is indicated and represents a face on view of the front of the DM. The size of the telescope pupil image is indicated by the inner circle and the edge of the usable mirror is indicated by the outer circle.

A.2.3 The Zero Voltage Surface of the DM

The most rudimentary test we conducted was to measure the optical quality of the mirror surface with no voltage applied to any of the actuators. Using a Zygo Corporation interferometer we measured the surface images shown in Figure A.2.

The peak-to-valley value of the surface is 0.5728 μm with an rms of 0.0753 μm in the first image taken on 21 September 1996. The second image, taken on 26 September 1996, after five days of moving the actuators in the tests described in §A.3, has a peak-to-valley value of 0.5747 μm and an rms of 0.0729 μm. These values differ curiously from those reported by Xinξtics, who reported similar numbers but with units of λ rather than μm. We do not understand this discrepancy. (See §A.2.1)

There was a minor change in the zero voltage shape of the DM over this five-day period of testing. Figure A.3 illustrates this best: It shows the difference of the two images in Figure A.2. The peak-to-valley in this difference image is 0.0957 μm, with an rms of 0.0441 μm. The banded structure in this difference is an artifact of the Zygo interferometer and should contribute fairly negligibly to the peak-to-valley value, though it corrupts the rms value. This change in the zero voltage offsets of the actuators may be due to "creep" or hysteresis in the actuators.[2]

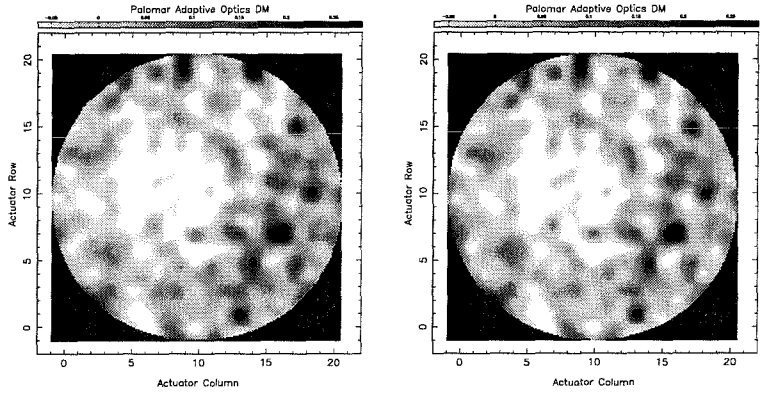

Figure A.2 The image on the left shows the surface of the DM with no voltages applied to any of the actuators. The image on the right shows the same such surface, but it was made five days later after various tests described in §A.3. The bar at the top of each plot explains the greyscale and the units are in μm. The x and y axes indicate the positions of the actuators behind the mirror surface.

Hysteresis refers to the effect by which an actuator will move a slightly different amount for the same change in voltage depending upon whether it is approaching the final voltage from above or below. It is a non trivial task to adjust the control loop to account for this non-ideal behavior because it would require an examination of the recent movement history of the actuator to determine the next movement. In principle, though, one could take the hysteresis into account when controlling the DM. We found in our tests described in §A.3.3 that the actuators in this DM have

[2]The phenomenon of creep and hysteresis in PZT and PMN actuators is well-known. See, for example, "Effect of PZT and PMN Actuator Hysteresis and Creep on Nanoindentation Microscopy" by S. M. Hues *et al.* in *Review of Scientific Instruments*, Vol. 65, pg. 1561 (May 1994).

hysteresis below 0.5% at room temperature. That is, the deviation from the ideal behavior is less than 0.5%.

Creep is a different effect whereby the actuator will continue to move slowly after its initial very fast movement. We have measured the time constant for creep in this DM's actuators. This is discussed further in §A.4.1.

One of the primary advantages of using PMN actuators as opposed to the more common lead zirconate titanate (PZT) actuators is that PMNs typically have far less hysteresis. In addition they tend to have fairly constant 0 V positions over significant aging periods (Cross et al. 1980). It has, however, been known for quite some time that the response of PMN actuators is rather temperature dependent (Uchino 1986). We will have to test this later, once the AO system is operational and on the telescope where the temperature varies significantly.

A.3 Tests of the Static DM

The tests described in this section were all conducted on time scales much greater than a few seconds. We believe that this timescale is much greater than the timescale in which the DM settles into a "semi-permanent" state after it has been given a command. Confirmation of this belief came only after we had carried out the dynamic tests described in §A.4.

A.3.1 Surface Control

The first set of active tests (meaning that voltages were applied to some or all of the actuators) on the DM demonstrated that we could control all of the 241 actuators. These tests were meant to show that the electronics were functioning as intended and that all of the actuators worked, at least on long timescales. This was accomplished

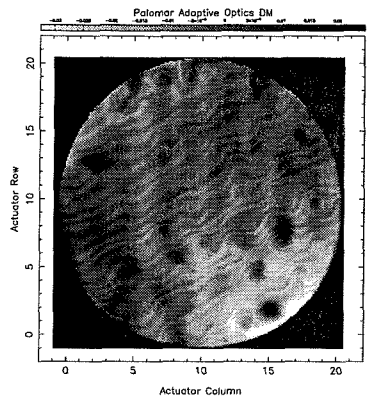

Figure A.3 The difference of the two images in Figure A.2. The scale at the top is in μm. See §A.2.3.

by applying patterns to the actuator voltages so that we could see with the Zygo interferometer that every actuator was functioning. We also applied tilts in x and y over the whole mirror surface, manipulated columns and rows and introduced a focus term to the actuator voltages, to produce a roughly parabolic shape in the DM.[3] All of these tests were successful, and they were repeated at various times between September 1996 and February 1997 to confirm that all the actuators and the electronics were working properly. At the end of February 1997 all of the actuators were functioning and were all still attached to the back of the mirror.

A.3.2 Influence Functions

Knowledge of how an actuator deforms the mirror surface is critical for good wavefront correction. Most correction algorithms currently in use assume that the shape of the mirror between two actuators is simply the slope that is a result of the difference in position of each of the actuators. In practice, however, there is an appreciable influence that a given actuator has on the mirror surface at and beyond the adjacent actuators. We performed tests to determine this influence. The influence function

[3]The shape was rough because the gains and offsets of the actuators were unknown, so the voltages were set as though all of the actuators had zero offset and identical gain. See §A.3.4 for a more detailed discussion of gains and offsets.

of an actuator is the actual surface deformation caused by the movement of that actuator.

To determine the influence function of a given actuator we applied a voltage to that actuator. Using the Zygo interferometer we then recorded the surface map and subtracted the zero volt image taken most recently. This provides an image of the actuator pushed up as though the rest of the mirror were perfectly flat. An example of this is shown in Figure A.4. The image in this figure is an expanded view of the center of the mirror. The actuator in the 10th column and 10th row has been pushed up to a setting of 1024 or 1/4 of the maximum voltage. Figure A.5 shows the same data but in horizontal line cuts through the image.

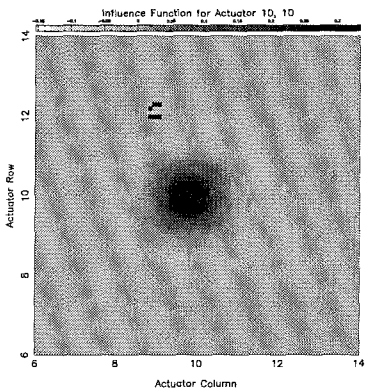

Figure A.4 Surface map of the central region of the mirror with a setting of 1024 applied to actuator 10, 10 (using the coordinate system defined in Figure A.1). The zero voltage offsets (as shown in Figure A.2) have also been subtracted from this map to show the movement of the actuator alone. The peak-to-valley value for the mirror in this case is 0.443 μm. There are a few bad data points near the top of the plot.

Upon examining many plots such as those in Figures A.4 and A.5, it was determined that the influence functions do not vary in shape from actuator to actuator by more than ~5%. (The gains of the actuators do, of course, vary, but that is discussed below in §A.3.3.) This variation is probably due to small differences in the placement of the actuators behind the mirror face sheet or perhaps variations in the thickness of the face sheet.

TABLE A.1 THE AVERAGE INFLUENCE FUNCTION
Measured every half interactuator distance

1.000	0.602	*0.110*	-0.024	*-0.014*	0.001	*0.000*
0.598	0.389	-	-	-	-	-
0.110	-	*0.018*	-	-	-	-
-0.025	-	-	-0.001	-	-	-
-0.015	-	-	-	*0.000*	-	-
-0.001	-	-	-	-	0.000	-
0.000	-	-	-	-	-	*0.000*

Values at neighboring actuators are italicized

The most apparent feature of the influence function is that it has a rounded square appearance when viewing the mirror face-on (see Figure A.4). This is because the actuators are arranged in a square grid pattern. In Table A.1 is a quantitative assessment of the influence function. This represents an influence function matrix oversampled so that the spacing between successive matrix elements is half the inter-actuator distance. The upper left corner of the matrix represents the actuator whose influence function is represented. Every other row corresponds to the next row of actuators on the face of the mirror. The influence function is symmetric about the central actuator.

The meaning of the numbers in the "Average Influence Function" is that the actual difference in position between nearby actuators will be adjusted by the fraction in the matrix. For example, if actuator (x, y) is commanded to move 0.700 μm further than actuator (x + 1, y), the actual difference in the positions will be $(1.000-0.110)\times 0.700$ or 0.623 μm. Similarly, if actuator (x, y) is commanded to move 0.700 μm farther than actuator (x + 2, y), and actuator (x + 1, y) is commanded to be at the same height as (x + 2, y), then the actual difference in height between actuator (x, y) and (x + 2, y) will be $(1.000 + 0.014) \times 0.700$ or 0.710 μm.

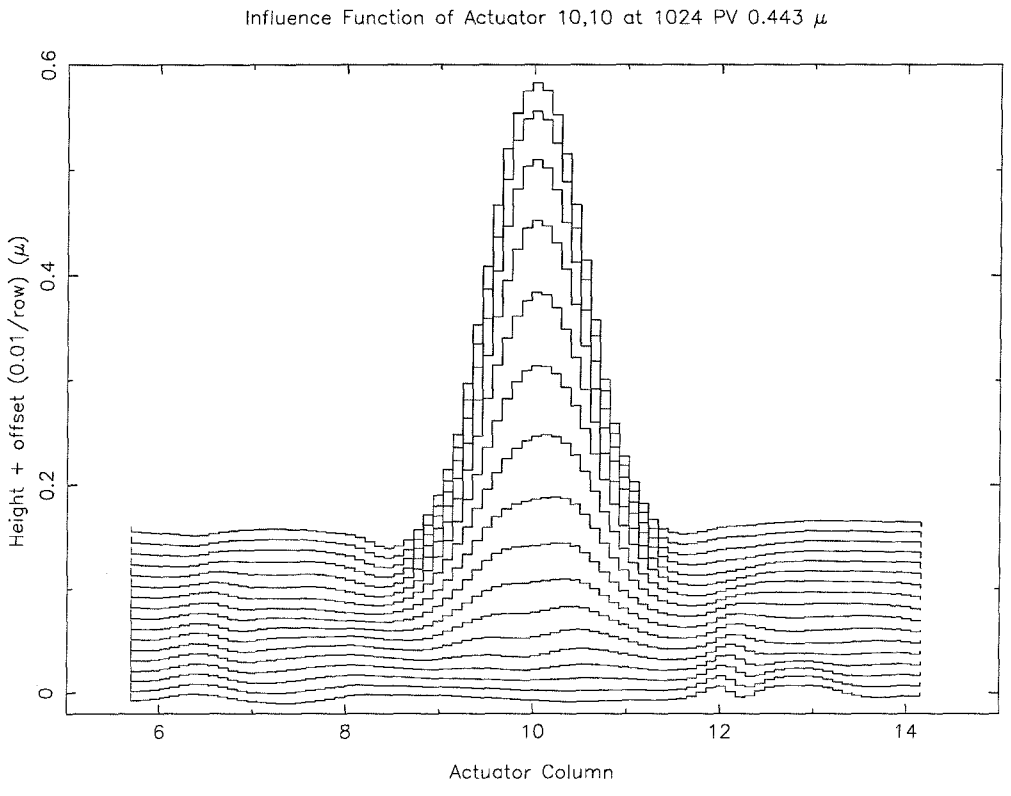

Figure A.5 A stack of horizontal cuts through the bottom half of the surface map in Figure A.4. Each horizontal cut is approximately one tenth of the interactuator distance, so the top plot corresponds to the tenth row of actuators on the mirror, while the bottom plot corresponds roughly to the eighth row. Each successive line plot is shifted up by 0.01 μm to make all of the horizontal cuts simultaneously visible.

A.3.3 Linearity Considerations

An important aspect of the DM performance is whether the actuators behave linearly and whether the influence functions of neighboring actuators combine linearly.

Figure A.6 shows the stroke of each of the actuators in the mirror as a function of actuator setting. (Only 3/4 of the full range of settings are shown in this plot.) Several pieces of important information can be derived from this plot. First one can easily recognize that for actuator settings above 1300, the gain for any given actuator is constant. To make this more quantitative, we represent the actuator height as a

function of the setting in the following form:[4]

$$H(s) = H(0) + as + bs^2$$

Here s is the setting, H is the height of the actuator, a is the so-called "linear gain" of the actuator and b is the "quadratic gain" of the actuator. One finds then by least squares fits to the data that the ratio b/a is on average 0.006, with an rms of 0.001. This shows the large relative importance of the so-called "linear" behavior over the quadratic behavior in the part of the setting range above 1300.

This linearity permits controlling the DM accurately with a linear algorithm in the range of settings above 1300. In that range, the total stroke has an average value of 4.2 μm, which corresponds to 8.4 μm of wavefront. The hysteresis we measured for the actuators was less than 0.5%.

The effect of moving adjacent actuators was investigated to determine whether the influence functions would simply add to produce the final surface on the DM. The assumption that the influence functions simply add seems to be correct to better than the 1% level.

A.3.4 Calibration and Precise Control of the Surface

Accurate, high-bandwidth operation of the deformable mirror requires a good determination of the gain of each individual actuator. By gain, we mean the multiplicative constant relating the actuator setting to its actual stroke in physical units (in this case μm), assuming the linearity discussed above.

In Appendix B we describe a scheme by which one can determine the gains of all of the actuators in an automated manner in a very short period of time, estimated to be less than two minutes under full automation. The utility of this approach is

[4]PMN actuators are known to behave quadratically in the sense described here over their full range, while PZTs behave more linearly. See, for example, J. A. Gallego-Juarez in *Journal of Physics E*, vol. 22, p. 804 (1989).

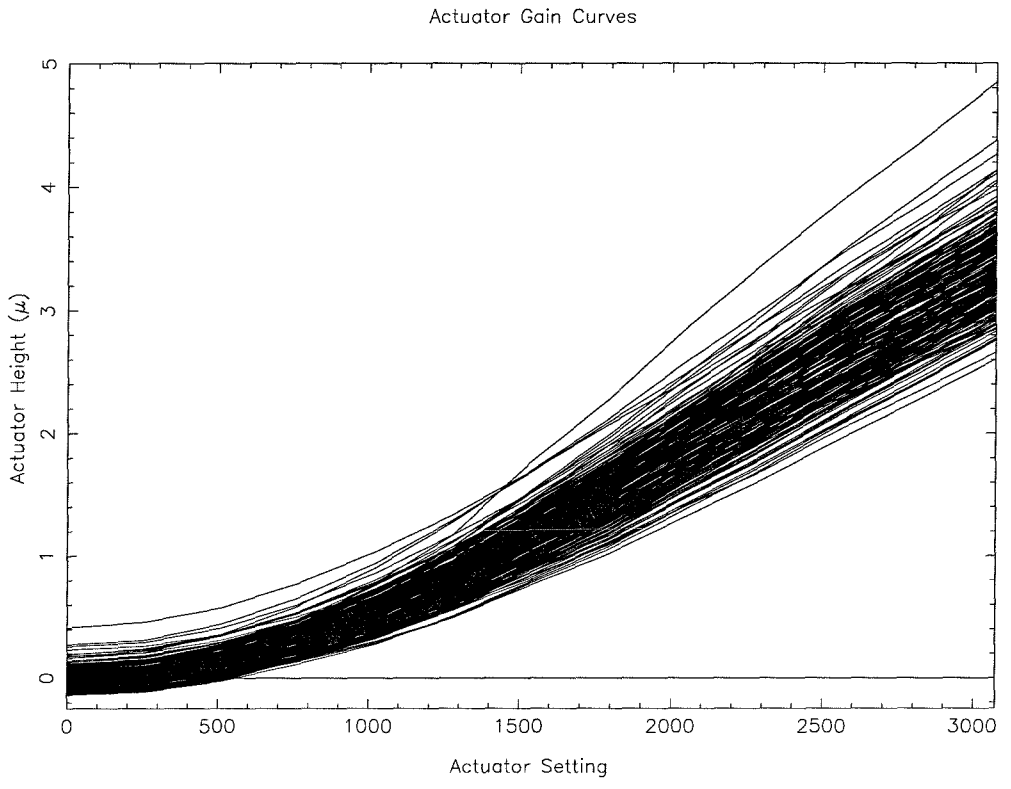

Figure A.6 This plot shows the gain curves for all of the actuators. Plotted on the ordinate is the stroke of the actuator in μm and on the abscissa is the digital setting of the actuator in the electronics. Only 3/4 of the full range of settings are shown here.

that one can quickly recalibrate the DM at any time during an observing run on the telescope. Although one would not expect the gains to change markedly during an individual observing run,[5] with this procedure implemented, one could in theory calibrate the DM many times a night. This allows for a quantitative assessment of how much the gains actually do change on many timescales. The scheme is fully described in Appendix B. Here we simply present the results of the scheme.

The scheme is iterative and attempts to flatten the mirror surface as accurately

[5]The AO team for the Keck observatory, at CARA, who are using an almost identical Xinξtics mirror, have reported that the actuators used in this type of mirror are rather sensitive to temperature variations. This might prove to be an important reason why one would want to calibrate the DM several times in a given night. See §A.5.1.

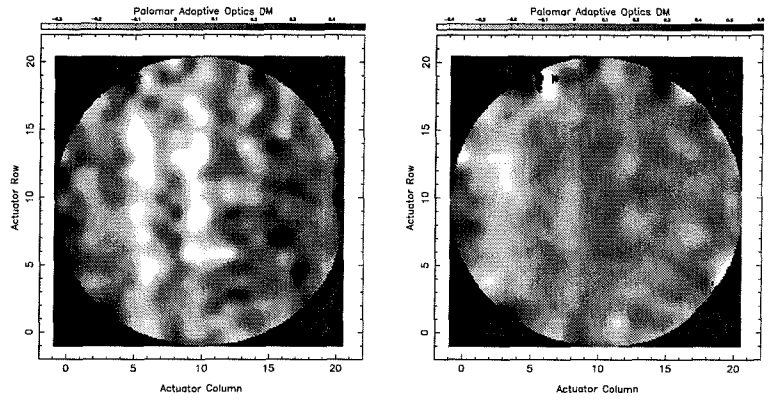

Figure A.7 The image on the left shows the surface of the DM in the first step of the flattening scheme. The peak-to-valley (PV) value in the inner controllable part of the mirror is 1.083 μm and the rms of that region is 0.189 μm. The right-hand figure shows the DM surface after the first iteration (PV = 0.656 μm, rms = 0.124 μm).

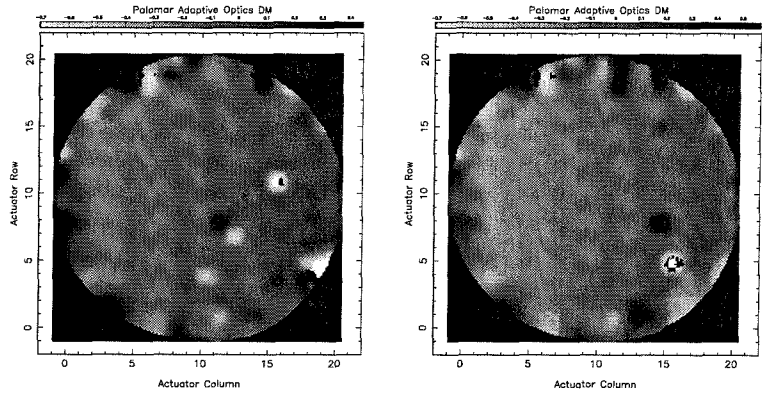

Figure A.8 The image on the left shows the surface of the DM after the second iteration of the flattening scheme (PV = 1.518 μm, rms = 0.093 μm). The right-hand figure shows the DM surface after the third iteration (PV = 2.159 μm, rms = 0.092 μm). In these images one can easily see that there are several actuators with far greater errors than the majority of the mirror. These are actuators whose gains were not well determined at these iterations.

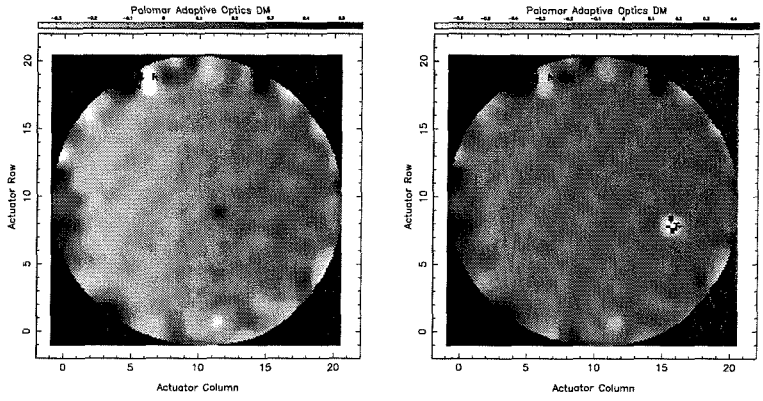

Figure A.9 The image on the left shows the surface of the DM in the fourth iteration of the flattening scheme (PV = 1.282 μm, rms = 0.066 μm). The right-hand figure shows the DM surface after the fifth iteration (PV = 0.436 μm, rms = 0.031 μm).

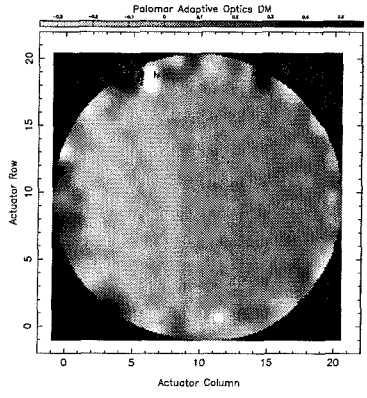

Figure A.10 The final surface of the DM after 6 iterations of the flattening scheme. The inner controllable surface has PV = 0.171 μm and rms = 0.019 μm. The edges of the mirror surface are not flat. This is because that portion of the surface is controlled by the slaved actuators. These actuators simply receive the same voltages as those they are slaved to. Since they have different gains, they will not be at the same height as the actuators inside the controlled surface. The beam fits easily within the flattened part of the surface.

as possible. It converges extremely rapidly, especially if the initial guesses for the gains are nearly correct. In six iterations during the first trial of this scheme, we were able to flatten the mirror's controllable surface to an rms figure of 19 nm with a peak-to-valley value of 171 nm. This requires a knowledge of the gains to three significant figures. Figures A.7 through A.10 demonstrate this result by showing the mirror surface at each iteration. Once this is fully automated, we believe we can do significantly better than this value of 19 nm rms. The accuracy of the scheme is only determined by the precision of the DM surface maps and how accurately the actuators can be controlled, which is nominally on the order of 5 to 10 nm.

A.3.5 The Effect of Zener Diode Protection of the DM

The electronics rack which Dean Palmer designed and constructed for controlling the DM has a built-in safety feature. The electronics will not permit a voltage difference of greater than 27.5 V between two adjacent actuators, or 55 V between two actuators separated by one in between. This is achieved with a grid of double zener diodes connecting all the actuators. The maximum difference in height between two actuators should not exceed 2 μm, to avoid risking damage to the bonds holding the actuator heads to the mirror face sheet. Setting the maximum voltage difference to 27.5 V places a more stringent restriction on the actuator behavior. This should only permit roughly 1 μm of position difference between adjacent actuators.

A.4 Dynamic Tests

In a dynamic test one moves the mirror while measuring its configuration many times per second in an attempt to resolve the temporal response of the actuators. The purpose of such tests is to determine how quickly a given actuator actually reaches its final position and whether one can operate the mirror at the desired closed loop

frequency of 500 Hz.

The dynamic tests were conducted with an optical heterodyne interferometer. This system is capable of measuring a single optical path length at a rate of 10 kHz. Since it can only measure one path length, we can only measure the movement of one point on the mirror at any given time. During these tests the laser beam was positioned at a number of locations on the mirror to ascertain whether different actuators respond differently. There are no measurable differences in the temporal characteristics of the ten different actuators measured.

A.4.1 Time Resolved Motion of Individual Actuators

Figure A.11 shows the mirror displacement as a function of time for a commanded motion of 1536 units. All of the actuators were commanded to move this amount and then back to the starting position at about a 10Hz rate. The position of the mirror was determined at a rate of 5 kHz. The initial and final positions of the actuators were chosen to be well within the linear part of the gain curves of the actuators (see Figure A.6). In later tests we ran the mirror at actuator update rates up to 1.5 kHz, to determine whether the response curve changes based on this frequency. It does not.

The plot in Figure A.11 has four important components. These are labeled with letters A through D. A corresponds to the movement of the actuator from the moment it receives a new voltage from the electronics. The rise time here is proportional to the distance the actuator has to move. It turns out that the slope of part A is the same regardless of the movement length. The slope is found to be the following (an average for several actuators):

$$v_{act} = 2.67 \times 10^{-4} \text{ m/s}$$

This is the speed of the actuator in meters per second. What this immediately reveals is that at a 500 Hz update rate, the maximum distance that an actuator can move is

0.53 μm. Commanding the actuator to move further than this is possible at a 500 Hz update rate, but the actuator will only have time enough to move 0.53 μm before it is commanded to move again. This actuator speed is determined by the capacitance of the actuator and the current used to drive it. The voltage on the actuator will obey the simple relation $dV/dt = I/C$. In this case I is 6.4 mA, and C is 1.6 μF. (We did not actually remeasure the capacitances of the actuators. This number comes from the original Xinξtics report.) This results in a slope of 3989 V/s which translates roughly to 2.11 $\times$ 10^{-4} m/s. Thus, the estimate is slightly slower than the measured value, but this is a rough calculation and a variation in the capacitance could cause such a discrepancy. The specifications provided by Xinξtics at the time of our electronics design quoted an actuator capacitance of 0.25 μF. With the present electronics rack, this capacitance would have yielded a speed of 1.3 $\times$ 10^{-3} m/s, and a maximum stroke at the 500 Hz update rate of 2.5 μm. This speed was chosen in the design of the electronics to exceed the needs of the AO system. As a result of this, the fact that the actuators have much larger capacitance has not had an adverse effect on the operability of the system: We expect that moves of 0.53 μm will be relatively rare except in very bad seeing conditions. If necessary, we can adjust the 6.4 mA current of the electronics rack simply by changing the current limit resistor on each of the 241 amplifiers.

Parts B and C of the plot represent the compensation of the overshoot of the actuator. The actuator reaches its commanded position and then overshoots in part A, by approximately 13 to 14% of the commanded distance. The reversal of the overshoot takes place in two separate phases. The first is a short phase which over compensates for the overshoot, but only to within 3% of the final position. This is designated B in the plot. This movement always seems to take the same amount of time, no matter what distance is commanded to the actuator. B has a time constant of 9.0 ms. Part C represents the final settling of the actuator to its commanded

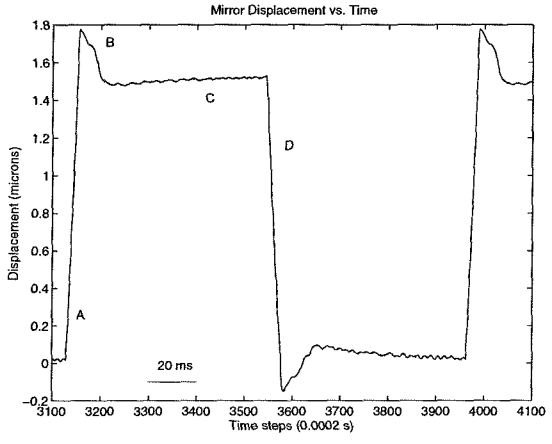

Figure A.11 The displacement of a single point on the mirror as a function of time. See the text for a full discussion.

position. This is the "creep" effect mentioned at the end of §A.2.3. It appears to be an exponential decay with a time constant on the order of half a second. However, within the 60 ms of part C shown here, the actuator reaches the final position to within 0.5%.

Finally, part D corresponds to the next voltage impulse from the electronics. It has the same slope magnitude as part A.

An important consideration is how long it takes for the settings to take effect. How much time elapses between the sending of a command from the computer to the actual physical motion of the actuators on the mirror? In the test set up, we issued commands from the VME crate to the DM electronics rack via a coaxial taxi line. Determining the time between the issuing of the command and the movement of the first actuator is difficult, but appeared to be approximately half a ms. In contrast, it was easy to determine the time between setting the first actuator and setting the last actuator on the mirror. This is 1.0 ms. These measurements were made using an oscilloscope attached to a diagnostic feed on the DM electronics and the output of the heterodyne interferometer's D/A. Clearly the dominating timescale is

the rise time of the actuator, which will average 3.1 ms for a 1 μm average movement. (That corresponds to fairly bad seeing conditions at the telescope, so one can expect better performance, of course, during calmer atmospheres.) The accuracy of the measurement presented here is ± 0.1 ms.

A.5 Unresolved Issues

A.5.1 Temperature Dependence of DM Performance

One issue which these tests were unable to resolve is whether the DM performance changes as a function of temperature. The CARA Adaptive Optics group, who are building the system for the Keck telescope, report that their 37 actuator Xinξtics DM, which is identical to our DM except in size, has greatly degraded performance in the lower temperatures characteristic of the Mauna Kea summit. All of our tests were done at the lab temperature which is held at approximately 20 degrees C. Some of these tests can be redone once the entire optics train is complete. Instead of the Zygo interferometer, we can use the phase shifting interferometer built into the AO system to redo all of the static tests at the range of temperatures at the top of the mountain. Unfortunately, the dynamic tests will not be repeatable on the mountain because of the lack of availability of the heterodyne interferometer.

More specifically, the CARA group report that the hysteresis and linearity of the actuator stroke functions degrade considerably at low temperatures. They also report that the equivalent of part C in Figure A.11—the creep of the actuators—has a much longer timescale at low temperatures. Unfortunately, we will not be able to remeasure the plot in Figure A.11 or conduct any of the dynamic tests at lower temperatures.

Appendix B

Deformable Mirror Calibration for Adaptive Optics Systems†

A. Sivaramakrishnan & B. R. Oppenheimer

Palomar Observatory, 105-24 California Institute of Technology, Pasadena, CA 91125

Abstract

We present a rapid technique for the simultaneous calibration and flattening of a deformable mirror in an adaptive optics system. We achieve an rms surface figure equivalent to better than $\lambda/100$ in the K band in our first application of the scheme. The technique requires the presence of a phase shifting interferometer within the adaptive optics system. Measurements of the mirror surface are made while each mirror actuator's gain is estimated, in a stable, iterative, convergent sequence. Knowledge of the mirror response function to single actuator activation (i.e., the so-called "influence function") is not needed. The iterative process ends when the mirror surface reaches some preset desired flatness, which can be specified by the rms deviation of the surface. An overall scale correction to the gains

†Previously published in *Adaptive Optical System Technologies*, Proceedings of the SPIE, Vol. 3353, D. Bonaccini, R. K. Tyson, eds. 1998.

is measured and applied after the iterations converge. Our technique uses the mirror under conditions similar to those present when the adaptive optics system is running. This technique provides the user the ability to calibrate the mirror in a matter of a minute or two, enabling re-calibration of the actuator gains many times during a night with minimal impact on observing duty cycle, in order to adapt to changing conditions.

B.1 Introduction

Adaptive optics (AO) systems using deformable mirrors with a few hundred channels of sensing and actuation are becoming quite common. Several functioning systems have demonstrated the feasibilty of this approach to ground-based, high-resolution imaging. The key to making an AO system work well is a thorough understanding of the many parts that comprise the instrument. A critical part of most AO systems is the deformable mirror (DM), the component that actually performs the wavefront correction.

During the development of the AO system for the Palomar Hale 5 m telescope, we spent considerable time on understanding the behavior of the 349 actuator deformable mirror made by Xinetics. The mirror and our work on understanding it are described elsewhere (Oppenheimer et al. 1997c; §A). The results of our previous work are an understanding of the DM's dynamics on millisecond timescales and the characterization of the behavior of the mirror surface under the influence of the actuators. During that exercise, we devised a rapid calibration scheme which we present in detail here. This scheme permits DM recalibration many times a night with little impact on the observing duty cycle. This is important because PMN-actuated DMs (such as our Xinetics mirror) exhibit strongly temperature-dependent behavior (Acton et al. 1996). In our first test of this calibration scheme, we controlled the

mirror surface to an accuracy of 19 nm rms. We anticipate doing much better once the process is fully automated.

It should be noted that it is possible to operate an AO system in closed loop with a fairly rough knowledge of the actuator response to specified voltages, because the AO loop is itself an iteration of a (usually) convergent process. However, such an approach achieves DM control at the expense of precious bandwidth, and the quality of the wavefront correction is degraded, especially for faint targets (Brigantic et al. 1997). Without well-calibrated gains, one cannot assert a specified shape onto the DM surface in one step.

B.2 The Calibration Scheme

In the case of the Palomar Xinetics DM, we need to determine the gains for 241 actuators of the DM—although there are 349 actuators, only the inner 241 are used in the system.

We define the gain of an actuator as that multiplicative constant which converts a digital actuator setting (which comes from the control computer) to a relative position of that actuator in physical units, such as microns. The actuators have been shown to behave linearly over most of their commanded range (Oppenheimer et al. 1997c), so the assumption of a constant gain is a useful approximation. Our calibration scheme flattens the DM and determines the relative gains of all of the commanded actuators simultaneously. The scheme is iterative, and it flattens the mirror surface to an arbitrarily chosen accuracy.[1] This calibration scheme requires the presence of an interferometer with which one can measure the surface figure of the DM. In our first tests

[1]The actual accuracy depends on how well the actuators can be controlled and on how well the mirror surface can be measured. Actuators with significant hysteresis or non-linearities will of course degrade the accuracy of the calibration and control. The final figure of merit, after convergence is achieved, is a measurement of some combination of all such errors. We suspect that the largest source of error is probably hysteresis.

of the scheme, we used a Zygo Corporation interferometer, and analyzed the data it took with our own software. Once the AO system is fully operational, we will be able to do this using the "stimulus" subsystem of the instrument (Dekany et al. 1997), which is capable of producing interferograms similar to those produced by the Zygo. In the following we refer to "the interferometer" generically. With the stimulus interferometer integrated into the AO system, the calibration and flattening scheme will be fully automated, since the computer that analyzes the interferograms will also be capable of issuing new commands directly to the DM.

The technique consists of the following steps.

1. We make an initial estimate of the gains for all the actuators. This could be either the set of gains from previous measurements, or simply the crude estimate that all the gains are equal to maximum movement (in μm) divided by the maximum digital setting on the actuators's DAC. In the case of the Palomar AO system, this estimate is $5.0\mu m/4096$. We represent the gains as g_i^j, the gain of actuator i at iteration j. Initially j is zero and i ranges from 1 through N, the total number of actuators.

2. We set all actuators to the midrange value

$$s_i^0 = 2048,$$

where s_i^0 is the setting for actuator i at the zeroth iteration. This moves each actuator to a height $h_i(s_i^0)$.

3. We then measure the height of the mirror surface with the interferometer. We call this measurement z_i^j, where i and j have the same meaning as they do in the notation for g and s. Because of the nature of the interferometric measurement, the value of z_i^j is actually the height of the mirror surface at actuator i relative to the *average* height of the mirror surface:

$$z_i^j = h_i(s_i^j) - \textstyle\sum_i h_i(s_i^j)/N$$

4. We attempt to reduce each z_i^j to zero in the next iteration by moving the actuators. To do this, we compute new settings for all the actuators:

$$s_i^{j+\frac{1}{2}} = s_i^j - z_i^j / g_i^j$$

These new settings are given the $j+\frac{1}{2}$ iteration number because they are not the actual settings we should assert on the mirror. An additional constraint on the settings is necessary for convergence of the scheme. Application of this constraint comprises step 5.

5. We constrain the average of the settings at all iterations to be s_i^0, the midrange value of the digital setting:

$$s_i^{j+1} = s_i^0 + s_i^{j+\frac{1}{2}} - (\textstyle\sum_i s_i^{j+\frac{1}{2}})/N$$

6. We apply these new settings, s_i^{j+1}, and make a new measurement with the interferometer, thereby determining a new set of deviations from the average height of the surface, z_i^{j+1}.

7. With the new measurements of z_i^{j+1}, we can correct the gains, with a proviso on the size of correction being larger than some threshold—we recompute new gains for all settings that have changed by more than a threshold value, which we chose to be some small fraction t of the largest setting s_{max}:

$$\text{If } |s_i^{j+1} - s_i^j| > t s_{max}, \text{ then}$$

$$g_i^{j+1} = (z_i^{j+1} - z_i^j)/(s_i^{j+1} - s_i^j)$$

The purpose of this tolerance is to prevent division by small numbers, and to set a tolerance on the final flatness of the mirror surface. In practice t should be chosen to reflect the level of controllability of the actuators, which in this case will be dictated by their intrinsic hysteresis. Before convergence of the gains is achieved, there may be small differences between the mean heights of the mirror in any two consecutive steps. This is essentially because the constraint in step 5 cannot be applied to h_i^j directly, which is unmeasurable. More detailed discussion of this follows step 8.

We have not proved rigorously why convergence of the gains is possible using the above expression, though we have demonstrated that this process does converge in practice.

8. We loop back to step 4 until the gains and settings no longer get changed during an iteration. After this convergence is achieved (which in practice occurs in less than ten iterations, depending on the value of the tolerance t), it is possible that some of the actuators will have g and s equal to their initial values (i.e., they were never changed during the iterations). Such actuators fortuitously start off within the tolerance setting of the correct position for the final flat surface with the initial midrange setting. The gains of these actuators will not be well determined, since they remain at whatever their initial estimate was. To account for this possibility, and to ensure that the gains are determined for all the actuators, we repeat the whole process at new values of the initial settings, $s_i'^0$. The new values are computed by imposing a 1 μm increase in the heights of all the actuators from the flattened position:

$$s_i'^0 = s_i^{final} + 1\mu m/g_i^{final}$$

This forces the mirror to a new position where most of it will still be as flat as before, but the actuators with poorly determined gains will be at incorrect heights (unless the initial gain estimates were very close to their real gains). Repeating the iterative flattening process at this height will determine accurate gains for all the actuators. If necessary, yet one more shift can be executed. Verification of a good gain determination is simply achieved by choosing an arbitrary height and trying to flatten the mirror at that height.

Finally gains have been determined, but an additional correction is necessary.

B.3 Gain Correction

The iterative process described above produces the ability to achieve good absolute flatness, but at a height that is known only approximately, unless all the actuator gains are equal. To see this, we note that after convergence the constant height of the flattened surface is related to the harmonic mean of the gains (we have dropped the iteration indices here for convenience):

$$h = h_i = s_i g_i$$

This means that all the heights are equal. Furthermore, we know that

$$N s^0 = \sum s_i,$$

so

$$N s^0 = h \sum (1/g_i).$$

If the variance of the gains is small compared to their values, this height is approximately (excluding terms or third or higher order)

$$h = \bar{g} s^0 (1 + \sigma_g^2 / \bar{g}^2),$$

where $\bar{g}$ is the mean of the gains produced by the iterative process, and σ_g^2 is the variance in these gains. Thus the surface is slightly higher than it would have been had all the gains been equal.

This has important ramifications for the gain calculations. In fact, the gains calculated in the iterative process, ending with the completion of step 8 will be scaled slightly from their true values by the amount $(1 + \sigma_g^2/\bar{g}^2)$, excluding higher order terms in the binomial expansion. In our case this scale change amounts to about a 4% error (because of the variance of the gains in our particular mirror). This scale change is easily calculated using the expression given above, or it can be ignored at the expense of very little bandwidth in the AO closed loop operation. However, the application of this correction is essentially trivial.

Another way to see this complication is by considering the constraint in step 5 again. By changing the settings we expect to apply after using the gain in step 4, we have slightly different new settings. The difference between $s_i^{j+\frac{1}{2}}$ and s_i^j is the key here and is related to the variance of the gains as described above.

A way to test our gains experimentally is to attempt to assert a flat but *tilted* surface on the DM. We expect the interferometric measurement of heights on the DM surface to be a plane with the slope that we have chosen. Fitting the measured heights with a plane will reveal the accuracy of our gain estimates. If the slope of the fitted surface is constrained to be equal to the asserted slope, spatially correlated errors in the resultant fit would probably reveal where our assumptions of linear gains break down.

B.4 Results

We present the results of this scheme in a series of surface maps which are presented in Appendix A, Figs. A.7 – A.10. These surface maps were made at each iteration. In this case, the scheme converged in only 6 iterations. The final image shows the flattened mirror. The central region of the mirror, which is the only controllable part of it, has a residual rms figure of 19 nm.

In practice, the final set of s_i can be used as initial offsets the next time the mirror is calibrated. The mirror can be set flat in the middle of its throw with these settings, and operation of the closed loop AO control can simply commence using the gains determined in this calibration procedure.

During the iterations of the loop occasionally single actuators will poke dramatically above or below the rest of the surface. This can be explained simply, if one considers exactly what the scheme does. Our tolerance requirement in step 7 does not disallow new updates of actuator settings. It only prevents gains from being updated

in a given iteration if the new actuator setting is within a certain tolerance of the last actuator setting. In fact, the scheme updates all of the acutator settings at every iteration. As a result, the actual height of the flattened mirror surface can fluctuate by a small amount from iteration to iteration. Thus, for an actuator whose original setting only changed slightly, within the tolerance in step 7, it may take several iterations before the mirror surface moves enough that the next setting will be outside the tolerance. Then since the gain for that actuator is not well known (i.e., it might never have been updated), the new setting will be quite wrong. The gain for this particular actuator then will be corrected in the next time step. Indeed, one can see from the figures that these actuators only poke up or down for a single iteration. Subsequently they have correct gains and are well-controlled for the rest of the iterations.

This particularly demonstrates why one needs step 8, in which the mirror is then flattened again at different heights. The actuators whose gains never get updated will be grossly out of place at the other heights.

B.5 Discussion

If we do not apply the constraint in step 5, the whole surface (or its average height) will drift away from its starting value. Such drift is a generic instability that must be dealt with in some fashion. If the iterative scheme is viewed as an abstract dynamical system in a phase space of the estimated gains, without the constraint the initial point representing out first guesses escapes in a few iterations to a globally attracting point at the origin. At this stage we would be attempting to assert a surface with infinite values of the settings s_i. Adding the constraint changes the dynamical system qualitatively: it removes this instability, and the resultant dynamics is enacted in the basin of the attracting fixed point which corresponds to the desired gains, which is colinear with both the point representing the true gains and the origin.

A second order analysis of the behavior of the unconstrained dynamical system in the neighborhood of the fixed point of the relative gains shows that the instability is quadratic in the rms of the gain errors at that iteration.

The computation required for these iterations is quite modest, since no gain matrix inversions are required. Estimates of actuator response functions are also not used in this scheme.

The authors wish to dedicate this work to Horace Babcock.

Appendix C

The Palomar Fast Steering Mirror

C.1 Purpose of the FSM

The design of the Palomar adaptive optics system (Dekany et al. 1997) calls for the insertion of a fast steering mirror (FSM) in the light train. The FSM causes the third reflection after the light reaches the adaptive optics bench (which is mounted at the Cassegrain focus of the telescope). The light train is presented in Fig. C.1 (Dekany et al. 1997). The principal purpose of the fast steering mirror is to provide a first order correction to the wavefront incident on the telescope aperture. The limited stroke of the deformable mirror (DM, §A) and the large contribution of the atmosphere to the wavefront tip-tilt energy requires an FSM independent of the DM. The manifestation of this first order, or tip-tilt, correction by the FSM is a compensation for image motion in the focal plane of the telescope. The image motion may be due to actual wavefront tip or tilt caused by atmospheric turbulence or may be the result of imprecise telescope tracking. In either case, the FSM is required to compensate up to $\pm$ 2″ of image motion in the science camera (labeled "PHARO" in Fig. C.1; Brandl et al. 1997) with a closed-loop bandwidth of 10 Hz. This bandwidth requires a dynamically stable operation at update rates above 100 Hz. This specification, which dates to the

preliminary design review on April 14, 1995,† has since been found to be inadequate. In §C.4 we detail why this is the case.

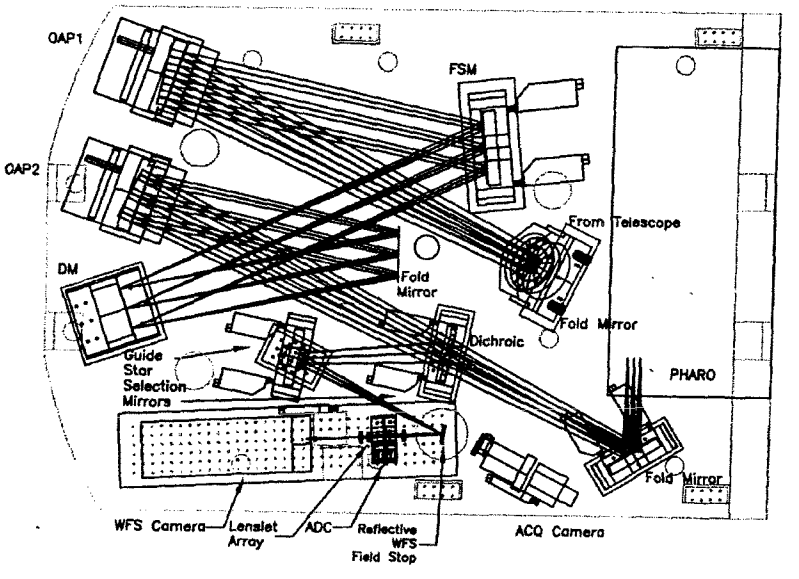

Figure C.1 Optical layout of the Palomar adaptive optics system. The prominent optical elements are labeled. The FSM is the third reflection in the system and is at the top of the figure just right of center. (Courtesy R. Dekany.)

In the following section we describe the mechanical design and implementation. §C.3 describes the performance of the FSM, as constructed, both in the lab and on the telescope.

C.2 Mechanical Design

The size of the beam at the location of the FSM requires that the mirror itself have an 8" diameter. This unfortunately poses difficult dynamical problems, because a mirror and mount of that size made of modified off-the-shelf products is necessarily massive. These sorts of massive objects generally have rather low resonant frequencies. The

† On this date I reached the 24^{th} year of my life.

mirror itself, which measures 8 × 1", made of Zerodur glass and polished to $\lambda/10$ at HeNe laser light over 95% of the central region by Precision Optical (Costa Mesa, CA), has a mass of 2.5 kg and a resonant frequency of 1.5 kHz. However, the moving parts of the gimbal mount itself adds another 3.5 kg. To actuate an object of this mass at frequencies above 100 Hz means that the mount requires modification, probably as sophisticated as a momentum compensation system for the moving parts. In spite of this, we built the mirror with minimal modifications to the mount at first. The performance, described in the next section, necessitated some improvements to raise the resonant frequency of the mirror mount.

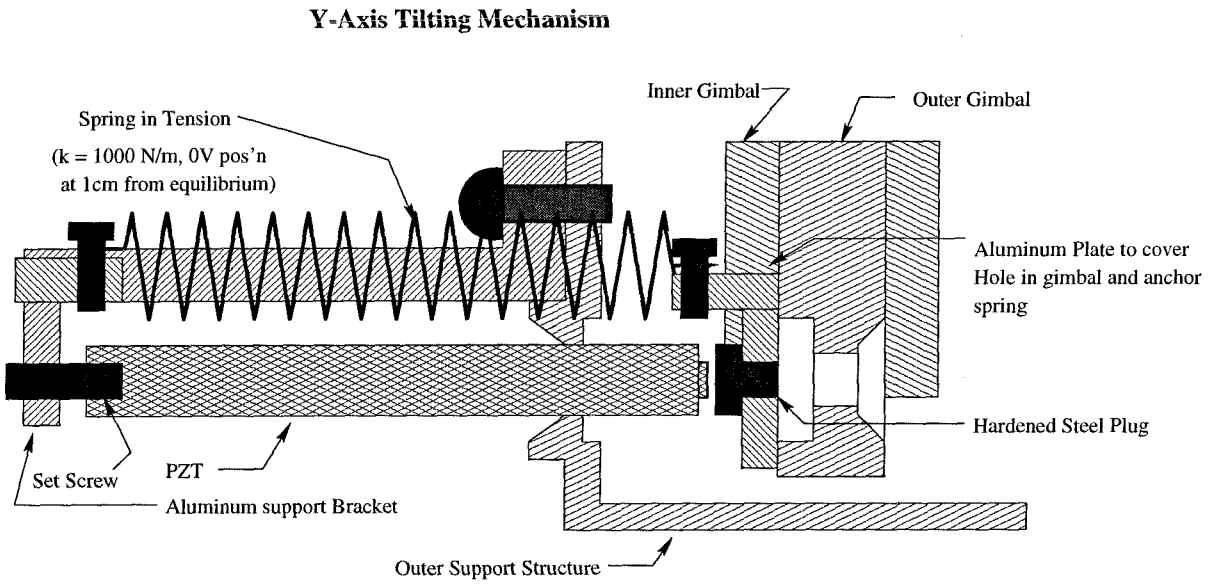

Figure C.2 FSM Y-axis tilting mechanism. This diagram shows the arrangement of the aluminum bracket and spring which hold the PZT in place on the modified Aerotech gimbal mount.

The optical mount, manufactured by Aerotech Inc. (Pittsburgh, PA; Model number AOM 110-8), is an 8" aluminum gimbal mount coated with black epoxy paint. The entire mount has a mass of 5.5 kg. The gimbal is comprised of inner and outer rings held in place with ball bearings between the two rings and between the outer ring and the mounting base. We had originally intended to replace these ball bearings

with flexure pivots of the same size as the balls. The flexure pivots provide stictionless rotation of the gimbals. We purchased these pivots from R. P. Luce and Co., Inc., (Sag Harbor, NY; Part No. 5020-800), but the first lab tests indicated that they were not necessary. They were never installed.

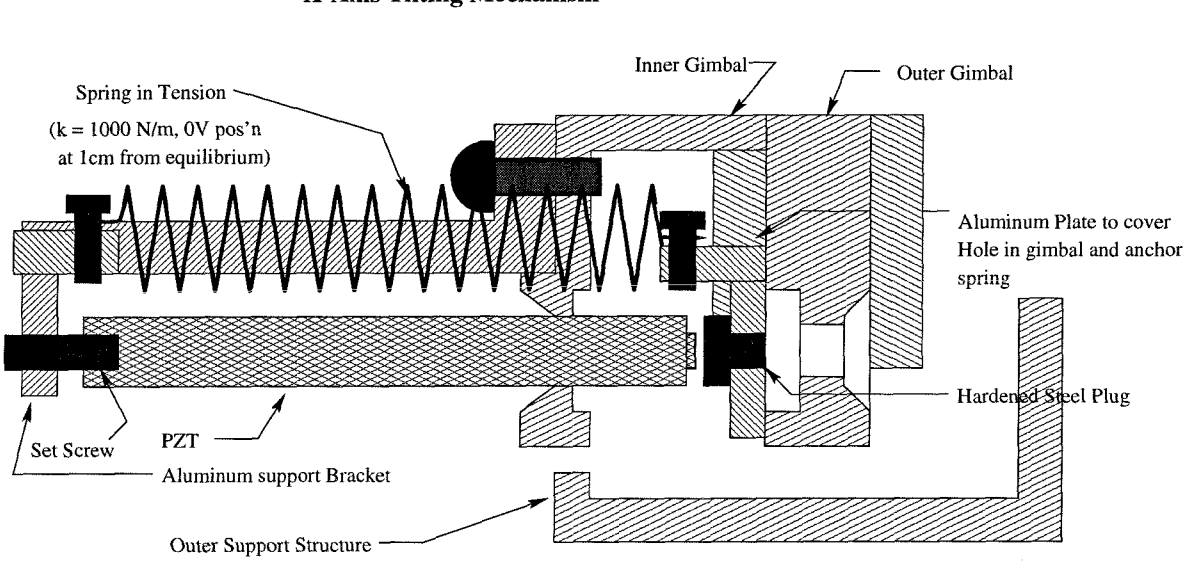

Figure C.3 FSM X-axis tilting mechanism. This diagram shows the arrangement of the aluminum bracket and spring which hold the PZT in place on the modified Aerotech gimbal mount.

After receiving the mount we made several modifications. The first was to install a three point support system for holding the mirror in place. The mount, as sold, has three Teflon-headed screws holding the back of the mirror against a ridge on the inside of the inner gimbal ring. This causes distortion of the optical surface. To account for this we cut away the ridge and positioned another set of three Teflon-headed screws directly opposite those in the back of the mount. (These same modifications were made to several other mounts in the AO system: those for Fold Mirror 1, Star Selector Mirrors 1 and 2 and Fold Mirror 3.) After this modification, we inserted the mirror and measured the optical surface with a Zygo Corporation interferometer. The figure displayed $\lambda/12$ rms surface quality at HeNe laser light (633 nm) over the

region illuminated by the science beam.

The next set of modifications permitted the installation of piezoelectric devices (PZTs) which would be directly controlled by the AO electronics. By chance, the holes for the positioning screws that came with the Aerotech mount were the same size as the PZTs we purchased to actuate the mount. The PZTs (manufactured by Physik Instrumente, Inc., Costa Mesa, CA) are 60 μm maximum expansion stacks operating between 0 and 100 V (Model 841.40 with modification 840.95). The casing measures 86 mm in length and 12 mm in diameter. The PZTs used include a strain gauge installed in the casing to provide feedback on the stack's expansion distance, and a non-magnetic, stainless steel, half-spheroidal end piece. These devices are capable of 800 N of maximum pushing force, but are extremely sensitive to non-axial forces. Torsion or lateral forces on the stack can break the stack's conductivity and cause electrical arcing. The result of this is the instant destruction of the usefulness of the device. In light of this we designed and constructed mounts for these PZTs (one for each axis) which would ensure minimal, if any lateral or torsional forces on the PZT stack. These designs are shown in Figs. C.2 and C.3. Fig. C.4 shows an expanded view of the interface between the moving part of the PZT and the modified mount.

The designs shown in Figs. C.2 and C.3 are essentially brackets which hold the PZTs into the mount. In the x-axis, the bracket is bolted to the inner gimbal, which rotates around the y-axis inside the outer ring. The bracket also has an arm protruding to one side. This arm keeps one end of a stainless steel extension spring, 3" long and 5/8" outer diameter, pinned in position. The other end of this spring is attached to the outer gimbal. This keeps the PZT pinned to the outer gimbal. The actual tip of the PZT (a spherical end piece) is in contact with a hardened steel slug screwed into a steel plate that covers the hole where Aerotech's original positioning screws passed through the gimbals. The spring is kept at a tension of approximately

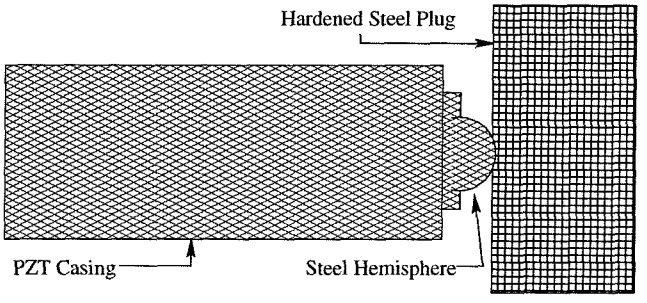

Figure C.4 PZT to steel plug interface. This diagram is a close-up view of the active end of the PZT. This end has a hardened stainless steel spherical attachment which is in constant contact with the smooth, hardened steel plug attached to the gimbal mount. This arrangement allows for the PZT to move back and forth while sliding a small amount along the tilting steel plug. This minimizes the lateral and torsional forces on the PZT stack. The set screw in this diagram permits the accurate positioning of the PZT, to ensure the extension of the spring to 1 cm from equilibrium.

10 N. This ensures that the PZT always remains in contact with the steel plug.

The y-axis bracket is almost identical to the x-axis, but the bracket is attached to the mount base and the spring attaches to the outer gimbal. This permits the PZT to move the outer gimbal relative to the mount base. Thus, the x-axis PZT moves the inner gimbal relative to the outer gimbal.

The brackets were machined out of aluminum. A picture showing the back of the FSM with both brackets, and PZTs installed is shown in Fig. C.5. The PZTs are hidden by the brackets, which are the silver pieces coming out of the black mount parallel to the optical bench. Two wires emerge from the PZTs, one for the applied voltage and the other for reading the strain gauge. The springs are visible as the shiny cylindrical components to the right of each bracket. The cable for voltage to the stack is attached to the voltage amplifier on the right side of the image.

C.3 Performance

To assess the performance of the FSM before installing it in the AO system, we created a milled piece of aluminum with the same dimensions as the glass mirror.

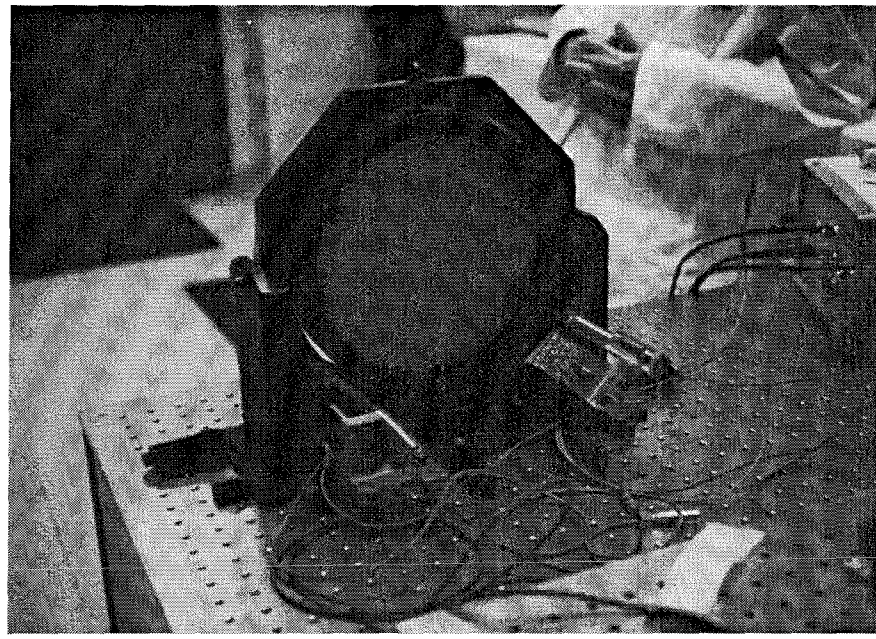

Figure C.5 Photograph of the back of the FSM. This photo shows the final implementation of the modifications to the mount to accommodate the PZTs. For a detailed description see the text. In this setup the actual mirror is not installed in the mount. Instead, a dummy mirror made of solid aluminum, which has almost exactly the same density as Zerodur glass, is installed to permit testing in the lab without risking damage to the mirror.

Aluminum and Zerodur glass have essentially the same density. Thus the dynamics of the mount with the mirror or the dummy mirror installed should be identical.

The first test involved driving each axis of the mount with a sine wave signal with an adjustable frequency and amplitude. This was done by attaching the PZT to a Physik Instrumente voltage amplifier with an input from a standard signal generator. Upon running each PZT through its maximum range (0 to 100 V) with a range of frequencies starting at 1 Hz and proceeding to 100 Hz, we found a dramatic, loud ringing at approximately 63 Hz. This was the first fundamental resonance of the mount. Unfortunately this is well below the specified operating frequency of 100 Hz. In order to quantify the resonance and understand what part of the mount was most susceptible to it, we (with the help of R. Grogan, JPL) attached accelerometers to the

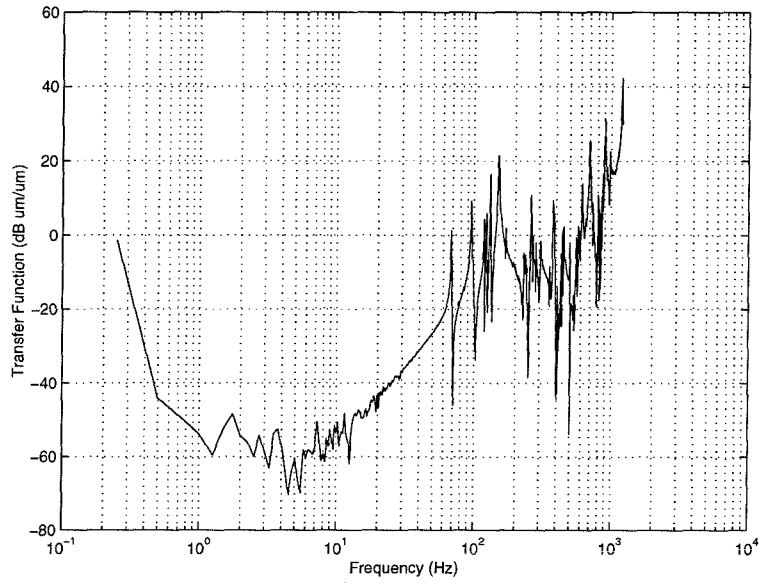

Figure C.6 Transfer function with accelerometer on the inner gimbal and the inner gimbal actuated. The first resonance is clearly visible here at 63 Hz.

mount in several locations and actuated the PZT with a white noise signal with rms amplitude of 30 V. The accelerometers were attached to a data acquisition system on a PC which was able to record the time series of the acceleration of the various parts of the mount. From this we were able to reconstruct the transfer function. The transfer function is one minus the ratio of the number of μm that the PZT moved to the number of μm that the accelerometer moved as a function of frequency.

In four tests we were able to determine that the part of the mount with the lowest resonant frequency was the outer gimbal ring. This ring is substantially thinner than the inner ring. Since this ring is thinner than the rest of the mount, it is more susceptible to flopping mode resonances. The accelerometer tests indicated that the first flopping mode over an axis in the plane of the ring and parallel to the optical bench was mostly responsible for the resonance. The way this was determined is as follows. The accelerometer was placed on the inner and outer ring and in each case the inner or the outer ring was actuated independently. The result is four different

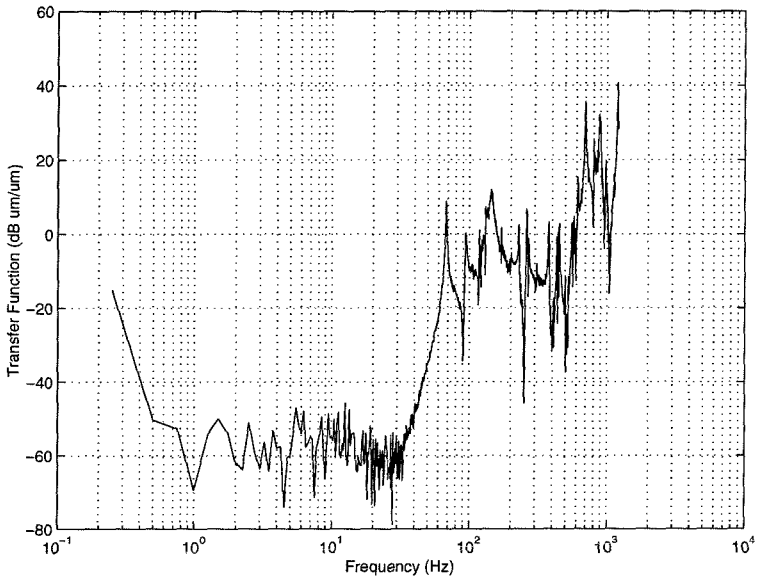

Figure C.7 Transfer function with accelerometer on the anner gimbal and the outer gimbal actuated. This figure along with Fig. C.8 show that there is substantial cross talk in the FSM mount.

transfer functions: (1) the motion of the inner ring while the inner ring is actuated, (2) the response of the inner ring when the outer ring is actuated, (3) the response of the outer ring while the inner ring is actuated, and (4) the response of the outer ring with the outer ring being actuated. The transfer functions for all four of these tests are presented in Figs. C.6, C.7, C.8 and C.9.

For the first trial run of the Palomar Adaptive Optics System (Dekany et al. 1997), we used the FSM in the configuration described so far. However, during that run, we were unable to run the FSM at update frequencies above 50 Hz, so the resonance shown in the figures had little impact on the tests performed.

The second trial run, in December 1998, required the capability to run the FSM at frequencies above 100 Hz. For this reason we stiffened the outer gimbal. To do this we purchased a 1 $\times$ 1" bar of cold pressed and hardened steel. Using a vice and several people, we were able to bend this bar into an arc with the same radius as the outer gimbal ring. We attached this bar to the gimbal by drilling holes through the

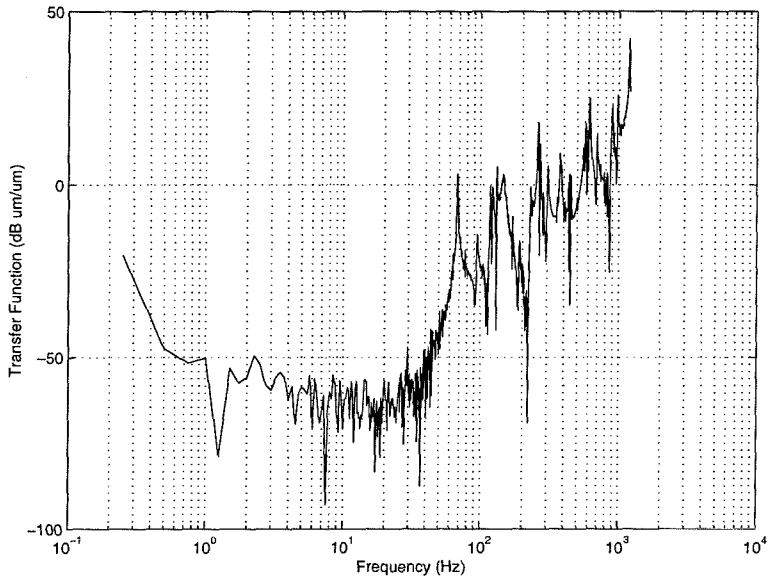

Figure C.8 Transfer function with accelerometer on the outer gimbal and the inner gimbal actuated. This figure along with Fig. C.7 show that there is substantial cross talk in the FSM mount.

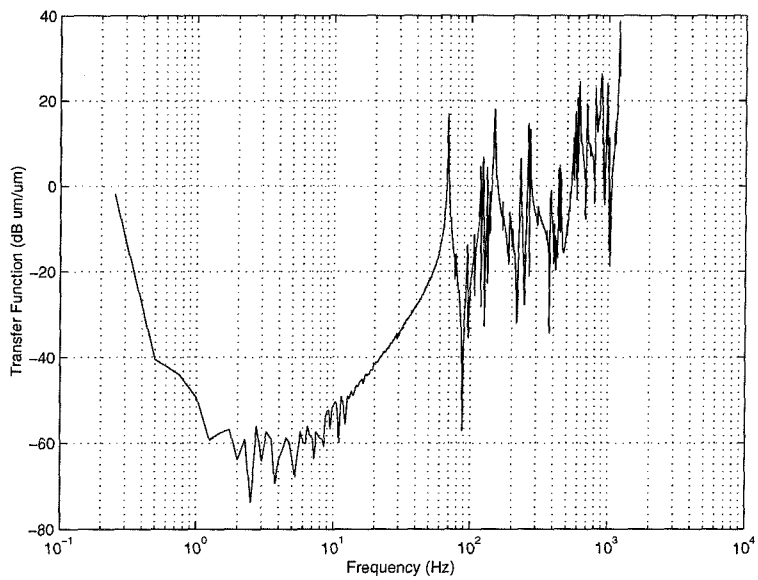

Figure C.9 Transfer function with accelerometer on the outer gimbal and the outer gimbal actuated. The first resonance is clearly visible here at 63 Hz. Notice that the amplitude of the resonance is highest in this figure (almost 20 dB above the value in Fig. C.6). This indicates that the outer gimbal is the predominant source of the resonance.

bar and into the gimbal. These holes were then tapped and 14 $1/4 - 20$ screws were used to bolt the bar securely to the outer gimbal. This had the effect of moving the first resonance in the system out to 94 Hz. Fig. C.10 shows the front side of the FSM mount with the steel bar bolted in place.

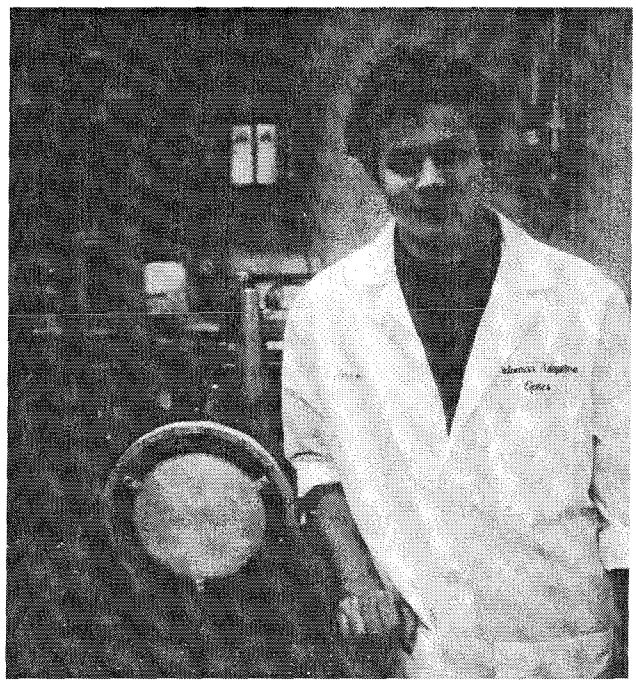

Figure C.10 Photograph of the mront of the FSM mount. This shows the cold pressed, hardened steel ring added to the outer gimbal in order to stiffen it and push the first resonance up to higher frequencies. The person provides a reference of scale.

The FSM performed $\pm$ 2.″1 of tip and tilt, but did not meet the update rate requirement. This is discussed briefly in the next section.

C.4 Required Improvements

Despite the addition of the steel bar to the outer gimbal of the FSM mount, this configuration was unacceptable. The observing run in December 1998 showed that when the FSM was updated at 100 Hz, there was still little rejection of tip-tilt energy

in the wavefront except below 1.0 Hz. Figs. C.11 and C.12 show power spectral distributions (PSD) of the energy in the deviation of the average centroid of the star image from the ideal value. In each plot the PSD is shown for a single axis with the loop open and the loop closed. Rejection of energy at the very lowest energies is good, on the level of two orders of magnitude. However, substantial energy still exists, even with the loop closed, at frequencies between 0.5 and 10 Hz. The only explanation for this is that the axes were not actuated independently because of the resonances in the mount. This "cross talk" between the axes is clearly visible in Figs. C.7 and C.8, which show the transfer function for each of the gimbals when the opposite gimbal was actuated.

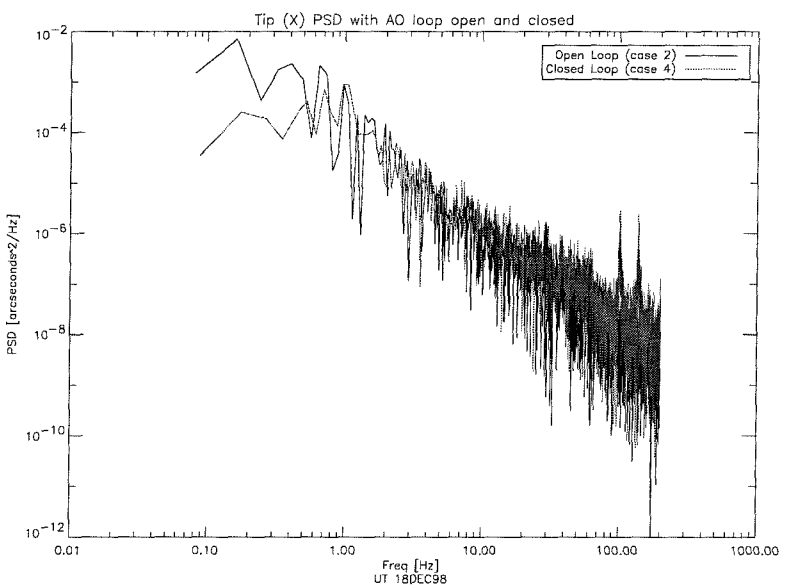

Figure C.11 Power spectral distribution of the FSM on the telescope: X-axis. The grey distribution shows the PSD with the adaptive optics loop closed. Note the rejection of energy at the very lowest frequencies. The black distribution is for open loop operation (no correction).

As a result of these measurements, it was decided that an entirely new FSM would be fabricated and the modified Aerotech mount would be abandoned.

For comparison we also present the PSD for all of the centroid residuals for the

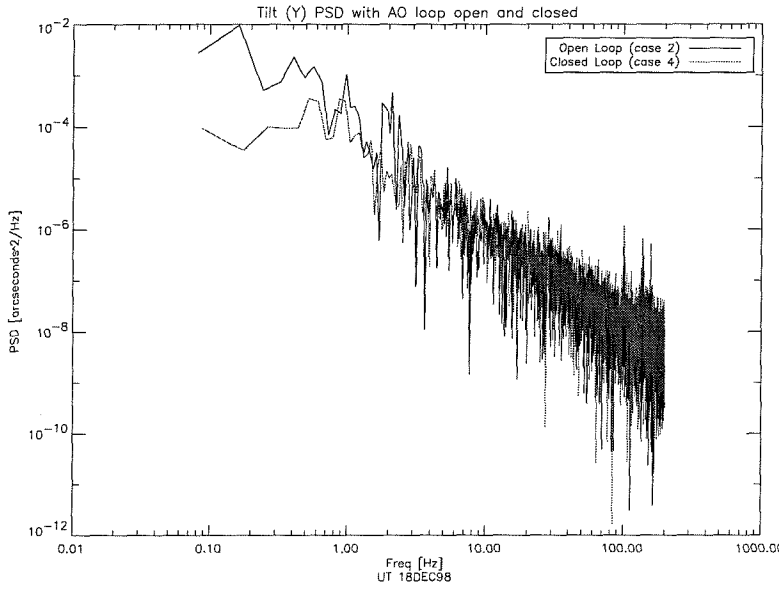

Figure C.12 Power spectral distribution of the FSM on the telescope: Y-axis. The grey distribution shows the PSD with the adaptive optics loop closed. Note the rejection of energy at the very lowest frequencies. The black distribution is for open loop operation (no correction).

same open and closed loop operation of the adaptive optics system (Fig. C.13). This shows that there is excellent rejection of the higher order wavefront distortions up to frequencies exceeding 10 Hz. This is ideally what the FSM should be able to do to the PSD of the average centroid residuals. Furthermore, the DM loop has not yet been optimized and should ultimately perform better than indicated in Fig. C.13.

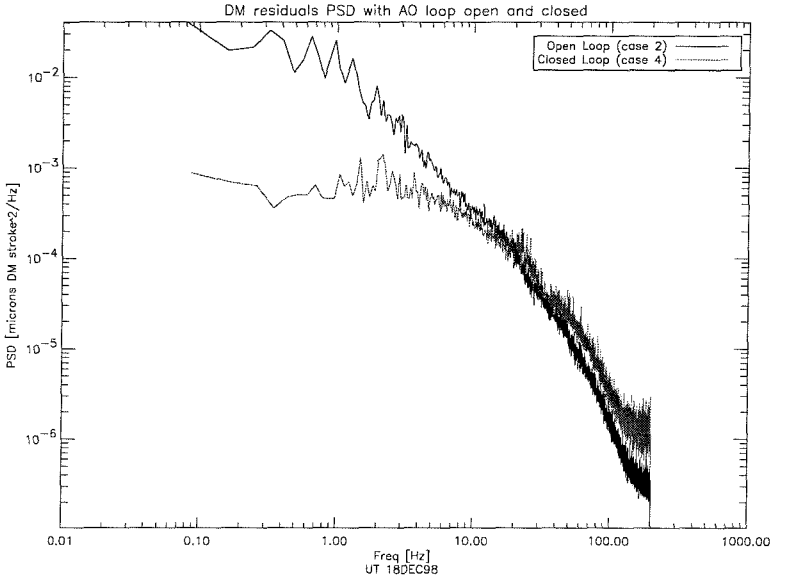

Figure C.13 Power spectral distribution of the DM on the telescope. The grey distribution shows the PSD of all the centroids of the individual subapertures with the adaptive optics loop closed. Note the rejection of energy below 10 Hz. The black curve shows the same distribution in open loop.

REFERENCES

Acton, S., Stomski, P., Wizinowich, P., Maute, J. and Gregory, T. 1996, *J. Opt. Soc. Am.*, **431**, 1542.

Alcock, C. et al. 1998, *Astrophys. J. Lett.*, **499**, L9.

Allard, F. and Hauschildt, P. H. 1995, *Astrophys. J.*, **445**, 433.

Allard, F., Hauschildt, P. H., Baraffe, I. and Chabrier, G. 1996, *Astrophys. J. Lett.*, **465**, L123.

Allard, F., Hauschildt, P. H., Alexander, D. R. and Starrfield, S. 1997, *Ann. Rev. Astron. Astrophys.*, **35**, 137.

Angel, J. R. P. 1994, *Nature*, **368**, 203.

Baraffe, I., Chabrier, G., Allard, F. and Hauschildt, P. H. 1995, *Astrophys. J. Lett.*, **446**, L35.

Barnes, S. and Sofia, S. 1996, *Astrophys. J.*, **462**, 746.

Basri, G. 1998, *ASP Conf. Ser.*, **134**, 394.

Basri, G. and Marcy, G. W. 1995, *Astron. J.*, **109**, 762.

Basri, G. and Marcy, G. 1997, in *Star Formation Near and Far* (New York: AIP Press, S. S. Holt and L. G. Mundy, eds.).

Basri, G., Marcy, G. and Graham, J. 1996, *Astrophys. J.*, **458**, 600.

Basri, G. and Martín, E.L. 1998, *ASP Conf. Ser.*, **134**, 284.

Basri, G. and Martín, E.L. 1999,*Astrophys. J.*, in press.

Becklin, E. E. and Zuckerman, B. 1988, *Nature*, **336**, 656.

Beichman, C. A. 1987, *Ann. Rev. Astron. Astrophys.*, **25**, 521.

Berriman, G. B. and Reid, I. N. 1987, *Mon. Not. Roy. Astron. Soc.*, **227**, 315.

Bildsten, L., Brown, E. F., Matzner C. D. and Ushomirsky G. 1997, *Astrophys. J.*, **482**, 442.

Black, D. C. 1997, *Astrophys. J. Lett.*, **490**, L171.

Boss, A. P. 1996, *Nature*, **379**, 397.

Boss, A. P. 1997, *Science*, **276**, 1836.

Bouvier, J., Stauffer, J., Martín, E., Barrado y Navascues, D., Wallace, B. and Bejar, V. 1998, *Astron. Astrophys.*, **335**, 183.

Brandl, B., Hayward, T. L., Houck, J. R., Gull, G. E., Pirger, B. and Schoenwald, J. 1997, *Proc. SPIE*, **3126**, 515.

Brigantic, R., Roggeman, M., Welsh, B. and Bauer, K. 1997, *Proc. SPIE*, **3126**, 151.

Burkert, A. and Bodenheimer, P. 1993, *Mon. Not. Roy. Astron. Soc.*, **264**, 798.

Burrows, A. and Liebert, J. 1993, *Rev. Mod. Phys.*, **65**, 301.

Burrows, A., Hubbard, W. B., Lunine, J. I., Guillot, T., Saumon, D. et al. 1996, *Nucl. Phys. B, Supp.*, **51B**, 76.

Burrows, A., Marley M., Hubbard W. B., Lunine J. I., Guillot T., Saumon D., Freedman R., Sudarsky D. and Sharp C. 1997, *Astrophys. J.*, **491**, 856.

Burrows, A., Marley, M. and Stauffer, J. R. 1999, in *Protostars and Planets IV* (Tucson: University of Arizona Press, V. Mannings, A. Boss and S. Russell, eds.).

Burrows, A. and Sharp, C. M. 1999, *Astrophys. J.*, **512**, 843.

Burrows, C. J. et al. 1995, *WFPC2 Instrument Handbook, Version 3.0* (Space Telescope Science Institute).

Butler, R. P., Marcy, G. W., Williams, E., Hauser, H. and Shirts, P. 1997, *Astrophys. J. Lett.*, **474**, L115.

Chabrier, G. and Baraffe, I. 1997, *Astron. Astrophys.*, **327**, 1039.

Chabrier, G. and Méra, D. 1998, *ASP Conf. Ser.*, **134**, 495.

Comeron, F., Rieke, G., Claes, P. and Torra, J. 1998, *Astron. Astrophys.*, **335**, 522.

Cross, L. E. et al. 1980, *Ferroelectrics*, **23**, 647.

Cudworth, K. M. 1976, *Astron. J.*, **81**, 519.

Cudworth, K. M. 1979, *Astron. J.*, **84**, 1866.

Da Costa, G. S. 1992, *ASP Conf. Ser.*, **23**, 121.

Danby, J. M. A. 1988, *Fundamentals of Celestial Mechanics, Second Edition* (New York: Willman-Bell), p. 165.

Danielson, R. E. 1966, *Astrophys. J.*, **143**, 949.

D'Antona, F. and Mazzitelli, I. 1994, *Astrophys. J. Suppl. Ser.*, **90**, 467.

D'Antona, F. 1995, in *The Bottom of the Main Sequence—and Beyond*, C. G. Tinney, ed. (New York: Springer).

Dekany, R., Wallace, K., Brack, G., Oppenheimer, B. R. and Palmer, D. 1997, *Proc. SPIE*, **3126**, 269.

Delfosse, X., Tinney, C., Forveille, T., Epchtein, N., Bertin, E., Borsenberger, J., Copet, E., de Batz, B., Fouque, P., Kimeswenger, S., LeBertre, T., Lacombe, F., Rouan, D. and Tiphene, D. 1997, *Astron. Astrophys.*, **327**, L25.

Delfosse, X., Forveille, T., Mayor, M., Perrier, C., Naef, D. and Queloz, D. 1998a, *Astron. Astrophys. Lett.*, **338**, L67.

Delfosse, X., Forveille, T., Beuzit, J.-L., Udry, S., Mayor, M. and Perrier, C. 1998b, in *Astron. Astrophys.* (submitted).

Drossart, P., Encrenaz, T., Schulz, R. and Stüwe, J. A. 1996, *Icarus*, **121**, 199.

Duquennoy, A. and Mayor, M. 1991, *Astron. Astrophys.*, **248**, 485.

Eggen, O.J. 1995, *Astron. J.*, **110**, 1749.

Elias, J. H., Frogel, J. A., Matthews, K. and Neugebauer, G. 1982, *Astron. J.*, **87**, 1029.

European Space Agency 1997, *Hipparcos and Tycho Catalogues*, ESA SP-1200.

Fegley, B. and Lodders, K. 1994, *Icarus*, **110**, 117.

Fegley, B. and Lodders, K. 1996, *Astrophys. J. Lett.*, **472**, L37.

Feigelson, E. D. 1996, *Astrophys. J.*, **468**, 306.

Forrest, W. J., Skrutskie, M. F. and Shure, M. 1988, *Astrophys. J. Lett.*, **330**, L119.

Geballe, T. R., Kulkarni, S. R., Woodward, C. E. and Sloan, G. C. 1996, *Astrophys. J. Lett.*, **467**, L101.

Giampapa, M. S. and Liebert, J. 1986, *Astrophys. J.*, **305**, 784.

Gilmozzi, R., Ewald, S. and Kinney, E. 1995, in *WFPC2 Instrument Science Report 95-02* (Space Telescope Science Institute).

Gizis, J. 1997, Ph.D. Thesis, California Institute of Technology.

Gliese, W. and Jahreiss, H. 1991, Preliminary Version of the Third Catalog of Nearby Stars.

Golimowski, D. A., Clampin, Durrance, S. T. and Barkhouser, R. H. 1992, *Appl. Opt.*, **31**, 4405.

Golimowski, D. A., Nakajima, T., Kulkarni, S. R. and Oppenheimer, B. R. 1995, *Astrophys. J. Lett.*, **444**, L101.

Golimowski, D. A., Kulkarni, S. R., Burrows, C. J., Brukardt, R. A. and Oppenheimer, B. R. 1998, *Astron. J.*, **115**, 2579.

Griffith, C. A., Yelle, R. V. and Marley, M. 1998, *Science*, **282**, 2063.

Guillot, T., Gautier, D., Chabrier, G. and Mosser, B. 1994, *Icarus*, **112**, 337.

Hambly, N., Hawkins, M.R.S. and Jameson, R.F. 1993, *Astron. Astrophys.*, **100**, 607.

Hambly, N. C. 1998, *ASP Conf. Ser.*, **134**, 11.

Haro, C. E, Chavira, A. and Gonzales, E. 1982, *Boll. del Instituto de Tonatzintla*, **3**, 1.

Hawkins, M. R. S. 1998, *ASP Conf. Ser.*, **134**, 20.

Hawley, S. L. 1995, in *The Bottom of the Main Sequence—and Beyond* (Springer, C. G. Tinney ed.).

Henry, T. J. and McCarthy, D. W. Jr. 1990, *Astrophys. J.*, **350**, 334.

Henry, T. J., McCarthy, D. W. Jr., Freeman, J. and Christou, J. C. 1992, *Astron. J.*, **103**, 1369.

Henry, T. J. and McCarthy, D. W. Jr. 1993, *Astron. J.*, **106**, 773.

Henry, T. J., Ianna, P. A., Kirkpatrick, J. D. and Jahreiss, H. 1997, *Astron. J.*, **114**, 388.

Herbig, G. H. 1962, *Astrophys. J.*, **136**, 736.

Herbig, G. H. 1996, *Astron. J.*, **111**, 1241.

Hirschfeld, A. and Sinnott, R. W. 1995, *Sky Catalog 2000.0, Vol. 2*,(Cambridge: Cambridge University Press and Sky Publishing Corporation).

Hodgkin, S. and Jameson, R. F. 1997., *Cont. Phys.*, **38**, 117.

Holtzman, J. A., Burrows, C. J., Casertano, S., Hester, J. J., Trauger, J. T., Watson, A. M. and Worthey, G. 1995a, *Pub. Astron. Soc. Pac.*, **107**, 1065.

Holtzman, J., Hester, J. J., Casertano, S., Trauger, J. T., Watson, A. M., Ballester, G. E., Burrows, C. J., Clarke, J. T., Crisp, D., Evans, R. W., Gallagher, J. S., Griffiths, R. E., Hoessel, J. G., Matthews, L. D., Mould, J. R., Scowen, P. A., Stapelfeldt, K. R., and Westphal, J. A. 1995b, *Pub. Astron. Soc. Pac.*, **107**, 156.

Horne, K. 1986, *Pub. Astron. Soc. Pac.*, **98**, 609.

Irwin, M., McMahon, R. and Hazard, C. 1991, *ASP Conf. Ser.*, **21**, 117.

Jameson, R. F. and Skillen, I. 1989, *Mon. Not. Roy. Astron. Soc.*, **239**, 247.

Jones, H. R. A., Longmore, A. J., Jameson, R. F. and Mountain, M. 1994, *Mon. Not. Roy. Astron. Soc.*, **267**, 413.

Jones, H. R. A. and Tsuji, T. 1997, *Astrophys. J. Lett.*, **48**, L39.

Kafatos, M. C., Harrington, R. S. and Maran, S. P. eds. 1986., in *Astrophysics of Brown Dwarfs* (New York: Cambridge University Press).

Karkoschka, E. 1994, *Icarus*, **111**, 174.

Kerins, E. and Wyn Evans, N. 1998, *Astrophys. J. Lett.*, **503**, L75.

Khlifi, M., Paillous P., Bruston P., Guillemin J. C., Benilan Y., Daoudi A. and Raulin F. 1997, *Spectrochimica Acta A*, **53**, 707.

Kirkpatrick, J. D., Henry, T. J. and McCarthy, D. W. 1991, *Astrophys. J. Supp. Ser.*, **77**, 417.

Kirkpatrick, J. D., Kelly, D. M., Rieke, G. H., Liebert, J., Allard, F. and Wehrse, R. 1993, *Astrophys. J.*, **402**, 643.

Kirkpatrick, J. D. and McCarthy, D. W. 1994, *Astron. J.*, **107**, 333.

Kirkpatrick, J.D. 1997, *ASP Conf. Ser.*, **134**, 405.

Kirkpatrick, J.D., Henry, T. and Irwin, M. 1997., *Astron. J.*, **113**, 1421.

Kirkpatrick, J. D., Allard, F., Bida, T., Zuckerman, B., Becklin, E. E., Chabrier, G. and Baraffe, I. 1998, in *Astrophys. J.* (submitted).

Krasnopolsky, V. A., Bjoraker, G. L., Mumma, M. J. and Jennings, D. E. 1997, *J. Geophys. Res.*, **102**, 6525.

Krist, J. E., Golimowski, D. A., Schroeder, D. J. and Henry, T. J. 1998, *Publ. Astron. Soc. Pac.*, **110**, 1046.

Kulkarni, S. R. 1997, *Science*, **276**, 1350.

Kumar, S. S. 1963, *Astrophys. J.*, **137**, 1121.

Leggett, S. and Hawkins, M.R. 1988, *Mon. Not. Roy. Astron. Soc.*, **234**, 1065.

Leggett, S. K. 1992, *Astrophys. J. Suppl. Ser.*, **82**, 351.

Leggett, S., Harris, H. and Dahn, C. 1994, *Astron. J.*, **108**, 944.

Leisawitz, D., Bash, F. N. and Thaddeus, P. 1989, *Astrophys. J. Suppl. Ser.*, **70**, 731.

Leitherer, C. et al. 1995, *HST Data Handbook, Version 2.0* (Space Telescope Science Institute).

Letokhov, V. S., Andreev, S. V. and Mishin, V. I. 1987, *Phys. Rev. Lett.*, **59**, 1274.

Liebert, J. 1995, in *The Bottom of the Main Sequence—And Beyond* (Springer, C. G. Tinney, ed.).

Lissauer, J., Butler, P. and Stauffer, J. R. 1999, in *Protostars and Planets IV* (Tucson: University of Arizona Press, V. Mannings, A. Boss and S. Russell, eds.).

Luhman, K. L., Liebert, J. and Rieke, G. H. 1997, *Astrophys. J. Lett.*, **489**, L165.

Luhman, K. L., Rieke, G. H., Lada, C. and Lada, E. 1998, *Astrophys. J.*, **508**, 347.

Luyten, W. and Kowal, C. 1975, *Proper Motion Survey with the 48 Inch Schmidt Telescope* (Minneapolis: Observatory of the University of Minnesota).

Lyot, M. B. 1939, *Mon. Not. Roy. Astron. Soc.*, **99**, 578.

Magazzù, A., Martín, E. L. and Rebolo, R. 1991, *Astron. Astrophys.*, **249**, 149.

Magazzù, A., Martín, E. L. and Rebolo, R. 1993, *Astrophys. J. Lett.*, **404**, L17.

Magazzù, A., Rebolo, R., Zapatero Osorio, M., Martín, E. and Hodgkin, S. 1998, *Astrophys. J. Lett.*, **497**, L47.

Marcy, G., Basri, G. and Graham, J. 1994, *Astrophys. J. Lett.*, **428**, L57.

Marcy, G., Butler, P. and Stauffer, J. R. 1999, in *Protostars and Planets IV* (Tucson: University of Arizona Press, V. Mannings, A. Boss and S. Russell, eds.).

Marley, M. S., Saumon, D., Guillot, T., Freedman, R. S., Hubbard, W. B., Burrows, A. and Lunine, J. I. 1996, *Science*, **272**, 1919.

Marley, M. S. 1997, *ASP Conf. Ser.*, **134**, 383.

Martín, E. L., Rebolo, R., Magazzù, A. and Pavlenko, Y. A. 1994, *Astron. Astrophys.*, **282**, 503.

Martín, E., Basri, G., Delfosse, X. and Forveille, T. 1997, *Astron. Astrophys.*, **327**, L29.

Martín, E. L., Zapatero-Osorio, M. R. and Rebolo, R. 1998, *ASP Conf. Ser.*, **134**, 507.

Martin, L. and Bradner, W. 1995, *Astron. Astrophys.*, **294**, 744.

Massey, P. and Gronwal, C. 1990, *Astrophys. J.*, **358**, 344.

Matthews, K. and Soifer, B. T. 1994, in *Infrared Astronomy with Arrays: The Next Generation* (Kluwer Academic Publishers, McLean, S. I., ed.).

Matthews, K., Nakajima, T., Kulkarni, S. R. and Oppenheimer, B. R. 1996, *Astron. J.*, **112**, 1678.

Mayor, M. and Queloz, D. 1997, *Nature*, **378**, 355.

McCarthy, D. W., Jr., Probst, R. G. and Low, F. J. 1985, *Astrophys. J. Lett.*, **290**, L9.

McCaughrean, M. J. and Stauffer, J. R. 1994, *Astron. J.*, **108**, 1383.

Meadows, V. S. and Crisp, D. 1996, *J. Geophys. Res.*, **101**, 4595.

Meynet, G., Mermilliod, J.-C. and Maeder, A. 1993, *Astron. Astrophys. Suppl. Ser.*, **98**, 477.

Micela, G., Sciortino, S., Kashyap, V., Harnden, F. R., Jr. and Rosner, R. 1996, *Astrophys. J. Suppl. Ser.*, **102**, 75.

Monet, D. G. 1992, *ASP Conf. Ser.*, **23**, 224.

Mould, J. R. 1978, *Astrophys. J.*, **226**, 923.

Nakajima, T. 1994, *Astrophys. J.*, **425**, 348.

Nakajima, T., Durrance, S. T., Golimowski, D. A. and Kulkarni, S. R. 1994, *Astrophys. J.*, **428**, 797.

Nakajima, T., Oppenheimer, B. R., Kulkarni, S. R., Golimowski, D. A., Matthews, K. and Durrance, S. T. 1995, *Nature*, **378**, 463.

Neugebauer, G. 1995, personal communication.

Neuhäuser, R., Sterzik, M. F., Schmitt, J. H. M. M., Wichmann, R. and Krautter, J. 1995a, *Astron. Astrophys.*, **295**, L5.

Neuhäuser, R., Sterzik, M. F., Torres, G. and Martín, E. L. 1995b, *Astron. Astrophys.*, **299**, L13.

Noll, K. S., Knacke, R. F., Geballe, T. R. and Tokunaga, A. T. 1988, *Astrophys. J.*, **324**, 1210.

Noll, K. S. 1993, *ASP Conf. Ser.*, **41**, 51.

Noll, K. S. and Marley, M. 1996, in *Planets Beyond the Solar System* (Space Telescope Science Institute).

Noll, K. S., Geballe, T. R. and Marley, M. S. 1997, *Astrophys. J. Lett.*, **489**, L87.

Oke, J. B., Cohen, J. G., Carr, M., Cromer, J., Dingizian, A., Harris, F. H., Labrecque, S., Lucinio, R., Schaal, W., Epps, H. and Miller, J. 1995, *Pub. Astron. Soc. Pac.*, **107**, 375.

Oppenheimer, B. R., Kulkarni, S. R., Matthews, K. and Nakajima, T. 1995, *Science*, **270**, 1478.

Oppenheimer, B. R. 1997, *ASP Conf. Ser.*, **134**, 196.

Oppenheimer, B. R., Basri, G., Nakajima, T. and Kulkarni, S. R. 1997b, *Astron. J.*, **113**, 296.

Oppenheimer, B. R., Palmer, D., Dekany, R., Sivaramakrishnan, A., Ealey, M. A. and Price, T. R. 1997c, *Proc. SPIE*, **3126**, 569.

Oppenheimer, B. R., Kulkarni, S. R., Matthews, K. and van Kerkwijk, M. H. 1998, *Astrophys. J.*, **502**, 932.

Oppenheimer, B. R., Kulkarni, S. R. and Stauffer, J. R. 1999a, in *Protostars and Planets IV* (Tucson: University of Arizona Press, V. Mannings, A. Boss and S. Russell, eds.).

Oppenheimer, B. R., Golimowski, D. A., Kulkarni, S. R., Matthews, K. and Nakajima, T. 1999b, in *Astron. J.* (submitted).

Osterbrock, D. E., Fulbright, J. P., and Bida, T. A. 1997, *Pub. Astron. Soc. Pac.*, **109**, 614.

Pallavicini, R. 1989, *Astron. Astrophys. Rev.*, **1**, 177.

Patenaude, M. 1978, *Astron. Astrophys.*, **66**, 225.

Pavlenko, Ya. V., Rebolo, R., Martín, E. L. and García López, R. J. 1995, *Astron. Astrophys.*, **303**, 807.

Pavlenko, Ya. V. 1998, *Astron. Rep.*, **42**, 787.

Pinfield, D., Hodgkin, S., Jameson, R., Cossburn, M. and von Hippel, T. 1997, *Mon. Not. Roy. Astron. Soc.*, **287**, 180.

Pinsonneault, M., Stauffer, J., Soderblom, D., King, J. and Hanson, R. 1998, *Astrophys. J.*, **504**, 170.

Pound, M. W. and Blitz, L. 1995, *Astrophys. J.*, **444**, 270.

Probst, R. G. 1983, *Astrophys. J.*, **274**, 237.

Raboud, D. and Mermilliod, J.-C. 1998, *Astron. Astrophys.*, **329**, 101.

Raulin, F. and Bruston, P. 1996, *Life Sci.*, **18**, 41.

Rebolo, R., Martín, E. and Magazzù, A. 1992, *Astrophys. J.*, **389**, L83.

Rebolo, R., Zapatero Osorio, M. and Martín, E. 1995, *Nature*, **377**, 129.

Rebolo, R., Martín, E. L., Basri, G., Marcy, G. and Zapatero Osorio, M.R. 1996, *Astrophys. J. Lett.*, **469**, L53.

Rebolo, R., Martín, E. L. and Zapatero-Osorio, M. R. eds. 1998, in *Brown Dwarfs and Extrasolar Planets* (San Francisco: Astronomical Society of the Pacific) Conference Series Vol. 134).

Reid, I. N., Hawley, S. L. and Mateo, M. 1995, *Mon. Not. Roy. Astron. Soc.*, **272**, 828.

Reid, I. N. and Gizis, J. E. 1997, *Astron. J.*, **113**, 2246.

Rieke, G. H. and Rieke, M. J. 1990, *Astrophys. J. Lett.*, **362**, L21.

Rossow, W. B. 1978, *Icarus*, **36**, 1.

Ruiz, M. T., Leggett, S. K. and Allard, F. 1997, *Astrophys. J. Lett.*, **491**, L107.

Saumon, D., Marley, M. S., Guillot, T. and Freedman, R. S. 1996, *Bull. American Astron. Soc.*, **28**, 1114.

Schiavon, R. P., Barbuy, B. and Singh, P. D. 1997, *Astrophys. J.*, **484**, 499.

Schroeder, D. J. and Golimowski, D. A. 1996, *Pub. Astron. Soc. Pac.*, **108**, 510.

Schultz, A. B., Allard, F., Clampin, M., McGrath, M., Bruhweiler, F. C., Valenti, J. A., Plait, P., Hulbert, S., Baum, S., Woodgate, B. E., Bowers, C. W., Kimble, R. A., Maran, S. P., Moos, H. W. and Roesler, F. 1998, *Astrophys. J. Lett.*, **492**, L181.

Shao, M. and Colavita, M. M. 1992, *Astron. Astrophys.*, **262**, 353.

Sharp, C. M. and Huebner, W. F. 1990, *Astrophys. J. Supp. Ser.*, **72**, 417.

Shu, F. H., Adams, F. C. and Lizano, S. 1987, *Ann. Rev. Astron. Astrophys.*, **25**, 23.

Simons, D. A., Henry, T. J. and Kirkpatrick, J. D. 1996, *Astron. J.*, **112**, 2238.

Soderblom, D. R., Stauffer, J. R., Hudon, J. D. and Jones, B. F. 1993a, *Astrophys. J. Suppl. Ser.*, **85**, 315.

Soderblom, D. R., Stauffer, J. R., MacGregor, K. B. and Jones, B. F. 1993b, *Astrophys. J.*, **409**, 624.

Stauffer, J. R. 1982, *Astron. J.*, **87**, 899.

Stauffer, J. R. 1984, *Astrophys. J.*, **280**, 189.

Stauffer, J. R. and Hartmann, L. W. 1987, *Astrophys. J.*, **318**, 337.

Stauffer, J., Hamilton, D., Probst, R., Rieke, G. and Mateo, M. 1989, *Astrophys. J. Lett.*, **344**, L21.

Stauffer, J. R., Giampapa, M. S., Herbst, W., Vincent, J. M., Hartmann, L. W. and Stern, R. A. 1991, *Astrophys. J.*, **374**, 142.

Stauffer, J., Liebert, J., Giampapa, M., MacIntosh, B., Reid, I. N. and Hamilton, D. 1994, *Astron. J.*, **108**, 160.

Stauffer, J. R., Liebert, J. and Giampapa, M. 1995, *Astron. J.*, **109**, 298.

Stauffer, J., Schultz, G. and Kirkpatrick, J.D. 1998, *Astrophys. J. Lett.*, **499**, L199.

Steele, I. A., Jameson, R. F. and Hambly, N. C. 1993, *Mon. Not. Roy. Astron. Soc.*, **263**, 647.

Steele, I. A., Jameson, R. F., Hodgkin, S. T. and Hambly, N. C. 1995, *Mon. Not. Roy. Astron. Soc.*, **275**, 841.

Steele, I. A. and Jameson, R. F. 1995, *Mon. Not. Roy. Astron. Soc.*, **272**, 630.

Sterzik, M. F. and Durisen, R. H. 1995, *Astron. Astrophys.*, **304**, L9.

Stevenson, D. J. 1986, in *Astrophysics of Brown Dwarfs* (Cambridge: Cambridge University Press, M. C. Kafatos, R. S. Harrington and S. P. Maran, eds.).

Stevenson, D. J. 1991, *Annu. Rev. Astron. Astrophys.*, **29**, 163.

Stringfellow, G. 1991, *Astrophys. J. Lett.*, **375**, L21.

Tartar, J. C. 1986, in *Astrophysics of Brown Dwarfs* (Cambridge: Cambridge University Press, M. C. Kafatos, R. S. Harrington and S. P. Maran, eds.).

ten Brummelaar, T. A., Mason, B. D., Bagnuolo, Jr., W. G., Hartkopf, W. I., McAlister, H. A. and Turner, N. H. 1996, *Astron. J.*, **112**, 1180.

Thackrah, A., Jones, H. and Hawkins, M. 1997, *Mon. Not. Roy. Astron. Soc.*, **284**, 507.

Tinney, C. G. 1995. ed. *The Bottom of the Main Sequence—and Beyond* (New York: Springer).

Tinney, C. G. 1997, *ASP Conf. Ser.*, **134**, 75.

Tinney, C. G., Mould, J. R. and Reid, I. N. 1993, *Astron. J.*, **105**, 1045.

Tinney, C. G., Reid, I. N., Gizis, J. E. and Mould, J. R. 1995, *Astron. J.*, **110**, 3014.

Tinney, C. G., Delfosse, X. and Forveille, T. 1997, *Astrophys. J. Lett.*, **490**, L95.

Tinney, C. G. 1998, *Mon. Not. Roy. Astron. Soc.*, **296**, L42.

Toth, R. A. 1997., *J. Mol. Spect.*, **186**, 276.

Tsuji, T. 1964, *Ann. Tokyo Astron. Obs. Ser. II*, **9**, 1.

Tsuji, T. and Ohnaka, K. 1995, in *Elementary Processes in Dense Plasmas* (Addison–Wesley, S. Ichimaru & S. Ogata, eds.).

Tsuji, T., Ohnaka, K. and Aoki, W. 1995, in *The Bottom of the Main Sequence—and Beyond* (New York: Springer, C. G. Tinney, ed.).

Tsuji, T., Ohnaka, K. and Aoki, W. 1996a, *Astron. Astrophys. Lett.*, **305**, L1.

Tsuji, T., Ohnaka, K., Aoki, W. and Nakajima, T. 1996b, *Astron. Astrophys. Lett.*, **308**, L29.

Uchino, K. 1986, *Ceramics Bulletins*, **65**, 647.

Ungerechts, H. and Thaddeus, P. 1987, *Astrophys. J. Suppl. Ser.*, **63**, 645.

van Altena, W. F., Lee, J. T. and Hoffleit, D. 1995, in *The General Catalog of Trigonometric Parallaxes, Fourth Edition* (New Haven, CT: Yale University Observatory).

Ventura, P., Zeppieri, A., Mazzitelli, I. and D'Antona, F. 1998, *Astron. Astrophys.*, **331**, 1011.

Vogt, S. S. 1992, in *ESO Workshop on High Resolution Spectroscopy with the VLT* (European Space Agency).

White, R. E. and Bally, J. 1993, *Astrophys. J.*, **409**, 234.

Wilking, B. A., Green, T. P. and Meyer, M. R., 1998, *Astron. J.*, **117**, 469.

Wolszczan, A. and Frail, D. A. 1992, *Nature*, **355**, 145.

Yuan, C. and Waxman, A.M. 1977, *Astron. Astrophys.*, **58**, 65.

Zapatero-Osorio, M. R., 1997, *Astrophys. J. Lett.*, **491**, L81.

Zuckerman, B. and Becklin, E. E. 1992, *Astrophys. J.*, **386**, 260.